InSAR CRUSTAL DEFORMATION MONITORING, MODELING AND ERROR ANALYSIS

EDITED BY: Yu Chen, Junshi Xia and Chen Yu
COORDINATED BY: Bingqian Chen
PUBLISHED IN: Frontiers in Environmental Science, Frontiers in Earth Science and Frontiers in Ecology and Evolution

frontiers Research Topics

frontiers

ISSN 1664-8714
ISBN 978-2-83250-213-6
DOI 10.3389/978-2-83250-213-6

About Frontiers

Frontiers is more than just an open-access publisher of scholarly articles: it is a pioneering approach to the world of academia, radically improving the way scholarly research is managed. The grand vision of Frontiers is a world where all people have an equal opportunity to seek, share and generate knowledge. Frontiers provides immediate and permanent online open access to all its publications, but this alone is not enough to realize our grand goals.

Frontiers Journal Series

The Frontiers Journal Series is a multi-tier and interdisciplinary set of open-access, online journals, promising a paradigm shift from the current review, selection and dissemination processes in academic publishing. All Frontiers journals are driven by researchers for researchers; therefore, they constitute a service to the scholarly community. At the same time, the Frontiers Journal Series operates on a revolutionary invention, the tiered publishing system, initially addressing specific communities of scholars, and gradually climbing up to broader public understanding, thus serving the interests of the lay society, too.

Dedication to Quality

Each Frontiers article is a landmark of the highest quality, thanks to genuinely collaborative interactions between authors and review editors, who include some of the world's best academicians. Research must be certified by peers before entering a stream of knowledge that may eventually reach the public - and shape society; therefore, Frontiers only applies the most rigorous and unbiased reviews.
Frontiers revolutionizes research publishing by freely delivering the most outstanding research, evaluated with no bias from both the academic and social point of view. By applying the most advanced information technologies, Frontiers is catapulting scholarly publishing into a new generation.

What are Frontiers Research Topics?

Frontiers Research Topics are very popular trademarks of the Frontiers Journals Series: they are collections of at least ten articles, all centered on a particular subject. With their unique mix of varied contributions from Original Research to Review Articles, Frontiers Research Topics unify the most influential researchers, the latest key findings and historical advances in a hot research area! Find out more on how to host your own Frontiers Research Topic or contribute to one as an author by contacting the Frontiers Editorial Office: frontiersin.org/about/contact

InSAR CRUSTAL DEFORMATION MONITORING, MODELING AND ERROR ANALYSIS

Topic Editors:
Yu Chen, China University of Mining and Technology, China
Junshi Xia, Riken, Japan
Chen Yu, Newcastle University, United Kingdom

Coordinator Editor:
Bingqian Chen, Jiangsu Normal University, China

Citation: Chen, Y., Xia, J., Yu, C., Chen, B., eds. (2022). InSAR Crustal Deformation Monitoring, Modeling and Error Analysis. Lausanne: Frontiers Media SA.
doi: 10.3389/978-2-83250-213-6

Table of Contents

frontiers | Frontiers in Environmental Science

TYPE Editorial
PUBLISHED 01 September 2022
DOI 10.3389/fenvs.2022.1009492

OPEN ACCESS

EDITED AND REVIEWED BY
Alexander Kokhanovsky,
Max Planck Institute for Chemistry, Germany

*CORRESPONDENCE
Yu Chen,
chenyu@cumt.edu.cn

SPECIALTY SECTION
This article was submitted to Environmental Informatics and Remote Sensing, a section of the journal Frontiers in Environmental Science

RECEIVED 02 August 2022
ACCEPTED 08 August 2022
PUBLISHED 01 September 2022

CITATION
Chen Y, Xia J, Yu C and Chen B (2022), Editorial: InSAR crustal deformation monitoring, modeling and error analysis. *Front. Environ. Sci.* 10:1009492. doi: 10.3389/fenvs.2022.1009492

Editorial: InSAR crustal deformation monitoring, modeling and error analysis

Yu Chen[1]*, Junshi Xia[2], Chen Yu[3] and Bingqian Chen[4]

[1]School of Environment and Spatial Informatics, China University of Mining and Technology, Xuzhou, China, [2]RIKEN Center for Advanced Intelligence Project (AIP), Chuo, Japan, [3]College of Geological Engineering and Geomatics, Chang'an University, Xi'an, China, [4]School of Geography and Geomatics and Urban-Rural Planning, Jiangsu Normal University, Xuzhou, China

KEYWORDS

InSAR, MT-InSAR, deformation monitoring and prediction, time series analysis, modeling

Editorial on the Research Topic
InSAR crustal deformation monitoring, modeling and error analysis

Background

Crustal deformation associated with endogenous forces of the earth (e.g., volcanic events, earthquakes, landslides, and collapses) and anthropogenic activities (e.g., urban construction, mining activities, oil and groundwater extraction) has been observed all over the world, which has become one of the most significant geological hazards globally. As one of the most effective means for measuring crustal deformation, interferometric synthetic aperture radar (InSAR) can provide high-resolution, high-precision, and large-scale land surface displacements as well as their spatio-temporal evolution behaviors. InSAR monitoring and modeling outputs can help understand the deformation mechanisms and minimize exposure of people and assets to potential damages. With the recent development and improvement in satellite technologies and extensive data computing methodologies, InSAR deformation monitoring, analyzing, and modeling, which is essential for disaster control, faces new and emerging challenges and produces remarkable progress.

Motivation for the topic

Over the past two decades, InSAR technology has become a powerful tool for measuring Earth's deformation with high spatial resolution and high precision and is playing a key role in monitoring various natural and anthropogenic hazards related to earthquakes, volcanoes, landslides, groundwater/oil extraction, urban construction, and

mining activities, etc. Nowadays, many efficient InSAR approaches, such as PS-InSAR, SBAS-InSAR, DS-InSAR, etc., have widely been exploited over the years and have already demonstrated their values. With the recent development and improvement in satellite technologies and extensive data computing methodologies, it is time that we present some of the latest advances in InSAR Crustal Deformation Monitoring, Modeling and Error Analysis.

Summary of the papers

This Research Topic contains eleven articles published, involving sixty authors from seventeen research institutions. Most papers utilize mainly InSAR, D-InSAR, multi-temporal InSAR or multi-sensors InSAR techniques to investigate and analyze the ground deformation related to earthquakes, mining activities, landslides and extraction of groundwater, aiming to understand their dynamical mechanisms and provide technical support for assessment and early-warning of related geohazards. Some authors focus on developing novel methods to improve the reliability of deformation results. Deep learning approaches are also integrated within InSAR processing and recognizing deformation patterns. In the following, we summarize the main work and achievements of the papers.

Liao et al. combined D-InSAR and pixel offset tracking techniques to characterize the co-seismic displacement and extract the trace of the rupturing fault for the 2022 Qinghai Menyuan (China) Ms 6.9 earthquake. They inverted the slip distribution by adopting the steepest descent method and analyzed the stress condition of the surrounding faults based on the calculated Coulomb stress change. They suggested that attentions should be paid to Lenglongling fault, Tolaishan fault, SunanQilian fault, and Minyue-Damaying fault in future research. Li et al. obtained the co-seismic deformation fields of the 21 May 2021 Mw 6.1 earthquake in Yangbi (China) by use of Sentinel-1 SAR images acquired from ascending and descending tracks. The slip distribution of the rupture plane was inverted with the particle swarm optimization method. Results indicated that a steeply dipping dextral strike-slip fault controlled the earthquake. Wang et al. gave a detailed joint analysis of the co-seismic and post-seismic deformation of the 2020 Mw 6.0 Jiashi earthquake in Xinjiang (China) using both D-InSAR and SBAS-InSAR techniques. The optimal geometric parameters and slip distribution were inverted based on the Okada model. All papers above researched the deformation fields of recent earthquakes, aiming to provide useful information to better understand the tectonic background and mechanisms of corresponding regions.

Qin et al. jointly used the finite difference method 3D model and the stacking InSAR to monitor the ground deformation in the Fangezhuang coal mining area. By detailed investigation of the correlation between the spatial pattern of deformation and the geological faults, they concluded that the spatial extent of the observed ground movement was controlled by a tectonic fault that mining activities had reactivated. Not only ground surface of mining area is affected by considerable deformation, and the mine waste dump experiences subsidence which should not be ignored since it could cause landslides. Tabish et al. proposed a strategy to characterize and predict the spatio-temporal evolution of the subsidence of mine waste dump with the aid of InSAR and a secondary consolidation model. The method was applied and tested over a mine waste dump in Weijiamao mine (China). Low coherence induced by land use cover and deformation gradient is always a challenge for deformation monitoring in mining areas using InSAR. To overcome this limitation, Du et al. developed an improved phase optimization algorithm to increase the density of measurement points and reduce the influence of phase noise. It was demonstrated that the proposed method was practically feasible for long time and wide scale deformation monitoring in mining areas. Wang et al. presented a novel phase unwrapping method based on U-Net convolutional neural network to reduce the uncertainties resulted from inaccurate interferometric phase unwrapping. The method was compared with the traditional minimum cost flow method and its effectiveness was verified in Peibei mining area of Xuzhou, China. Yu et al. also integrated a deep learning algorithm (named Light YOLO-Basin model) but with different objective with Wang et al. The model was used to automatically recognize the subsidence basins in two typical mining areas with wide swath InSAR interferograms. It showed potentials in terms of detection speed and detection accuracy.

Identifying slope active deformation areas (SADAs) is important to early-warning and prevention of potential geological hazards. Wang et al. observed the long-term deformation in Zhouqu region (China) from January 2019 to February 2021 using DS-InSAR technique. They proposed a method for automatically identifying SADA based on the large-scale deformation results. It could effectively eliminate the region affected by geometric distortion. Zhu et al. focused on fully using multi-source, multi-sensor, and multi-temporal SAR images to detect ground deformation. With the help of spatial coherence estimated from Sentinel-1 interferograms, Ali et al. discriminated between active and stagnant dune regions, assisting in assessing aeolian activity in Bodélé Depression (Chad).

Future perspectives

The contributions of this research topic convey that InSAR has been a unique tool among the geoscience communities for making precise measurements of ground motions of various types. Distinguished authors have made rigorous and meticulous analyses of InSAR-derived deformation maps to

reveal the geophysical fundamentals that underlie earthquakes, rock slides, ground subsidence, and underground mining activities. These have inspired us to explore more exciting technical and scientific breakthroughs in many aspects of InSAR. First, technological advances in InSAR will enable innovative applications where the usage of traditional InSAR is complex, such as recording glacier movements, flood coverages, fire scars, land cover types, and soil moisture contents. Second, nearly all studies in this special issue focus on using Sentinel-1 images owing to its availability and continuance.Nevertheless, other satellites with diverse signal wavelengths, polarizations, and orbit geometries offer more comprehensive deformation mapping capabilities, such as Sentinel-1C/D, Gaofen-3B/C, GeoSAR, and NISAR. Finally, automated InSAR processing systems will be more widely available such as the COMET-LiCS Sentinel-1 InSAR portal (https://comet.nerc.ac.uk/comet-lics-portal/), and Jet Propulsion Laboratory's (JPL's) ARIA Science Data System (https://asf.alaska.edu/data-sets/derived-data- sets/sentinel-1-interferograms/). These services provide rapid and continuous InSAR interferograms, which largely facilitate the routine monitoring of natural hazards and natural resources.

Author contributions

Editorial written by YC, CY, and BC, modified by JX.

Conflict of interest

The authors declare that the research was conducted in the absence of any commercial or financial relationships that could be construed as a potential conflict of interest.

Publisher's note

frontiers in Earth Science

ORIGINAL RESEARCH
published: 16 November 2021
doi: 10.3389/feart.2021.761653

A Novel Phase Unwrapping Method Used for Monitoring the Land Subsidence in Coal Mining Area Based on U-Net Convolutional Neural Network

Zhiyong Wang[1], Lu Li[2], Yaran Yu[1], Jian Wang[1], Zhenjin Li[1] and Wei Liu[1]*

[1]College of Geodesy and Geomatics, Shandong University of Science and Technology, Qingdao, China, [2]Changzhou Construction Research Institute Group Co., Ltd, Changzhou, China

OPEN ACCESS

Edited by:
Yu Chen,
China University of Mining and Technology, China

Reviewed by:
Sen Du,
Universitat Politecnica de Catalunya, Spain
Hongdong Fan,
China University of Mining and Technology, China
Peng Liu,
Southern University of Science and Technology, China
Francescopaolo Sica,
German Aerospace Center, Germany

***Correspondence:**
Zhiyong Wang
skd994177@sdust.edu.cn

Specialty section:
This article was submitted to Environmental Informatics and Remote Sensing, a section of the journal Frontiers in Earth Science

Received: 20 August 2021
Accepted: 07 October 2021
Published: 16 November 2021

Citation:
Wang Z, Li L, Yu Y, Wang J, Li Z and Liu W (2021) A Novel Phase Unwrapping Method Used for Monitoring the Land Subsidence in Coal Mining Area Based on U-Net Convolutional Neural Network. Front. Earth Sci. 9:761653. doi: 10.3389/feart.2021.761653

Large-scale and high-intensity mining underground coal has resulted in serious land subsidence. It has caused a lot of ecological environment problems and has a serious impact on the sustainable development of economy. Land subsidence cannot be accurately monitored by InSAR (interferometric synthetic aperture radar) due to the low coherence in the mining area, excessive deformation gradient, and the atmospheric effect. In order to solve this problem, a novel phase unwrapping method based on U-Net convolutional neural network was constructed. Firstly, the U-Net convolutional neural network is used to extract edge to automatically obtain the boundary information of the interferometric fringes in the region of subsidence basin. Secondly, an edge-linking algorithm is constructed based on edge growth and predictive search. The interrupted interferometric fringes are connected automatically. The whole and continuous edges of interferometric fringes are obtained. Finally, the correct phase unwrapping results are obtained according to the principle of phase unwrapping and the wrap-count (integer jump of 2π) at each pixel by edge detection. The Huaibei Coalfield in China was taken as the study area. The real interferograms from D-InSAR (differential interferometric synthetic aperture radar) processing used Sentinel-1A data which were used to verify the performance of the new method. Subsidence basins with clear interferometric fringes, interrupted interferometric fringes, and confused interferometric fringes are selected for experiments. The results were compared with the other methods, such as MCF (minimum cost flow) method. The tests showed that the new method based on U-Net convolutional neural network can resolve the problem that is difficult to obtain the correct unwrapping phase due to interrupted or partially confused interferometric fringes caused by low coherence or other reasons in the coal mining area. Hence, the new method can help to accurately monitor the subsidence in mining areas under different conditions using InSAR technology.

Keywords: InSAR, phase unwrapping, U-Net convolutional neural network, mining subsidence, interferometric fringe

INTRODUCTION

The coal industry is a significant part of China's energy system. On the one hand, coal mining has promoted the rapid development of China's economy and made great contributions to social development (Fan et al., 2014; Chen et al., 2020a). On the other hand, wide-spread and high-intensity mining of underground coal resources for a long time has caused some serious problems of ground subsidence and damaged the ecological environment, such as the subsidence of building foundations, the cracking of wall, the destruction of farmland, and the abandonment of land resources (Zhou et al., 2013). Moreover, mining coal also has caused soil erosion, debris flow, and other geological disasters, which endanger the life and property safety of the people in the mining area and seriously restrict the sustainable development of the mining areas. Therefore, it is particularly important to continuously monitor the land subsidence caused by mining underground mineral resources.

With the development of geodetic surveying technology, more and more new technologies are applied to monitor the mining subsidence (Zhou et al., 2009; Xia et al., 2018; Chen et al., 2020a). Among those technologies, as a research hotspot, InSAR technology can monitor large area deformation with all-weather imaging capability and day/night data acquisition (Du et al., 2016; Ma et al., 2016; Ng et al., 2017; Yang et al., 2018; Zheng et al., 2018). The study of monitoring the subsidence in mining areas using InSAR technology began in 1996 (Carnec et al., 1996). Carnec et al. researched the subsidence of French Gardanne coal mine and found a large annular subsidence area through SAR images at intervals of 35 days. D-InSAR technology was used to monitor a salt mine in Vauvert region of France and optimized the ground level observation plan according to the monitoring results (Carnec et al., 1996; Raucoules et al., 2003). The classical approach of differential radar interferometry (D-InSAR) with short temporal baselines (6 days) was used and the radar results were compared with prediction models based on the Knothe–Budryk theory for mining subsidence (Ilieva et al., 2019). Zheng et al. analyzed land subsidence induced by coal mining in a 200 km^2 area in the Ordos Basin for the time period 2006–2015 using SBAS InSAR and D-InSAR (Zheng et al., 2020). Pawluszek-Filipiak et al. indicated that the Kriging-based integration method of D-InSAR and SBAS can be effectively applied to monitor mining-related subsidence (Pawluszek-Filipiak and Borkowski, 2020). Malinowska et al. evaluated the impact of mining-induced earthquakes in Poland through time-series InSAR technology (Malinowska et al., 2018). Pawel et al. focused on describing vertical surface displacements in the Upper Silesian Coal Basin in the south of Poland (Pawel et al., 2020). The surface deformations are identified using D-InSAR technology. A D-InSAR-based illegal-mining detection system (DIMDS) was proposed to exploit the geometric, spatial, and temporal characteristics of those subsidence patterns (Hu et al., 2013). It can be seen that InSAR technology has become a new technical means of mining subsidence monitoring.

Due to the complexity of mining environment and the limitation of InSAR technology, the accuracy and reliability of InSAR in monitoring the mining subsidence are not high. Low coherence, excessive deformation gradient, interferometric phase discontinuity caused by large displacement, and the atmospheric effect will influence the accuracy of InSAR technology when monitoring the deformation in the mining area (Chen et al., 2021). The deformation in the mining area is special, which is mainly characterized by uneven settlement rate, large deformation in the mining area, and small and dispersive settlement range (Fan et al., 2014; Du et al., 2016; Du et al., 2019). In addition, the surface of the mining area is mostly covered by vegetation and farmland, which leads to the low coherence of interferometric pair. In order to improve the accuracy and reliability of InSAR monitoring results, it is necessary to combine InSAR technology with other methods. For example, a method that relied on the principle of the probability integral method (PIM) and interferometric synthetic aperture radar (InSAR) was proposed to retrieve the location of an underground goaf (Xia and Wang, 2020). A solution was proposed to obtain complete deformation fields using the probability integral method to fuse deformation data derived from differential interferometric SAR (D-InSAR), sub-band InSAR, and offset-tracking (Wang et al., 2020). Du et al. used the probability integral method (PIM) and D-InSAR to locate the goaf (Du et al., 2019). An improvement of PSI processing, named as external model-based deformation decomposition PSI (EMDD-PSI) was proposed to address the limitations when monitoring large gradient deformations when there is phase ambiguity (Du et al., 2020). Liu et al. obtained the spatial–temporal characteristics of land subsidence caused by drilling solution mining activities using the time-series analysis (Liu et al., 2019). Sui et al. proposed an approach based on a combination of a differential interferometric synthetic aperture radar (D-InSAR) technique and a support vector machine (SVM) regression algorithm optimized by grid search (GS-SVR) to predict mining subsidence (Sui et al., 2020). Chen et al. employed the small baseline subset interferometric synthetic aperture radar (SBAS-InSAR) technology to obtain the time-series residual surface deformation based on the 40 Sentinel-1A images acquired from February 14, 2017, to May 17, 2020 (Chen et al., 2020b).

With the continuous development of InSAR technology, the applications of InSAR technology for monitoring the mine subsidence are also increasing. The main research directions have evolved from obtaining single surface deformation information to parameter inversion or subsidence prediction based on deformation theory (Du et al., 2019; Sui et al., 2020; Wang et al., 2020). Most of these works are targeted at one or more subsidence basins, which have high requirements on the interferogram and phase unwrapping quality of the interferometric pair. But influenced by the complex surface environment of the mining area, interferograms are seriously affected by noise which will interrupt or confuse the interferometric fringes.

Phase unwrapping is an important factor affecting the accuracy of InSAR measurement (Wang et al., 2017). Although many methods for InSAR phase unwrapping have been proposed (Chiglia and Pritt, 1998; Costantini, 1998; Xu et al., 2016; Wang et al., 2017; Yu et al., 2019; Luo et al., 2020; Liu and Pan, 2020; Zhou et al., 2020; Sica et al., 2020; Dai et al., 2020; Gao et al., 2020), traditional methods cannot unwrap the interferometric phase correctly and the reliability of InSAR monitoring results is not high in monitoring the large deformation in the mining areas. There are several learning-based phase unwrapping methods, including back-projection neural network in 1D phase unwrapping (Tipper et al., 1996; Hamzah et al., 1997), supervised feedforward multilayer perceptron neural network for 2D phase unwrapping (Schwartzkopf et al., 2000), a deep learning-based phase unwrapping network that uses the fully convolutional network (FCN) (Spoorthi et al., 2019), and also a deep convolutional neural network-based robust phase gradient estimation for 2D phase unwrapping (Li et al., 2020). Sica et al. also proposed a convolutional neural network-based coherence-driven approach for InSAR phase unwrapping (Sica et al., 2020). So, a reliable phase unwrapping method is still the guarantee for obtaining reliable land subsidence with high precision using SAR interferometry.

When monitoring the subsidence in the coal mining area using InSAR technology, the interferometric fringes are usually interrupted or confused because the interferograms are contaminated by noise or other reasons, so the existing phase unwrapping methods are difficult to accurately realize the phase unwrapping. To solve this problem, a novel phase unwrapping method based on the characteristics of subsidence basin is proposed in this paper. First, a U-Net convolutional neural network is introduced into the phase unwrapping of InSAR mining subsidence basin to accurately extract the edge of interferometric fringes, which is the wrap-count (integer jump of 2π) at each pixel. Then, based on the rule of phase unwrapping, accurate and reliable phase unwrapping of mine subsidence can be realized. The main purpose of the new method is to obtain the wrap-count (integer jump of 2π) at each pixel by edge detection.

The main sections of this paper are organized as follows: In *Data and Materials*, the study area and data are introduced in detail. The new method proposed in this paper is introduced in the *Methods*. To improve the accuracy and reliability of InSAR measurements in monitoring the subsidence in the coal mining area, a new phase unwrapping method based on U-Net convolutional neural network is constructed, and the detailed algorithm and flow of the method are introduced. Results and accuracy verification are presented in *Results*, where phase unwrapping experiments are carried out with clear interferometric fringes and are compared with other 5 phase unwrapping methods. The *Discussion* is the analysis and discussion section, focusing on evaluating the performance of the new method for the interrupted and confused interferometric fringes. Finally, some important conclusions drawn from this study are given in *Conclusions*.

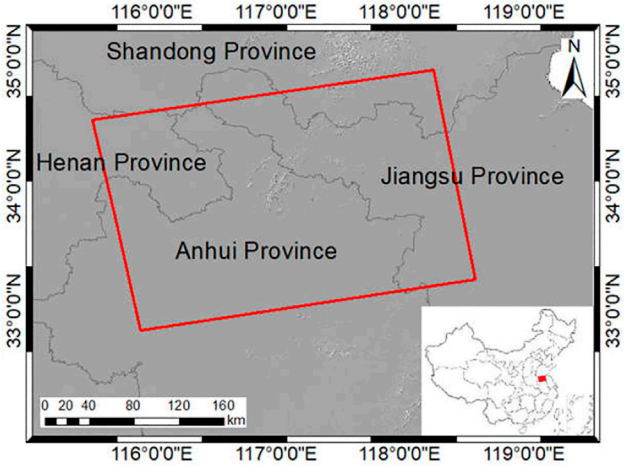

FIGURE 1 | Location of Huaibei Coalfield. It covers an area of about 9,600 square kilometers. The area containing coal is about 4,100 square kilometers.

DATA AND MATERIALS

Study Area

The Huaibei Coalfield (115°58′–117°12′E, 33°20′–34°28′N), located in the north of Anhui Province of China, was selected as the study area. It has a temperate monsoon climate with distinct seasons and mild climate. There are many coal mines in this region. Here, the terrain is flat, the surface vegetation is rich, and the farmland is numerous. The cumulatively proved coal reserves are nearly 13 billion tons. The large-scale and long-time exploitation of underground coal resources has resulted in a lot of ground subsidence in large area. It has seriously affected the local ecological environment and economic and social development. The study area is shown in **Figure 1**.

Experimental Data

In order to evaluate the performance of the new phase unwrapping method proposed in this paper, 4 Sentinel-1A SAR data from ESA (European Space Agency) acquired from December 2017 to March 2018 were selected. Two interferometric pairs are constructed by the Sentinel-1A data which are acquired in the IW (interferometric wide) mode, C-band (with 5.6 cm wavelength), VV polarization, and ascending orbit. The Sentinel-1A radar data used in this study has an incident angle of 38.9° and a pixel size of about 2.33*13.90 m. The detail characteristics of the interferometric pairs are shown in **Table 1**.

Moreover, the SRTM (Shuttle Radar Topography Mission) DEM (digital elevation model) released by NASA (National Aeronautics and Space Administration) was applied to D-InSAR data processing in this study. The spatial resolution of DEM used in this study is about 90 m.

TABLE 1 | The two interferometric pairs are used for the test. They contain 4 Sentinel-1A images.

No.	Date	Orbit	Relative orbit	Frame	Temporal baseline (d)	Spatial baseline (m)
1	December 10, 2017	19,639	142	106	12	89.9
	December 22, 2017	19,814	142	106		
2	February 08, 2018	20,514	142	106	24	29.04
	March 04, 2018	20,864	142	106		

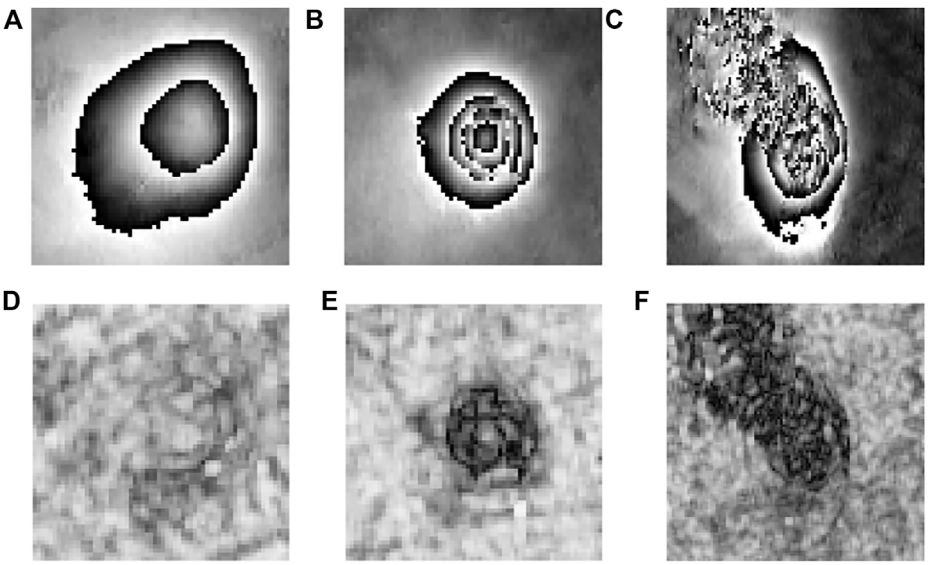

FIGURE 2 | Subsidence basins with different interferometric fringes quality are used to verify the reliability of new method. **(A)** The subsidence basin with clear interferometric fringes. The size of this interferogram is 64*64 pixel; **(B)** the subsidence basin with discontinuous interferometric fringes. The size of this interferogram is 64*64 pixel; **(C)** the subsidence basin with partially confused interferometric fringes. The size of this interferogram is 100*100 pixel. **(D)**, **(E)**, and **(F)** The coherence images corresponding to **(A)**, **(B)** and **(C),** respectively.

The data processing flow of InSAR can be referenced in (Massonnet and Feigl, 1998; Hanssen, 2001). The interferometric pairs were processed by D-InSAR (differential radar interferometry) and two interferograms of the whole area were obtained. The subsidence of the mining area will form a series of circular or elliptical interferometric fringes on the InSAR interferogram. Therefore, the subsidence basin is the object of our phase unwinding research to obtain the accurate land subsidence in the coal mining area. The subsidence basin is defined as the position where the subsidence is about 1 cm. The subsidence basins in study area were obtained by detection model based on HOG (histogram of oriented gradient) feature (Ronneberger et al., 2015) automatically. Then, the interferograms and coherence images including one complete subsidence basin were cut out from the original interferograms. Therefore, there are more than 25 subsidence basins within the coverage of a single Sentinel-1A.

Three subsidence basins with different interferometric quality were selected from interferograms generated by two interferometric pairs for phase unwrapping experiment, as shown in **Figure 2**. **Figure 2A** is a subsidence basin with good interferometric quality. It contains two interferometric fringes that resemble elliptical shapes. The interferometric fringe edges are characterized as smooth and continuous, without interruption or confusion, and the coherence is also very high, as shown in **Figure 2D**. **Figure 2B** is a subsidence basin with common interferometric quality. It contains approximately four interferometric fringes that resemble elliptical shapes. It is obvious that the interferometric fringes inside are partially interrupted or discontinuous, and the coherence value is poor, as shown in **Figure 2E**. **Figure 2C** is a subsidence basin with poor interferometric quality, in which the interferometric fringes are partially confused due to the massive noise. The coherence value is terrible, as shown in **Figure 2F**.

METHODS

The Rules of Phase Unwrapping

After underground coal mining, a series of goaf will be formed (Hu et al., 2013; Yang et al., 2018). In the InSAR interferograms, it is usually manifested as a series of concentric circles or concentric

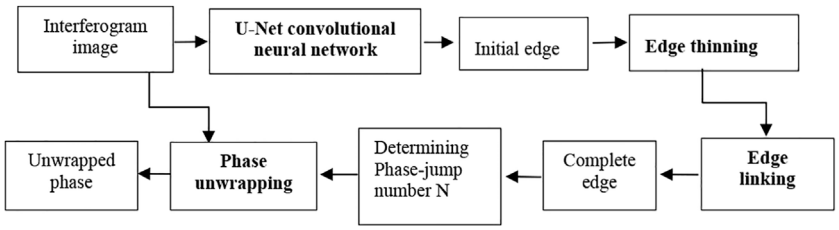

FIGURE 3 | Flow chart of the new method of phase unwrapping based on U-Net convolutional neural network used for monitoring the land subsidence in coal mining area.

ellipses with similar shapes (Du et al., 2019; Wang et al., 2021). According to the principle of phase unwrapping (Chiglia and Pritt, 1998; Yu et al., 2019), the number of phase-jump (or wrap-count) is calculated by the interferometric fringes of subsidence basin and the phase unwrapping is realized through adding or subtracting 2N in the position corresponded to the interferogram.

The purpose of the edge detection algorithm is to achieve the boundary of subsidence basin in the interferogram. The wrap-count (integer jump of 2π) is determined by number of interferometric fringes. Thus, the phase values of subsidence basins are added or subtracted 2N based on some certain rules. The specific rules of phase unwrapping are that 2N is added to the phase value when there is the change from $+\pi$ to $-\pi$ or subtracted in the opposite condition.

In mathematical language, it can be expressed as follows:

$$\phi = \varphi + \mathbf{2\pi} \cdot \mathbf{N}, \mathbf{N} = \mathbf{0}, \pm\mathbf{1}, \pm\mathbf{2} \ldots, \quad (1)$$

where Φ represents the value after phase unwrapping, and φ and N are the wrapping phase and the number of phase-jump, respectively.

Flow Chart of the Novel Method

The swath of SAR image is large, such as Sentinel-1 image with the swath of 250 km, but no land surface deformation occurred in most areas. Only several subsidence basins will be formed in some areas, such as the underground coal mining area. Some factors, such as vegetation growth, surface water, temporal decorrelation, and spatial decorrelation (Zhou et al., 2009; Ronneberger et al., 2015), will bring a lot of phase noise into interferograms, which will result in great difference among interferograms in the mined-out area. For example, some interferometric fringes are clear and continuous, but some are partially interrupted or discontinuous. Moreover, some fringes are even indistinct or confused. Above on these problems, we will not obtain the correct results of phase unwrapping using the traditional phase unwrapping methods, which leads to unreliable monitoring results of land subsidence in the mining area.

To solve this problem, a novel phase unwrapping method based on U-Net convolutional neural network is proposed. Firstly, the U-Net convolutional neural network that has been trained according to some samples is used to extract the edge of the fringes. Then, it can automatically obtain the boundary information of the interferometric fringes in the region of subsidence basin. Secondly, an edge-linking algorithm is constructed based on edge growth and predictive search to connect the break of interferometric fringe automatically. Then, a complete and continuous edge of interferometric fringe is obtained. Finally, according to the rules of phase unwrapping, the number of phase-jump N or the wrap-count is calculated and the phase unwrapping is realized through adding or subtracting 2N at the corresponding position in the interferogram. The flow chart of the novel method is shown in **Figure 3**.

Extracting the Edge of Interferometric Fringes

The phases of interferogram are wrapped (Hanssen, 2001; Wang et al., 2021). If the position of phase jump (that is wrap-count) in the interferometric fringe can be obtained, the true phase can be obtained. Therefore, the phase unwrapping can be turned into an image segmentation problem to a certain extent. For image edge extraction, many methods have been proposed. Although the FCN (fully convolutional network) can identify the spatial relationship between pixels and realize the segmentation at the semantic level, the process of restoring the image is relatively simple and the obtained fringe boundary is not accurate enough (Jonatnan et al., 2014; Liang et al., 2020). As for InSAR interferometric images, there are not a large amount of training data available for public use, so we can only collect and generate them by ourselves, and the number of samples generated is generally small. Due to the practicality of U-Net convolutional neural network and its learning ability with fewer samples (Ronneberger et al., 2015; Parente et al., 2019), the U-Net convolutional neural network is used to obtain the edge information (or the wrap-count at each pixel) of the interferometric fringes automatically, which is the first step of the new phase unwrapping method. The main role of U-Net convolutional neural network in new phase unwrapping method is to obtain the wrap-count (integer jump of 2π) at each pixel by edge detection.

The U-Net convolutional neural network is basically same as the FCN. Through multiple convolutions and pooling operations, the feature dimensions are improved and the images are compressed (Kando et al., 2019; Esch et al., 2020). In the process of image restoration, the U-Net convolutional neural

network also convolved the fused images for many times (Qin et al., 2020), which enhanced the detailed information of images and achieved the better segmentation effect.

The training sample set of U-Net convolutional neural network came from 21 interferometric pairs composed of Sentinel-1A data corresponding to Huaibei Coalfield and Yanzhou Coalfield in China. A total of 150 training samples have been established and these samples have been uniformly resampled to 256 × 256×1. For the convolutional neural network, the number of samples is little. However, the U-Net convolutional neural network has a good generalization ability. This can compensate for shortage of samples to a certain extent.

Edge Thinning and Edge Linking

As there are lots of surface vegetation and farmlands in the mining area, it will cause incoherence phenomena in monitoring the land subsidence by InSAR technology, which results in some discontinuous or interrupted interferometric fringes in the interferogram. Thus, it is impossible to extract the continuous and complete fringe boundary directly. Although the U-Net convolutional neural network can extract relatively clear interferometric fringe boundary, the edge thinning and edge linking are needed to carry out to obtain the closed and complete edge, especially in case of discontinuous, interrupted, or even confused interferometric fringes.

Edge Thinning

An improved algorithm is adopted for edge thinning (Xu et al., 2014), which is described as follows:

Step 1: the edge points in the image are traversed and the current edge point is recorded as P_0
Step 2: the edge points in the eight-connected domain centered on P_0 are counted as $E(P_0)$. If $E(P_0) = 0$, this edge point is eliminated
Step 3: if $2 < E(P_0) < 6$, and $S(P_0) = 1$, it is marked as the point to be eliminated, and it is eliminated after the traversal is complete. $S(P_0)$ is the point that is based on P_1, P_2, P_8 to sort., which is the number of changes from the edge point to the non-edge point.

The above three steps constitute a traversal and carry out as repeated iteration until that no points satisfy the rule to be marked.

Edge Linking

In order to obtain the complete edge of the interferometric fringes, an edge linking operation is required. Based on edge growth and predictive search, a new algorithm is constructed by improving the edge growth method (Farag and Delp, 1995; Lin and Shi, 2000). The specific steps are as follows:

Step 1: search the endpoint P in the edge graph
Step 2: five edge points are searched in the reverse from the endpoint and the direction of the edge is determined by the coordinates of these edge points
Step 3: according to the edge trend determined in the previous step, the range of the edge growth is limited. The edge growth is carried out according to the gradient of the original image to obtain the new endpoint P'
Step 4: with the new endpoint P' as the starting point, the edge growth continues until it connects to another endpoint.

The operation of edge thinning and edge linking is based on binary images. So, before the edge thinning and linking, the threshold segmentation of edge image is carried out to obtain the binary image of the result from the U-Net convolutional neural network.

RESULTS

In order to evaluate the performance of the new method, some interferograms including the whole mining subsidence basins obtained by Sentinel-1A data were used.

Model Training

Neural networks have been applied to InSAR phase unwrapping (Jonathan et al., 2015; Parente et al., 2019; Kando et al., 2019; Sica et al., 2020). As an important branch of machine learning, neural networks should be trained with sample data before edge extraction (Lin and Shi, 2000). Firstly, 60 targets of subsidence basins were extracted by HOG (histogram of oriented gradient) model (Wang et al., 2021) and their edge images were obtained to form the basic training samples. Secondly, in order to obtain more samples, the basic samples were uniformly resampled to 256 × 256 pixels by the resampling method of bilinear interpolation. Then, other 90 subsidence basins and corresponding edge images were achieved through transformation of rotation, translation, and zoom for the basic samples. Finally, a total of 150 training samples were obtained and some samples are shown as **Figure 4**. In the model established in this paper, the training group consists of 150 pairs of images, the test group consists of 10 images, and the validation group consists of 5 images.

The loss function is used to evaluate the difference between predicted and real values in the training process of neural network. The purpose of training or optimization operation is to minimize the loss function (Parente et al., 2019; Esch et al., 2020). The smaller the loss function value is, the closer the predicted value of the model is to the real value, and the result will be more accurate. The essence of edge extraction is a binary classification, so the binary cross entropy function is used as the loss function of U-Net convolutional neural network to represent the model accuracy. The overfitting problem is avoided by using the dropout function before and after the last convolutional layer and discarding some parameters randomly.

In order to further evaluate the performance of the new method quantitatively, the mean phase difference (M) and mean square error (MSE) are selected as assessment indexes to compare the results of new method with those of other methods quantitatively. The expressions are as follows:

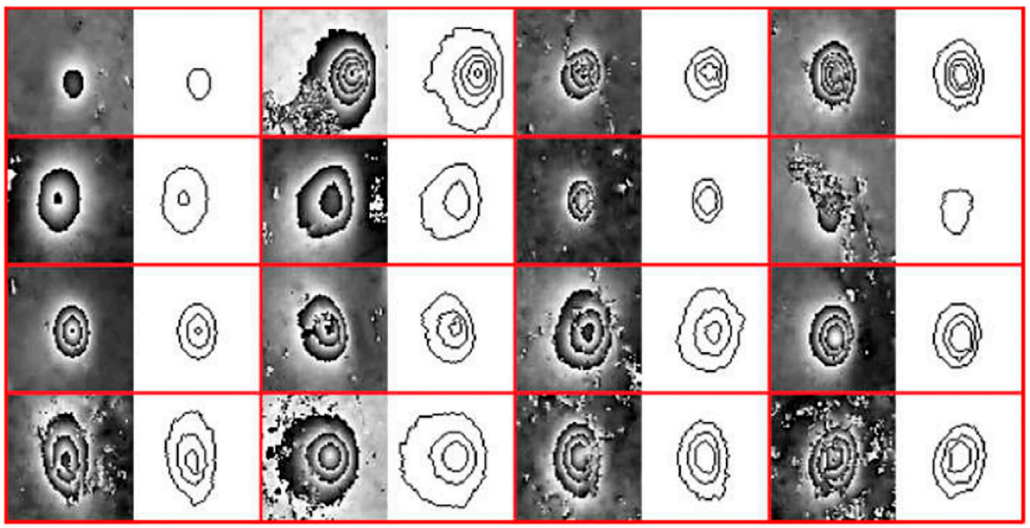

FIGURE 4 | Some training samples are used for the U-Net convolutional neural network model in this paper. A total of 150 samples are used for model training. Interferograms and extracted fringe edges are alternately presented in different columns.

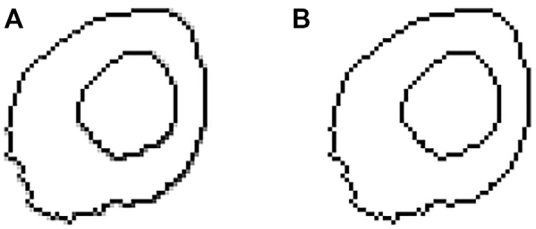

FIGURE 5 | The edges are extracted based on U-Net convolutional neural network in the case of clear interferometric fringes. **(A)** The initial edge using U-Net convolutional neural network. **(B)** The final edge after edge thinning and edge linking.

$$M = \frac{1}{mn}\sum_{i=0}^{m-1}\sum_{i=0}^{n-1}\left(I\left(i,j\right) - K\left(i,j\right)\right), \tag{2}$$

$$MSE = \frac{1}{mn}\sum_{i=0}^{m-1}\sum_{i=0}^{n-1}\left(I\left(i,j\right) - K\left(i,j\right)\right)^2, \tag{3}$$

where m and n are the number of columns and rows of the image; I and K represent the phase unwrapping result of new method proposed in this paper and other methods, respectively. (i,j) represents the position of the pixel.

Phase Unwrapping for the Clear Interferometric Fringes

A subsidence basin with clear interferometric fringes from real interferometric data was selected to evaluate the performance of the new method. As shown in **Figure 2A**, the subsidence basin had good interferometric quality which is characterized with smooth and continuous interferometric fringe edges, and the coherence value is also very high in the coherence image. The results of edge thinning and linking after binarization process are shown in **Figure 5** and the result of phase unwrapping is shown in **Figure 6A**. In order to verity the effectiveness of the new method proposed in this paper, the results are compared with other phase unwrapping methods, such as minimum cost flow (MCF) method, Goldstein's branch-cut method, quality-guided phase unwrapping (QG) method, Flynn's minimum discontinuity (MD) method, LP minimum norm method (LP), and so on. Goldstein's branch-cut (Goldstein) algorithm (Yu et al., 2019) is the most representative of the residue-theorem-based methods, connecting the nearby positive and negative residues so that the residues are balanced. The minimum cost flow (MCF) PU method (Costantini, 1998; Liu and Pan, 2020) and Flynn's minimum discontinuity (MD) method (Xu et al., 2016) can be classified as the LP-norm phase unwrapping method. Quality-guided (QD) phase unwrapping method assumes that pixels with high quality are less likely to cause PU error (Yu et al., 2019). The methods always attempt to first make the integration path that visits the highest-quality pixel provided by the quality map. The specific results are shown as **Figures 6B–F**. The quantitative comparisons are shown in **Table 2**.

It can be seen from **Figure 6** and **Table 2** that the result of new method proposed in this paper is generally consistent with those of other methods under the condition of clear interferometric fringes. The ranges of unwrapping phases from different methods are within the theoretical ranges. The values of M and MSE from different methods are all small. The results of unwrapping are highly consistent in images and values. In other words, in the case of clear interferometric fringes from real interferometric data, different phase unwrapping methods can achieve correct unwrapping. It also indicates that the new method can achieve correct phase unwrapping result in the case of clear interferometric fringes.

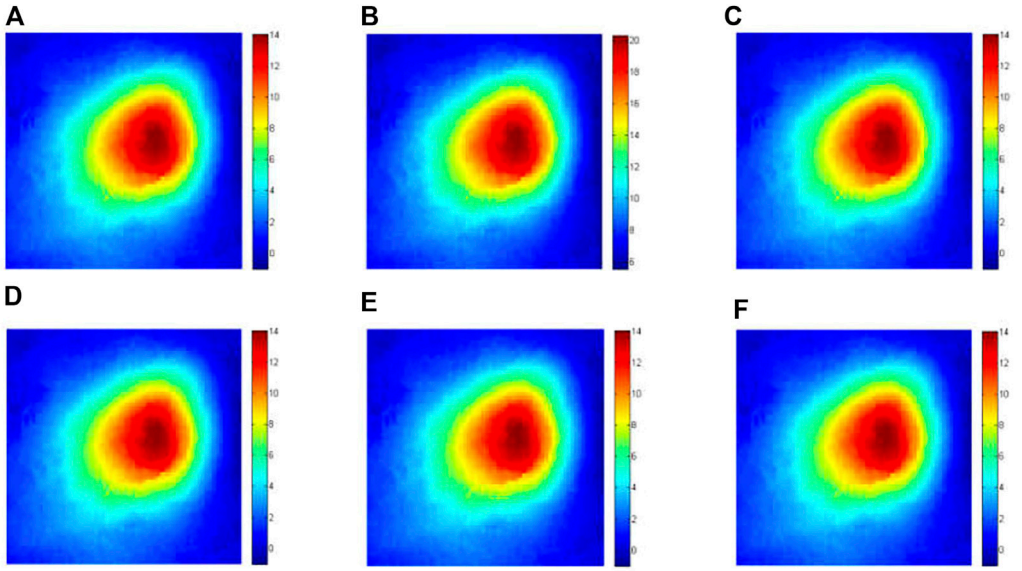

FIGURE 6 | Phase unwrapping of InSAR based on U-Net convolutional neural network in the case of clear interferometric fringes. **(A)** Result of phase unwrapping based on the new method; **(B)** result of phase unwrapping based on the minimum cost flow (MCF) method; **(C)** result of phase unwrapping based on the Goldstein method; **(D)** result of phase unwrapping based on the Minimum discontinuity (MD) method; **(E)** result of phase unwrapping based on the quality-guided (QG) method; **(F)** result of phase unwrapping based on the LP minimum norm (LP) method.

TABLE 2 | The quantitative comparison of unwrapping phase between different methods is counted in the case of clear interferometric fringes.

Method	Phase minimum	Phase maximum	Whether within the theoretical range	M	MSE
New method	−1.0110	14.0628	Yes	—	—
MCF	−0.7281	14.0768	Yes	3.762×10^{-4}	2.602×10^{-7}
Goldstein	−1.0090	14.0347	Yes	-7.396×10^{-4}	1.024×10^{-6}
MD	−1.0080	14.0206	Yes	1.095×10^{-3}	2.306×10^{-6}
QG	−1.0130	14.0909	Yes	7.397×10^{-4}	1.025×10^{-6}
LP	−1.0141	14.1049	Yes	1.193×10^{-4}	2.415×10^{-6}

DISCUSSION

According to the experiments, the result of the new method proposed in this paper is generally consistent with those obtained by other methods in the case of clear interferometric fringes from real interferometric data. All these methods can achieve the correct unwrapping phase of the interferogram. The unwrapping results are different obviously, however, when the interferometric fringes are interrupted or confused. The subsidence basin caused by underground coal mining in the mining area should show a series of concentric circles or concentric ellipses with similar shapes on the InSAR interferogram. There are one or more interferometric fringes according to the different land subsidence. Ideally, the interferometric fringes are continuous. But affected by noise or other reasons, there will be a gap of 2-3 pixels in the one interferometric fringe in some area. But the boundary of the interferometric fringe can still be clearly defined. This is called “interrupted interferometric fringe.” If the noise is larger or the ground subsidence in the mining area exceeds the maximum deformation gradient, it is not easy to distinguish the boundary of two or more interferometric fringes in the InSAR interferogram, and confusion occurs locally or globally. This is called “confused interferometric fringe.” The phase unwrapping results obtained

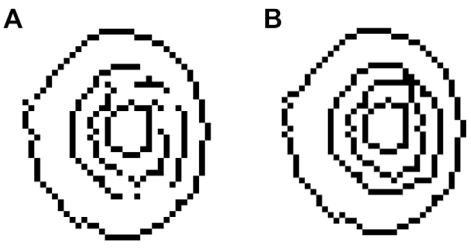

FIGURE 7 | Edge extraction results in the case of interferometric fringes discontinuity. **(A)** The initial edge using U-Net convolutional neural network. **(B)** The final edge after edge thinning and edge linking.

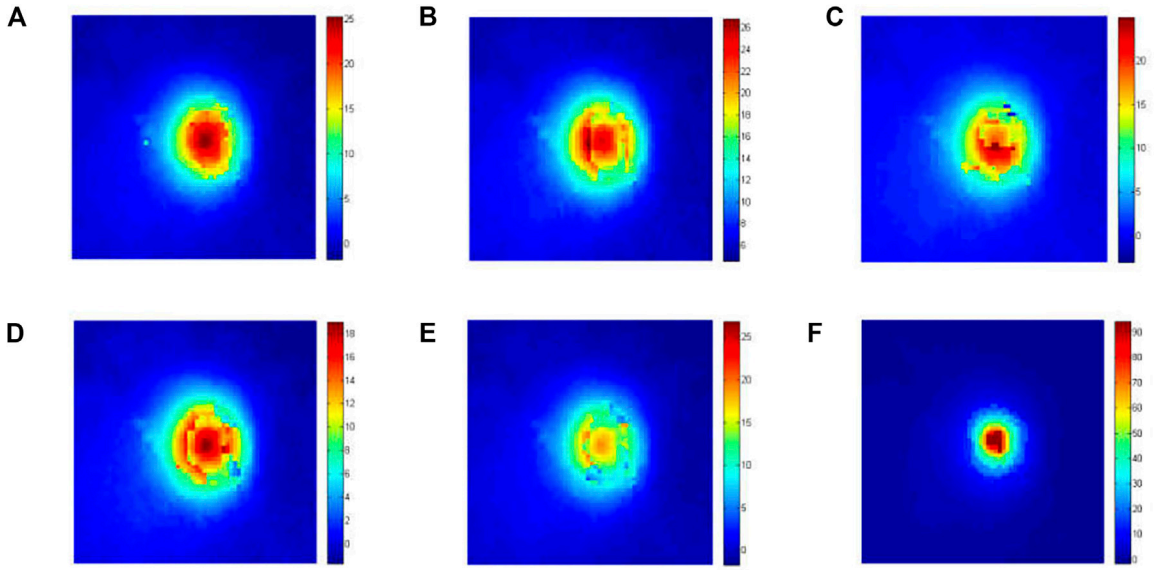

FIGURE 8 | Comparison of phase unwrapping results in the case of discontinuous interferometric fringes. **(A)** Result of phase unwrapping based on the new method; **(B)**, **(C)**, **(D)**, **(E),** and **(F)** the result of phase unwrapping based on MCF, Goldstein, MD, QG, and LP methods, respectively.

TABLE 3 | The quantitative comparison of unwrapping phase between different methods is counted in the case of discontinuous interferometric fringes.

Method	Phase minimum	Phase maximum	Whether within the theoretical range	M	MSE
New method	−1.689	25.278	Yes	—	—
MCF	−1.689	20.559	No	−0.2255	1.4168
Goldstein	−3.040	24.985	Yes	−0.1212	1.0698
MD	−1.689	18.995	No	−0.2669	1.6963
QG	−1.689	19.314	No	−0.2608	1.7156
LP	−1.689	94.393	No	1.2011	44.7120

by different methods under the two conditions are particularly discussed.

In the Case of Interrupted Interferometric Fringes

A subsidence basin with interrupted interferometric fringes from real interferometric data, as shown in **Figure 2B**, was selected to study. The interferometric quality of this subsidence basin is common, and the interferometric fringes inside are partially interrupted and discontinuous. Especially, the coherence value is poor, as shown in **Figure 2E**. The results of edge extraction and phase unwrapping obtained by the new method proposed in this paper are displayed in **Figure 7** and **Figure 8A**, respectively. Moreover, in order to compare with other five methods, the subsidence basin is resolved by other methods, and the phase unwrapping results are displayed in **Figures 8B–F**. The quantitative comparison is shown in **Table 3**.

As shown in **Figure 8**, the result of new method proposed in this paper is obviously different between those of other five methods in the case of discontinuous interferometric fringes. The unwrapping result of new method in this paper is closer with that of Goldstein method than others. The results from MCF, QG, and LP minimum norm methods all have the regions which are not completely unwrapped, but the sizes of the regions are different. From the results of phase unwrapping, the result of new method in this paper is great and without any incompletely unwrapped regions. The detailed comparisons are shown in **Table 3**. Only the results of new method and Goldstein method are in the theoretical ranges. From the assessment indexes of M and MSE of different methods, the result obtained by LP minimum norm method is the worst among these methods, which had many incompletely unwrapped regions. The results of other four methods also have some obvious regions that are incompletely unwrapped, though the difference is small in M and MSE when compared with the method proposed in this study.

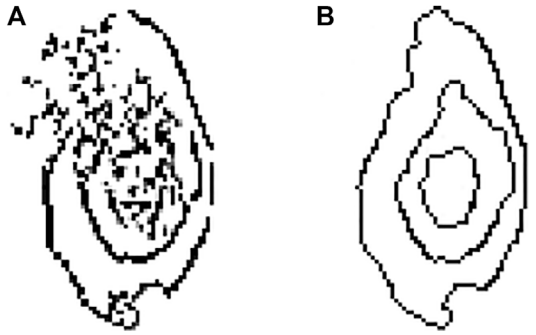

FIGURE 9 | Edge extraction results in the case of partially confused interferometric fringes. **(A)** The initial edge using U-Net convolutional neural network. **(B)** The final edge after edge thinning and edge linking.

In the Case of Confused Interferometric Fringes

In order to validate the reliability of the method under the influence of extreme noise, a subsidence basin with confused interferometric fringes from real interferometric data is selected for the experiment. As shown in **Figure 2C**, the quality of the interferometric fringe of the subsidence basin is poor and the fringe is confused due to a large amount of noise. Especially, the coherence value is very poor, as shown in **Figure 2F**. The edge extraction results are displayed in **Figure 9** and the phase unwrapping result is shown in **Figure 10A**. Moreover, in order to compare with other five methods, the subsidence basin is resolved by other methods and the phase unwrapping results are displayed in **Figures 10B–F**. The quantitative comparisons are shown in **Table 4**.

It can be seen from **Figure 10** and **Table 4** that the phase unwrapping result of the method proposed in this paper is relatively consistent with that of the MCF method in the case of confused interferometric fringes. In addition, two phase unwrapping results from the new method and MCF method are also within the theoretical ranges. Therefore, it can be considered that the phase unwrapping results of these two methods are correct. However, in terms of the results of Goldstein method and other four phase unwrapping methods, all of them have the regions that are not unwrapped correctly and they are not within the theoretical ranges. Moreover, there are many unwrapped pixels existing in the phase unwrapping results of Goldstein method and QG method, and the whole effect of the phase unwrapping is not good. Especially, the MSE of the result of Goldstein method is larger than others. Hence, under the condition of extreme noise, the result obtained by the new method proposed in this paper is better than others and it can greatly achieve the correct phase unwrapping results in the case of confused interferometric fringes of mining area.

CONCLUSION

When monitoring the mining subsidence using radar interferometry, the reliable method of phase unwrapping is the key to obtain subsidence values. It is difficult to correctly resolve the condition where the interferometric fringes are discontinuous or partially confused by using existing methods. In order to solve the problem, a novel method based on the edge extraction using U-Net convolutional neural network was proposed. The method can extract the edge of interferometric fringes and connect discontinuous fringes automatically to obtain the wrap-count at each pixel by edge detection. Finally, the phase results of

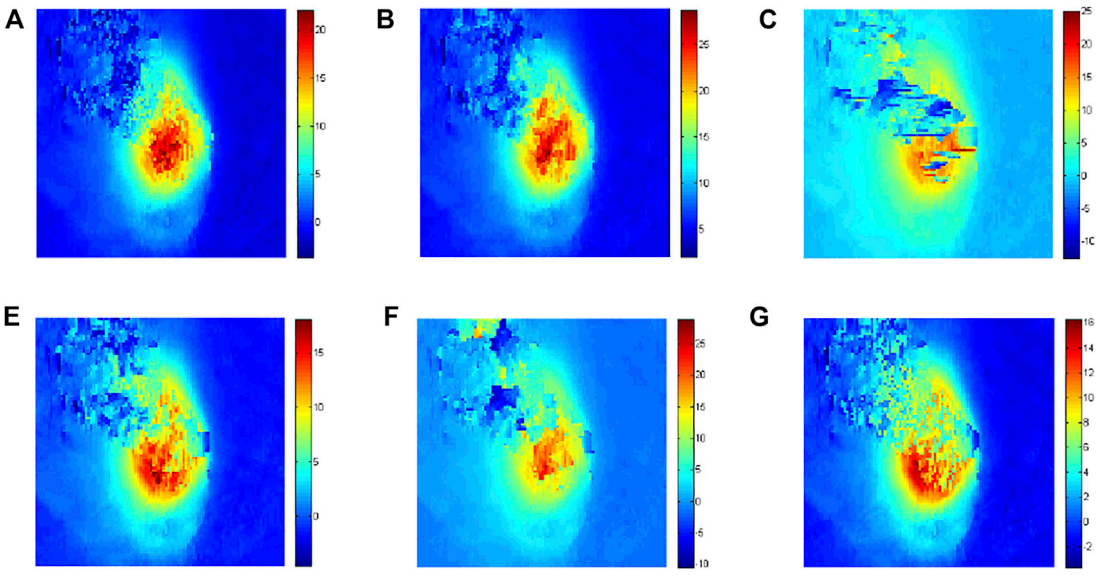

FIGURE 10 | Comparison of phase unwrapping results in the case of partially confused interferometric fringes. **(A)** Result of phase unwrapping based on the new method; **(B)**, **(C)**, **(D)**, **(E)**, and **(F)** the result of phase unwrapping based on MCF, Goldstein, MD, QG, and LP methods, respectively.

TABLE 4 | The quantitative comparison of unwrapping phase between different methods is counted in the case of partially confused interferometric fringes.

Method	Phase minimum	Phase maximum	Whether within the theoretical range	M	MSE
New method	−3.6482	22.0781	Yes	—	—
MCF	−4.2959	22.4704	Yes	0.0597	1.220
Goldstein	−12.5783	25.0858	No	−0.6155	10.350
MD	−4.5349	18.0847	No	−0.2287	2.811
QG	−10.5077	25.7394	No	−0.0270	3.833
LP	−3.6482	16.2900	No	−0.2205	4.047

mining subsidence basins are obtained according to the rules of phase unwrapping and the wrap-count (integer jump of 2π) at each pixel by edge detection. Three kinds of subsidence basins with different interferometric fringes were selected for experiment. The results showed that the method proposed in this paper can obtain more accurate phase unwrapping results under the conditions of clear, interrupted, or partially confused interferometric fringes by compared with other methods. Hence, the greatly reliable results of mining subsidence are achieved.

Through the study in this paper, some important conclusions can be drawn as follows:

1) In the case of clear and uninterrupted interferometric fringes, the results obtained by the new method proposed in this paper are consistent with those obtained by the MCF method, Goldstein method, and other methods. In other words, different methods can obtain correct results of phase unwrapping in the ideal case.
2) The discontinuous boundary of interferometric fringe can be detected and linked by using the new method proposed in this paper automatically, and the complete interferometric fringe edge is obtained in further. The phase unwrapping results of new method are close to that obtained by Goldstein method. The mean phase difference and mean square error are −0.12 and 1.07, respectively. Overall, the new method in this paper is superior to the other five phase unwrapping methods.
3) In the case of partially confused interferometric fringes, it can also realize the detection and linking in position of interrupted boundary to obtain the complete ones. The results obtained in this study are consistent with those obtained by MCF method. The mean phase difference and mean square error are 0.06 and 1.22, respectively. The results showed that the new method proposed in this paper can completely solve the issues of phase unwrapping under the condition that part fringes are partially confused.

The proposed phase unwrapping method for InSAR technology is suitable to monitor the land subsidence caused by underground mining, especially for a circular or elliptic subsidence basin presented in the interferogram. Based on the existed sample data, the method can accurately resolve the issues of the phase unwrapping of discontinuous or partially confused interferometric fringes by using the U-Net convolutional neural network. It can realize the phase unwrapping of interrupted or even partially confused interferometric fringes, but for the interferometric fringes that are not circular or elliptical, the algorithm cannot be solved well. In the next study, the phase unwrapping method will be improved deeply so that it can be adapted to most InSAR phase unwrapping for monitoring land subsidence to achieve the reliable results.

DATA AVAILABILITY STATEMENT

The original contributions presented in the study are included in the article/Supplementary Material; further inquiries can be directed to the corresponding author.

AUTHOR CONTRIBUTIONS

ZW proposed the method, wrote the manuscript, designed its structure, and revised the manuscript. LL collected and analyzed the data. YY and JW helped in collecting and analyzing the data. ZL and WL critically revised the manuscript.

FUNDING

This research was funded by the National Natural Science Foundation of China (No. 41876202) and the Natural Science Foundation of Shandong Province (No. ZR2017MD020). This research was also supported by funding from the Major Science and Technology Innovation Projects of Shandong Province (No. 2019JZZY020103).

ACKNOWLEDGMENTS

We thank the European Space Agency (ESA) for providing the Sentinel-1A remote sensing data. We thank the NASA (National Aeronautics and Space Administration) for providing the SRTM DEM data. We want to thank the reviewers for their valuable suggestions and comments which improved the quality of the manuscript.

REFERENCES

Carnec, C., Massonnet, D., and King, C. (1996). Two Examples of the Use of SAR Interferometry on Displacement fields of Small Spatial Extent. *Geophys. Res. Lett.* 23, 3579–3582. doi:10.1029/96GL03042

Chen, B. Q., Li, Z. H., Yu, C., Fairbarin, D., Kang, J. R., Hu, J. S., et al. (2020a). Three-dimensional Time-Varying Large Surface Displacements in Coal Exploiting Areas Revealed through Integration of SAR Pixel Offset Measurements and Mining Subsidence Model. *Remote Sens Environ.* 240, 111663. doi:10.1016/j.rse.2020.111663

Chen, B. Q., Mei, H., Li, Z. H., Wang, Z. S., Yu, Y., and Yu, H. (2021). Retrieving Three-Dimensional Large Surface Displacements in Coal Mining Areas by Combining SAR Pixel Offset Measurements with an Improved Mining Subsidence Model. *Remote Sens* 13, 2072–4292. doi:10.3390/rs13132541

Chen, D. H., Chen, H., Zhang, W., Cao, C., Zhu, K. X., and Yuan, X. Q. (2020b). Characteristics of the Residual Surface Deformation of Multiple Abandoned Mined-Out Areas Based on a Field Investigation and SBAS-InSAR: A Case Study in Jilin, China. *Remote Sens* 12, 3752. doi:10.3390/rs12223752

Chiglia, D. C., and Pritt, M. D. (1998). *Two-dimensional Phase Unwrapping: Theory, Algorithms, and Software*. New York, USA: Wiley.

Costantini, M. (1998). A Novel Phase Unwrapping Method Based on Network Programming. *IEEE Trans. Geosci. Remote Sens.* 36, 813–821. doi:10.1109/36.673674

Dai, Y. W., Ng, A. H., Wang, H., Li, L. Y., Ge, L. L., and Tao, T. Y. (2020). Modeling-Assisted InSAR Phase-Unwrapping Method for Mapping Mine Subsidence. *IEEE Geosci. Remote Sens. Lett.* 18 (6), 1059–1063. doi:10.1109/LGRS.2020.2991687

Du, S., Mallorqui, J. J., Fan, H. D., and Zheng, M. N. (2020). Improving PSI Processing of Mining Induced Large Deformations with External Models. *Remote Sens* 12, 3145. doi:10.3390/rs12193145

Du, S., Wang, Y. J., Zheng, M. N., Zhou, D. W., and Xia, Y. P. (2019). Improving PSI Processing of Mining Induced Large Deformations with External ModelsGoaf Locating Based on InSAR and Probability Integration Method. *Remote Sens* 11, 812. doi:10.3390/rs11070812

Du, Z. Y., Ge, L. L., Li, X. J., Ng, A. H., Lu, Z., and Thenkabail, P. S. (2016). Subsidence Monitoring over the Southern Coalfield, Australia Using Both L-Band and C-Band SAR Time Series Analysis. *Remote Sens* 8, 543. doi:10.3390/rs8070543

Esch, C., Köhler, J., Gutjahr, K., and Schuh, W-D. (2020). One-Step Three-Dimensional Phase Unwrapping Approach Based on Small Baseline Subset Interferograms. *Remote Sens* 12, 1473. doi:10.3390/rs12091473

Fan, H.-d., Gu, W., Qin, Y., Xue, J.-q., and Chen, B.-q. (2014). A Model for Extracting Large Deformation Mining Subsidence Using D-INSAR Technique and Probability Integral Method. *Trans. Nonferrous Met. Soc. China* 24, 1242–1247. doi:10.1016/S1003-6326(14)63185-X

Farag, A., and Delp, J. (1995). Edge Linking by Sequential Search. *Pattern Recognit* 28, 611–633. doi:10.1016/0031-3203(94)00131-5

Gao, Y. D., Tang, X. M., Li, T., Chen, Q. F., Zhang, X., Li, S. J., et al. (2020). Bayesian Filtering Multi-Baseline Phase Unwrapping Method Based on a Two-Stage Programming Approach. *Appl. Sci.* 10, 3139. doi:10.3390/app10093139

Hamzah, S., Pearson, J. D., Lisboa, P. J., and Hobson, C. A. (1997). "Phase Unwrapping in 3-D Shape Measurement Using Artificial Neural Networks," in 1997 Sixth International Conference on Image Processing and Its Applications, Dublin, Ireland, July 14–17, 1997, 680–683. doi:10.1049/cp:1997098

Hanssen, R. F. (2001). *Radar Interferometry: Data Interpretation and Error Analysis*. Dordrecht, Netherland: Kluwer Academic Publisher.

Hu, Z., Ge, L. L., Li, X. J., Zhang, K., and Zhang, L. (2013). An Underground-Mining Detection System Based on DInSAR. *IEEE Trans. Geosci.* 51, 615–625. doi:10.1109/TGRS.2012.2202243

Ilieva, M., Polanin, P., Borkowski, A., Gruchlik, P., Smolak, K., Kowalski, A., et al. (2019). Mining Deformation Life Cycle in the Light of InSAR and Deformation Models. *Remote Sens* 11, 745. doi:10.3390/rs11070745

Jonathan, L., Evan, S., and Trevo, D. (2015). "Fully Convolutional Networks for Semantic Segmentation," in 2015 IEEE Conference on Computer Vision and Pattern Recognition (CVPR). Boston, MA, USA, June 8–10, 2015, 3431–3440. doi:10.1109/CVPR.2015.7298965

Kando, D., Tomioka, S., Miyamoto, N., and Ueda, R. (2019). Phase Extraction from Single Interferogram Including Closed-Fringe Using Deep Learning. *Appl. Sci.* 9, 3529. doi:10.3390/app9173529

Li, F. Z., Han, W. Y., and Yang, L. (2020). Deep Convolutional Neural Network-Based Robust Phase Gradient Estimation for Two-Dimensional Phase Unwrapping Using SAR Interferograms. *IEEE Trans. Geosci. Remote Sens.* 58, 4653–4665. doi:10.1109/TGRS.2020.2965918

Liang, J., Zhang, J. C., Shao, J. B., Song, B. F., Yao, B. L., and Liang, R. G. (2020). Deep Convolutional Neural Network Phase Unwrapping for Fringe Projection 3D Imaging. *Sensors* 20, 3691. doi:10.3390/s20133691

Lin, T., and Shi, Q. Y. (2000). An Edge Growing Approach for Segmentation of Grey and Color Images. *J. Image Graphics* 5, 911–915. doi:10.3969/j.issn.1006-8961.2000.11.005

Liu, F., and Pan, B. (2020). A New 3-D Minimum Cost Flow Phase Unwrapping Algorithm Based on Closure Phase. *IEEE Trans. Geosci. Remote Sens.* 58, 1857–1867. doi:10.1109/tgrs.2019.2949926

Liu, X. B., Xing, X. M., Wen, D. B., Chen, L. F., Yuan, Z. H., Liu, B., et al. (2019). Mining-Induced Time-Series Deformation Investigation Based on SBAS-InSAR Technique: A Case Study of Drilling Water Solution Rock Salt Mine. *Sensors* 19, 5511. doi:10.3390/s19245511

Luo, X. M., Li, H. T., Dong, Z. L., and Zhu, S. Q. (2020). InSAR Phase Unwrapping Based on Square-Root Cubature Kalman Filter. *IEEE J. Sel. Top. Appl. Earth Observ. Remote Sens. PP* 1, 1. doi:10.1109/jstars.2020.3015739

Ma, C., Cheng, X. Q., Yang, Y. L., Zhang, X. K., Guo, Z. Z., and Zou, Y. F. (2016). Investigation on Mining Subsidence Based on Multi-Temporal InSAR and Time-Series Analysis of the Small Baseline Subset—Case Study of Working Faces 22201-1/2 in Bu'ertai Mine, Shendong Coalfield, China. *Remote Sens* 8, 951. doi:10.3390/rs8110951

Malinowska, A. A., Witkowski, T. T., Guzy, A., and Hejmanowski, R. (2018). Mapping Ground Movements Caused by Mining-Induced Earthquakes Using Sentinel-1 TOPS Time Series Interferometry. *Eng. Geol.* 246, 402–411. doi:10.1016/j.enggeo.2018.10.013

Massonnet, D., and Feigl, K. L. (1998). Radar Interferometry and its Application to Changes in the Earth's Surface. *Rev. Geophys.* 36, 8755–1209. doi:10.1029/97RG03139

Ng, A. H., Ge, L. L., Du, Z. Y., Wang, S. R., and Ma, C. (2017). Satellite Radar Interferometry for Monitoring Subsidence Induced by Longwall Mining Activity Using Radarsat-2, Sentinel-1 and ALOS-2 Data. *Int. J. Appl. Earth Obs. Geoinf.* 61, 92–103. doi:10.1016/j.jag.2017.05.009

Parente, L., Taquary, E., Silva, A. P., Souza, C., and Ferreira, L. (2019). Next Generation Mapping: Combining Deep Learning, Cloud Computing, and Big Remote Sensing Data. *Remote Sens* 11, 2881. doi:10.3390/rs11232881

Pawel, S., Tomasz, S., Artur, W., and Dawid, M. (2020). Land Surface Subsidence Due to Mining-Induced Tremors in the Upper Silesian Coal Basin (Poland)—Case Study. *Remote Sens* 12, 3923. doi:10.3390/rs12233923

Pawluszek-Filipiak, K., and Borkowski, A. (2020). Integration of DInSAR and SBAS Techniques to Determine Mining-Related Deformations Using Sentinel-1 Data: The Case Study of Rydułtowy Mine in Poland. *Remote Sens* 12, 242. doi:10.3390/rs12020242

Qin, X. F., Wu, C. Z., Chang, H., Lu, H., and Zhang, X. D. (2020). Match Feature U-Net: Dynamic Receptive Field Networks for Biomedical Image Segmentation. *Symmetry* 12, 1230. doi:10.3390/sym12081230

Raucoules, D., Maisons, C., Carnec, C., Mouelic, S. L., King, C., and Hosford, S. (2003). Monitoring of Slow Ground Deformation by ERS Radar Interferometry on the Vauvert Salt Mine (France): Comparison with Ground-Based Measurement. *Int. J. Remote Sens.* 88, 468–478. doi:10.1016/j.rse.2003.09.005

Ronneberger, O., Fischer, P., and Brox, T. (2015). U-net: Convolutional Networks for Biomedical Image Segmentation. *Med. Image Comput. Computer-Assisted Intervention (Miccai)* 9531, 234–241. doi:10.1007/978-3-319-24574-4_28

Schwartzkopf, W., Milner, T. E., Ghosh, J., Evans, B. L., and Bovik, A. C. (2000). "Two-dimensional Phase Unwrapping Using Neural Networks," in 4th IEEE Southwest Symposium on Image Analysis and Interpretation, Austin, TX, April 2–4, 2000, 274–277. doi:10.1109/IAI.2000.839615

Sica, F., Calvanese, F., Scarpa, G., and Rizzoli, P. (2020). A CNN-Based Coherence-Driven Approach for InSAR Phase Unwrapping. *IEEE Geosci. Remote Sens. Lett.* 13, 2541. doi:10.1109/LGRS.2020.3029565

Spoorthi, G. E., Gorthi, S., and Gorthi, R. K. S. S. (2019). PhaseNet: A Deep Convolutional Neural Network for Two-Dimensional Phase Unwrapping. *IEEE Signal. Process. Lett.* 26, 54–58. doi:10.1109/LSP.2018.2879184

Sui, L. C., Ma, F., and Chen, N. (2020). Mining Subsidence Prediction by Combining Support Vector Machine Regression and Interferometric Synthetic Aperture Radar Data. *ISPRS Int. J. Geo-inf.* 9, 390. doi:10.3390/ijgi9060390

Tipper, D. J., Burton, D. R., and Lalor, M. J. (1996). A Neural Network Approach to the Phase Unwrapping Problem in Fringe Analysis. *Nondestructive Test. Eval.* 12, 391–400. doi:10.1080/10589759608952862

Wang, L. Y., Deng, K. Z., and Zheng, M. N. (2020). Research on Ground Deformation Monitoring Method in Mining Areas Using the Probability Integral Model Fusion D-InSAR, Sub-band InSAR and Offset-Tracking. *Int. J. Appl. Earth Obs. Geoinf.* 85, 101981. doi:10.1016/j.jag.2019.101981

Wang, Z. Y., Li, L., Wang, J., and Liu, J. (2021). A Method of Detecting the Subsidence basin from InSAR Interferogram in Mining Area Based on HOG Features. *J. CHINA U. MIN TECHNO.Journal China Univ. Mining Tech.* 50, 404–410. doi:10.13247/j.cnki.jcumt.001264

Wang, Z. Y., Wang, S. C., Sun, Y., and Wang, S. S. (2017). A New Phase Unwrapping Algorithm Based on the GVF-Snake Model of Edge Detection. *J. China Univ. Mining Tech.* 46, 1394–1401. doi:10.13247/j.cnki.jcumt.000767

Xia, Y. P., and Wang, Y. J. (2020). InSAR- and PIM-Based Inclined Goaf Determination for Illegal Mining Detection. *Remote Sens* 12, 3884. doi:10.3390/rs12233884

Xia, Y., Wang, Y., Du, S., Liu, X., and Zhou, H. (2018). Integration of D-InSAR and GIS Technology for Identifying Illegal Underground Mining in Yangquan District, Shanxi Province, China. *Environ. Earth Sci.* 77, 1–19. doi:10.1007/s12665-018-7488-1

Xu, H. K., Qin, Y. Y., and Pan, Y. (2014). Improved Edge Thinning Method. *LASER & INFRARED* 44, 319–324. doi:10.3969/j.issn.1001-5078.2014.03.22

Xu, J. Y., An, D. X., Huang, X. T., and Yi, P. (2016). An Efficient Minimum-Discontinuity Phase-Unwrapping Method. *IEEE Geosci. Remote Sens. Lett.* 13, 666–670. doi:10.1109/LGRS.2016.2535159

Yang, Z., Li, Z., Zhu, J., Yi, H., Feng, G., Hu, J., et al. (2018). Locating and Defining Underground Goaf Caused by Coal Mining from Space-Borne SAR Interferometry. *Isprs-j. Photogramm. Remote Sens.* 135, 112–126. doi:10.1016/j.isprsjprs.2017.11.020

Yu, H. W., Lan, Y., Yuan, Z. H., Xu, J. Y., and Lee, H. (2019). Phase Unwrapping in InSAR : A Review. *IEEE Geosci. Remote Sens. Mag.* 7, 40–58. doi:10.1109/MGRS.2018.2873644

Zheng, L., Zhu, L., Wang, W., Guo, L., and Chen, B. B. (2020). Land Subsidence Related to Coal Mining in China Revealed by L-Band InSAR Analysis. *Int. J. Environ. Res. Public Health* 17, 1170. doi:10.3390/ijerph17041170

Zheng, M. N., Deng, K. Z., Fan, H. D., and Du, S. (2018). Monitoring and Analysis of Surface Deformation in Mining Area Based on InSAR and GRACE. *Remote Sens* 10, 1392. doi:10.3390/rs10091392

Zhou, L. F., Yu, H. W., and Lan, Y. (2020). Deep Convolutional Neural Network-Based Robust Phase Gradient Estimation for Two-Dimensional Phase Unwrapping Using SAR Interferograms. *IEEE Trans. Geosci. Remote Sens.* 58, 4653–4665. doi:10.1109/tgrs.2020.2965918

Zhou, L., Zhang, D., Wang, J., Huang, Z., and Pan, D. (2013). Mapping Land Subsidence Related to Underground Coal Fires in the Wuda Coalfield (Northern China) Using a Small Stack of ALOS PALSAR Differential Interferograms. *Remote Sensing* 5, 1152–1176. doi:10.3390/rs5031152

Zhou, X., Chang, N.-B., and Li, S. (2009). Applications of SAR Interferometry in Earth and Environmental Science Research. *Sensors* 9, 1876–1912. doi:10.3390/s90301876

Conflict of Interest: Author LL was employed by the company Changzhou Construction Research Institute Group Co., Ltd.

The remaining authors declare that the research was conducted in the absence of any commercial or financial relationships that could be construed as a potential conflict of interest.

Publisher's Note: All claims expressed in this article are solely those of the authors and do not necessarily represent those of their affiliated organizations, or those of the publisher, the editors, and the reviewers. Any product that may be evaluated in this article, or claim that may be made by its manufacturer, is not guaranteed or endorsed by the publisher.

frontiers in Environmental Science

ORIGINAL RESEARCH
published: 06 December 2021
doi: 10.3389/fenvs.2021.787053

Study of Ground Movement in a Mining Area with Geological Faults Using FDM Analysis and a Stacking InSAR Method

Zhengyuan Qin[1], Vivek Agarwal[1], David Gee[1,2], Stuart Marsh[1], Stephen Grebby[1], Yong Chen[3]* and Ningkang Meng[3]*

[1]Nottingham Geospatial Institute, Faculty of Engineering, University of Nottingham, Nottingham, United Kingdom, [2]Terra Motion Limited, Nottingham, United Kingdom, [3]State Key Laboratory of Coal Resources and Safe Mining, China University of Mining and Technology, Xuzhou, China

OPEN ACCESS

Edited by:
Junshi Xia,
Riken, Japan

Reviewed by:
Bruno Adriano,
Riken Center for Advanced Intelligence Project (AIP), Japan
Yosuke Aoki,
The University of Tokyo, Japan

***Correspondence:**
Zhengyuan Qin
zhengyuan.qin@nottingham.ac.uk
Yong Chen
chenyong@cumt.edu.cn

Specialty section:
This article was submitted to Environmental Informatics and Remote Sensing, a section of the journal Frontiers in Environmental Science

Received: *30 September 2021*
Accepted: *16 November 2021*
Published: *06 December 2021*

Citation:
Qin Z, Agarwal V, Gee D, Marsh S, Grebby S, Chen Y and Meng N (2021) Study of Ground Movement in a Mining Area with Geological Faults Using FDM Analysis and a Stacking InSAR Method. Front. Environ. Sci. 9:787053. doi: 10.3389/fenvs.2021.787053

Underground coal mining activities and ground movement are directly correlated, and coal mining-induced ground movement can cause damage to property and resources, thus its monitoring is essential for the safety and economics of a city. Fangezhuang coal mine is one of the largest coalfields in operation in Tangshan, China. The enormous amount of coal extraction has resulted in significant ground movement over the years. These phenomena have produced severe damages to the local infrastructure. This paper uses the finite difference method (FDM) 3D model and the stacking interferometric synthetic aperture radar (InSAR) method to monitor the ground movement in Fangezhuang coalfield during 2016. The FDM 3D model used calibrated Fangezhuang geological parameters and the satellite InSAR analysis involved the use of ascending C-band Sentinel-1A interferometric wide (IW) data for 2016. The results show that the most prominent subsidence signal occurs in mining panel 2553N and the area between panel 2553N and fault F0 with subsidence up to 57 cm. The subsidence observed for the FDM 3D model and stacking InSAR to monitor land deformation under the influence of fault are in close agreement and were verified using a two-sample *t*-test. It was observed that the maximum subsidence point shifted towards the fault location from the centre of the mining panel. The tectonic fault F0 was found to be reactivated by the coal mining and controls the spatial extent of the observed ground movement. The impact of dominant geological faults on local subsidence boundaries is investigated in details. It is concluded that ground movement in the study area was mainly induced by mining activities, with its spatial pattern being controlled by geological faults. These results highlight that the two methods are capable of measuring mining induced ground movement in fault dominated areas. The study will improve the understanding of subsidence control, and aid in developing preventive measures in Fangezhuang coalfield with fault reactivation.

Keywords: finite difference method, ground movement, Interferometric SAR, stacking, geological fault, 3D modelling

1 INTRODUCTION

As China's primary source of energy, coal it is critical to the country's social and economic growth. Large-scale coal mining, however, has the potential to substantially harm the environment in mining areas, as well as causing a variety of geological issues and societal problems (Diao et al., 2019). As one of the main effects, a thorough understanding of mining-induced subsidence is essential for preventing or mitigating such issues.

With regards to measuring surface movement, traditional methods like levelling, Global Navigation Satellite System (GNSS), 3D laser scanning, and similar provide accurate information, but can be time-consuming, expensive, and have low spatial extent and are therefore unsuited to surveying large (basin level) areas. A better alternative is to use the satellite Interferometric Synthetic Aperture Radar (InSAR) technique, which provides weather independence, sunlight independence (active sensor), high (basin-level or greater) spatial coverage, and is less tedious and more economical. Therefore, InSAR offers a spatial resolution comparable to other traditional methods of land surveying. Many researchers have used InSAR to study land movement resulting from earthquakes (Fialko, Simons, and Agnew 2001), glacial movements (Wang et al., 2015), landslides (Sun et al., 2015; Kang et al., 2017; Zhang et al., 2020), volcanic bulging (Fournier et al., 2010; Albino et al., 2020), groundwater extraction (Bell et al., 2008; Motagh et al., 2017; Castellazzi et al., 2018) and coal mining (Zhang et al., 2015; Yang et al., 2017; Diao et al., 2018; Dong et al., 2021).

Extensive research has been carried out to study ground movement induced by underground mining activities (Park et al., 2012; Yang et al., 2019). In recent years, several research tools, such as numerical analysis (Deck and Anirudh 2010; Shabanimashcool and Li 2012; Shi M et al., 2021) and InSAR time-series analysis (Sowter et al., 2016; Gee et al., 2017; Grebby et al., 2019; Ghayournajarkar and Fukushima 2020) have been widely employed to analyse the mechanism of ground movement. Furthermore, several studies have also focused on ground movement associated with fault activation. Bell et al. (2005) reported mining subsidence from Great Britain, Germany and Colombia, and stated that mining area experiencing reactivation of faults should be surveyed properly before construction and a safe gap of at least 10 m should be maintained between the fault zone's edge and any structures. Moreover, Mohammady et al. (2019) employed Random Forest theory to analyse subsidence susceptibility and found that gap from the fault, elevation, slope angle and water table had the largest influence on ground deformation. Gumilar et al. (2015) and Pacheco-Martínez et al. (2013) discovered a direct link between fault position and high land deformation rates.

In terms of numerical analysis, the finite difference method (FDM) is commonly utilised within the FLAC^{3D} software because of its efficacy as a tool for solving rock mechanics and geo-mechanical issues. It can handle material heterogeneity, nonlinearity, complicated boundary conditions, ground condition pressures and gravity. The FDM model idealises the rock mass as a continuous medium that deforms according to a given constitutive law, satisfying compatibility and equilibrium criteria, and yields approximate partial differential equation solutions. Due to the discontinuities (e.g., geological fault) in the study area, a discontinuous numerical method was chose to study the ground movement based on the FDM analysis with FLAC^{3D} software. In FLAC^{3D}, the ground movement value of any point in the model can be monitored; it is typically more applicable for continuous and uniform subsidence. FDM analysis is widely used to study the ground movement in coal fields (Cheng et al., 2019; Parmar et al., 2019; Sikora and Wesołowski 2021; Yan et al., 2021).

Only a few attempts have been made to study 3D model simulation of ground movement in conjunction with InSAR-derived ground movement to understand the effect of a geological fault (Jeanne et al., 2019; Perry et al., 2020; Francioni et al., 2021; Shi Y et al., 2021). Although these previous studies suggest that faults do affect the ground movement, the nature and magnitude of effects have not been fully explored. The current approach uses the hybrid method, which is the combination of the numerical method and stacking InSAR analysis to study how the fault affects the ground movement induced by mining. To study the ground movement associated with subsurface mineral extraction at Fangezhuang coal mine, a fully 3-D elastoplastic FDM model was constructed. The results of the developed FDM model were verified by comparing the outputs of the model with the ground movement revealed by stacking InSAR analysis. Finally, the ground movement under the influence of fault in Fangezhuang coal mine is discussed.

This paper is divided in five sections. The **section 1** provides an Introduction, and the **section 2** describes the study area. **Section 3** describes the methodology for studying the ground movement with the 3D FDM model and stacking InSAR technique. In **section 4**, we reveal the ground movement in Fangezhuang coal mine using FDM model and InSAR technique and perform a comparison between FDM model and InSAR result and the ground movement trend in Fangezhuang coal mine is revealed. Finally, conclusions and future scope of the study are discussed in **section 5**.

2 STUDY AREA

Fangezhuang coal mine lies in the Kailuan area, Hebei Province, China, approximately 23 km east of Tangshan city. While most coal lies in plain, the ground surface consists of farmland, villages, mining factories and ground sunk fissure caused by mining subsidence. Fangezhuang coal mine has an area of 32.33 km^2 in which the north-south direction is 12.25 km, and the highest east-west inclination is 3.92 km. The coal seam is nearly horizontal, with a mean thickness of 3 m. This region is characterised by large ground movements, with thick loose layers and fast advancement of the working panel. The study area is marked in **Figure 1**.

2.1 Geological Structure

Within the Fangezhuang coal mine, one major fault exists: F0 (**Figure 1**). F0 fault is a normal fault that runs through the Fangezhuang coal mine in a north-south direction. According to

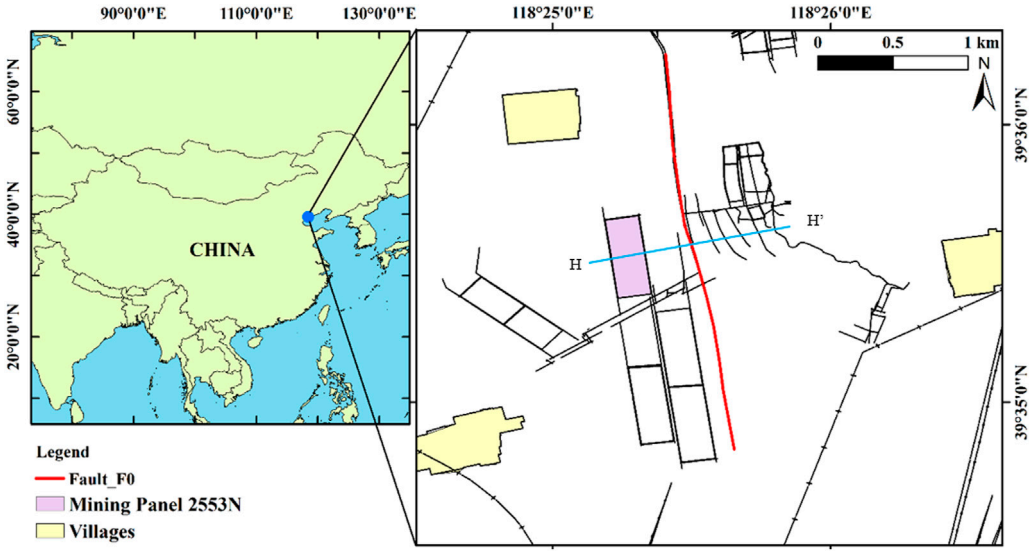

FIGURE 1 | Location of the study area. Blue spot is Fangezhuang coal mine in Tangshan city. Purple rectangle area is mining panel 2553N. Red line shows the F0 geological fault.

the drilling data, the fault extends about 3,000 m, and the drop ranges from 14 m to 37 m. The fault is a high-angle normal fault, inclined to SWW, with a dip angle of 70°–84°. F0 fault runs through the whole monocline structural area and has a significant impact on mining production. Meanwhile, there are associated faults of a specific scale with a significant drop on both sides of the F0 fault, and most of the associated faults here develop along the strike of the F0 fault.

2.2 Coal Seam and Rock Strata

Figure 2 shows the cross-section along H-H'. The strata revealed through exploration of Fangezhuang coal mine are Ordovician (O), Carboniferous (C), Permian (P) and Quaternary (Q), as described below.

1) The O stratum, 500–900 m thick, comprises fine-grained dolomite, stratified limestone.
2) The C stratum, 140–290 m thick, comprises siltstone, mudstone and fine sandstone. This formation also contains 1-3 layers of unstable thin coal seams.
3) The P stratum has a mean thickness of 550 m. From bottom to top, the sequence is split into the four forms showed below.
   - The Damiaozhuang formation mainly contains siltstone, mudstone and medium sandstone. Four layers of the coal seam can be mined, namely No. 5 coal seam, No. 7 coal seam, No. 8 coal seam and No. 9 coal seam.
   - The Tangjiazhuang formation is mainly composed of coarse-to-medium sandstone, followed by fine sandstone. The lower strata are interbedded with 1–4 layers of thin coal lines.
   - The Guye formation mainly comprises of medium-coarse sandstone with a small amount of mudstone and siltstone.
   - The Wali formation is mainly composed of medium-coarse sandstone, fine sandstone and siltstone. At the bottom, a layer of aluminum mudstone with a thickness of about 4–5 m is developed.
4) The Q stratum is mainly composed of clay, sand and gravel layer. The Quaternary alluvium covers the whole Fangezhuang mine field. The thickness of alluvium varies from 54 m to 424 m and gradually thickens from north to south.

In this research, No. 5 coal seam, located at around 560 m deep in Permian strata, is the main workable seam. The mining panel 2553N which started in January 2016 and terminated in December 2016 along the northwest-southeast direction, is chosen to analyse ground movement. For the geological structure, F0 fault cut No. 5 coal seam along the southeast direction, resulting in a decrease of the depth of No. 5 coal seam at the east side of F0.

3 METHODOLOGY AND DATA USED

In this study, FLAC^{3D} was adopted for numerically predicting ground movement caused due by coal mining. FLAC^{3D} is a 3-D finite-difference computer program to solve geological problems (Kumar et al., 2016; Shi M et al., 2021). In FLAC^{3D}, the initial model is the geomechanical model with the engineering scale, which is able to simulate the real geological condition in the mining coalfield. The null model plugged in FLAC^{3D} is used to delete the elements to simulate the mining extraction activities. When the elements representing the coal are deleted to leave a void, the overlying elements will have a free displacement boundary and the stress field will redistribute, resulting in the overlying elements caving. The caving is spread upwards to the top surface, which represent the ground movement. The InSAR analysis used 25 Sentinel-1 ascending, Interferometric Wide (IW)

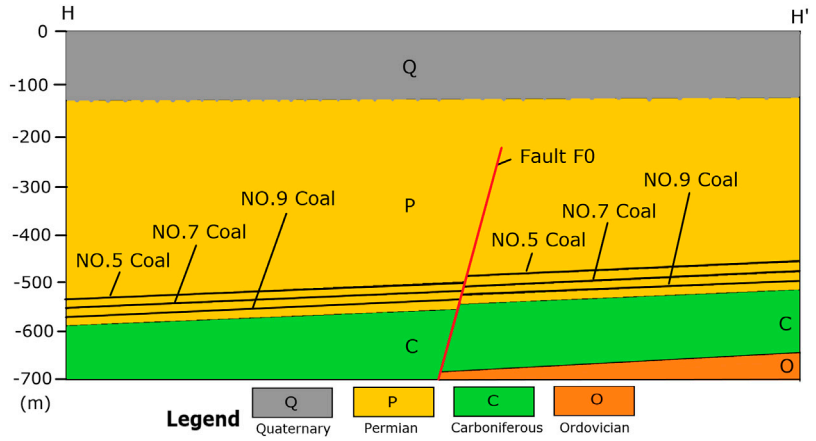

FIGURE 2 | Cross section view along H-H' (marked in **Figure 1**).

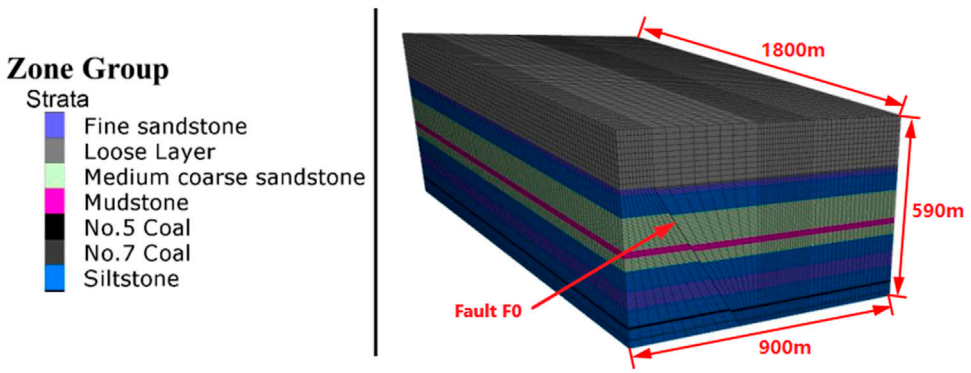

FIGURE 3 | FLAC^{3D} FDM model.

Single Look Complex (SLC) images between January 2, 2016 and December 21, 2016. The C-Band (wavelength of 5.6 cm) data have a pixel spacing of 2.3 m in range and 13.9 m in azimuth, and a revisit period of 12 days (Torres et al., 2012).

3.1 Establishment of the 3D FDM Model

The mining panel 2553N shown in **Figure 1** is selected as the computational model domain on the basis of spatial distribution of the considered mining area. Based on the geological properties of the Fangezhuang coalfield, a 3D FDM simulation model of panel 2553N and F0 fault is set up, which is shown in **Figure 3**. The parameters of the FDM model are set as follows: the size of panel 2553N is 900 m × 180 m, No.5 coal thickness is 3 m, mining depth is 560 m, angle of the fault F0 is 70°, and step excavation distance is 75 m. The coal mineral extraction was simulated as long-wall mining with step by step excavation. The ground surface deformation map was obtained for the study area from January 2016 to December 2016 when the ground surface was stable (where the unbalanced force is less than 10^{-5} of the maximum unbalanced force) (Du et al., 2019). The dimensions of the model are 1800 m long, 900 m wide, and 590 m high. The top surface does not show any geomorphic feature and is assumed horizontal in the model. The shortest horizontal distance between the mining boundary and the model boundary is 360 m to remove the boundary effect.

3.1.1 Generalisation of Strata and Faults

Mining panel 2553N lies in the Permian strata, and No. 5 coal seam is the main workable coal seam. As a result, two geological strata Quaternary and Permian, as well as No. 5 coal seam are simulated in a FDM model. The structure of each strata is made with reference to the geological report of Fangezhuang coal mine and borehole data. The fault could be designed with interface elements in FLAC^{3D} if the thickness of the fault is small (Cai et al., 2021). However, when the thickness of a fault is more than 10 m, it is appropriate to use a layer with a certain thickness to simulate a fault (Xu et al., 2013). In this paper, we choose a layer with two boundary surfaces to model the F0 fault around 10–20 m thick.

3.1.2 Computational Mesh

FLAC^{3D} supports numerous element shapes, including hexahedrons, tetrahedrons, pyramids, triangular prisms, and others (Abbasi et al., 2013). With a consideration of achieving a balance between processing time and simulation accuracy, a set of

octahedral elements was adopted to mesh the simulation model. The meshing approach is as follows. It can be seen in **Figure 3**, from top to bottom, the model is divided into 13 layers which are loose layer, fine sandstone, siltstone, medium coarse sandstone, mudstone, medium coarse sandstone, siltstone, fine sandstone, siltstone, No. 5 coal, siltstone, No. 7 coal and siltstone. Each layer has a thickness of 3–160 m. The closer a layer is to the coal seam roof, the thinner the layer is set; the farther it is from the roof, the thicker it is set.

3.1.3 The Constitutive Model and Boundary Conditions

The Mohr-Coulomb model is used as the constitutive model and Mohr–Coulomb yield criterion are used in this study, along with displacement boundary conditions. No vertical displacement is allowed at the bottom of the simulation model, and no displacement is allowed in the direction perpendicular to the lateral boundaries. Trapezoidal distributed load is applied in the horizontal direction. Gravity force is applied to the model. A numerical model is obtained from these results, which reflects the mining and geological condition of the region after long-wall panel exploitation.

3.1.4 Monitor Points

The 3D FDM model simulates the whole No. 5 coal extraction of panel 2553N which commenced in January 2016 and stopped in December 2016. Based on the mesh of the FDM model, on the top boundary of the model we set up 224 monitoring points (16 × 14) to obtain the ground movement during the coal mining process.

3.1.5 Mechanical Parameters of Rock Strata

Intact rock and discontinuities make up rock layers. The mechanical properties of complete rock samples acquired through laboratory testing differ substantially from the mechanical properties of rock strata (Hoek and Brown 1997). However, to some extent, the reliability of numerical simulation results depends on the choice of rock mechanical parameters. The methods for determining mechanical parameters mainly include empirical reduction method, engineering rock mass classification method and displacement back analysis method. This research adopts the back analysis with orthogonal test and numerical simulation to determine the rock mechanical parameters.

The detailed procedure is as follows (Xu et al., 2013):

1) Based on the geological report of Fangezhuang coal mine, the initial rock parameters are shown in **Table 2** (Ren 2017). The average value of the deformation modulus $\bar{E}$, Poisson's ratio $\bar{\mu}$, cohesion $\bar{C}$ and internal friction angle $\bar{\varnothing}$ are chosen as the experimental factors. The initial mechanical parameter divided by the corresponding average value is calculated for each mechanical parameter of each strata. These values are listed as K_E^i , K_μ^i , K_C^i, and $K_\varnothing^i$ in **Table 1**. Therefore, each strata mechanical parameters could be given as $K_E^i\bar{E}$, $K_\mu^i\bar{\mu}$, $K_C^i\bar{C}$ and $K_\varnothing^i\bar{\varnothing}$. The maximum ground movement W_{max} is chosen as the test indicator.
2) The orthogonal test with four factors and five levels L_{25} (5^4) was set up to test the rock parameters (**Table 2**). All the testing schemes are listed in an orthogonal table (**Table 3**).
3) 25 numerical simulations were conducted using FLAC^{3D} and the results for each scheme were listed in **Table 3**. According to the result in **Table 3**, it was found that the maximum ground movement of the 4th scheme is closest to the measured ground movement of 16.2 cm (geological report of Fangezhuang coal mine). Therefore, the parameters of the four factors are $\bar{E} = 3.6GPa$, $\bar{\mu} = 0.31$, $\bar{C} = 6.3MPa$ and $\bar{\varnothing} = 37°$. The final parameters for each layer shown in **Table 4**.

3.2 Stacking InSAR Analysis

An InSAR stacking method was employed to map the ground deformation due to the decimetre scale rates of deformation expected to occur following the long- wall extraction of panel 2553N. The processing chain utilised is summarized in **Figure 4**. The Sentinel-1 SLC data were initially deburst and merged before co-registration to the slant-range coordinate system of the master image (January 2, 2016). Phase ramps attributed to orbital errors were subtracted using the precise orbit determination and topographic phase was simulated and removed using a DLR digital elevation model (DEM) from the TanDEM-X mission (Rizzoli et al., 2017). The data were multi-looked by a factor of 4 in range and 1 in azimuth and interferograms, with approximately a 10 m resolution, were generated between consecutive SAR acquisitions irrespective of the perpendicular baseline. The interferometric fringes (phase cycles that correspond to a displacement of half of the sensor wavelength) are related to the surface deformation. Generating interferograms only over the shortest epochs the minimises like likelihood of quantitatively underestimating the deformation due to the ambiguity effect when deformation gradients are high, such as over active mining sites. Further, an accurate estimation of the deformation depends upon high coherence (or phase correlation) between the two forming SAR images, hence, utilizing consecutive image pairs helps maintain coherence. In addition, the interferograms were filtered using a modified Goldstein filter to further improve coherence and the quality of phase. The interferograms were unwrapped from modulo-2π phase to relative deformation using a statistical-cost network-flow algorithm (Chen and Zebker 2001) with respect to a reference point located at Tangshan (39.6309° N, 118.1802° E). The unwrapped interferograms were subsequently stacked and an average rate of motion was derived from a least squares covariance analysis of the unwrapped phase. Once linear velocities had been generated, the relative height change for each image acquisition was calculated in accordance with that of Berardino et al. (2002). Finally, the line-of-sight time-series were projected into the vertical, by means of dividing by the cosine of the incidence angle (~ 0.639 radians), to facilitate an appropriate comparison with the model.

4 RESULTS AND DISCUSSION

4.1 Comparison Between FDM Model and Stacking InSAR Result

Figure 5 shows the vertical surface deformation over the study period as generated by (a) InSAR stacking, (b) 3D FDM model

TABLE 1 | Initial mechanical parameters of rock formations.

Rock formation	E (GPa)	μ	C (MPa)	Ø (°)	K_E^i	K_μ^i	K_C^i	$K_Ø^i$
Loose layer	0.06	0.36	0.015	20	0.006	1.268	0.003	0.625
Fine sandstone	11.63	0.28	5	47	1.209	0.987	1.079	1.469
Siltstone	9.01	0.28	3.7	30	0.937	0.987	0.799	0.938
Medium-coarse sandstone	18.6	0.23	13.05	47	1.934	0.810	2.819	1.469
Mudstone	8.46	0.29	2	23	0.880	1.022	0.432	0.719
Medium-coarse sandstone	18.6	0.23	13.05	47	1.934	0.810	2.819	1.469
Siltstone	9.01	0.28	3.7	30	0.937	0.987	0.799	0.938
Fine sandstone	11.63	0.28	5	47	1.209	0.987	1.079	1.469
Siltstone	9.01	0.28	3.7	30	0.937	0.987	0.799	0.938
Coal	5.5	0.31	1.8	18	0.572	1.092	0.389	0.563
Siltstone	9.01	0.28	3.7	30	0.937	0.987	0.799	0.938
Coal	5.5	0.31	1.8	18	0.572	1.092	0.389	0.563
Siltstone	9.01	0.28	3.7	30	0.937	0.987	0.799	0.938
Average	9.618	0.284	4.63	32	3.6	0.31	6.3	37

TABLE 2 | Levels of test factors.

Scheme	Deformation modulus	Poisson's ratio	Cohesion	Internal friction angle
	$\bar{E}$ GPa	$\bar{\mu}$	$\bar{C}$ MPa	$\bar{Ø}$ (°)
I	3.6	0.22	1.8	16
II	6.1	0.25	3.3	23
III	8.6	0.28	4.8	30
IV	11.1	0.31	6.3	37
V	13.6	0.34	7.8	44

TABLE 3 | Orthogonal test design and results.

Scheme	$\bar{E}$ (GPa)	$\bar{\mu}$	$\bar{C}$ (MPa)	$\bar{Ø}$ (°)	W_{max} (cm)	Scheme	$\bar{E}$ (GPa)	$\bar{\mu}$	$\bar{C}$ (MPa)	$\bar{Ø}$ (°)	W_{max} (cm)
1	3.6	0.22	1.8	16	26.1	14	8.6	0.31	4.8	16	7.6
2	3.6	0.25	3.3	23	19.6	15	8.6	0.34	6.3	23	7.2
3	3.6	0.28	4.8	30	17.8	16	11.1	0.22	3.3	37	5.8
4	3.6	0.31	6.3	37	16.6	17	11.1	0.25	4.8	44	6.5
5	3.6	0.34	7.8	44	15.2	18	11.1	0.28	6.3	16	4.6
6	6.1	0.22	4.8	23	11.1	19	11.1	0.31	7.8	23	8.2
7	6.1	0.25	6.3	30	10.4	20	11.1	0.34	1.8	30	6.7
8	6.1	0.28	7.8	37	10.2	21	13.6	0.22	6.3	44	5.2
9	6.1	0.31	1.8	44	10.5	22	13.6	0.25	7.8	16	4.9
10	6.1	0.34	3.3	16	11.5	23	13.6	0.28	1.8	23	6.8
11	8.6	0.22	7.8	30	7.5	24	13.6	0.31	3.3	30	4.7
12	8.6	0.25	1.8	37	8.2	25	13.6	0.34	4.8	37	4.5
13	8.6	0.28	3.3	44	7.4						

and (c) Residual of the InSAR movement minus FDM model. Surface uplift is represented by a positive value and subsidence by a negative value. Both the InSAR and 3D FDM model results show the severe subsidence pattern nearby the mining panel 2553N. For the FDM model, the ground movement ranges from 34.2 to 57.6 cm, while for the stacking InSAR result, the vertical deformation ranges from 15.2 to 58.3 cm. Based on the mining ground movement theory, if the ground movement is greater than ±10 mm/ year then the area is considered unstable (Zheng et al., 2018). From the perspective of ground movement, both the FDM model and InSAR measurements confirm that the area is unstable due to the coal mineral extractions. The ground movement basin is located within the mining panel 2553N and the area between the panel and fault F0.

It can be seen from **Figure 5A** that the shape of the subsidence basin is not symmetrical over the mining area (mining panel 2553N), and the maximum subsidence point is located at point B, which is about 75 m from point A (centre of panel 2553N). The subsidence map shows a clear boundary nearby Fault F0. The boundary corresponds to the fault F0 and clear ground movement differences can be seen either side of fault F0. **Figure 5B** shows the similar subsidence basin revealed by FDM modelling. The maximum subsidence point is also located at point B but with a marginally smaller magnitude

TABLE 4 | Calibrated mechanical parameters used in 3D model.

No	Rock formation	Thickness(m)	*E* (GPa)	*μ*	*C* (MPa)	Ø (°)
1	Loose layer	160	0.022	0.39	0.02	23
2	Fine sandstone	15	4.35	0.31	6.8	54
3	Siltstone	55	3.37	0.31	5	35
4	Medium-coarse sandstone	90	6.96	0.25	17.8	54
5	Mudstone	15	3.17	0.32	2.7	27
6	Medium-coarse sandstone	35	6.96	0.25	17.8	54
7	Siltstone	50	3.37	0.31	5.03	35
8	Fine sandstone	60	4.35	0.31	6.8	54
9	Siltstone	50	3.37	0.31	5.03	35
10	No. 5 Coal	3	2.06	0.34	2.5	21
11	Siltstone	30	3.37	0.31	5.03	35
12	No.7 Coal	4	2.06	0.34	2.5	21
13	Siltstone	23	3.37	0.31	5.03	35

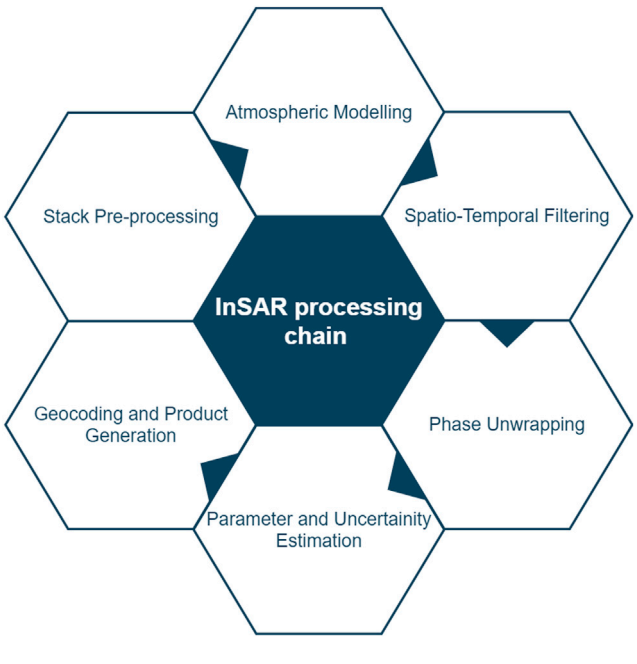

FIGURE 4 | Stacking InSAR processing chain used for the study.

compared with InSAR. The relative severe ground movement with a maximum value of 58 cm is located in the northeast part of panel 2553N. In the east of the fault F0, the maximum ground movement is approximately 15 cm. The east of panel 2553N presents relatively uniform and homogeneous subsidence, with a magnitude of up to 20 cm. **Figure 5C** shows the residual map of the FDM model and the InSAR result. The red colour represents where the ground movement of FDM model is less than the InSAR result. In other words, negative residual measurements represent underestimation of the FDM model with respect to the InSAR result. It can be seen that the average ground movement obtained by InSAR is smaller, especially in the area of severe ground movement between panel 2553N and fault F0. Nonetheless, the surface subsidence caused by long-wall mining is significant. InSAR only detects the medium-scale ground movement. As a result, the 3D FDM model proposed in this study is a valuable tool for ground movement analysis.

Since the numerical model does not take the rock fissure and other geological properties of rock mass into account, the simulated results appear relatively smoother than the InSAR result. In addition, the InSAR measurements are relative to a reference point and are therefore not absolute. Thus, when comparing the InSAR results directly to the results from the FDM-model, it is worth noting that there may be some offset if the InSAR reference point was not entirely stable (i.e., it has a non-zero displacement) during the observed period. Furthermore, InSAR results may be affected by noise such as atmospheric, ionospheric (Liao et al., 2018) and unwrapping correlation error (Yunjun et al., 2019). Thus, any differences between the measurements could be due to several aspects relating to the InSAR processing, e.g., noise and the fact that the InSAR measurements are relative to a reference point that may be moving slightly.

The ground movement pattern may result from underground mining, fault reactivation and other factors. **Figure 6** shows the time series surface deformation of the FDM model and InSAR analysis at points A, B, C and D. It can be seen that the maximum subsidence values gradually increase from 14th January to 20th September. After 20th September, both the FDM model and InSAR result show that the rate of increase of the maximum ground movement value decreases. Although the mining panel is advancing from September to December, the ground movement is increasing slowly at a relatively steady pace. According to mining subsidence theory, when the advancing distance reaches 1.2–1.4 times the average mining depth, the mining activity will reach full mining condition (Wang et al., 2020). This suggests that after 9 months of mineral extraction (panel 2553N advancing 675 m along the strike direction), the mineral extraction reached supercritical mining. From January to March, uplift is observed in the InSAR time series, which might be the noise effect in the stacking analysis. Compared with the ground movement value at point A, point B experiences less ground movement, confirming that the maximum ground movement is not located at the centre of panel 2553N. There is a clear difference in ground movement between C and D, which are located on different sides of fault F0.

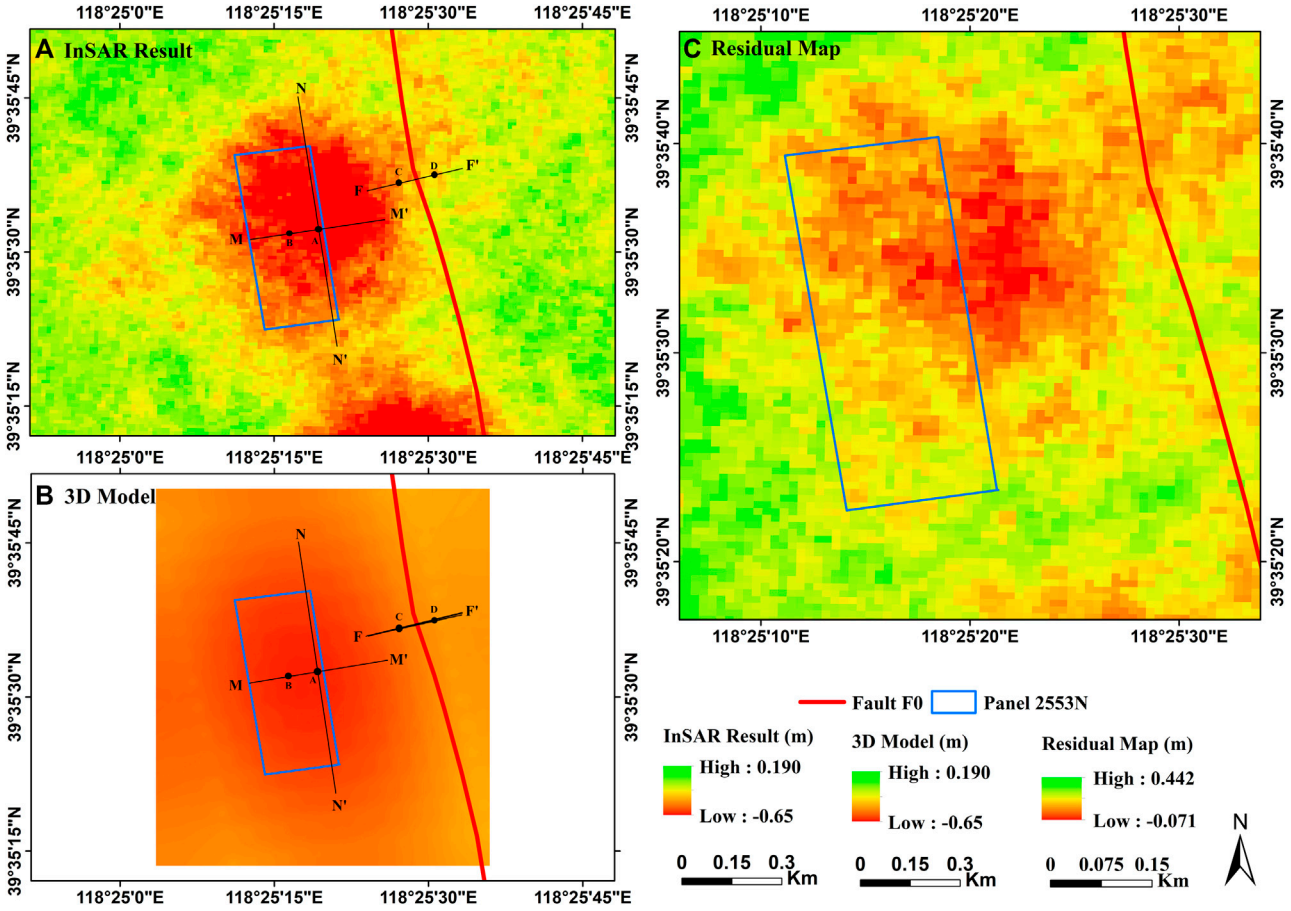

FIGURE 5 | Three-dimensional deformation generated by **(A)** InSAR result **(B)** 3D FDM model result **(C)** Residual result (InSAR—3D FDM model).

Table 5 summarises the two-sample *t*-test results for points A, B, C and D (marked in **Figure 5**) to determine, quantitatively, whether the differences between the InSAR and FDM model series at these points are within the acceptable range (Agarwal et al., 2020). The mean difference between the InSAR and the FDM model is not the same at each of these points. As a result, it is necessary to investigate if the difference is significant. For the test, the Null Hypothesis (H0) is taken as the average difference is zero ($\mu = 0$) and alternate Hypothesis (HA) as the average difference is not zero ($\mu \neq 0$).

The t-value computed for the comparison of the InSAR and FDM modelling outputs at point A is 1.32. This means that these values are 1.32 standard deviations off of the mean. A t-value less than the critical t-value (2.069 for point A) is necessary to accept the null hypothesis. The t-value for point A is less than the crucial t-value, meaning that the null hypothesis is accepted, indicating that there is no significant difference between the InSAR result and the FDM model at point A. Another approach to confirm this is to look at the p-value (0.25) and alpha (0.05 for the 95 percent confidence limit), where a p-value greater than alpha means the null hypothesis is accepted. Acceptance of the null hypothesis in both cases demonstrates that the InSAR-derived subsidence exists, and that the FDM model is consistent at point A. From **Table 5**, similar results can be seen for points B, C, and D. As a result, we have sufficient evidence that InSAR-based subsidence is consistent and agrees well with FDM model values for all four points A, B, C, and D.

In order to examine the ground movement trends, the transect lines M–M′ along the coal seam strike direction, N–N′ along the coal seam dip direction and F-F′ vertically across the fault F0 were extracted (as shown in **Figure 5**). **Figure 7** shows the land subsidence profiles of observation lines M–M′, N–N′ obtained from the FDM model and stacking InSAR analysis. It can be seen that the ground movement trends of the two lines are almost identical. The root-mean-square error along M–M′ in the dip direction is 0.113 m, with a maximum difference 0.141 m. The root-mean-square error along N–N′ in the strike direction is 0.105 m, with the largest difference of 0.210 m. The blue and orange lines show InSAR and FDM-model subsidence, respectively. The grey shading shows the standard deviation of the displacements observed at each location for both InSAR and FDM subsidence. The overlapping darker area for both the curves highlights that the deviation between the methods is small and within the standard deviation error limits. It can be seen that the

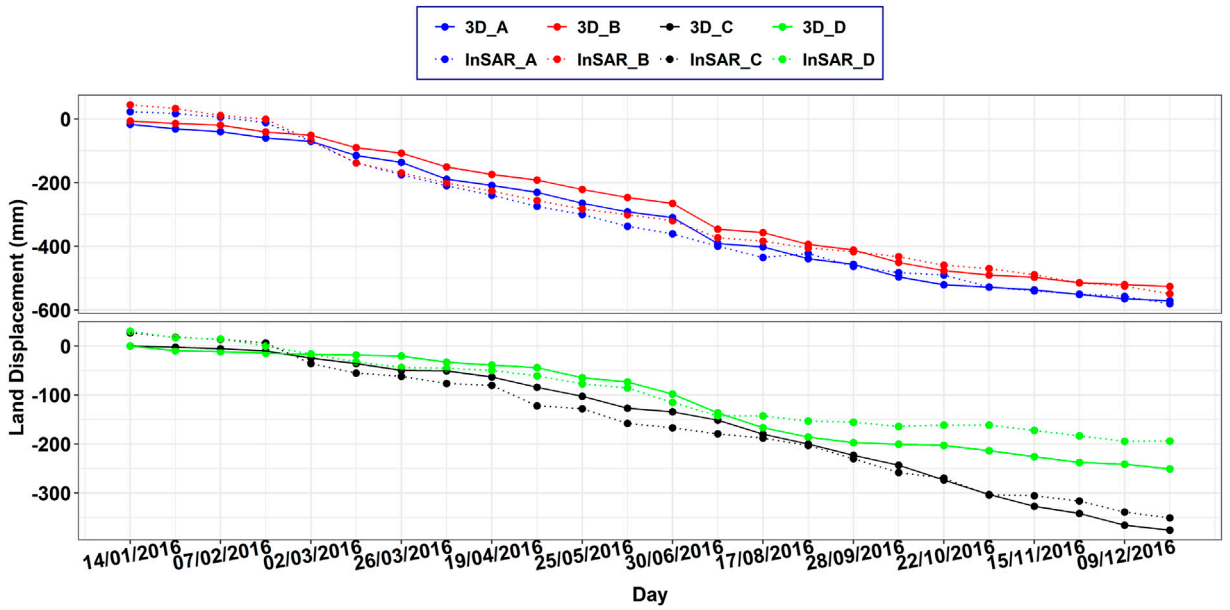

FIGURE 6 | Time series comparison for FDM model and InSAR subsidence and at point A, B, C and D.

TABLE 5 | Two-paired *t*-test for FDM model and InSAR result.

Parameter	Point A	Point B	Point C	Point D
Mean (InSAR)	−291.32	−262.35	−143.78	−88.67
Mean (FDM)	−309.14	−273.41	−153.08	−112.54
Standard Deviation of difference	29.16	36.61	27.48	31.15
Observations	24	24	24	24
Pearson Correlation	0.98	0.98	0.98	0.96
Df (Degree of freedom)	23	23	23	23
t Stat	1.32	1.81	1.42	1.74
P(T ≤ t) two-tail	0.25	0.087	0.059	0.321
t Critical two-tail	2.069	2.069	2.069	2.069

subsidence curves along with M–M′ and N–N' do not remain horizontal at the bottom of the basin but appear to be fluctuating somewhat.

From the subsidence profile of N–N′ in **Figure 7B**, it can be seen that the InSAR result shows the ground movement in the southern part of N–N' is slightly greater than that in the northern part. This is likely because the ground movement obtained by InSAR includes some residual subsidence caused by adjacent goaf (Fan et al., 2021). According to the geological report of Fangezhuang coal mine, mining along a panel to the south of panel 2553N stopped in 2015 and may cause the residual ground movement in 2016.

4.2 Influence of Fault F0 on Ground Movement

Figure 8 shows the land subsidence profiles of observation lines F–F' obtained from the FDM model and stacking InSAR analysis. The grey shading shows the standard deviation of the displacements observed at each location for both InSAR and FDM model subsidence. The overlapping darker area for both the curves highlight that the deviation obtained from both the methods is small and within the standard deviation error limits.

For the profile along F-F′, it can be observed that at the distance of around 155 m there is a distinct change in slope in the subsidence profile. Interestingly, the fault F0 also lies at this location, which appears to be controlling this subsidence pattern. At this location, the fault is attributable for subsidence of 100–300 mm/ year on its right, and a subsidence rate of 300–500 mm/ year on its left. It can also be seen from **Figure 5** that fault F0 has a noticeable effect on the spatial distribution of ground movement. This is most likely due to differential vertical compaction of various thicknesses of compressible soil deposited on both sides of the faults, which is greater in the hanging wall in normal faults (Burbey 2002). This observed structural control of land subsidence causes differential subsidence rates on either side of the fault line, which could potentially cause damage to villages, trains, and other infrastructure.

Fault F0 crosses the Fangezhuang coal mine in a north-south direction. The fault trace divides the subsidence rates and the arrows in **Figure 8** indicate the relative displacement of the fault. To the west of F0, along F-F', the relative severe subsidence has a maximum value of 425 mm obtained for the FDM model result and 433 mm measured by InSAR. The east of F0 exhibits relatively stable subsidence, with a value up to 225 and 152 mm obtained with the FDM model and InSAR, respectively. In addition, **Figure 5** shows the maximum subsidence point (point A) is not above the centre of panel 2553N, but it approaches F0. It can be seen that fault F0 has a blocking effect on overburden movement. The surface subsidence morphology under the influence of fault is not symmetric about

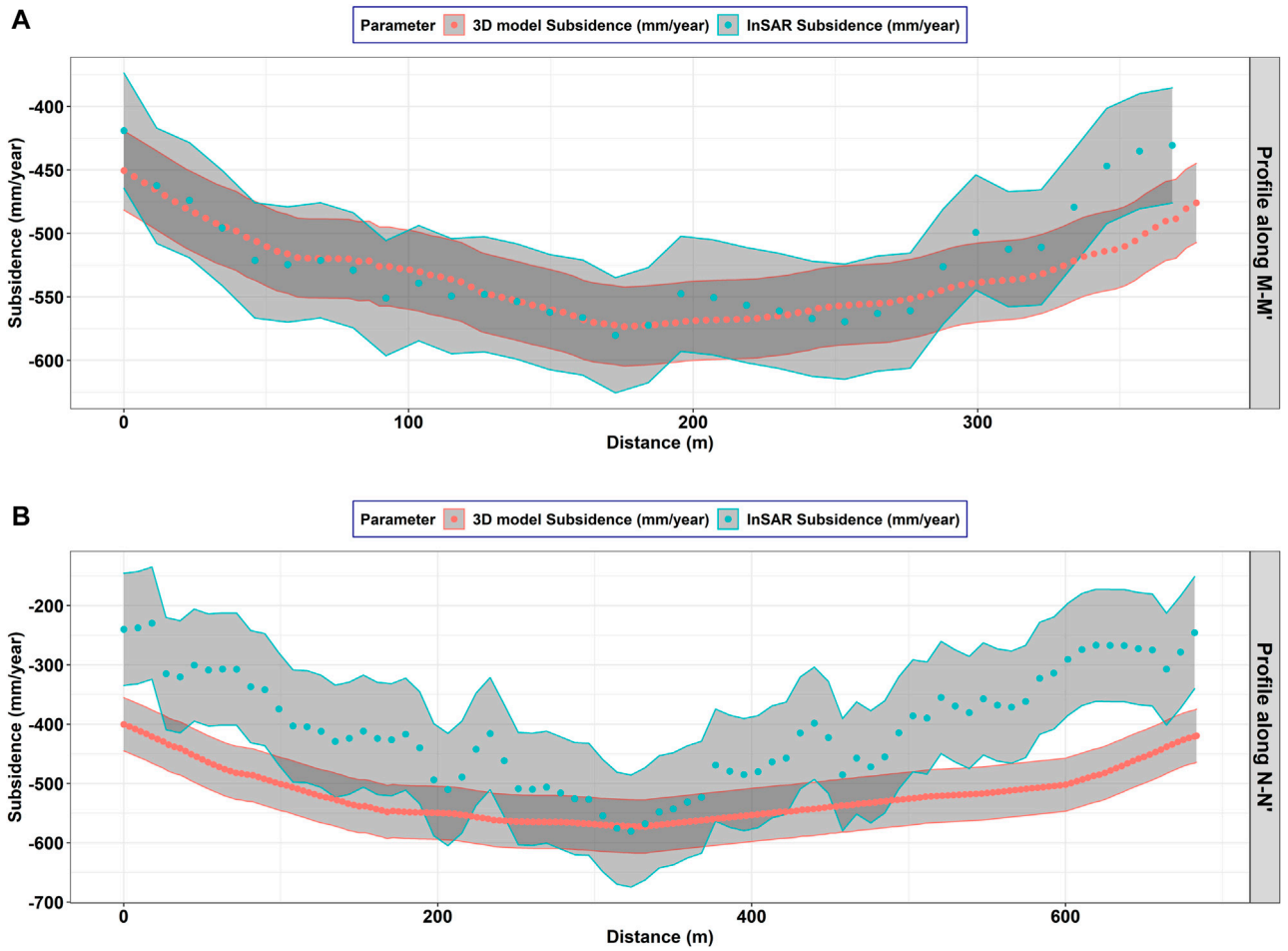

FIGURE 7 | Land subsidence profiles of FDM model and InSAR result along **(A)** M–M′ and **(B)** N-N′.

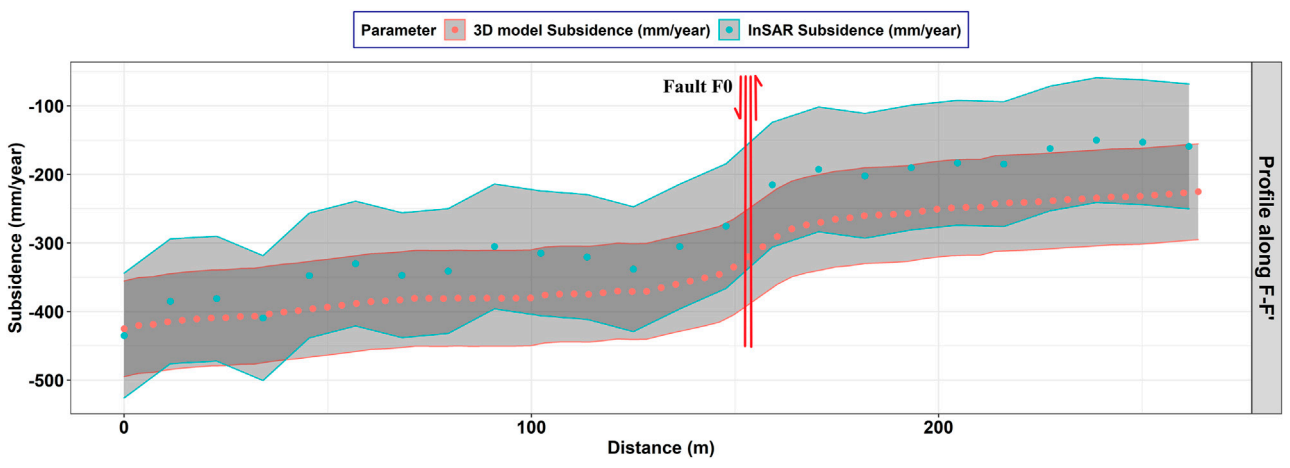

FIGURE 8 | Land subsidence profiles of FDM model and InSAR result along F-F′.

the centre of goaf. The maximum subsidence is shifted towards the fault. The ground movement patterns show a good agreement with the results derived from the recent study (Yu 2020). The precise different ground movement on both sides of F0 indicates that the fault is reactivated by panel 2553N coal mining. These results suggest that the subsidence in the study area is a dynamic process. Overall, the deviation obtained from the FDM model and InSAR method is small and within the standard deviation error limits. The InSAR- derived surface subsidence curve coincides with the FDM model simulation result.

5 CONCLUSION

This paper studies the ground movement in Fangezhuang coalfield in Tangshan city using a complete 3D FDM analysis in conjunction with stacking InSAR analysis. In order to obtain a reliable model, an orthogonal test was applied to back analyse the strata parameters, and the subsequent FDM model result was compared with the ground movement measured using InSAR. The differences in the maximum ground movement obtained from the FDM model analysis and stacking InSAR analysis were within 25%. Both results show that when the fault is activated by underground mining, the maximum subsidence value will not be located precisely above the centre of the mining panels. Instead, it is shifted towards the fault, and the geological fault clearly affects the spatial distribution of ground movement. The most dominant subsidence occurs in mining panel 2553N and the area between panel 2553N and fault F0, and has subsided by up to 57 cm. Overall, the ground movement patterns and magnitudes obtained by two different methods have a relatively good consistency, which attests the efficacy of the FDM numerical model in simulating the impact of the mining activity. The ground movement pattern in the Fangezhuang coal mine is spatially controlled by the geological fault to some degree, causing differential subsidence that could affect infrastructures. The method proposed in this paper can help to improve the understanding of subsidence control, develop preventive measures in Fangezhuang coalfield that consider fault reactivation, and forecast the impact of future underground mining activities in Fangezhuang coal mine. Further numerical analyses are required at a more realistic mine scale to study the ground movement trends in more detail.

DATA AVAILABILITY STATEMENT

The original contributions presented in the study are included in the article/Supplementary Materials, further inquiries can be directed to the corresponding authors.

AUTHOR CONTRIBUTIONS

All authors listed have made a substantial, direct, and intellectual contribution to the work and approved it for publication.

FUNDING

The project was supported by the University of Nottingham Faculty of Engineering Research Excellence PhD scholarship. The work was supported financially by the Fundamental Research Funds for the Central Universities (2019XKQYMS63).

ACKNOWLEDGMENTS

The authors would like to thank the European Space Agency (ESA) for providing Sentinel-1 data for the analysis. The authors would also like to thank Fangezhuang coal mine for providing the geological report with levelling data and strata parameters.

REFERENCES

Abbasi, B., Russell, D., and Taghavi, R. (2013). "FLAC3D Mesh and Zone Quality," in *FLAC/DEM Symposium* (China: Itasca Consulting Group).

Agarwal, V., Kumar, A., L. Gomes, R., and Marsh, S. (2020). Monitoring of Ground Movement and Groundwater Changes in London Using InSAR and GRACE. *Appl. Sci.* 10, 8599. doi:10.3390/app10238599

Albino, F., J Biggs, C. Y., and Li, Z. (2020). 'Automated Methods for Detecting Volcanic Deformation Using Sentinel-1 InSAR Time Series Illustrated by the 2017–2018 Unrest at Agung, Indonesia. *J. Geophys. Res. Solid Earth* 125, e2019JB017908. doi:10.1029/2019jb017908

Bell, F. G., Donnelly, L. J., Genske, D. D., and Ojeda, J. (2005). Unusual Cases of Mining Subsidence from Great Britain, Germany and Colombia. *Environ. Geol.* 47, 620–631. doi:10.1007/s00254-004-1187-9

Bell, J. W., Falk, A., Ferretti, A., Bianchi, M., and Novali, F. (2008). *Permanent Scatterer InSAR Reveals Seasonal and Long-term Aquifer-system Response to Groundwater Pumping and Artificial Recharge*, 44. Water Resources Research. doi:10.1029/2007wr006152

Berardino, P., Fornaro, G., Lanari, R., and Sansosti, E. (2002). A New Algorithm for Surface Deformation Monitoring Based on Small Baseline Differential SAR Interferograms. *IEEE Trans. Geosci. Remote Sensing* 40, 2375–2383. doi:10.1109/tgrs.2002.803792

Burbey, T. (2002). The Influence of Faults in basin-fill Deposits on Land Subsidence, Las Vegas Valley, Nevada, USA. *Hydrogeology J.* 10, 525–538. doi:10.1007/s10040-002-0215-7

Cai, W., Dou, L., Si, G., and Hu, Y. (2021). 'Fault-induced Coal Burst Mechanism under Mining-Induced Static and Dynamic Stresses. *Engineering* 7, 687–700.

Castellazzi, P., Longuevergne, L., Martel, R., Rivera, A., Brouard, C., and Chaussard, E. (2018). Quantitative Mapping of Groundwater Depletion at the Water Management Scale Using a Combined GRACE/InSAR Approach. *Remote Sensing Environ.* 205, 408–418. doi:10.1016/j.rse.2017.11.025

Chen, C. W., and Zebker, H. A. (2001). Two-dimensional Phase Unwrapping with Use of Statistical Models for Cost Functions in Nonlinear Optimization. *J. Opt. Soc. Am. A.* 18, 338–351. doi:10.1364/josaa.18.000338

Cheng, Q., Shi, Y., and Zuo, L. (2019). Numerical Simulation and Analysis of Surface and Surrounding Rock Failure in Deep High-Dip Coal Seam Mining. *Geotech Geol. Eng.* 37, 4285–4299. doi:10.1007/s10706-019-00907-z

Deck, O., and Anirudh, H. (2010). Numerical Study of the Soil-Structure Interaction within Mining Subsidence Areas. *Comput. Geotechnics* 37, 802–816. doi:10.1016/j.compgeo.2010.07.001

Diao, X., Bai, Z., Wu, K., Zhou, D., and Li, Z. (2018). Assessment of Mining-Induced Damage to Structures Using InSAR Time Series Analysis: a Case Study of Jiulong Mine, China. *Environ. Earth Sci.* 77, 1–14. doi:10.1007/s12665-018-7353-2

Diao, X., Wu, K., Chen, R., and Yang, J. (2019). Identifying the Cause of Abnormal Building Damage in Mining Subsidence Areas Using InSAR Technology. *IEEE Access* 7, 172296–172304. doi:10.1109/access.2019.2956094

Dong, L., Wang, C., Tang, Y., Tang, F., Zhang, H., Wang, J., et al. (2021). Time Series InSAR Three-Dimensional Displacement Inversion Model of Coal Mining Areas Based on Symmetrical Features of Mining Subsidence. *Remote Sensing* 13, 2143. doi:10.3390/rs13112143

Du, S., Wang, Y., Zheng, M., Zhou, D., and Xia, Y. (2019). Goaf Locating Based on InSAR and Probability Integration Method. *Remote Sensing* 11, 812. doi:10.3390/rs11070812

Fan, H., Wang, L., Wen, B., and Du, S. (2021). A New Model for Three-Dimensional Deformation Extraction with Single-Track InSAR Based on Mining Subsidence Characteristics. *Int. J. Appl. Earth Observation Geoinformation* 94, 102223. doi:10.1016/j.jag.2020.102223

Fialko, Y., Simons, M., and Agnew, D. (2001). The Complete (3-D) Surface Displacement Field in the Epicentral Area of the 1999MW7.1 Hector Mine Earthquake, California, from Space Geodetic Observations. *Geophys. Res. Lett.* 28, 3063–3066. doi:10.1029/2001gl013174

Fournier, T. J., Pritchard, M. E., and Riddick, S. N. (2010). 'Duration, Magnitude, and Frequency of Subaerial Volcano Deformation Events: New Results from Latin America Using InSAR and a Global Synthesis. *Geochem. Geophys. Geosystems* 11. doi:10.1029/2009gc002558

Francioni, M., Stead, D., Sharma, J., Clague, J. J., and Brideau, M. A. (2021). An Integrated InSAR-Borehole Inclinometer-Numerical Modeling Approach to the Assessment of a Slow-Moving Landslide. *Environ. Eng. Geosci.* 27 (3), 287–305. doi:10.2113/EEG-D-20-00109

Gee, D., Bateson, L., Sowter, A., Grebby, S., Novellino, A., Cigna, F., et al. (2017). Ground Motion in Areas of Abandoned Mining: Application of the Intermittent SBAS (ISBAS) to the Northumberland and Durham Coalfield, UK. *Geosciences* 7, 85. doi:10.3390/geosciences7030085

Ghayournajarkar, N., and Fukushima, Y. (2020). 'Determination of the Dipping Direction of a Blind Reverse Fault from InSAR: Case Study on the 2017 Sefid Sang Earthquake, Northeastern Iran. *Earth, Planets and Space* 72, 1–15. doi:10.1186/s40623-020-01190-6

Grebby, S., Orynbassarova, E., Sowter, A., Gee, D., and Athab, A. (2019). Delineating Ground Deformation over the Tengiz Oil Field, Kazakhstan, Using the Intermittent SBAS (ISBAS) DInSAR Algorithm. *Int. J. Appl. earth observation geoinformation* 81, 37–46. doi:10.1016/j.jag.2019.05.001

Gumilar, I., AbidinAbidin, H. Z., HutasoitHutasoit, L. M., Hakim, D. M., Sidiq, T. P., and Andreas, H. (2015). Land Subsidence in Bandung Basin and its Possible Caused Factors. *Proced. Earth Planet. Sci.* 12, 47–62. doi:10.1016/j.proeps.2015.03.026

Hoek, E., and Brown, E. T. (1997). Practical Estimates of Rock Mass Strength. *Int. J. rock Mech. mining Sci.* 34, 1165–1186. doi:10.1016/s1365-1609(97)80069-x

Jeanne, P., Farr, T. G., Rutqvist, J., and Vasco, D. W. (2019). Role of Agricultural Activity on Land Subsidence in the San Joaquin Valley, California. *J. Hydrol.* 569, 462–469. doi:10.1016/j.jhydrol.2018.11.077

Kang, Y., Zhao, C., Zhang, Q., Lu, Z., and Li, B. (2017). Application of InSAR Techniques to an Analysis of the Guanling Landslide. *Remote Sensing* 9, 1046. doi:10.3390/rs9101046

Kumar, R., Choudhury, D., and Bhargava, K. (2016). Simulation of Rock Subjected to Underground Blast Using FLAC3D. *JGS Spec. Publ.* 2, 508–511. doi:10.3208/jgssp.ind-27

Liao, H., Meyer, F. J., Scheuchl, B., Mouginot, J., Joughin, I., and Rignot, E. (2018). Ionospheric Correction of InSAR Data for Accurate Ice Velocity Measurement at Polar Regions. *Remote Sensing Environ.* 209, 166–180. doi:10.1016/j.rse.2018.02.048

Mohammady, M., Pourghasemi, H. R., and Amiri, M. (2019). 'Land Subsidence Susceptibility Assessment Using Random forest Machine Learning Algorithm. *Environ. Earth Sci.* 78, 1–12. doi:10.1007/s12665-019-8518-3

Motagh, M., Shamshiri, R., Haghshenas HaghighiHaghighi, M., Wetzel, H.-U., Akbari, B., Nahavandchi, H., et al. (2017). Quantifying Groundwater Exploitation Induced Subsidence in the Rafsanjan plain, southeastern Iran, Using InSAR Time-Series and *In Situ* Measurements. *Eng. Geology.* 218, 134–151. doi:10.1016/j.enggeo.2017.01.011

Pacheco-Martínez, J., Hernandez-Marín, M., Burbey, T. J., González-Cervantes, N., Ortíz-LozanoZermeño-De-Leon, J. Á., Zermeño-De-Leon, M. E., et al. (2013). Land Subsidence and Ground Failure Associated to Groundwater Exploitation in the Aguascalientes Valley, México. *Eng. Geology.* 164, 172–186. doi:10.1016/j.enggeo.2013.06.015

Park, I., Choi, J., Jin Lee, M., and Lee, S. (2012). Application of an Adaptive Neuro-Fuzzy Inference System to Ground Subsidence hazard Mapping. *Comput. Geosciences* 48, 228–238. doi:10.1016/j.cageo.2012.01.005

Parmar, H., Bafghi, A. Y., and Najafi, M. (2019). Impact of Ground Surface Subsidence Due to Underground Mining on Surface Infrastructure: the Case of the Anomaly No. 12 Sechahun, Iran. *Environ. Earth Sci.* 78, 1–14. doi:10.1007/s12665-019-8424-8

Perry, A. P., Kalenchuk, K. S., and McKinnon, S. D. (2020). "A Numerical Modeling Investigation of Coupled-Mechanism Subsidence over an Underground Carlin Trend Mine," in 54th US Rock Mechanics/Geomechanics Symposium (OnePetro).

Ren, X. (2017). *'Law of Underground Pressure and Deformation Control in Fangezhaung Mining Panel*. North China University of Science and Technology.

Rizzoli, P., Martone, M., Gonzalez, C., Wecklich, C., Borla Tridon, D., Bräutigam, B., et al. (2017). Generation and Performance Assessment of the Global TanDEM-X Digital Elevation Model. *ISPRS J. Photogrammetry Remote Sensing* 132, 119–139. doi:10.1016/j.isprsjprs.2017.08.008

Shabanimashcool, M., and Li, C. (2012). Numerical Modelling of Longwall Mining and Stability Analysis of the gates in a Coal Mine. *Int. J. rock Mech. mining Sci.* 51, 24–34. doi:10.1016/j.ijrmms.2012.02.002

Shi, M., Yang, H., Wang, B., Peng, J., Gao, Z., and Zhang, B. (2021). Improving Boundary Constraint of Probability Integral Method in SBAS-InSAR for Deformation Monitoring in Mining Areas. *Remote Sensing* 13, 1497. doi:10.3390/rs13081497

Shi, Y., Zhao, Minmin., and Jian, Hao. (2021). Study on Numerical Models in Predicting Surface Deformation Caused by Underground Coal Mining. *Geotechnical Geol. Eng.* 39 (6), 1–17.

Sikora, P., and Wesołowski, M. (2021). Numerical Assessment of the Influence of Former Mining Activities and Plasticity of Rock Mass on Deformations of Terrain Surface. *Int. J. Mining Sci. Tech.* 31, 209–214. doi:10.1016/j.ijmst.2020.11.001

Sowter, A., Bin Che Amat, M., Cigna, F., Marsh, S., Athab, A., and Alshammari, L. (2016). Mexico City Land Subsidence in 2014-2015 with Sentinel-1 IW TOPS: Results Using the Intermittent SBAS (ISBAS) Technique. *Int. J. Appl. earth observation geoinformation* 52, 230–242. doi:10.1016/j.jag.2016.06.015

Sun, Q., Zhang, L., Ding, X. L., Hu, J., Li, Z. W., and Zhu, J. J. (2015). Slope Deformation Prior to Zhouqu, China Landslide from InSAR Time Series Analysis. *Remote Sensing Environ.* 156, 45–57. doi:10.1016/j.rse.2014.09.029

Torres, R., Snoeij, P., Geudtner, D., Bibby, D., Davidson, M., Attema, E., et al. (2012). GMES Sentinel-1 mission. *Remote Sensing Environ.* 120, 9–24. doi:10.1016/j.rse.2011.05.028

Wang, L., Deng, K., and Zheng, M. (2020). Research on Ground Deformation Monitoring Method in Mining Areas Using the Probability Integral Model Fusion D-InSAR, Sub-band InSAR and Offset-Tracking. *Int. J. Appl. Earth Observation Geoinformation* 85, 101981. doi:10.1016/j.jag.2019.101981

Wang, Y., Wang, L., Zhang, Y., and Yang, T. (2015). "Investigation of Snow Cover Change Using Multi-Temporal PALSAR InSAR Data at Dagu Glacier, China," in 2015 IEEE International Geoscience and Remote Sensing Symposium (IGARSS) (IEEE), 747–750. doi:10.1109/igarss.2015.7325872

Xu, N., Kulatilake, P. H. S. W., Tian, H., Wu, X., Nan, Y., and Wei, T. (2013). Surface Subsidence Prediction for the WUTONG Mine Using a 3-D Finite Difference Method. *Comput. Geotechnics* 48, 134–145. doi:10.1016/j.compgeo.2012.09.014

Yan, Y., Yan, W., Liu, J., and Guo, J. (20212021). *The Prediction Model of Super Large Subsidence in High Water Table Coal Mining Areas Covered with Thick Unconsolidated Layer*. Geofluids.

Yang, X., Wen, G., Dai, L., Sun, H., and Li, X. (2019). Ground Subsidence and Surface Cracks Evolution from Shallow-Buried Close-Distance Multi-Seam

Mining: a Case Study in Bulianta Coal Mine. *Rock Mech. Rock Eng.* 52, 2835–2852. doi:10.1007/s00603-018-1726-4

Yang, Z., Li, Z., Zhu, J., Yi, H., Hu, J., and Feng, G. (2017). Deriving Dynamic Subsidence of Coal Mining Areas Using InSAR and Logistic Model. *Remote Sensing* 9, 125. doi:10.3390/rs9020125

Yu, Q. (2020). *'Study on Mechanism of Mininig Subsidence Affected by Fault'*. China Coal Research Institute.

Yunjun, Z., Fattahi, H., and Amelung, F. (2019). Small Baseline InSAR Time Series Analysis: Unwrapping Error Correction and Noise Reduction. *Comput. Geosciences* 133, 104331. doi:10.1016/j.cageo.2019.104331

Zhang, Y., Meng, X. M., Dijkstra, T. A., Jordan, C. J., Chen, G., Zeng, R. Q., et al. (2020). Forecasting the Magnitude of Potential Landslides Based on InSAR Techniques. *Remote Sensing Environ.* 241, 111738. doi:10.1016/j.rse.2020.111738

Zhang, Z., Wang, C., Tang, Y., Zhang, H., and Fu, Q. (2015). Analysis of Ground Subsidence at a Coal-Mining Area in Huainan Using Time-Series InSAR. *Int. J. Remote Sensing* 36, 5790–5810. doi:10.1080/01431161.2015.1109725

Zheng, M., Deng, K., Fan, H., and Du, S. (2018). Monitoring and Analysis of Surface Deformation in Mining Area Based on InSAR and GRACE. *Remote Sensing* 10, 1392. doi:10.3390/rs10091392

Conflict of Interest: Author DG was employed by the company Terra Motion Limited

The remaining authors declare that the research was conducted in the absence of any commercial or financial relationships that could be construed as a potential conflict of interest.

frontiers in Environmental Science

ORIGINAL RESEARCH
published: 21 January 2022
doi: 10.3389/fenvs.2021.808802

Assessment of Aeolian Activity in the Bodélé Depression, Chad: A Dense Spatiotemporal Time Series From Landsat-8 and Sentinel-2 Data

Eslam Ali[1], *Wenbin Xu*[2]*, *Lei Xie*[1] *and Xiaoli Ding*[1]

[1]Department of Land Surveying and Geo-Informatics, The Hong Kong Polytechnic University, Hong Kong, China, [2]School of Geosciences and Info-Physics, Central South University, Changsha, China

There are several hotspots of dust production in the central Sahara, the Bodélé Depression (BD) in northern Chad is considered the largest source of aerosol dust worldwide, with the fastest Barchan dunes that migrate southwesterly. Less is known about the complex patterns of dune movement in the BD, especially on a short time scale. Time-series inversion of optical image cross-correlation (TSI-OICC) proved to be a valuable method for monitoring historical movements with low uncertainties, high spatial coverage, and dense temporal coverage. We leveraged ~8 years of Landsat-8 and ~6 years of Sentinel-2 data to capture the dune migration patterns at BD. We used TSI-OICC, creating four independent networks of offset maps from Landsat-8 and Sentinel-2 images, and forming three networks by fusing data from the two sensors. We depended on the multi spatial coherence estimated from Sentinel-1 interferograms to automatically discriminate between the active and stagnant regions, which is important for the postprocessing steps. We combined the data from the two sensors in areas of overlap to assess the performance of the fusion between two sensors in increasing the temporal scale of the observations. Our results suggest that dune migration at BD is subject to seasonal and multiyear variations that differed spatially across the dune field. Seasonal variations were observed with migration slowing during the summer months. We estimated the median for velocities belonging to the same season and calculated the seasonal sliding coefficient (SSC) representing the ratio between seasonal velocities. The median SSC reached a maximum value of ~2 for winter/summer, while the ratios were ~1.10 and ~1.35 for winter/spring and winter/autumn, respectively. The seasonal variability of the temporal patterns was strongly supported by the wind observations. Between (1984–1998 and 1998–2007) and (1998–2007 and 2013–2021), decelerations in dune velocities were observed with percentages of ~4 and ~28%, respectively, and these decelerations were supported by a deceleration in wind velocities. Inversion of time series provides dense spatiotemporal monitoring of the dune activity. The fusion between two sensors allows condensing the temporal sampling up to a weekly scale especially for locations exposed to contamination of high cloud cover or dust.

Keywords: Bodélé depression, dune migration, COSI-Corr, image matching, time series inversion

OPEN ACCESS

Edited by:
Yu Chen,
China University of Mining and Technology, China

Reviewed by:
Qunming Wang,
Tongji University, China
Ming Hao,
China University of Mining and Technology, China

***Correspondence:**
Wenbin Xu
wenbin.xu@csu.edu.cn

Specialty section:
This article was submitted to Environmental Informatics and Remote Sensing, a section of the journal Frontiers in Environmental Science

Received: *04 November 2021*
Accepted: *13 December 2021*
Published: *21 January 2022*

Citation:
Ali E, Xu W, Xie L and Ding X (2022) Assessment of Aeolian Activity in the Bodélé Depression, Chad: A Dense Spatiotemporal Time Series From Landsat-8 and Sentinel-2 Data. Front. Environ. Sci. 9:808802. doi: 10.3389/fenvs.2021.808802

1 INTRODUCTION

In areas that lack vegetation cover and water resources and exhibit low soil fertility, low rainfall, high temperatures, high evaporation levels, and high sand availability, effective wind plays a crucial role in aeolian processes. In several desert areas, the instability of dunes and sand sheets poses an important threat to transportation networks, water supply routes, urban areas, cultural sites, and human activities (Middleton and Sternberg, 2013; Ahmady-Birgani et al., 2017; Ding et al., 2020a). Monitoring dune migrations in spatiotemporal domains contributes to a deeper understanding of the aeolian process and its relationship with environmental changes (Hugenholtz et al., 2012). Moreover, information on dune migration can be used as an indicator of the presence or absence of large-scale trends in windiness over major deserts (e.g., the Sahara Desert), and these wind trends may influence the global dust budget (Vermeesch and Leprince, 2012).

Observations with high spatiotemporal resolution are required to decipher the complex patterns of dune migration (Hugenholtz et al., 2012). Ground-based measurements offer higher accuracy but provide sparse coverage in spatiotemporal domains. The development of remote sensing techniques, including optical and radar imagery and digital elevation models (DEMs), allows the investigation of geomorphological changes with dense spatiotemporal measurements. The majority of studies addressing the evolution of dune dynamics have been conducted using optical imagery (Manzoni et al., 2021). Compared to the optical imageries, the dependency on synthetic-aperture radar (SAR) imagery to monitor dune migration is not extensive. Previous studies that employed SAR imagery (e.g., Rozenstein et al., 2016; Gaber et al., 2018; Ullmann et al., 2019; Manzoni et al., 2021) mainly depended on interferometric coherence as an indicator of dune and sand sheet instability. Notably, these coherence-based techniques do not provide any quantitative representation of dune dynamics, however, can be used as a proxy for the fine movements of dunes and sand sheets. Several approaches to optical imagery have been used to capture information about dune dynamics at various resolutions, including classical methods and visual interpretation (e.g., Hereher, 2010; Hamdan et al., 2016), GIS strategies (e.g., Ghadiry et al., 2012; El-magd et al., 2013), and optical image cross-correlation (OICC) (e.g., Vermeesch and Drake, 2008; Hermas et al., 2012; Scheidt and Lancaster, 2013; Sam et al., 2015; Ali et al., 2021).

With the rapid development of OICC, mapping the surface displacement of large areas at very high spatiotemporal resolution is now feasible and reliable (Stumpf et al., 2016). Various types of data were used to perform such correlations, including optical and SAR images and DEMs. Optical images were the most commonly used due to the availability of free archives (Dille et al., 2021). Co-registration of optical image matching and correlation (COSI-Corr) (Leprince et al., 2007) is considered the most widely used method for retrieving surface deformations due to its excellent performance in terms of processing time, output variables, and provision of multiple pre- and post-processing modules (Jawak et al., 2018). COSI-Corr has been used to monitor various targets, including earthquakes (e.g., Ayoub et al., 2009; Avouac et al., 2014; Chen et al., 2020), landslides (e.g., Stumpf et al., 2014; Lacroix et al., 2019; Yang et al., 2021), glaciers (e.g., Scherler et al., 2008; Shukla and Garg, 2020; Das and Sharma, 2021), and dunes (e.g., Necsoiu et al., 2009; Vermeesch and Leprince, 2012; Hermas et al., 2019). OICC provides subpixel measurements of surface deformations with an accuracy of up to a tenth of the ground resolution (Leprince et al., 2007).

TSI-OICC measurements has recently been used to monitor the temporal evolution of various targets, including landslides (e.g., Bontemps et al., 2018; Lacroix et al., 2019; Dille et al., 2021; Ding et al., 2021), glaciers (Altena et al., 2019), and dunes (e.g., Ali et al., 2020; Ding et al., 2020a; Ding et al., 2020b). Bontemps et al. (2018) were the first to construct a complete network of matching pairs from 16 SPOT–5 images covering 35 years and inverted it to monitor landslide deformations. Large differences in solar angles affected the matching results, leading to seasonal signals, while large temporal separation affected the temporal decorrelation (Bontemps et al., 2018; Lacroix et al., 2019). The inversion of the full network is promising for controlling uncertainties and improving spatial coverage; however, generating full networks from the available free archives [i.e., Landsat-8 (L-8) and Sentinel-2 (S-2)] would increase the computational cost and data burden. Recently, some studies (e.g., Ali et al., 2020; Ding et al., 2020b; Ding et al., 2021) have simulated small baseline subset (SBAS) approaches used in InSAR for application in the optical image matching domain, selecting only pairs with certain baseline thresholds. SBAS-based optical image matching mainly aims to reduce computation times and data burdens (Bui et al., 2020) and improve the quality of pairs by limiting probable cast shadows, while achieving higher spatial coverage with lower uncertainty. The presented SBAS-based optical image matching approach has shown potential for capturing the temporal patterns of various targets, including dunes (Ding et al., 2020a; Ali et al., 2020; Ding et al., 2020b) and landslides (Ding et al., 2021), with low uncertainty and high spatial coverage.

The Bodélé depression (BD) in Chad is a 133,532 km^2 elongated paleolake that is gaining importance as a global source of mineral dust and a natural aeolian laboratory because it is considered the dustiest place on the Earth (Bristow et al., 2009). Barchan dunes are the predominant dune morphology in the BD, but their geochemical formation differs between the center and the margins of the BD (Hudson-Edwards et al., 2014). The crust of the Barchan dunes inside the depression is composed of diatomite with a lower density than quartz, which is the major dune constituent along the margins of the depression. Accordingly, dune migration is faster in the center of the BD than elsewhere, and these Barchan dunes are considered the fastest worldwide (Bristow et al., 2009). The geomorphological formation of the dunes detected by the two L-8 frames varied between the two formations (see **Figure 1B**). The Barchan dunes in the BD, have been studied using OICC three times in the existing literature. Vermeesch and Drake (2008) first used COSI-Corr, along with ASTER images, to test the performance of the correlation as the temporal separation was adjusted. They reported the effect of temporal decorrelation in reducing the signal-to-noise ratio of the results. Vermeesch and

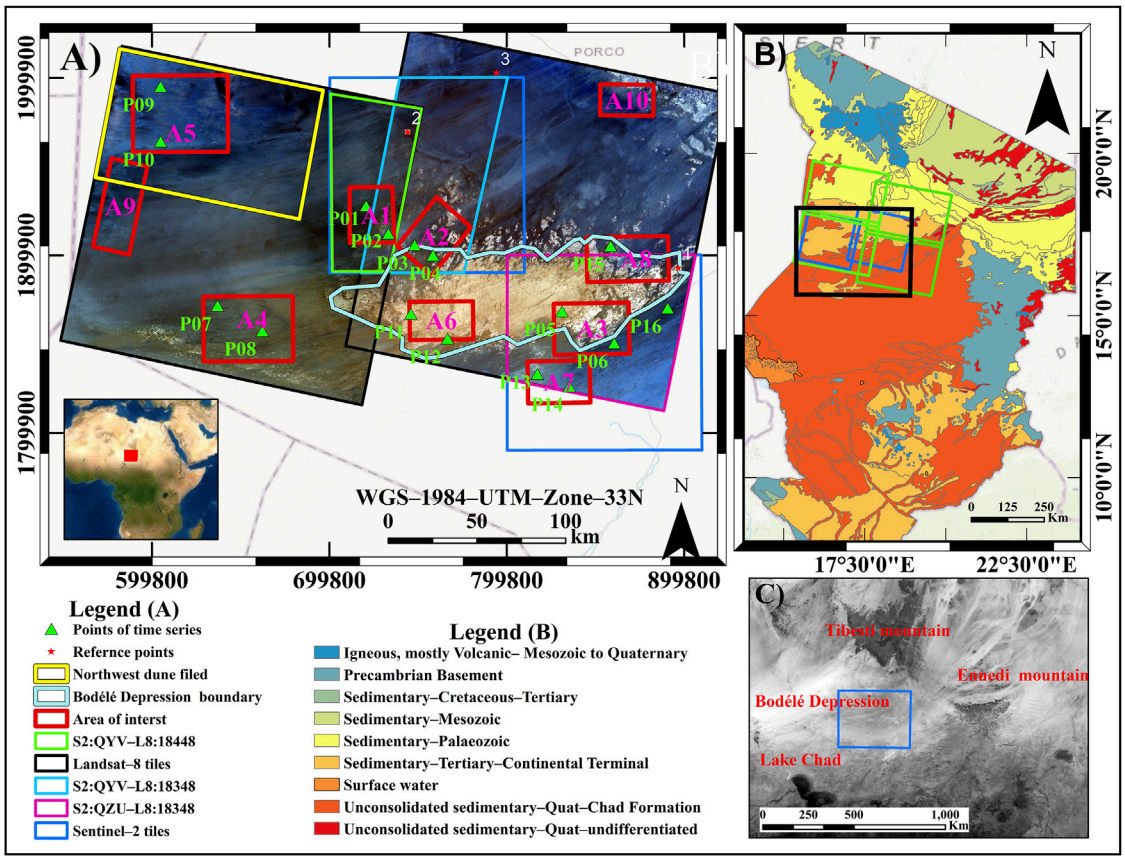

FIGURE 1 | Geographical position and geological formation of the study area. Panel **(A)** indicates the location of the Bodélé Depression. The inset shows the location of the BD in Africa. The background in panel **(A)** is a mosaic of Landsat-8 false colors. The black rectangles denote the coverage of Landsat-8 (i.e., P:183/R:48 and P:184/R:48). The blue rectangles denote the coverage of Sentinel-2A/B (i.e., TR33QYV and TR33QZU). The red rectangles represent the dune fields for which we discuss the spatiotemporal variability in **Section 4.6**. The red pentagrams represent the reference points used for absolute calibration, while the green triangles represent the points for which we extracted the temporal evolution of dune migration in **Section 4.5**. The three colored polygons in panel **(A)** represent the overlap areas between Landsat-8 and Sentinel-2, where we performed the inversion of the fused offset maps. Panel **(B)** shows the geological and geomorphological formations of Chad. The black rectangle represents the area shown in panel **(A)**. The green rectangles denote the Sentinel-1A coverage (i.e., descending tracks 07 and 80). Panel **(C)** shows the location of the BD in the gap between the Tibesti and Ennedi mountains, and the current coverage of Lake Chad to the southwest. The background is the MODIS surface reflectance.

Leprince (2012) matched seven adjacent optical images from different sensors to track dune migration over 26 years. They reported that variations in migration rates were up to 10%, equivalent to a 0.2% variation in wind speed per year, indicating stability in wind conditions. Recently, Baird et al. (2019) proposed a workflow to extract representative dune migration rates by feeding Landsat-5 data into the correlation engine.

From the existing literature, previous studies at BD have not provided a complete picture of the behavior of dune migration on short time scales (i.e., monthly, or weekly). Only the study by Vermeesch and Leprince (2012) produced long time series of matching measurements, using seven images covering the period from 1984–2010. The time-series presented did not provide information on the behavior of dune migration and associated wind patterns on a short time scale due to the sparse temporal samplings. Furthermore, the adjacent paring criterion of matching images to produce time series fails to provide high spatial coverage and low uncertainties. Moreover, monitoring the fast-moving targets requires matching images with short time separation, however, these short time spans would be affected by a large fraction of geolocation errors (Fahnestock et al., 2016). To best monitor the temporal evolution of dune migration with dense spatial and temporal coverage and low uncertainties, the application of optical image matching selection and inversion algorithm is feasible in monitoring the temporal evolution. The inversion algorithm first selects the appropriate images by constraining the cloud coverage. However, the number of available scenes (i.e., cloud-free) is primarily limited by cloud cover, especially during the rainy seasons prevalent in tropical regions, resulting in a reduction in temporal sampling. Therefore, the fusion of two or more sensors is considered feasible in providing a dense temporal sampling, to reveal the complex deformation patterns up to a weekly time scale. The main objectives of the study can be summarized as follows: 1) to broadly apply the time series selection algorithm from optical images and inversion to monitor the status of dune activity of the Bodélé Depression dunes with dense time series in the last decade (2013–2021), 2) to test the feasibility of merging the matching

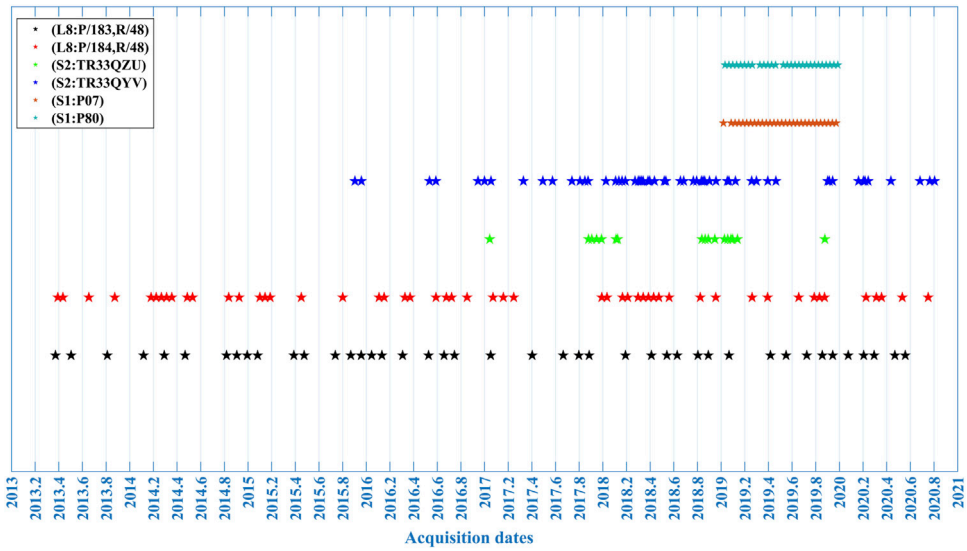

FIGURE 2 | Temporal distribution of data used in the study. Landsat-8 frames (P:183/R:48) and (P:183/R:48) (43 and 52 scenes, respectively), Sentinel-2 tiles (TR33QYV and TR33QZU) (56 and 17 scenes, respectively), and Sentinel–1 descending orbits (07 and 80) (30 and 29 scenes, respectively). The cloud cover threshold for Sentinel-2 tile TR33QZU was set to 20% due to the cloud and dust. Detailed acquisition information is listed in **Supplementary Tables S1–S5**.

measurements from two sensors in condensing the time series and increasing the redundancy level, and 3) to study the spatiotemporal variability of dune migration in both seasonal and decadal changes. The rest of this study is organized as follows: the description of the geographical and geomorphological location and the data used are discussed in **Section 2**. Secondly, the methodology and rationale employed in this study are outlined in **Section 3**. Thirdly, the results and discussion of the temporal evolution of the Bodélé depression dunes are discussed in **Section 4**. After that, reflection on previous studies and the merit of the optical mage matching selection and inversion algorithm are investigated. At the end, the concluded remarks are summarized in **Section 5**.

2 STUDY AREA AND DATASETS

2.1 Geological and Environmental Settings of the Bodélé Depression

There are several localized "hotspots" of dust production in the central Sahara, the most important being the BD in northern Chad (Goudie and Middleton, 2001; Chappell and Bristow, 2005). Historically, the BD hosted Lake Mega-Chad, which has now completely disappeared, exposing the lake sediments to deflation (Bristow et al., 2009). The BD is considered the largest source of aerosol dust worldwide; it is a 24,000 km^2 area that delivers about 6.5 million tons of Fe and 0.12 million tons of P to the Atlantic Ocean and Amazon Basin annually (Bristow et al., 2009). This can be explained by the following two factors: 1) A strong surface wind, known as the Bodélé low-level jet (LLJ), is directed at the BD (Washington et al., 2006). The location of the depression on the downwind side of the gap between the Tibesti and Ennedi Mountains on the border with Libya (**Figure 1C**) increases the leverage and activity of the northeast trade winds in the depression. 2) As a sub-basin of the Mega-Chad paleolake, the BD is a large source of erodible sediments, including lacustrine diatomaceous Earth (Washington et al., 2006; Warren et al., 2007). In addition, the area is a sparsely vegetated, hyper-arid region that provides extreme erodibility (Koren et al., 2006). The sediments produce white crusts of diatomaceous Earth that are easily mined and transported by the wind, forming some of the largest and fastest-moving Barchan dunes worldwide (**Figure 1**). There are two types of dunes in the area; the dunes at the edges of the depression are composed mainly of quartz, while those in the center contain diatomaceous Earth pellets. It is noteworthy that the central dunes have higher dune velocities than the marginal dunes because of their low density (Warren et al., 2007).

2.2 Datasets

2.2.1 Optical Images

We used satellite imagery from the free archives of L-8 and S-2 to feed into the COSI-Corr correlation engine to capture quantitative measurement of the dune migration up to 1/10 of pixel size (Leprince et al., 2007). The two sensors have similar characteristics in terms of their spectral properties and spatial and temporal resolutions (Roy et al., 2014; Kääb et al., 2016). We selected images with low cloud cover (less than 1%), and we have checked visually the images to avoid the selection of images contaminated by haze or dust, yielding a total of 168 images: 95 images obtained from two L-8 frames and 73 images from two S-2 tiles (**Figure 1A**). The temporal coverage of the L-8 and S-2 images is summarized in **Figure 2**, while **Supplementary Tables S1–S4** provide an inventory of the metadata of the images. Both products are orthoimages with atmospheric correction of the reflectance values and geometric correction based on a refined geometric model. The processing chains of the L-8 products and S-2 data are

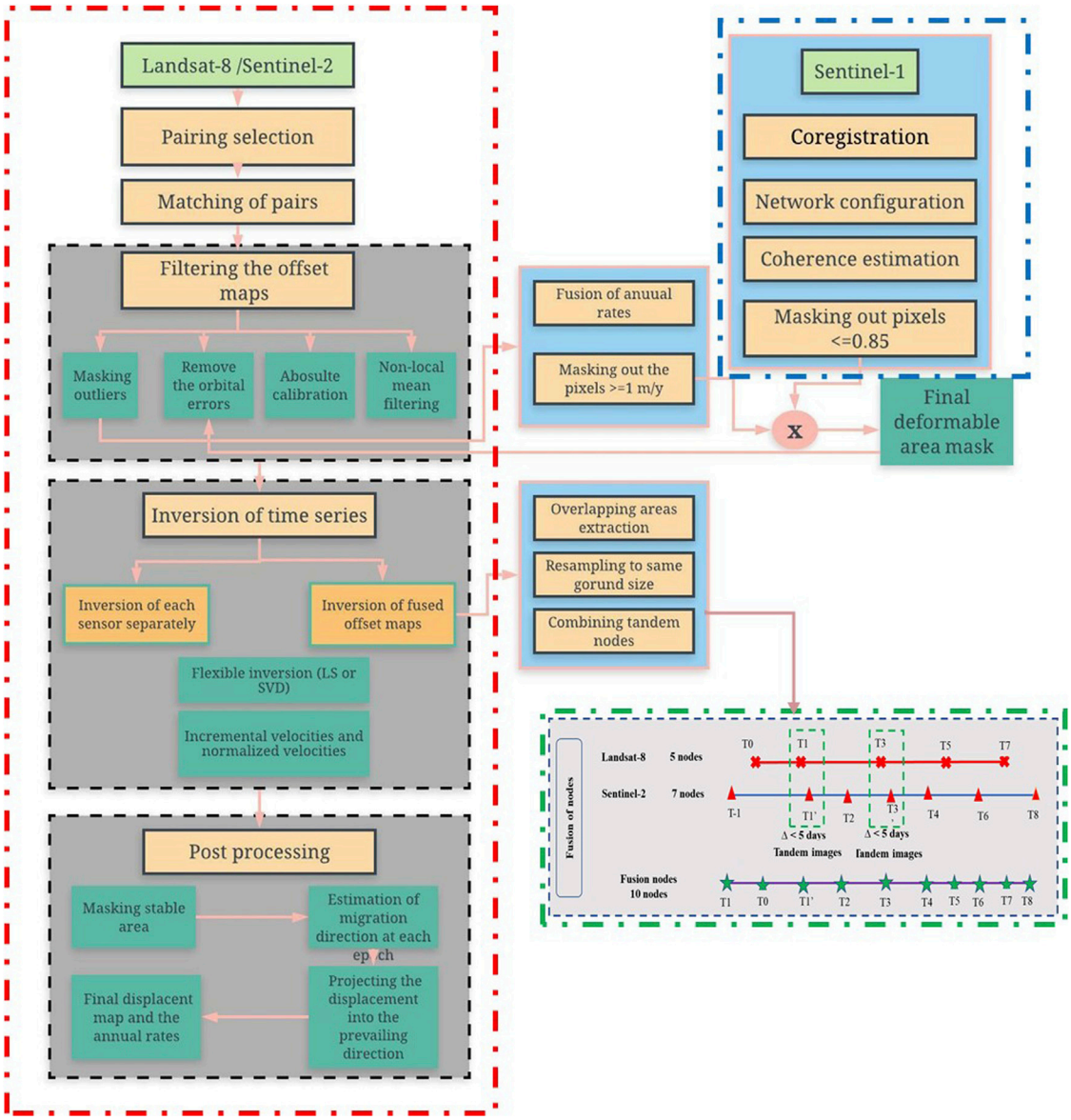

FIGURE 3 | Flowchart of the processing chain. The steps outlined by the blue dashed rectangle represent the processing steps to estimate the multitemporal spatial coherence. The steps outlined by the red dashed rectangle denote the optical image matching selection and inversion algorithm. The green dashed rectangle denotes the concept of combining tandem images when merging data from the two sensors.

considered identical in terms of the radiometric and geometric corrections, orthorectification, and resampling to a map grid (Roy et al., 2014; Kääb et al., 2016). We used the panchromatic (band 8) and NIR infrared band (8a) of S-2 to feed the correlation engine, according to the recommendations of Ali et al. (2020).

2.2.2 SAR Images

Radar imagery was used to determine the mobility of the sand dunes. In the dune environment, the phase from interferometric synthetic-aperture radar (InSAR) may not be suitable for tracking the rapid movement of sand dunes directly (i.e., 50 m/y). Alternatively, we used the metric of coherence, which represents the degree of similarity between repeat-pass observations, to map the stability of sand dunes (Wegmüeller et al., 2000; Ullmann et al., 2019). To provide an extensive spatial coverage and a stable revisit time (i.e., 12 days), we used two descending paths (**Figure 1B**) of Sentinel-1B data in 2019. Details of the images used for interferogram generation are presented in (**Figure 2**; **Supplementary Table S5**).

2.2.3 ECMWF/ERA Interim Metrological Data

We acquired the average monthly U and V wind components for each year from 2013 to 2021, measured in m/s with a resolution of 0.1 × 0.1 °, from the European Centre for Medium-Range Weather Forecasts (ECMWF) (Dee et al., 2011). The U and V components

represent the eastward and northward components of the wind, respectively, at a height of 10 m above the surface of the Earth. The two components were combined to estimate the wind speed and direction. The average monthly wind speed and direction values for a selected region inside the BD for each year are displayed in **Supplementary Figure S1**. Also, we acquired the wind records for selected years (**Supplementary Figure S1**) from 1984 to 2007 to validate the comparison of dune velocities between the different decades in **Section 4.5.4**.

3 METHODS

Figure 3 shows a flowchart outlining the main methodology and the structure of this article, including the following four main parts. In part 1, we used the Sentinel-1 imagery to delineate the stagnant regions by estimating the mean spatial coherence map (MSC) (see **Section 3.1**). We generated a network of interferograms from two descending tiles covering the study area during (Jan/2019-Dec/2019) and stacked the coherence maps to estimate the MSC to help define the stagnant regions. In Part 2, we applied optical image matching selection and the inversion algorithm to create a time series of dune movement from 2013–2021. The inversion algorithm involved several steps: Generation of a network of offset maps from the selected images, feature tracking of the selected pairs in the COSI-Corr environment, application of refinement steps to control the aberrant measurements, before the inversion of the time series we introduced the fusion between the offset maps of the two sensors, and post-processing of the inverted results. The fusion between time series was introduced to address the feasibility of the fusion in condensing the temporal coverage of time series especially when images are contaminated by large cloud cover. In part 3, we investigated the spatiotemporal variability of dune velocities in seasonal and decadal scales. In part 4, we compared the time series results from the inversion of each sensor individually and to the inversion of the fused time series. Additionally, we evaluated the performance of the inversion algorithm in controlling the uncertainties, whereas we compared the uncertainties of the individual offset maps before and after the inversion.

3.1 Multitemporal Spatial Coherence From SAR Images

Interferogram generation was performed by the InSAR Scientific Computing Environment (Agram et al., 2016). For each orbital path, we first generated a co-registered stack using geometrical co-registration and the enhanced spectral diversity method (Fattahi et al., 2017). We then removed the contribution of topography using the 1-arc Shuttle Radar Topography Mission DEM (Farr et al., 2007). We formed a network configuration that connected each image with two subsequent acquisitions. We did not filter the wrapped interferograms further to avoid potential contamination of the signal. The resultant interferograms were multi-looked using a 5 × 20 azimuth and range directions. From the resultant interferograms, we estimated the complex coherence, which represents the correlation between two SAR acquisitions (Touzi et al., 1999), as follows:

$$\gamma = \frac{\left|\sum_{k=1}^{N} f_k g_k^{\star}\right|}{\sqrt{\sum_{K=1}^{N}\left|f_k\right|^2 \sum_{K=1}^{N}\left|g_k\right|^2}} \quad (1)$$

where f_k and g_k are the complex values from the primary and secondary SAR images surrounding the given pixel with window size N, and $f_k g_k^{\star}$ is the complex conjugate operation for each interferogram. Using the coherence map stacks, the mean value of the spatial coherence γ_{MSC} was estimated to delineate the spatial coherence in the study area, as follows:

$$\gamma_{MSC}(i) = \frac{1}{2N-3}\sum_{n=1}^{2N-3}\left|\gamma_n(i)\right| \quad (2)$$

where i is the target pixel, N is the total number of acquisitions, and $\gamma_n(i)$ is the coherence of the interferogram.

We used multitemporal spatial coherence (MSC) as a proxy for stagnant areas delineation, similar to the method used by Manzoni et al. (2021). The spatial distribution of the MSC is displayed in **Supplementary Figure S2**. The threshold used to define the stagnant areas in that study was set by trial and error, whereas we iteratively tested several threshold values from 0.70 to 0.90. The optimum threshold was selected to achieve the best match with the average annual magnitudes (AAMs) extracted from the inversion of one rate solution. AAMs were determined after removing outliers representing the linear velocity of the dunes. AAMs below 0.5 m/y were assumed to be stagnant. The threshold MSC used to define stagnant areas was set iteratively to best match the lower values of the AMMs. Practically, we set the threshold of the MSC to 0.85 to define the stagnant areas. The spatial distribution of the active and stagnant areas is displayed in **Supplementary Figure S3**.

3.2 Optical Image Matching Selection and Inversion

3.2.1 Image Selection and Network Establishment

For the selected images $(N+1)$, a number of pairs can be generated that is between $N \le M \le \frac{N(N+1)}{2}$ (Berardino et al., 2002). In previous studies (Ali et al., 2020; Ding et al., 2020b), the baselines of the matching process (i.e., radiometric, temporal, and spatial baselines) were defined and weighted according to their effect on the measurement uncertainties as follows: Sun elevation difference, Sun angle difference, temporal baseline, and spatial baseline. We estimated the baselines for all possible pairing combinations and then set the thresholds to limit the choices. The thresholds were determined iteratively by considering their prior weights and preserving the network configuration (i.e., the connectivity of the established networks) (Reinisch et al., 2017). Increasing the maximum temporal baseline allows more pairs to be selected; however, it is recommended to limit the maximum temporal baseline to reduce surface changes and temporal decorrelations. We set the maximum temporal baseline to 6.5 and 3.5 years for L-8 and S-2, respectively, considering the nature of migration in the study area, and the selected window size. No limits were set for the shortest temporal baseline to promote good network connectivity. Short temporal separation values preserve surface changes and are necessary for

monitoring fast targets; however, they are prone to large geolocation error effects (Fahnestock et al., 2016). Thus, we assigned a weighting criterion for the deformation maps based on their temporal separation (**Section 3.2.5**). After several trials, baseline thresholds were determined for both the L-8 and S-2 networks (**Supplementary Table S6**). Details of the baselines of all pairs are listed in **Supplementary Tables S7–S13**.

3.2.2 Optical Images-based Feature Tracking

The selected pairs were matched in the frequency domain of the correlation engine (COSI-Corr) (Leprince et al., 2007). Such correlations are generally performed in two steps: 1) a coarse estimation is provided using large sliding windows, and 2) subpixel accuracy is provided using smaller windows (Beaud et al., 2021). Three parameters were determined: the step size, which determines the spatial resolution of the displacement maps, and the initial and final window sizes. The optimal window size was selected after testing several window sizes and comparing the results in terms of the uncertainty of the stable targets. The parameters used to complete the matching process for L-8 and S-2 are summarized in **Supplementary Table S6**. These parameters were prepared in text files and fed into the batch processor of the correlation engine to decrease human intervention. The ground resolution of the deformation maps was unified as 60 m by setting step sizes of four and six pixels for L-8 and S-2, respectively. Each deformation map yielded displacement in the East–West (EW) and North–South (NS) directions, together with a signal-to-noise-ratio (SNR) map, which is considered a measure of correlation quality (Bontemps et al., 2018; Beaud et al., 2021).

3.2.3 Refinement of the Deformation Fields

Prior to the inversion of the offset maps, several filtering processes were applied to control the uncertainty and help capture real deformations (**Figure 3**): 1) The outliers were discarded. We estimated the yearly migration rates of all the deformation maps and pixels with $SNR \leq 0.90$ and velocities $\geq 250\, m/y$ were discarded from the EW and NS deformation maps. 2) Orbital noise was removed from the deformation fields. The orbital residual usually stems from the orthorectification and co-registration residuals (Ali and Xu, 2019; Ding et al., 2020b). Notably, the removal of such orbital errors generally requires the identification of stable ground. To better identify stable regions, we used a mask based on the MSC and AAMs (**Section 3.1**). After masking the deformable regions, polynomial surfaces were fitted and then removed from the raw deformations. 3) Absolute calibration of the deformation fields was conducted. Co-registration bias is assumed to be a uniform shift in both directions (i.e., EW and NS) over the entire deformation field (Friedl et al., 2021). We extracted a small stable area and estimated the median of the measurements, then corrected the deformation fields by adding or subtracting the determined medians (Friedl et al., 2021). 4) Non-local mean filtering was applied to the COSI-Corr environment to preserve the fine details of the correlation and control additive white noise (Shukla and Garg, 2020). This was achieved using the parameters summarized in **Supplementary Table S6**.

3.2.4 Preparation of the Fusion Between Two Sensors

The following points summarize the preparation of the fused deformation maps before inversion (see the green dashed rectangle in **Figure 3**): 1) The deformation maps of each sensor for the overlapping regions were extracted, resampled to a common geographic grid, and reordered chronologically. 2) The epochs from the two sensors were merged and reordered, and two epochs were considered tandem nodes (Usai, 2003) when the images were separated by less than 5 days. 3) Boundary adjustment was applied to account for variation in the temporal span owing to the merging process (Samsonov et al., 2020). The deformation maps were adjusted by multiplying the deformation values by the ratio between the new and old-time intervals. 4) The deformation maps, with identical start and end dates, were merged using median fusion (Samsonov et al., 2020).

3.2.5 Inversion of Displacement Time Series

We inverted the deformation maps associated with each sensor, and the overlapping zones between the two sensors, separately. We used the parameterization of Berardino et al. (2002) to construct the relationship between the displacement d and the mean velocity between each adjacent epoch v through design matrix B, according to **Eq. 3**. Design matrix B is an $M \times N$ matrix, where each row contains the time increments between the master and slave of the pair (Berardino et al., 2002). The mean velocities between adjacent epochs can be obtained by inverting the matrix ($B^{'}PB$) where P is the weight of each deformation map. We performed the inversion using a pixel-wise strategy with a flexible design matrix B using either least-squares inversion (Usai, 2003), according to **Eq. 4**, or singular value decomposition, according to **Eq. 5** (Berardino et al., 2002), based on the matrix condition (i.e., full rank or rank deficient). We restricted the inversion to pixels for which the stack size exceeded a certain threshold (75%) to strike a balance between ensuring good spatial coverage and reducing the oscillation of the singular value decomposition solution caused by a large number of subsets (Reinisch et al., 2017). We retrieved the pairs by back substitution after the first round of inversion, and then a second round of inversion was executed as per Bontemps et al. (2018). For the fusion between the two sensors, similar inversion procedures were applied. We determined the weight of each map according to the assumption that the error of the velocity reaches $0.1 \times PS$ for a 1-year separation (Mouginot et al., 2017). Consequently, the velocity expression deteriorates, especially for short-time separations TS, according to **Eq. 6** (Mouginot et al., 2017) (see **Supplementary Table S14**). Accordingly, we applied weighting criteria considering the precision of the estimated velocities. The estimated weights assigned for each time interval are listed in **Supplementary Table S14**.

$$\boldsymbol{Bv} = \boldsymbol{d} \tag{3}$$

$$\boldsymbol{v_{LS}} = \left(\boldsymbol{B'PB}\right)^{-1}\boldsymbol{B'Pd} \tag{4}$$

$$\boldsymbol{v_{SVD}} = \boldsymbol{VS^{+}U'B'Pd} \tag{5}$$

$$\boldsymbol{\epsilon} = 0.1 \times \boldsymbol{PS} \times \frac{365.25}{\boldsymbol{TS}} \tag{6}$$

where the U is an orthogonal matrix with dimension $M \times M$, including the eigenvector of matrix $B^{'}PB$; the S^{+} matrix is an

$M \times M$ diagonal matrix including the singular values of σ_i; V is a matrix with the dimensions of N × N including the eigenvectors of $(B^{'}PB)$; ϵ is the velocity error; and PS is the pixel ground resolution. The symbols $'$ and -1 denote the transpose and the inverse of matrix, respectively.

3.3 Post-Processing

We converted the mean velocities between each adjacent epoch obtained by the inversion into cumulative displacement D_m for both EW and NS, according to **Eq. 7**. The values were temporally related to the first scene (**Supplementary Tables S1–S4**) and spatially to the reference points (see **Figure 1**). The AAM and the corresponding prevailing migration direction (PMD) were estimated according to **Eqs 8**, **9**, respectively. After acquiring the displacement, we applied the following refinement steps: 1) Masking pixels comes from the inversion of offset maps belonging to more than two subsets. 2) Masking non-active pixels using the stagnant mask obtained in previous steps. 3) Estimating the migration direction at each time stamp and then applying a median filter with a 3 × 3 window size. 4) Calculating the Euclidean norm representing the magnitudes. 5) Estimating the cumulative projected displacements (CPD) by projecting the displacement of each epoch in the PMD. The projection was performed by multiplying the magnitude of migration of each epoch by the cosine of the difference between the migration direction and the PMD.

$$\boldsymbol{D_m} = \sum_{i=2}^{m} \boldsymbol{v_i t_i} \tag{7}$$

$$\bar{\boldsymbol{v}} = \left(\bar{\boldsymbol{B}}' \boldsymbol{P} \bar{\boldsymbol{B}}\right)^{-1} \bar{\boldsymbol{B}}' \boldsymbol{P} \boldsymbol{d} \tag{8}$$

$$\boldsymbol{PMD} = \mathbf{atan}\left(\frac{\overline{\boldsymbol{EW}}}{\overline{\boldsymbol{NS}}}\right) \tag{9}$$

where $\overline{EW}$ and $\overline{NS}$ are linear velocity in the east-west and the north-south directions, respectively; $\bar{B}$ is a $M \times 1$ matrix includes the time separation between the master and slave images for each offset map and $\bar{v}$ is the AAM in m/yr.

3.4 Assessment of the Spatiotemporal Variability of Dune Migration

The BD exhibited large spatial variability in dune migration rates owing to the presence of different dune morphologies, chemical formations, and the interactions between wind speed and topography (Hudson-Edwards et al., 2014). To better capture the spatiotemporal variability of dune migration, we investigated four aspects as follows: 1) We compared the AAMs of the active aeolian features extracted from the L-8 solution with various dune fields spatially distributed across the study area (see **Figure 1**). For each selected dune field, we calculated the median, first and third quartiles, and interquartile range. We performed two significance tests (F-test and Welch's two-sample test) to compare the extent to which the variance and mean of each dune field were significantly different compared to other dune fields, as described by Rouyet et al. (2019). Similarly, the tests were applied to assess the significance of the PMDs and MSCs. 2) To gain new insights into the variability of migration rates and direction, we used the redundancy of the offset maps and extracted the dune velocities (m/y) from all pairs. We then estimated the geometric mean of all active pixels associated with each dune field for each deformation map and extracted boxplots of each dune field representing the distribution of the geometric mean of the dune velocities between the different offset maps. The geometric mean was used rather than the normal mean to avoid overestimation as recommended by Baird et al. (2019). Similarly, we estimated the average migration direction and the corresponding concentration ratio (CR) of the active pixels associated with each dune field for all the deformation maps, according to **Eqs 10**, **11**, respectively. We also drew a boxplot representing the variability of migration direction to examine the probable migration directions expected in the study area. 3) We examined the spatiotemporal variability of migration rates between different seasons from the inversion of the fused offset maps. We estimated the median velocity of the velocity values in similar seasons over the entire time series and estimated the seasonal sliding coefficients (SSC) representing the ratio of the median velocities between two seasons. 4) We examined the variability of dune velocities between different decades, by employing the matching between three Thematic Mapper images (17/01/1984, 1/12/1998, and 24/1/2007) to capture dune migration in two previous decades (see **Table 1**) and compare the results to our more recent rates (i.e., from 2013 to 2021). We mainly used the Thematic Mapper instead of the Enhanced Thematic Mapper due to the failure of Scan Line Corrector (SLC) after May 2003. We used band 4) of the Thematic Mapper sensor to fed into the correlation engine as per Baird et al. (2019).

$$\bar{\boldsymbol{\theta}} = \boldsymbol{atan}\left(\frac{\sum_{i=1}^{i=n} (\boldsymbol{sin}\, \boldsymbol{\theta_i})}{\sum_{i=1}^{i=n} (\boldsymbol{cos}\, \boldsymbol{\theta_i})}\right) \tag{10}$$

$$\boldsymbol{CR} = \frac{1}{\boldsymbol{n}} \sqrt{\left[\sum_{i=1}^{i=n} (\boldsymbol{sin}\, \boldsymbol{\theta_i})\right]^2 + \left[\sum_{i=1}^{i=n} (\boldsymbol{cos}\, \boldsymbol{\theta_i})\right]^2} \tag{11}$$

where θ_i is the migration direction at velocity location. $\overline{\theta}$ is the average direction and CR is the degree of concentration, where it ranges from 0 to 1.

4 RESULTS AND DISCUSSION

4.1 Network Configurations

In total, 222 and 219 groups of L-8 (183/48, and 184/48) and 295 and 81 groups of S-2 (TR33QYV, and TR33QZU) were matched, respectively, to generate the deformation networks (**Supplementary Table S15**). The temporal distributions of the selected pairs are shown in **Supplementary Figures S4, S5**. The inversion ratio defined by Ding et al. (2020b) ranged from 4.26 to 5.26 for the separated networks. The fusion between L-8 and S-2 at the overlapping regions (see **Figure 1**) allowed us to obtain three dense temporal networks; the numbers of pairs are shown in **Supplementary Table S15**. The temporal distribution of the fused networks is attached in **Supplementary Figure S6**. Owing to the fusion, the inversion ratio reached a maximum of 5.95, with a

TABLE 1 | Dune migration rates and average migration direction over three observation periods.

Period ID	Observation period dd.mm. yyyy	Active area (Km^2)	Median celerity (m/y)	Average migration direction (°)
Period 1	17.01.1984–01.12.1998	2,457.47	9.66	240.72
Period 2	01.12.1998–24.01.2007	2,736.85	9.25	237.17
Period 3	16.05.2013–22.07.2021	2,303.28	6.61	238.72

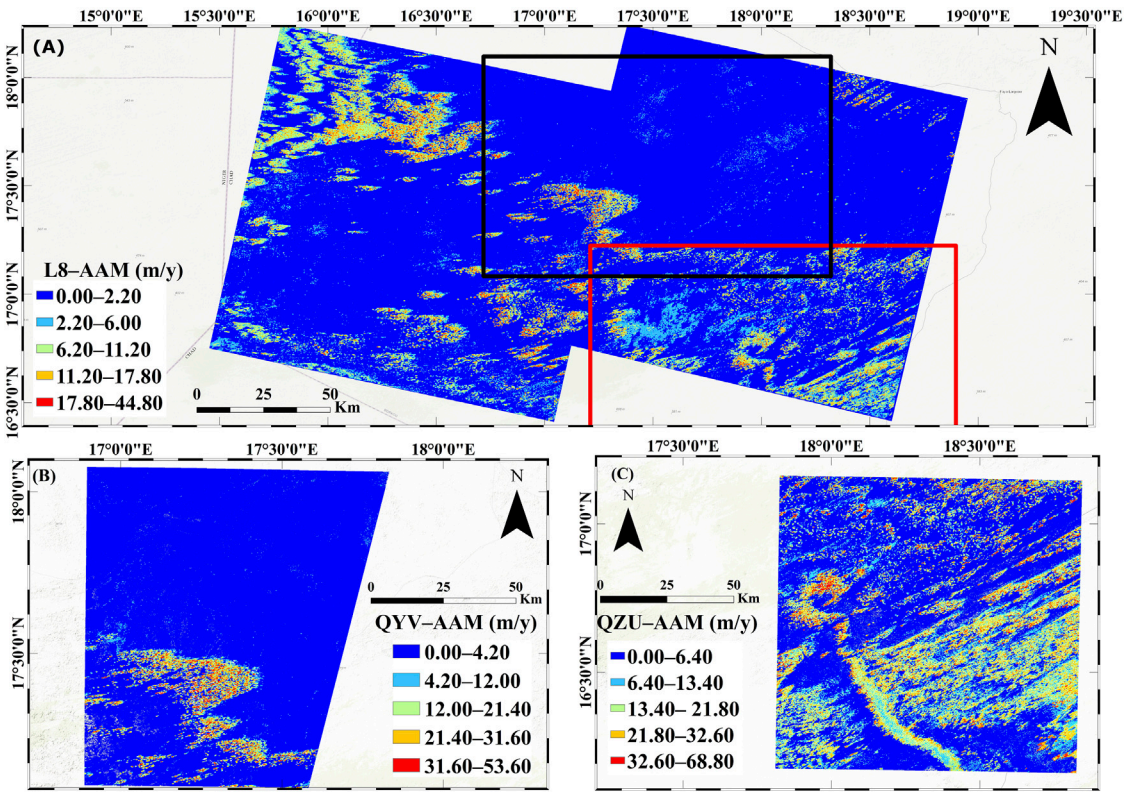

FIGURE 4 | Average annual magnitudes of dune migration for Landsat-8 **(A)** and two Sentinel-2 images: TR33QYV **(B)** and TR33QZU **(C)**. The black and red polygons in panel **(A)** denote the coverage of TR33QYV and TR33QZU, respectively. The background is light gray canvas© using Esri ArcMap 10.3.

maximum epoch of 95 time points covering the observation period. The inversion of the time series was performed pixel-by-pixel using a flexible design matrix, where only pixels with more offset maps than the threshold number (**Supplementary Table S15**) were considered in the inversion. During inversion, the number of subsets for each pixel was estimated. The percentages of valid pixels belonging to up to two subsets are listed in **Supplementary Table S15**. Owing to the flexible inversion procedure, the spatial coverage of the different inversion networks reached 100%, with a lower limit of 98%.

4.2 Spatial Patterns of Dune Migrations and Sand Transport

Figure 4 shows the AAMs within the coverage area of the two overlapping L-8 images. Notably, the AMMs of the L-8 frames were merged into a mosaic after being spatially linked to the reference points. Spatial heterogeneity was observed in the dune migration patterns; a detailed examination of the evidence for such spatial variability is presented in **Section 4.5**. It is common to find considerable geographic variability as a function of surface characteristics (e.g., vegetation cover, soil moisture, soil geochemical formation, and particle size), meteorological factors (e.g., wind speed and stability), and the presence of human activity. As shown in **Figure 4**, the maximum velocity of the aeolian features covered by the two L-8 frames was 44.80 m/y, while the maximum velocities for tiles TR33QYV and TR33QZU were 53.60 and 68.80 m/y, respectively. In terms of migration direction, most of the active dune fields migrated toward the southwest, which is consistent with the LLJ blowing from the northeast. We focused mainly on the following two areas in our detailed analysis: area in the BD and area in the northwest dune field (see **Figure 1A**). To better understand the magnitude and directional variability, we

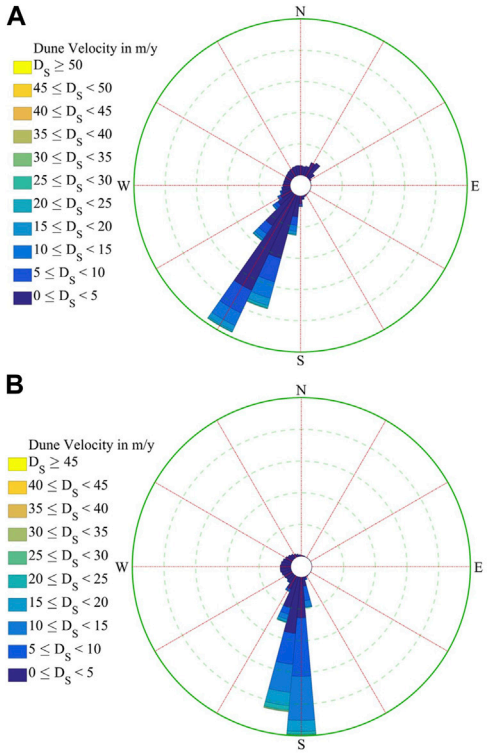

FIGURE 5 | Sand roses illustrating the relationship between dune migration rates and migration direction for active dune areas in the Bodélé Depression **(A)** and the northwestern dune field **(B)**.

extracted sand roses from the L-8, representing the frequency distributions of the AAMs and PMDs of the active aeolian features within the BD and the dune fields in the northwest of the study area, as shown in **Figure 5**. Similar sand roses for the S-2 tiles are shown in **Supplementary Figure S7**. The active features in the BD migrated 10.85 ± 4.80 m/y on average toward 244.6° ± 15.26°, while those in the dune fields in the northwest migrated 11.10 ± 4.48 m/y on average toward 266.57° ± 9.16°. On average, the active aeolian features within the coverage of the TR33QZU and TR33QYV S-2 tiles migrated 6.88 ± 9.04 m/y toward 237.69° ± 22.13° and 4.69 ± 9.54 m/y toward 235.22° ± 45.60°, respectively.

4.3 Assessment of Activity Status and Sand Transport

We used the mask generated by the MSC to mask out the stagnant areas. Active aeolian features covered approximately 6,100 km^2 of the total area of the L-8 frames, and the spatial distribution of the active dune fields is shown in **Supplementary Figure S3**. Active aeolian features accounted for approximately 1,096 and 2,310 km^2 within the depression and in the northwestern dune fields, respectively, representing 60% of the active area covered by the L-8 frames. To better capture the abilities of dunes to act as a source of sand supply, move to support other dune fields resulting in variability in dune morphology, or move into stable areas and convert to semi-active/active dune fields, we estimated the area of encroachment (AE) of sand features and dunes, as described by Ding et al. (2020b). We divided the ground covered by the L-8 frames into patches of 100 km^2, and estimated the AE of each patch. All sand features and dunes associated with each patch were included in the AE calculations. The higher the AE, the greater the ability of the patch to act as a sand supplier. The AEs ranged from 25 to 4,200 m^2/y. The spatial distribution of the patch AEs is shown in **Supplementary Figure S8**. The active dune areas within the BD can encroach approximately ~530 m^2/y, and the dune fields located in the northwest can encroach approximately ~1,330 m^2/y. The average PMDs and CRs of each patch were estimated and displayed in **Supplementary Figure S9**. The average PMDs of most of the patches were aligned toward the southwest and west, although those of some patches were aligned toward the northeast. The CRs estimated for each patch were higher in the northwestern dune field, while the patches within the BD showed less consistency in their migration directions, revealing large directional variability. This variability within the BD is consistent with Baird et al. (2019), who reported a median directional change of up to 39.26°. This considerable variability in PMDs can be interpreted by the presence of seasonal variations in the prevailing wind direction, changes in the morphology of the sand features, and the complexity of the wind regime. Such directional variability associated for the aeolian features in the BD may interpret the small AE scored in the BD in compared to the Northwest dune field.

4.4 Temporal Evaluation of Dune Migration Patterns

4.4.1 Historical Movement Patterns

We extracted the cumulative displacement time series for 16 sites spatially distributed across the dune fields covered by the L-8 frames (see **Figure 1A**). These sites were carefully selected for their migration rates to represent the migration patterns across the different dune fields. The median and standard deviation were measured over 3 × 3 adjacent pixels around each point. Our time series inversion provided continuous monitoring of dune migration patterns for nearly 9 and 6 years, as shown in **Figures 6**,**7**, respectively. Some of these points were selected in the overlapping areas between the two sensors, and we compared the time series extracted from the independent sensors with each other and with the fusion between the two sensors (**Section 4.6.1**). **Figure 6** shows the temporal evolution of the points (P01-P08) extracted from the L-8 inversion, whereas points from P09-P16 are displayed in **Supplementary Figure S10**. The S-2 time series results for nine points located in the ground coverage of the S-2 frames are shown in **Figure 7**, while the time series results of these points as extracted from the inversion of the fusion between the two sensors are shown in **Supplementary Figure S11**. The maximum migration rates (~30 m/y) occurred at points P02, P04, P07, P13, P14, and P16. The minimum migration rate occurred at P06 (~10 m/y). The other nine points showed moderate migration rates of 15.5–23.5 m/y.

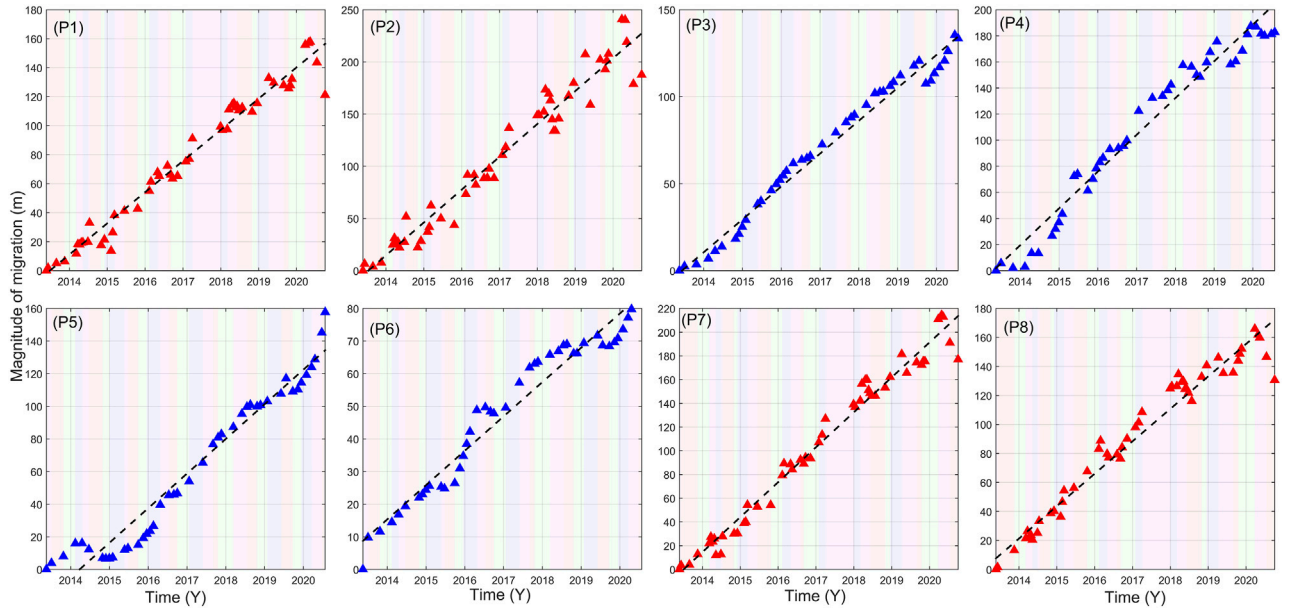

FIGURE 6 | Cumulative projected displacements over time extracted from the inversion of the deformation maps belong to two Landsat-8 frames. The dashed colored areas in the background represent the different seasons: red, blue, green, and magenta refer to summer, winter, autumn, and spring, respectively. The black dashed lines denote the best linear fit of the cumulative projected displacement. Red and blue triangles denote the points belonging to the coverage of (183/48) and (184/48), respectively.

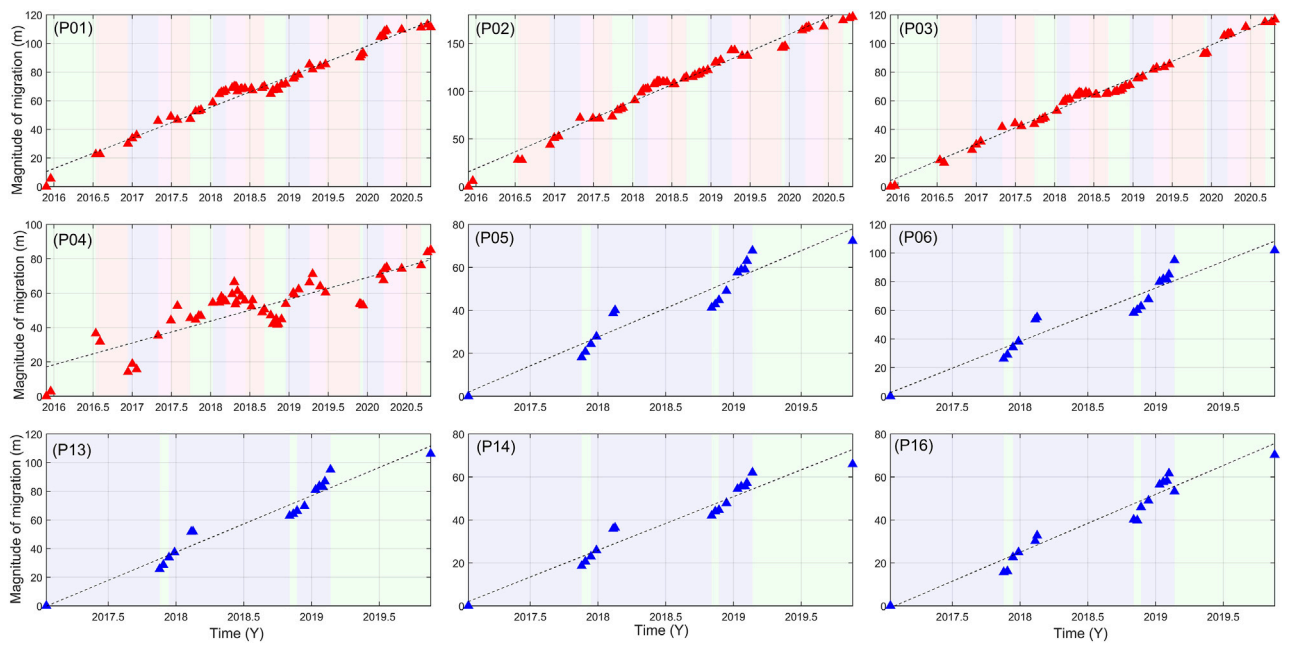

FIGURE 7 | Similar to **Figure 6**, the time series extracted from the inversion of two Sentinel-2 tiles. Red and blue triangles denote the inversion of pairs belonging to T33QYV and T33QZU, respectively.

4.4.2 Seasonality of Movement Patterns and Interpretations

The degree of correlation between the cumulative time series and the best linear fit (black lines, **Figures 6**, **7**) exceeded 97%, showing an almost linear increasing trend. However, seasonal signals in the time series displacements were also observed. To better assess the seasonality in the temporal patterns, we subtracted the value of the linear fit from the CPD (**Supplementary Figure S12**). The

magnitude of the seasonality reached a maximum of ~30 m/y at points P02 and P03. The presence of these seasonal signals can be attributed to the seasonality of the effective wind regime and dust storms. The seasonality of the dune pattern was supported by observing the direction of migration in each epoch; epochs with a migration direction against the PMD experienced a decrease in net migration. The temporal evolution of the CPDs denoted an inactive status when the migration direction was aligned in the opposite direction to the PMD, leading to a decrease in net migration. Temporally, the dunes experienced lower migration rates during the summer months (i.e., June to August). However, the activity status improved during the winter months, when the dune migration direction was consistent with the PMD. The ECMWF data (see **Supplementary Figure S1**) showed that the wind was from the northeast in all months except the summer months, when it blew from the southwest. As for the wind speed, the data also showed that the speed reached its minimum values in the summer months. Interestingly, the variability in wind direction was observed in all years from 2013 to 2020, indicating the presence of seasonal fluctuations in the wind regime. As the BD is one of the dustiest places worldwide, dust storms occur frequently, leading to changes in the sand transport system. Previous studies have reported that dust storms are most common in winter because of the northeasterly direction of Bodélé LLJ. These reports are consistent with the observed temporal patterns of dune migration and the activity states extracted from the CPDs. It is assumed that the seasonal signals observed in the time series are not closely coupled with the residuals of seasonal illumination, especially in our study area, which is dry, vegetation-free, and has nearly flat terrain. Consequently, this seasonal variability may be closely related to the activity of the wind regime in the study area. Despite the selection criteria applied to limit the radiometric baselines, which aim to control both seasonal signals and cast shadows, the probability of finding such seasonal signals is still present. Moreover, seasonal signals may be a natural characteristic of dune dynamics owing to the tightly coupled relationship between wind activity and dune migration. It is worth noting that dunes are considered complex monitoring targets compared to glaciers and landslides, as the latter targets are mainly controlled by gravitational forces and melting conditions (Stumpf et al., 2016). Such controlling factors allow filtering out divergent directions from the deformation fields and provide a strong indication of the quality of the matching results and inversion (Stumpf et al., 2016). Consequently, in extracting the time series of dune migration, we paid close attention to the possibility of such seasonal signals being present within the temporal patterns. We attempted to control the presence of divergent seasonal signals through the selection criterion, post-processing, and the projection of the displacement in the PMD, to help capture the true temporal patterns.

4.5 Spatiotemporal Variability of Dune Velocities

4.5.1 Evidence of Spatial Variability of AAMs, MSCs and PMDs

The AAMs, PMDs, and MSCs were analyzed for the ten dune fields, as shown in **Figure 8**. The AAMs varied spatially between the ten dune fields: 1) The median AAMs value varied from 3.0 to 9.0 m/y, with a maximum value in "Area-10" in the northwest of the study area, consistent with previous results of high encroachment areas in the northwest dune filed. The interquartile values of the active aeolian features varied from 3.85 to 17 m/y. 2) The median PMDs varied from approximately 240–269°, with an interquartile range of 6.2–14.2°, consistent with previous reports of northeasterly winds prevailing in the study area. 3) The median MSC of the active features varied from 0.32 to 0.48. The results of the F-test and Welch's test are presented in **Supplementary Tables S16, S17**. The results show that the hypothesis of no significant difference in the means and variance between different dune field pairs can be rejected in most cases, with some exceptions, indicating that the migration rates and corresponding directions varied significantly in the spatial domain. The hypothesis of similar AAM means and variances was accepted for 4 and 3 pairs out of 45 pairs, respectively. The hypothesis of similar PMD means and variances was accepted for 5 pairs out of 45 pairs. Interestingly, the rejection of the hypothesis highlighted spatial variability in the dune migration patterns, which can be attributed to variability in geochemical formation, wind energy, sand transport conditions, dune height and orientation, and wind–topography interactions.

4.5.2 Spatiotemporal Variability in Dunes Velocity Between Different Offset Maps

Figure 9 shows boxplots of the estimated geometric means of the active features associated with each dune field extracted from different offset maps, for both migration magnitudes and directions. The median of the geometric mean varied from 11.12 to 17.83 m/y, with an interquartile range of 3.07–12.86 m/y. The geometric means extracted from the AAMs of the same ten dune fields are shown as blue diamonds in **Figure 9A**. It appears that the fusion of all annual rates tends to underestimate the migration rates; the medians of the geometric means estimated from the AAMs were lower in all cases. This may be attributed to the fact that the fusion of offset maps showing different directions would lead to a reduction in net migration rates. The median of the average directions of the ten dune fields varied between 236.15° and 269.40° with an interquartile range of 3.21°–19.94°. The large interquartile range in "Area 1" may be attributed to the presence of protodunes or sandy patches with variable migration directions. The median CR ranged from 0.117 to 0.928, with an interquartile range of 0.095–0.243. It is worth noting that large CRs indicate the homogeneity of PMDs of active aeolian features associated with each dune field. In particular, the maximum variation in migration direction up to 20° corresponds to a CR of 0.98. The mean values estimated from the PMDs are shown as black diamonds in **Figure 9B**. The means of the PMDs were nearly identical to the medians of the boxplots, demonstrating the potential of fusion in reliably estimating migration direction.

4.5.3 Spatiotemporal Variability of Dunes Velocities in Different Seasons

Figure 10 shows the variability of the horizontal velocity for ten selected points during the measurement period from 2013 to

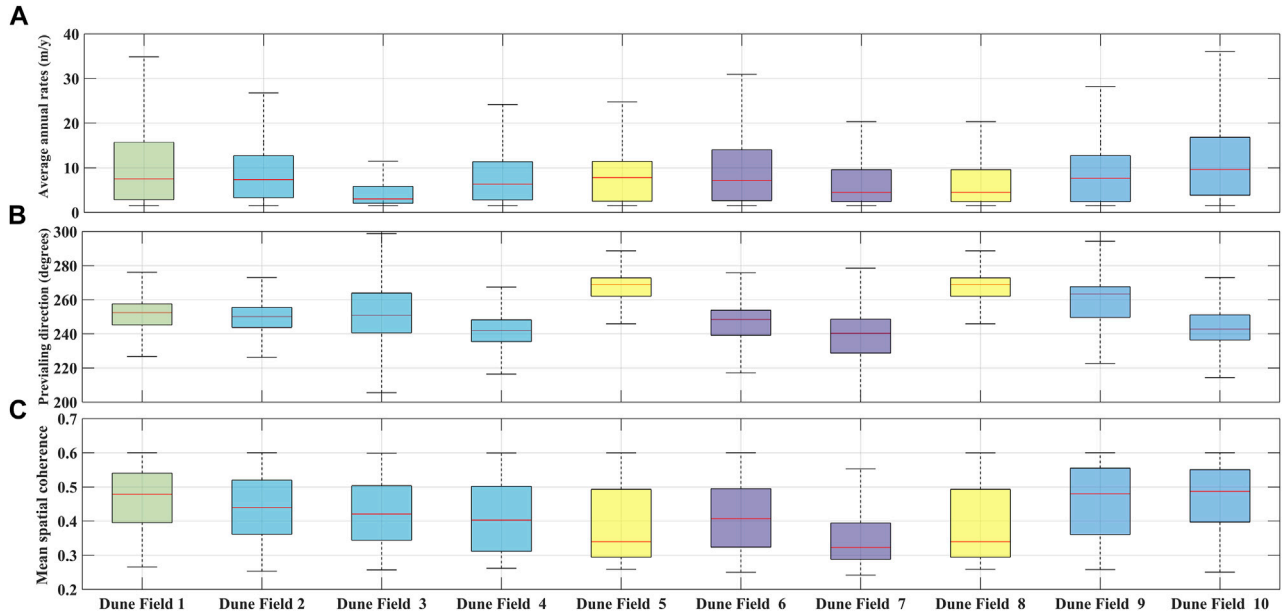

FIGURE 8 | Boxplots of the AAM **(A)**, PMD **(B)**, and MSC **(C)**. The box plots were plotted for 4,000 pixels belonging to ten dune fields (see **Figure 1**). The outliers were discarded from the visualization; however, they were considered in estimating the median, and the interquartile ranges.

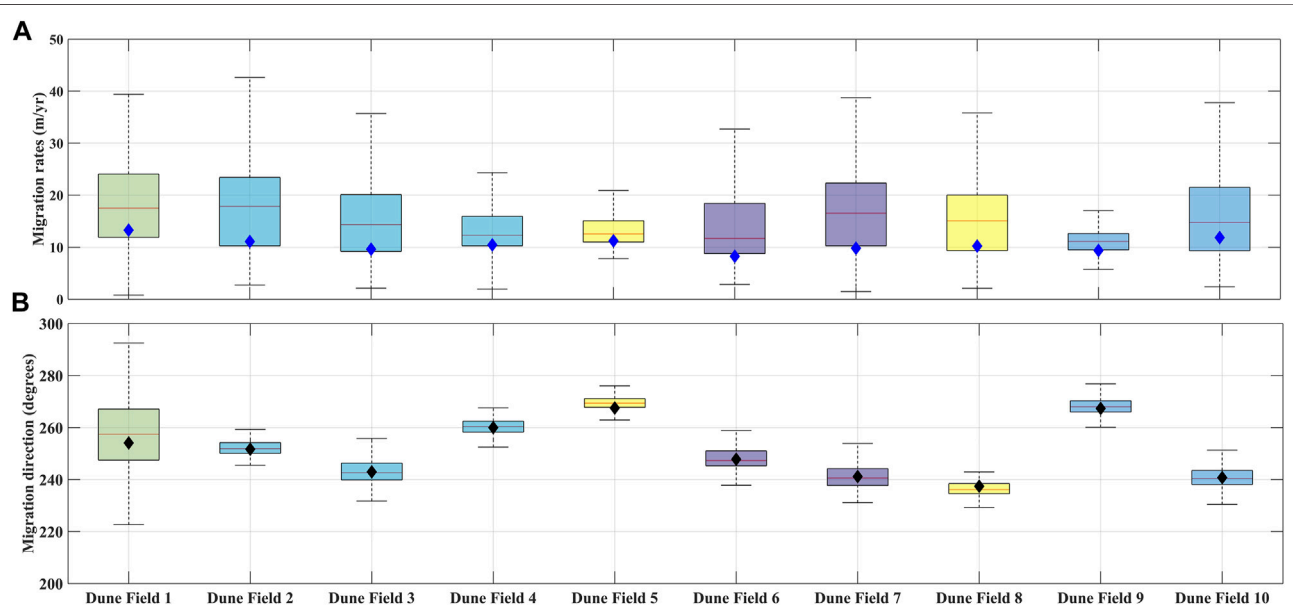

FIGURE 9 | Spatiotemporal variability of the dune migration rates **(A)**, and directions **(B)**. Box plots represent the variability of geometric means of dune velocities and the average migration direction of the active aeolian features belonging to each dune field for all the pairs. The blue and black diamonds in **(A,B)**, respectively, represent the geometric means estimated for the active aeolian features belonging to the AAM and PMD solutions.

2020. The velocity varied during the observation period, with an almost increasing trend during the winter and autumn months. The velocities reached a maximum of ~220 m/y at P13. Although no clear trend was found to represent the behavior of velocity variation, seasonal variability was observed in the velocity patterns of all the points. The seasonal variability in dune velocity was supported by the wind records extracted from the ECMWF data (**Supplementary Figures S13, S14**), where the wind speed and direction for the ten selected points were displayed. It was observed that the wind speed showed a

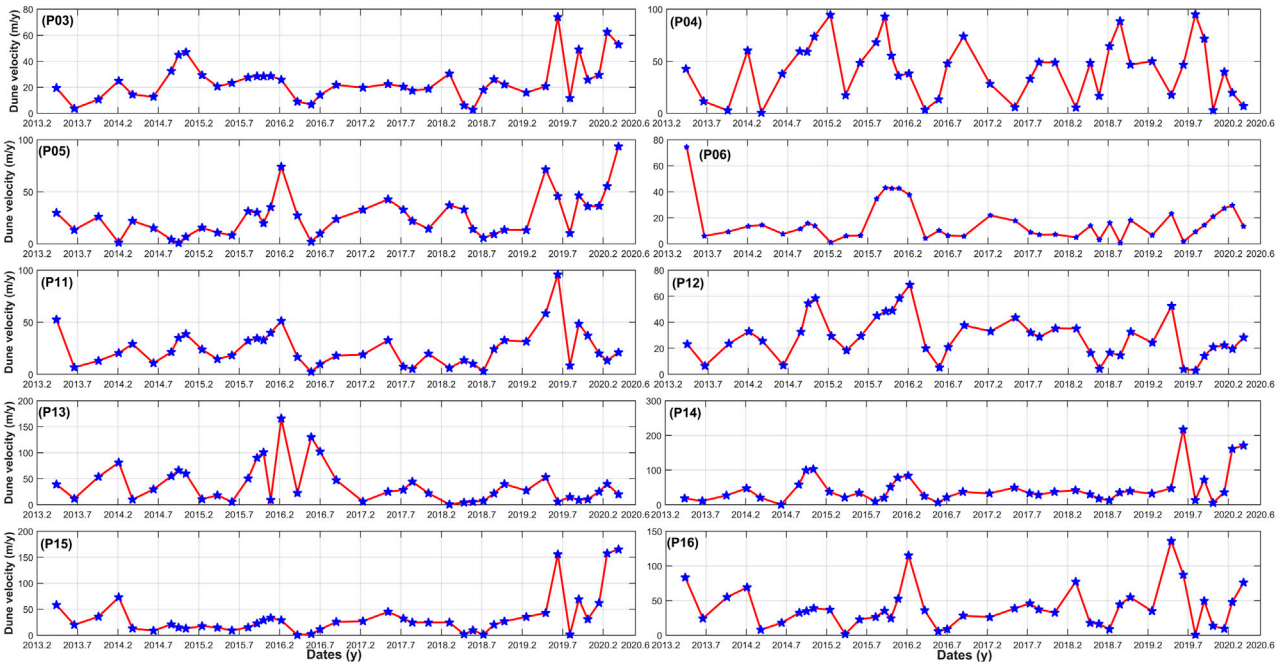

FIGURE 10 | Time series of dune velocities as extracted from the inversion of offset maps belong to Landsat-8 frame 183/48. The blue pentagrams represent the acquisition epochs. The red lines denote the continuous dune velocities.

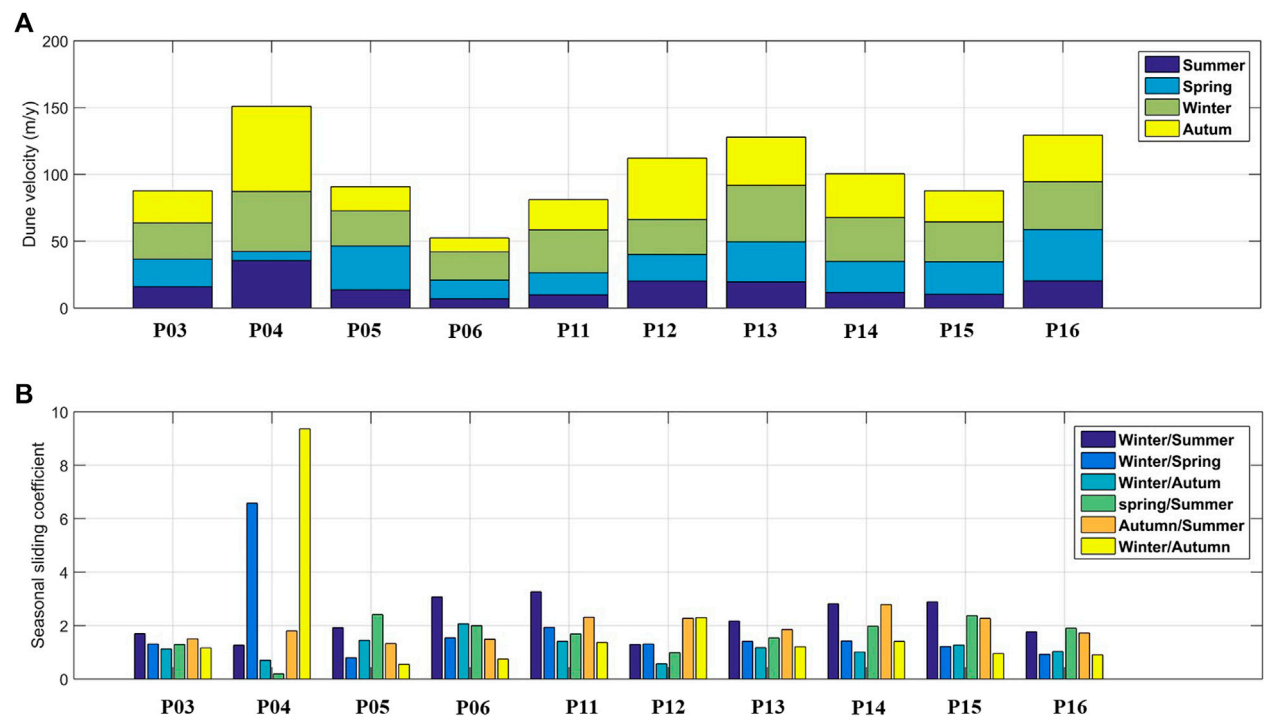

FIGURE 11 | Median seasonal velocity at different points belong to Landsat-8 frame 183/48 **(A)**. The seasonal sliding coefficients denote the ratio between the different seasonal velocities **(B)**.

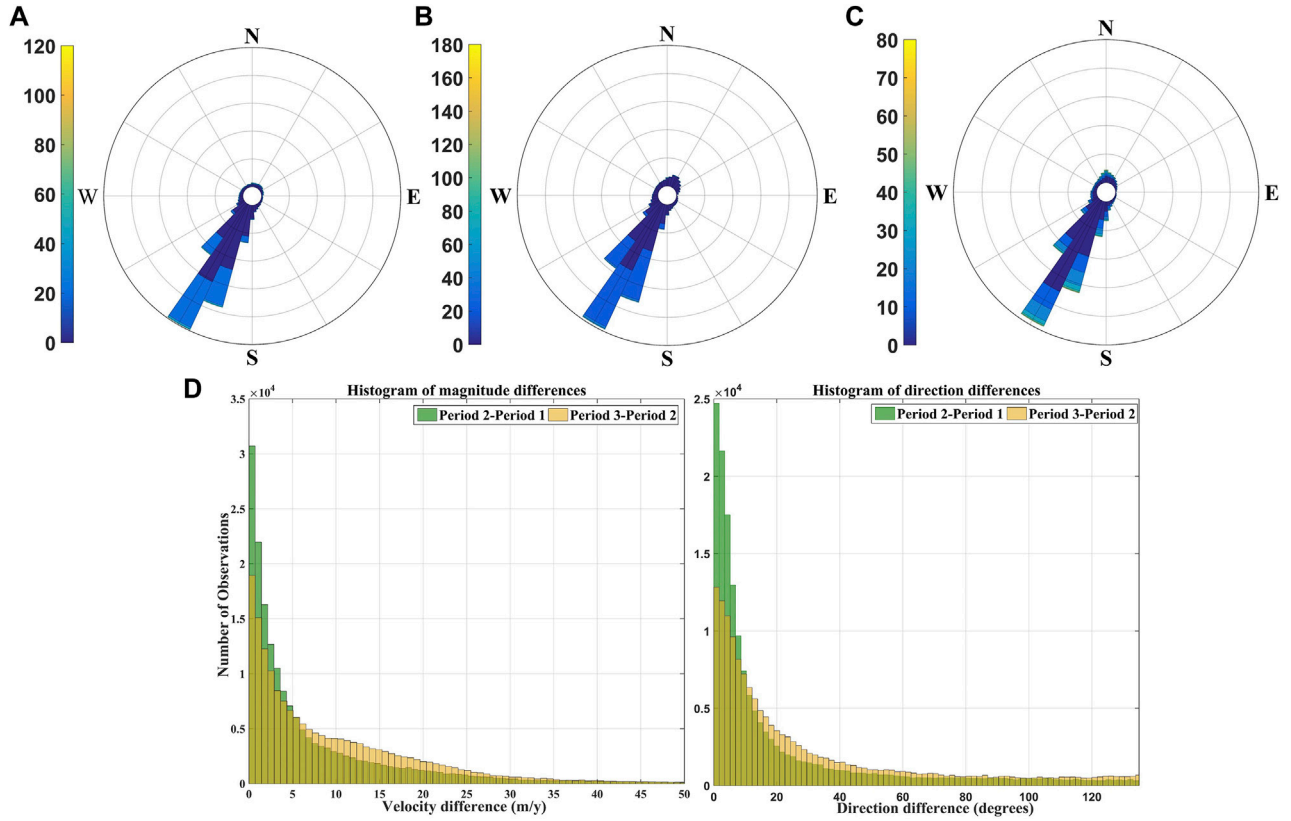

FIGURE 12 | Frequency distribution of the active dune and sandy patches in the Bodélé Depression for three observation periods: **(A)** 1984–1998, **(B)** 1998–2007, and **(C)** 2013–2021. Units in **(A–C)** are in m/y. **(D)** Histogram of the difference between period 1 and 2 and periods 2 and 3 in terms of magnitude **(Right)** and direction **(Left)**.

fluctuation with lower speeds in the summer months (June to August). Additionally, the wind directions mainly from the northeast with variable directions mainly in summer months. To better capture the seasonal variability in the measured velocity, we estimated the median velocities for the acquisition epochs belonging to each season. **Figure 11A** shows the variability in the median velocities between different seasons. Interestingly, the median velocities recorded during the summer showed the lowest velocities. We estimated the SSC, which represents the variability of the median velocities between different seasons (**Figure 11B**). The winter/summer sliding coefficient showed the highest values, ranging from 1.30 to 2.90 with a median of 2.05. In contrast, the median velocities changed slightly in spring and autumn compared to winter, and the median SSCs were 1.14 and 1.36 for winter/spring and winter/autumn, respectively (**Figure 11B**). The maximum median velocity peaked during the autumn and winter months. The variability in dune velocities at different times of year is expected and can be attributed to seasonal changes in wind strength. The wind records extracted from ECMWF data between 2013 and 2020 (**Supplementary Figure S1**) showed that the median monthly wind speeds from May to September ranged from 1.20 to 3.40 m/s, with the lowest values in the summer months (June to August). The median wind speed increased up to ~6.5 m/s in the winter months. In terms of migration direction, the medians of the monthly directions ranged from 233.24° to 250.03° for all months except July and August, when they were 44.95° and 32.74°, respectively. The observed seasonal velocity patterns were consistent with the behavior of the wind regime, and both were consistent with previous reports of the prevailing northeasterly LLJ, especially during winter (Vermeesch and Leprince, 2012).

4.5.4 Spatiotemporal Variability of Dune Velocities Between Different Decades (1984–2021)

Figure 12 shows the frequency distributions of the magnitude and direction of the active features within the BD (**Figure 1**) over three periods (**Table 1**). The active features within the BD had a strong tendency to migrate toward the southwest and south-southwest; the average migration directions are summarized in **Table 1**. The differences between the average directions reached a maximum of 3.5°, demonstrating the consistency of the dune migration direction over longer time. Individual examination of the directional differences (**Figure 12D**) showed variability in the directions between periods 1–2 and between periods 2–3 (**Table 1**), with median differences of 9.45° and 21.4°, respectively. These individual variations can be attributed to

the presence of sand features and protodunes, as well as the formation of new sand features owing to the deflation of sand and dust storms. The large median directional difference between periods 2–3 may also be owing to the high ground resolution of L-8, which could capture more detailed information than Landsat-5. Directional differences of up to 90° may occur owing to change in morphological interactions and the inability of the correlation to capture these morphological changes, especially over longer time intervals. In addition, continuous sand transport and dust storms may affect sand flux in the BD, leading to the birth of new dune generations or the conversion of stable fields to active/semi-active status. The percentage of active areas within the BD ranged from 26 to 30% of the total area, with the lowest value between 2013 and 2021. The geometric mean velocities ranged from 6.61 to 9.66 m/y, with the lowest values recorded for the most recent observation periods. Comparatively, Baird et al. (2019) reported accelerating dune velocities averaging 2.56 ± 12.60 m/y, with some accelerating aeolian elements moving at more than 20 m/y. Here, a comparison between the migration velocities recorded in periods 1 and 2 showed nearly stable conditions with an average acceleration of 0.36 ± 14.20 m/y. In contrast, an average deceleration of 3.2 ± 15.20 m/y was observed when comparing periods 2 and 3. To add new insights to the comparison between migration patterns captured at different observation periods, we compared the average annual wind speed with the geometric mean of the migration rates between similar observation periods. Vermeesch and Leprince (2012) reported that a 1% increase in wind speed results in a ~3% change in dune velocity and associated dust production. The median annual average wind speeds were 5.24 and 4.84 m/s for periods 2 and 3, respectively, representing a 7.63% decrease in wind speed. The percentage decrease in the migration rate was 28.2%. The ratio between the changes in dune speed and wind speed was approximately 3.50%, which corresponds to the ideal ratio between wind speed and dune speed. The comparison showed strong agreement between the wind speed extracted from the ECMWF and the migration rates estimated from the image matching. However, despite the good agreement between the wind speed and dune velocities, dependence on the matching results rather than the wind speeds could still be considered valuable because 1) the wind speeds from the ECMWF have a coarse resolution (i.e., 0.1 × 0.1 °), 2) the matching measurements can be validated and evaluated, and 3) the matching results provide indications of the migration rates that can be used in vulnerability analysis, stability planning, and modeling.

4.6 Validation and Uncertainty Estimation

4.6.1 Cross-Validation

Table 2 summarizes the AAM and PMD values, and the slope of the linear fit for the points covered by L-8 and the points overlapped by L-8 and S-2. There are some inconsistencies between the slope of the linear fit of the CPDs extracted from S-2 and from both L-8 and the fusion; the medians of the absolute difference (MAD) reached ~4.23 and 6.81 m/y for the differences between S-2/L-8 and S-2/fusion, respectively. The comparison between L-8 and the fusion showed the worst consistency, with a MAD of ~9.25 m/y. These large differences can be attributed to 1)

TABLE 2 | Slope of linear fit (SLF), correlation coefficient (CC), average annual magnitude (AAM), and prevailing migration direction (PMD) of the test sites from Landsat-8, Sentinel-2, and the fusion between two sensors.

ID	Landsat-8				Sentinel-2				Fusion			
	SLF (m/y)	CC (%)	AAM (m/y)	PMD (°)	SLF (m/y)	CC (%)	AAM (m/y)	PMD (°)	SLF (m/y)	CC (%)	AAM (m/y)	PMD (°)
P01	21.51	98.43	21.59 ± 1.23	253.49 ± 2.24	21.42	96.81	21.23 ± 1.17	252.85 ± 1.98	19.75	93.51	21.8 ± 0.44	254.03 ± 2.38
P02	31.48	97.54	30.53 ± 2.10	254.45 ± 0.42	35.18	97.47	33.73 ± 4.10	255.47 ± 2.19	31.87	93.00	29.13 ± 4.49	256.34 ± 3.97
P03	18.90	99.05	13.81 ± 1.98	249.08 ± 2.88	23.15	98.56	23.65 ± 3.84	252.26 ± 2.18	24.77	92.00	15.98 ± 1.54	249.99 ± 3.25
P04	28.20	98.13	23.23 ± 8.28	229.53 ± 58.85	12.71	71.27	11.34 ± 7.69	226.05 ± 35.56	49.05	95.50	21.61 ± 8.15	236.34 ± 43.43
P05	21.22	97.42	19.98 ± 3.36	238.32 ± 4.85	26.81	90.39	25.22 ± 6.42	248.38 ± 7.46	34.02	98.19	20.44 ± 2.66	239.58 ± 3.78
P06	10.52	97.72	15.04 ± 3.39	227.47 ± 8.01	37.29	91.32	36.32 ± 0.48	237.21 ± 1.02	45.38	96.70	16.16 ± 2.02	234.51 ± 4.11
P07	29.47	98.74	24.65 ± 4.91	259.51 ± 2.31								
P08	22.37	97.80	21.19 ± 1.72	255.92 ± 2.48								
P09	18.93	96.82	19.95 ± 6.12	271.19 ± 3.24								
P10	23.47	98.74	21.02 ± 5.86	268.04 ± 1.15								
P11	18.83	98.93	14.98 ± 1.81	246.64 ± 3.62								
P12	15.49	97.34	14.78 ± 1.85	247.56 ± 7.05								
P13	30.63	97.75	23.85 ± 0.75	244.06 ± 3.05	39.42	94.48	39.85 ± 5.71	246.81 ± 0.97	20.34	91.10	23.15 ± 1.55	248.08 ± 6.17
P14	29.06	99.34	18.71 ± 2.93	238.26 ± 2.52	24.94	93.49	24.91 ± 4.09	251.19 ± 7.56	18.11	77.50	18.4 ± 2.62	237.70 ± 3.98
P15	19.53	97.47	14.39 ± 1.40	237.30 ± 3.21								
P16	30.96	99.48	20.36 ± 2.37	247.13 ± 7.24	26.94	94.00	27.40 ± 2.15	242.11 ± 1.97	28.81	96.20	20.57 ± 2.40	246.51 ± 6.68

differences in the observation periods in the S-2 time series and both the L-8 and the fusion time series; 2) the different performance of the inversion networks (i.e., the different condition numbers of the design matrices); and 3) the radical differences in the temporal and spatial resolutions of the sensors and their orthorectification and co-registration accuracy. With respect to AAMs, the comparisons between S-2/L-8 and S-2/ fusion showed MADs of ~7.0 and 6.81 m/y, respectively. The comparison between the AAMs of L-8 and the fusion showed a MAD of 0.7 m/y. Despite the stability of the inversion of one rate owing to large redundancy and good network connectivity, we noticed a larger differences between the AAMs of S-2 and both L-8 and the fusion than between L-8 and the fusion. This can be interpreted by the different observation periods between S-2/L-8 and S-2/fusion. In terms of the PMDs, the directions extracted from S-2 showed strong agreement with both L-8 and the fusion; the MAD were 3.4° and 2.7° for S-2/L-8 and S-2/fusion, respectively. Moreover, the MAD between L-8 and the fusion was 2.5°. From a detailed examination of the temporal patterns extracted from the different inversions, we observed that, for networks with lower temporal sampling (i.e., T33QZU which had only 17-time epochs owing to cloud and haze constraints), the cumulative time series showed two increasing trends with almost stable conditions where no epochs were included (see **Figure 7**). In comparison, the inversion of TR33QYV captured more details, showing almost linearly increasing trends with low seasonality signals, except for P4 (see **Figure 7**). However, the fusion between the two sensors (**Supplementary Figure S11**) provided higher temporal sampling that allowed observation of the temporal evolution up to a weekly time scale. This led to design matrices with higher condition numbers, consequently affecting the stability of the inversion. More seasonality was recorded in the inversion of the merged networks than in the inversions of either L-8 or S-2. The comparisons between the different inversions at different points showed some inconsistencies, especially in the migration magnitudes, but the migration directions showed higher homogeneity regardless of the network configuration and the observation period.

4.6.2 Uncertainty Estimation

We used a stable area of 7.25 km^2, as shown in **Figure 1**, to evaluate the uncertainty of the inverted results. We estimated the standard deviation of the measurements as an indicator of uncertainty (Bontemps et al., 2018; Lacroix et al., 2019; Ali et al., 2021). We captured the effect of the inversion in controlling uncertainty by comparing the uncertainties of the individual offset maps before and after inversion (Bontemps et al., 2018). **Figure 13** shows the uncertainties of the individual offset maps after inversion and the percentage of improvement in the uncertainties for the L-8 frames. Similar maps for S-2 and the fusion can be found in **Supplementary Figure S15**. After inversion, the uncertainties varied from 0.27 to 1.90 m and from 0.29 to 1.36 m with averages of 0.70 and 0.62 m for L-8 and S-2, respectively. The percentages of improvement in the uncertainty after inversion were, on average, 35 and 44% for L-8 and S-2, respectively. We also extracted the uncertainties in the inverted results of the CPDs; the uncertainties were, on average, 0.95 m and 0.74 for L-8 and S-2, respectively. It is interesting to note that the uncertainty levels of the inverted results were within the resolution of the matching technique (i.e., about a fifth to a tenth of the ground resolution).

4.7 Reflections on Previous Studies

To date, three studies have focused on monitoring dune migration in the BD using optical image matching techniques with different image sources and with different study periods. Vermeesch and Drake (2008) first used a correlation engine with ASTER images at different time intervals and integrated the displacements with dune heights extracted from ASTER stereo images to estimate sand flux. They reported variability in dune velocities, noting that the velocities were 2.5 times higher between December 2006 and January 2007 than between October 2005 and January 2007, and attributed this to the presence of the Bodélé LLJ, which is prevalent during the winter months. A similar trend was observed in our time series, with the winter and summer velocities scoring the highest and the lowest velocities, respectively.

Vermeesch and Leprince (2012) monitored dune acceleration over a 26-year period between 1984 and 2010 using a matching procedure along with seven images from different archives. They used the time series of dune velocities to draw conclusions about the wind conditions in the Sahara Desert, especially in the absence of meteorological observations. They reported that dune velocities of less than 10% over 26 years, equivalent to a ~0.2% change in wind speed. We believe that the sparse temporal sampling of the extracted time series (i.e., seven images spanning 26 years) missed many details about dune movement and seasonal patterns. In our study, due to the dense temporal sampling, we estimated the median velocity for each season and found that the SSC of the velocities between winter and summer scored ~2 revealing the activity of the wind in the winter due to the Bodélé LLJ. The effect of acquisition epochs on the temporal patterns was supported in our study, while the inversion of the S2TR33QZU offset maps was limited to 17 epochs due to cloud cover and dust. The inversion showed two increasing linear trends (see **Figure 7**) with a plateau in between, lacking provide details that can be captured in case of dense acquisition dates. In summary, our study introduced dense spatiotemporal monitoring of dune dynamics and associated drivers inside and outside the BD. It is worth noting that detailed studies on the spatiotemporal patterns of dune dynamics in the BD have been lacking in the literature.

4.8 Contribution of the Inversion of Optical Image Matching for Monitoring the Earth's Surface

The optical image matching selection and inversion algorithm provides a valuable tool for monitoring surface processes over time, with the advantage of reducing uncertainty and enhancing spatial coverage, especially when using free archives that provide a huge amount of data with dense temporal resolution (Ali et al., 2020; Ding et al., 2020b). As free archives of optical imagery (i.e., L-8 and S-2) offer temporal sampling ranges of 5–16 days,

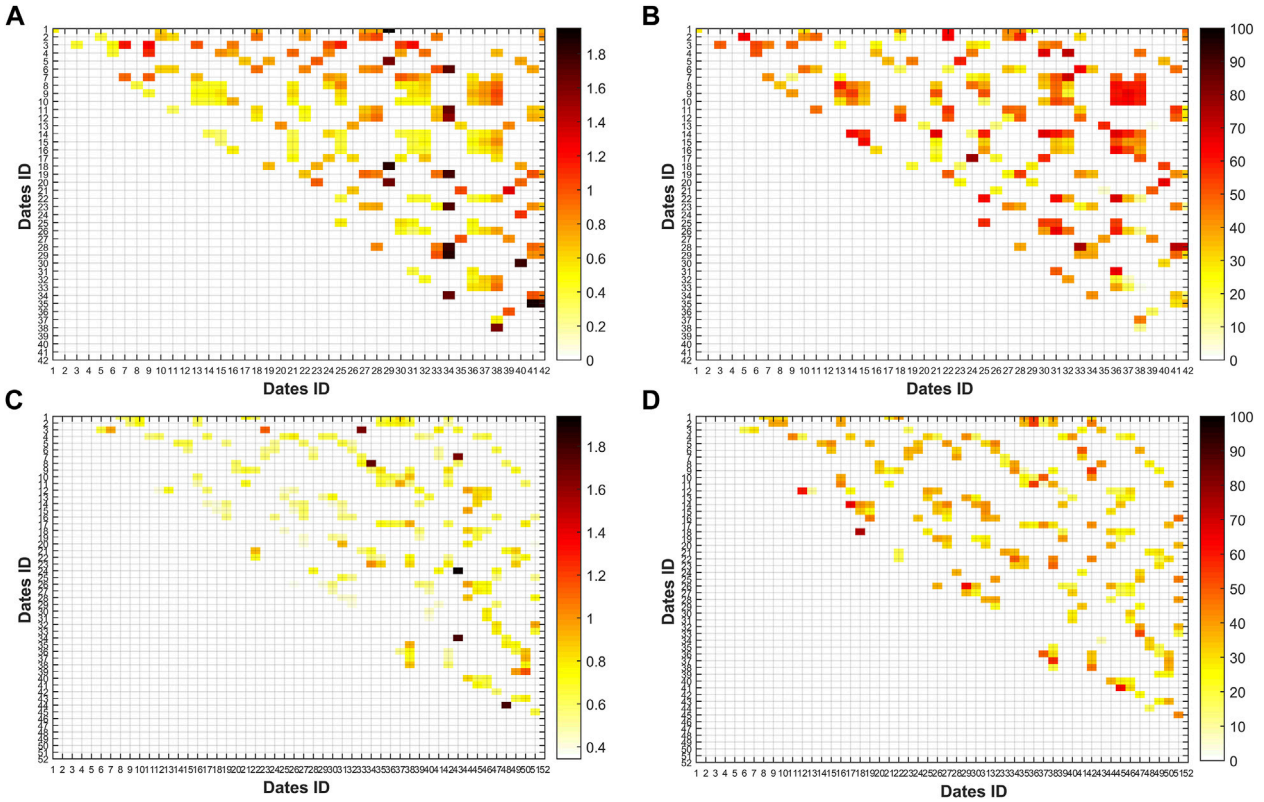

FIGURE 13 | Uncertainty of the offset maps after inversion **(A)** and the percentage of improvement in the uncertainty before and after inversion **(B)** for the Landsat-8 frame P183/R48. **(C)** and **(D)**, similar to **(A,B)** but for the Landsat-8 frame P184/R48. The colored cells represent the pairs with the master on the *y*-axis and slave on the *x*-axis. Each pair is defined by the acquisition dates. The acquisition dates of each frame can be found in **Supplementary Tables S1, S2**. Units in A and C are in (m) while **(B, D)** are percentages.

the number of available images is inherently limited by cloud cover, especially in wet seasons in tropical regions (Dille et al., 2021). Limiting the selection of images to those with no/low cloud cover to preserve the matching uncertainty (Lacroix et al., 2018) would affect the number of images and consequently limit the temporal sampling of the time series. Additionally, slow-moving targets require large time separation to help measure real displacement and avoid a large fraction of geolocation errors in the matching results (Fahnestock et al., 2016). However, long temporal baselines affect the temporal sampling of the time series (Dille et al., 2021). Therefore, dependence on the fusion between the time series of two or more sensors with overlapping temporal coverage provides a good alternative to increase the temporal sampling of the time series especially at locations where the images usually contaminated by cloud or haze and enhance understanding of the surface process. In this work, we introduced the fusion of time series from two sensors at overlapping locations to increase the density of the temporal sampling. The comparison between the individual time series from each sensor with the fused time series revealed the potential of the fusion of offset maps with similar ground resolutions in providing dense temporal sampling at up to a weekly time scale. The fusion procedure avoids the high computational costs and data burdens associated with the inversion of a full network. However, fusion provides higher inversion ratios, and the configuration of the network and condition number of the matrix should be considered to preserve the quality of the inverted results. The density of the temporal sampling of the time series can, therefore, be improved by matching images from different sensors, considering the effect of the radiometric variation of both images (Necsoiu et al., 2009). Although the matching of different sensors would provide a simple framework for inversion, differences in the radiometric properties and Sun angles between the two images could affect the quality of the offset maps. Matching networks created via matching images from different sensors can be applied to guarantee good connectivity of the design network and dense temporal sampling, revealing the complex patterns of surface deformations.

5 CONCLUSION

In this work, we extended the application of the optical image matching selection and inversion algorithm using L-8 and S-2 data to gain new insights into the spatiotemporal patterns of dune

migration in the BD during 2013–2021. Images from the L-8 and S-2 archives with low cloud cover were selected to control uncertainty and improve spatial coverage. The selected images were used to generate networks of matched pairs by setting radiometric and temporal baselines. Using the MSC, stagnant and moving targets were automatically differentiated. The inversion was performed using a pixel-by-pixel strategy and flexible design matrices that covered a large area (up to 98% of the total area of the two L-8 frames). The AAMs and their corresponding PMDs exhibited large spatial variability that can be attributed to various factors such as soil moisture, soil particles, sand transport, wind energy, and wind–topography interactions. The PMDs showed a tendency of migration toward the southwest, which is consistent with the prevailing northeasterly direction of the Bodélé LLJ. The temporal patterns of dune migration showed significant seasonal variation, which can be attributed to the seasonality of the effective wind regimes and dust storms. The average monthly wind speeds and directions extracted from the ECMWF showed that northeasterly winds were predominant in all months except the summer months. In addition, the wind speed was lowest during the summer months and highest during winter. Comparison between the inversions of the different networks showed some discrepancies owing to the different performances of the inversions, based on the different networks. Inversion reduced the uncertainty by, on average, 35 and 44% for L-8 and S-2, respectively. In addition, fusion between the two sensors allowed the temporal sampling to be condensed to reveal complex short-term patterns of surface deformation. The fusion of two or more sensors would be a promising alternative for monitoring temporal evolution with dense temporal coverage, especially in regions with heavy cloud cover in tropical areas.

DATA AVAILABILITY STATEMENT

The original contributions presented in the study are included in the article/**Supplementary Material**, further inquiries can be directed to the corresponding author.

AUTHOR CONTRIBUTIONS

EA: Writing-original draft, conceptualization, methodology, investigation, validation, and visualization. WX: Conceptualization, investigation, writing—review and editing, and supervision. LX: Writing—review and editing, Visualization. XD: Funding acquisition, Writing—review and editing, supervision. All authors were involved in the final preparation of the draft and have read and approved the manuscript.

FUNDING

This research was jointly supported by the Research Grants Council (RGC) of the Hong Kong Special Administrative Region (PolyU 152232/17E, PolyU 152164/18E, and PolyU 152233/19E), the Research Institute for Sustainable Urban Development (RISUD), the Hong Kong Polytechnic University, and the Innovative Technology Fund (ITP/019/20LP).

ACKNOWLEDGMENTS

We are extremely grateful to the ESA for providing the Copernicus Sentinel-2 data through the Sentinel Science Hub and the Sentinel-2 Expert Users Data Hub, to the USGS for providing the Landsat data through Earth Explorer http://earthexplorer.usgs.gov/, to the European Center for Medium-Range Weather Forecasts (ECMWF) for providing the wind records, to Alaska Satellite Facility https://www.ecmwf.int/ for providing the Sentinel-1A data, and to the Caltech Group for providing COSI-Corr. We used ArcMap 10.3 software for map generation and spatial analysis. We also used MATLAB 2016a for coding and scripting.

SUPPLEMENTARY MATERIAL

The Supplementary Material for this article can be found online at: https://www.frontiersin.org/articles/10.3389/fenvs.2021.808802/full#supplementary-material

REFERENCES

Agram, P. S., Gurrola, E. M., Agram, P., Cohen, J., Lavalle, M., and Riel, B. V. (2016). "The InSAR Scientific Computing Environment 3.0: a Flexible Framework for InSAR Operational and User-Led Science Processing," in *AGU Fall Meeting Abstracts* (United States: AGU), 4901–4904.

Ahmady-Birgani, H., McQueen, K. G., Moeinaddini, M., and Naseri, H. (2017). Sand Dune Encroachment and Desertification Processes of the Rigboland Sand Sea, Central Iran. *Sci. Rep.* 7, 1523. doi:10.1038/s41598-017-01796-z

Ali, E., and Xu, W. (2019). "An Optical Image Time Series Inversion Method and Application to Long Term Sand Dune Movements in the Sinai Peninsula," in *European Geosciences Union* (Vienna, Austria: EGU).

Ali, E., Xu, W., and Ding, X. (2020). Improved Optical Image Matching Time Series Inversion Approach for Monitoring Dune Migration in North Sinai Sand Sea: Algorithm Procedure, Application, and Validation. *ISPRS J. Photogrammetry Remote Sensing* 164, 106–124. doi:10.1016/j.isprsjprs.2020.04.004

Ali, E., Xu, W., and Ding, X. (2021). Spatiotemporal Variability of Dune Velocities and Corresponding Uncertainties, Detected from Optical Image Matching in the North Sinai Sand Sea, Egypt. *Remote Sensing* 13, 3694. doi:10.3390/rs13183694

Altena, B., Scambos, T., Fahnestock, M., and Kääb, A. (2019). Extracting Recent Short-Term Glacier Velocity Evolution Over Southern Alaska and the Yukon From a Large Collection of Landsat Data. *Cryosph* 13, 795–814. doi:10.5194/tc-13-795-2019

Avouac, J.-P., Ayoub, F., Wei, S., Ampuero, J.-P., Meng, L., Leprince, S., et al. (2014). The 2013, Mw 7.7 Balochistan Earthquake, Energetic Strike-Slip Reactivation of a Thrust Fault. *Earth Planet. Sci. Lett.* 391, 128–134. doi:10.1016/j.epsl.2014.01.036

Ayoub, F., Leprince, S., and Avouac, J.-P. (2009). Co-registration and Correlation of Aerial Photographs for Ground Deformation Measurements. *ISPRS J. Photogrammetry Remote Sensing* 64, 551–560. doi:10.1016/j.isprsjprs.2009.03.005

Baird, T., Bristow, C., and Vermeesch, P. (2019). Measuring Sand Dune Migration Rates with COSI-Corr and Landsat: Opportunities and Challenges. *Remote Sensing* 11, 2423. doi:10.3390/rs11202423

Beaud, F., Aati, S., Delaney, I., Adhikari, S., and Avouac, J.-P. (2021). Generalized Sliding Law Applied to the Surge Dynamics of Shisper Glacier and Constrained by Timeseries Correlation of Optical Satellite Images. *Cryosph. Discuss.* 4, 1–35. doi:10.5194/tc-2021-96

Berardino, P., Fornaro, G., Lanari, R., and Sansosti, E. (2002). A New Algorithm for Surface Deformation Monitoring Based on Small Baseline Differential SAR Interferograms. *IEEE Trans. Geosci. Remote Sensing* 40, 2375–2383. doi:10.1109/TGRS.2002.803792

Bontemps, N., Lacroix, P., and Doin, M.-P. (2018). Inversion of Deformation fields Time-Series from Optical Images, and Application to the Long Term Kinematics of Slow-Moving Landslides in Peru. *Remote Sensing Environ.* 210, 144–158. doi:10.1016/j.rse.2018.02.023

Bristow, C. S., Drake, N., and Armitage, S. (2009). Deflation in the Dustiest Place on Earth: The Bodélé Depression, Chad. *Geomorphology* 105, 50–58. doi:10.1016/j.geomorph.2007.12.014

Bui, L. K., Featherstone, W. E., and Filmer, M. S. (2020). Disruptive Influences of Residual Noise, Network Configuration and Data Gaps on InSAR-Derived Land Motion Rates Using the SBAS Technique. *Remote Sens. Environ.* 247, 111941. doi:10.1016/j.rse.2020.111941

Chappell, A., and Bristow, C. (2005). Dustiest Place on Earth. *Nature* 434, 1.

Chen, K., Avouac, J.-P., Aati, S., Milliner, C., Zheng, F., and Shi, C. (2020). Cascading and Pulse-like Ruptures during the 2019 Ridgecrest Earthquakes in the Eastern California Shear Zone. *Nat. Commun.* 11, 3–10. doi:10.1038/s41467-019-13750-w

Das, S., and Sharma, M. C. (2021). Glacier Surface Velocities in the Jankar Chhu Watershed, Western Himalaya, India: Study Using Landsat Time Series Data (1992-2020). *Remote Sensing Appl. Soc. Environ.* 24, 100615. doi:10.1016/j.rsase.2021.100615

Dee, D. P., Uppala, S. M., Simmons, A. J., Berrisford, P., Poli, P., Kobayashi, S., et al. (2011). The ERA-Interim Reanalysis: Configuration and Performance of the Data Assimilation System. *Q.J.R. Meteorol. Soc.* 137, 553–597. doi:10.1002/qj.828

Dille, A., Kervyn, F., Handwerger, A. L., d'Oreye, N., Derauw, D., Mugaruka Bibentyo, T., et al. (2021). When Image Correlation Is Needed: Unravelling the Complex Dynamics of a Slow-Moving Landslide in the Tropics with Dense Radar and Optical Time Series. *Remote Sensing Environ.* 258, 112402. doi:10.1016/j.rse.2021.112402

Ding, C., Feng, G., Liao, M., Tao, P., Zhang, L., and Xu, Q. (2021). Displacement History and Potential Triggering Factors of Baige Landslides, China Revealed by Optical Imagery Time Series. *Remote Sensing Environ.* 254, 112253. doi:10.1016/j.rse.2020.112253

Ding, C., Feng, G., Liao, M., and Zhang, L. (2020a). Change Detection, Risk Assessment and Mass Balance of mobile Dune fields Near Dunhuang Oasis with Optical Imagery and Global Terrain Datasets. *Int. J. Digital Earth* 13, 1604–1623. doi:10.1080/17538947.2020.1767222

Ding, C., Zhang, L., Liao, M., Feng, G., Dong, J., Ao, M., et al. (2020b). Quantifying the Spatio-Temporal Patterns of Dune Migration Near Minqin Oasis in Northwestern China with Time Series of Landsat-8 and Sentinel-2 Observations. *Remote Sensing Environ.* 236, 111498. doi:10.1016/j.rse.2019.111498

El-magd, I. A., Hassan, O., and Arafat, S. (2013). Quantification of Sand Dune Movements in the South Western Part of Egypt, Using Remotely Sensed Data and GIS. *Jgis* 05, 498–508. doi:10.4236/jgis.2013.55047

Fahnestock, M., Scambos, T., Moon, T., Gardner, A., Haran, T., and Klinger, M. (2016). Rapid Large-Area Mapping of Ice Flow Using Landsat 8. *Remote Sensing Environ.* 185, 84–94. doi:10.1016/j.rse.2015.11.023

Farr, T. G., Rosen, P. A., Caro, E., Crippen, R., Duren, R., Hensley, S., et al. (2007). The Shuttle Radar Topography Mission. *Rev. Geophys.* 45, RG2004. doi:10.1029/2005RG000183

Fattahi, H., Agram, P., and Simons, M. (2017). A Network-Based Enhanced Spectral Diversity Approach for TOPS Time-Series Analysis. *IEEE Trans. Geosci. Remote Sensing* 55, 777–786. doi:10.1109/TGRS.2016.2614925

Friedl, P., Seehaus, T., and Braun, M. (2021). Global Time Series and Temporal Mosaics of Glacier Surface Velocities, Derived From Sentinel-1 Data. *Earth Syst. Sci. Data Discuss.*, 1–33. doi:10.5194/essd-2021-106

Gaber, A., Abdelkareem, M., Abdelsadek, I., Koch, M., and El-Baz, F. (2018). Using InSAR Coherence for Investigating the Interplay of Fluvial and Aeolian Features in Arid Lands: Implications for Groundwater Potential in Egypt. *Remote Sens.* 10, 1–18. doi:10.3390/rs10060832

Ghadiry, M., Shalaby, A., and Koch, B. (2012). A New GIS-Based Model for Automated Extraction of Sand Dune Encroachment Case Study: Dakhla Oases, Western Desert of Egypt. *Egypt. J. Remote Sensing Space Sci.* 15, 53–65. doi:10.1016/j.ejrs.2012.04.001

Goudie, A. S., and Middleton, N. J. (2001). Saharan Dust Storms: Nature and Consequences. *Earth-Science Rev.* 56, 179–204. doi:10.1016/S0012-8252(01)00067-8

Hamdan, M. A., Refaat, A. A., and Abdel Wahed, M. (2016). Morphologic Characteristics and Migration Rate Assessment of Barchan Dunes in the Southeastern Western Desert of Egypt. *Geomorphology* 257, 57–74. doi:10.1016/j.geomorph.2015.12.026

Hereher, M. E. (2010). Sand Movement Patterns in the Western Desert of Egypt: an Environmental Concern. *Environ. Earth Sci.* 59, 1119–1127. doi:10.1007/s12665-009-0102-9

Hermas, E., Alharbi, O., Alqurashi, A., Niang, A. J., Al-Ghamdi, K., Al-Mutiry, M., et al. (2019). Characterisation of Sand Accumulations in Wadi Fatmah and Wadi Ash Shumaysi, KSA, Using Multi-Source Remote Sensing Imagery. *Remote Sensing* 11, 2824. doi:10.3390/rs11232824

Hermas, E., Leprince, S., and El-Magd, I. A. (2012). Retrieving Sand Dune Movements Using Sub-pixel Correlation of Multi-Temporal Optical Remote Sensing Imagery, Northwest Sinai Peninsula, Egypt. *Remote Sensing Environ.* 121, 51–60. doi:10.1016/j.rse.2012.01.002

Hudson-Edwards, K. A., Bristow, C. S., Cibin, G., Mason, G., and Peacock, C. L. (2014). Solid-Phase Phosphorus Speciation in Saharan Bodélé Depression Dusts and Source Sediments. *Chem. Geol.* 384, 16–26. doi:10.1016/j.chemgeo.2014.06.014

Hugenholtz, C. H., Levin, N., Barchyn, T. E., and Baddock, M. C. (2012). Remote Sensing and Spatial Analysis of Aeolian Sand Dunes: A Review and Outlook. *Earth-Science Rev.* 111, 319–334. doi:10.1016/j.earscirev.2011.11.006

Jawak, S. D., Kumar, S., Luis, A. J., Bartanwala, M., Tummala, S., and Pandey, A. C. (2018). Evaluation of Geospatial Tools for Generating Accurate Glacier Velocity Maps from Optical Remote Sensing Data. *Proceedings* 2, 341. doi:10.3390/ecrs-2-05154

Kääb, A., Winsvold, S., Altena, B., Nuth, C., Nagler, T., and Wuite, J. (2016). Glacier Remote Sensing Using Sentinel-2. Part I: Radiometric and Geometric Performance, and Application to Ice Velocity. *Remote Sensing* 8, 598. doi:10.3390/rs8070598

Koren, I., Kaufman, Y. J., Washington, R., Todd, M. C., Rudich, Y., Martins, J. V., et al. (2006). The Bodélé Depression: a Single Spot in the Sahara that Provides Most of the mineral Dust to the Amazon forest. *Environ. Res. Lett.* 1, 014005. doi:10.1088/1748-9326/1/1/014005

Lacroix, P., Araujo, G., Hollingsworth, J., and Taipe, E. (2019). Self-Entrainment Motion of a Slow-Moving Landslide Inferred from Landsat-8 Time Series. *J. Geophys. Res. Earth Surf.* 124, 1201–1216. doi:10.1029/2018JF004920

Lacroix, P., Bièvre, G., Pathier, E., Kniess, U., and Jongmans, D. (2018). Use of Sentinel-2 Images for the Detection of Precursory Motions before Landslide Failures. *Remote Sensing Environ.* 215, 507–516. doi:10.1016/j.rse.2018.03.042

Leprince, S., Barbot, S., Ayoub, F., and Avouac, J.-P. (2007). Automatic and Precise Orthorectification, Coregistration, and Subpixel Correlation of Satellite Images, Application to Ground Deformation Measurements. *IEEE Trans. Geosci. Remote Sensing* 45, 1529–1558. doi:10.1109/TGRS.2006.888937

Manzoni, M., Molinari, M. E., and Monti-Guarnieri, A. (2021). Multitemporal inSAR Coherence Analysis and Methods for Sand Mitigation. *Remote Sensing* 13, 1362. doi:10.3390/rs13071362

Middleton, N. J., and Sternberg, T. (2013). Climate Hazards in Drylands: A Review. *Earth-Science Rev.* 126, 48–57. doi:10.1016/j.earscirev.2013.07.008

Mouginot, J., Rignot, E., Scheuchl, B., and Millan, R. (2017). Comprehensive Annual Ice Sheet Velocity Mapping Using Landsat-8, Sentinel-1, and RADARSAT-2 Data. *Remote Sensing* 9, 364. doi:10.3390/rs9040364

Necsoiu, M., Leprince, S., Hooper, D. M., Dinwiddie, C. L., McGinnis, R. N., and Walter, G. R. (2009). Monitoring Migration Rates of an Active Subarctic Dune Field Using Optical Imagery. *Remote Sensing Environ.* 113, 2441–2447. doi:10.1016/j.rse.2009.07.004

Reinisch, E. C., Cardiff, M., and Feigl, K. L. (2017). Graph Theory for Analyzing Pair-wise Data: Application to Geophysical Model Parameters Estimated from Interferometric Synthetic Aperture Radar Data at Okmok Volcano, Alaska. *J. Geod.* 91, 9–24. doi:10.1007/s00190-016-0934-5

Rouyet, L., Lauknes, T. R., Christiansen, H. H., Strand, S. M., and Larsen, Y. (2019). Seasonal Dynamics of a Permafrost Landscape, Adventdalen, Svalbard, Investigated by InSAR. *Remote Sensing Environ.* 231, 111236. doi:10.1016/j.rse.2019.111236

Roy, D. P., Wulder, M. A., Loveland, T. R., Woodcook, C. E., Anderson, M. C., Helder, D., et al. (2014). Landsat-8: Science and Product Vision for Terrestrial Global Change Research. *Remote Sensing Environ.* 145, 154–172. doi:10.1016/j.rse.2014.02.001

Rozenstein, O., Siegal, Z., Blumberg, D. G., and Adamowski, J. (2016). Investigating the Backscatter Contrast Anomaly in Synthetic Aperture Radar (SAR) Imagery of the Dunes along the Israel-Egypt Border. *Int. J. Appl. Earth Observation Geoinformation* 46, 13–21. doi:10.1016/j.jag.2015.11.008

Sam, L., Gahlot, N., and Prusty, B. G. (2015). Estimation of Dune Celerity and Sand Flux in Part of West Rajasthan, Gadra Area of the Thar Desert Using Temporal Remote Sensing Data. *Arab. J. Geosci.* 8, 295–306. doi:10.1007/s12517-013-1219-4

Samsonov, S., Tiampo, K., and Cassotto, R. (2020). Measuring the State and Temporal Evolution of Glaciers Using SAR-Derived 3D Time Series of Glacier Surface Flow. *Cryosph. Discuss.* 34, 1–21. doi:10.5194/tc-2020-257

Scheidt, S. P., and Lancaster, N. (2013). The Application of COSI-Corr to Determine Dune System Dynamics in the Southern Namib Desert Using ASTER Data. *Earth Surf. Process. Landforms* 38, 1004–1019. doi:10.1002/esp.3383

Scherler, D., Leprince, S., and Strecker, M. (2008). Glacier-surface Velocities in alpine Terrain from Optical Satellite Imagery-Accuracy Improvement and Quality Assessment. *Remote Sensing Environ.* 112, 3806–3819. doi:10.1016/j.rse.2008.05.018

Shukla, A., and Garg, P. K. (2020). Spatio-temporal Trends in the Surface Ice Velocities of the central Himalayan Glaciers, India. *Glob. Planet. Change* 190, 103187. doi:10.1016/j.gloplacha.2020.103187

Stravalaci, M., Davi, F., Parente, R., Gobbi, M., Bottazzi, B., Mantovani, A., et al. (2020). Control of Complement Activation by the Long Pentraxin PTX3: Implications in Age-Related Macular Degeneration. *Front. Pharmacol.* 11, 591908. doi:10.3389/fphar.2020.591908

Stumpf, A., Malet, J.-P., Allemand, P., and Ulrich, P. (2014). Surface Reconstruction and Landslide Displacement Measurements with Pléiades Satellite Images. *ISPRS J. Photogrammetry Remote Sensing* 95, 1–12. doi:10.1016/j.isprsjprs.2014.05.008

Stumpf, A., Malet, J.-P., Puissant, A., and Travelletti, J. (2016). "Monitoring of Earth Surface Motion and Geomorphologic Processes by Optical Image Correlation," in *Land Surface Remote Sensing* (Elsevier), 147–190. doi:10.1016/B978-1-78548-105-5.50005-0

Touzi, R., Lopes, A., Bruniquel, J., and Vachon, P. W. (1999). Coherence Estimation for SAR Imagery. *IEEE Trans. Geosci. Remote Sensing* 37, 135–149. doi:10.1109/36.739146

Ullmann, T., Sauerbrey, J., Hoffmeister, D., May, S. M., Baumhauer, R., and Bubenzer, O. (2019). Assessing Spatiotemporal Variations of Sentinel-1 InSAR Coherence at Different Time Scales Over the Atacama Desert (Chile) Between 2015 and 2018. *Remote Sens.* 11, 2960. doi:10.3390/rs11242960

Usai, S. (2003). A Least Squares Database Approach for SAR Interferometric Data. *IEEE Trans. Geosci. Remote Sensing* 41, 753–760. doi:10.1109/TGRS.2003.810675

Vermeesch, P., and Drake, N. (2008). Remotely Sensed Dune Celerity and Sand Flux Measurements of the World's Fastest Barchans (Bodélé, Chad). *Geophys. Res. Lett.* 35, 1–6. doi:10.1029/2008GL035921

Vermeesch, P., and Leprince, S. (2012). A 45-year Time Series of Dune Mobility Indicating Constant Windiness over the central Sahara. *Geophys. Res. Lett.* 39, a–n. doi:10.1029/2012GL052592

Warren, A., Chappell, A., Todd, M. C., Bristow, C., Drake, N., Engelstaedter, S., et al. (2007). Dust-raising in the Dustiest Place on Earth. *Geomorphology* 92, 25–37. doi:10.1016/j.geomorph.2007.02.007

Washington, R., Todd, M. C., Lizcano, G., Tegen, I., Flamant, C., Koren, I., et al. (2006). Links between Topography, Wind, Deflation, Lakes and Dust: The Case of the Bodélé Depression, Chad. *Geophys. Res. Lett.* 33, 1–4. doi:10.1029/2006GL025827

Wegmüller, U., Strozzi, T., Farr, T., and Werner, C. L. (2000). Arid Land Surface Characterization With Repeat-Pass SAR Interferometry. *IEEE Trans. Geosci. Remote Sens.* 38, 776–781. doi:10.1109/36.842006

Yang, W., Fang, J., and Liu-Zeng, J. (2021). Landslide-lake Outburst Floods Accelerate Downstream Slope Slippage. *Earth Surf. Dyn. Discuss.* 2021, 1–19.

Conflict of Interest: The authors declare that the research was conducted in the absence of any commercial or financial relationships that could be construed as a potential conflict of interest.

Publisher's Note: All claims expressed in this article are solely those of the authors and do not necessarily represent those of their affiliated organizations, or those of the publisher, the editors and the reviewers. Any product that may be evaluated in this article, or claim that may be made by its manufacturer, is not guaranteed or endorsed by the publisher.

frontiers in Environmental Science

ORIGINAL RESEARCH
published: 24 February 2022
doi: 10.3389/fenvs.2022.799946

DS-InSAR Based Long-Term Deformation Pattern Analysis in the Mining Region With an Improved Phase Optimization Algorithm

Yuling Du[1,2], *Shiyong Yan*[1,2]*, *Feng Zhao*[1,2], *Ding Chen*[1,2] *and Haolei Zhang*[1,2]

[1]MNR Key Laboratory of Land Environment and Disaster Monitoring, China University of Mining and Technology, Xuzhou, China, [2]School of Environment Science and Spatial Informatics, China University of Mining and Technology, Xuzhou, China

The environment management and land utilization of the abandoned mining region is critically dependent on precise monitoring and comprehensive understanding of mining subsidence. In order to overcome the shortcomings of the traditional distributed target phase optimization method in the space continuity constraints of adjacent pixels, an improved phase optimization algorithm was proposed, which combines region growing and time series interferometric synthetic aperture radar with distributed scatterers (DS-InSAR). By using 17 L-band and 51 C-band SAR images, the characteristics of temporal and spatial distribution in Peibei mining area of Xuzhou, China, were obtained during the period from 2007 to 2011 and the period from 2017 to 2020. With the long-term monitoring, the evolution of deformation in the mining area was carried out. The modified phase optimization technique has proven its ability in the density of measurement points and the influence of noise in space, which is promising for the detection of large gradient deformation and the accurate analysis of surface deformation in mining areas. The study has been concentrated toward detecting continuous subsidence in the mining region. Coal mines in operation are usually accompanied by unstable ground, and the uplift or second subsidence has sometime occurred in the closed mine region. Conclusively, the presented methodology is practically feasible for long-term deformation pattern analysis in coal-exhausted mining areas.

Keywords: DS-InSAR technology, phase optimization algorithm, surface deformation, comparative analysis, mining region

OPEN ACCESS

Edited by:
Chen Yu,
Newcastle University, United Kingdom

Reviewed by:
Ruya Xiao,
Hohai University, China
Bingqian Chen,
Jiangsu Normal University, China

***Correspondence:**
Shiyong Yan
yanshiyong@cumt.edu.cn

Specialty section:
This article was submitted to Environmental Informatics and Remote Sensing, a section of the journal Frontiers in Environmental Science

Received: *22 October 2021*
Accepted: *18 January 2022*
Published: *24 February 2022*

Citation:
Du Y, Yan S, Zhao F, Chen D and Zhang H (2022) DS-InSAR Based Long-Term Deformation Pattern Analysis in the Mining Region With an Improved Phase Optimization Algorithm. Front. Environ. Sci. 10:799946. doi: 10.3389/fenvs.2022.799946

INTRODUCTION

The exploitation and utilization of coal resources play an important role in global economic development. Peibei mining area, the largest coal production base in East China, has made outstanding contributions to rapid growth of China's economy in the 20th century. However, many environmental problems and geological disasters caused by the high-intensity and large-scale mining bring severe damage to our lives and property (Yang et al., 2017; Dong et al., 2021). Due to the strong hysteresis property of surface subsidence caused by underground mining, the phenomenon of ground subsidence has occurred even in some coal mines that are idled or closed (Zhao, 2003). Meanwhile, the transformation and development of the old mining areas are also hindered by surface unstable phenomena (Mi et al., 2017). Moreover, with the impact of coal capacity reduction and

urban economic development on land demand, the land in mining regions needs to be urgently reutilized for urban construction and development. Therefore, it is of great significance to carry out the long-term monitoring and comparative analysis of surface deformation in the mining area.

The time series interferometric synthetic aperture radar (TS-InSAR) technology with advantages in efficient monitoring of large scale is less affected by spatiotemporal incoherence (Wang et al., 2013); thus, it has been widely used for accurate measurements of surface deformation, such as cities (Chen et al., 2013), landslides (Ao et al., 2019), glacier movements (Lin et al., 2019), and mining areas (Li et al., 2016; Lu et al., 2016). Nevertheless, the capability of the traditional InSAR time series approach is often limited by the scarcity of artificial targets and the coverage of sparse vegetation, which increases the difficulty in obtaining deformation features because of the lack of monitoring points (Zhang et al., 2015), especially in the mining region. The SqueeSAR technology has been widely used in recent years, whereby the concepts of distributed scatterer (DS) and persistent scatterer (PS) are first being introduced, respectively (Ferretti et al., 2011; Cao et al., 2015; Du et al., 2018). In order to make full use of distributed targets, a number of phase optimization methods are proposed. Phase optimization determines the phase quality and affects the measurement point's density, the application of which provides a practical value about the monitoring of surface deformation in mining areas. The maximum likelihood estimation (MLE) (Monti and Stefano, 2008) method assumes that only subscatterers with a single dominant scattering mechanism exist in the resolution cell, and a probability density function model of the distributed target is required. The eigenvalue decomposition (EVD) (Gianfranco et al., 2014) method is used in covariance matrix or coherent matrix, while the corresponding eigenvector with the largest eigenvalue can be considered to be the reconstructed interferometric signals. The eigen-decomposition-based maximum-likelihood-estimator of interferometric phase (EMI) (Ansari et al., 2018) was proposed, which increases the model complexity of conventional phase estimators to improve the estimation performance. Although the aforementioned methods adopt different strategies to reduce the decorrelation of DS pixels, however, the phase continuity between adjacent pixels is not carefully considered, and noise on the deformation monitoring results is neglected in the process of optimizing the DS phase value.

According to the aforementioned issues, an improved phase optimization method combining region-growing algorithm and T-EVD is presented. The subsidence area of Peibei mining area in Xuzhou city, Jiangsu Province, China, is selected as the research area, and the ALOS/PALSAR data and Sentinel-1 data covering the study area are processed by this method. Then, deformation in the mining area from February 2007 to March 2011 and January 2017 to December 2020 is obtained, and the evolution of surface subsidence in the mining area in the last 10 years is shown. The final results obtained from the synthesized analysis are promising to identify potential risks and develop further techniques to mitigate the impact of mining areas on environment and resources.

STUDY AREA AND DATASETS

Peibei mining region, located in the northwest of Xuzhou city, Jiangsu Province, is one of the important mine resource basements in the eastern part of China. There are main eight mines in the study area as indicated in **Figure 1** (Dong et al., 2014), including Yaoqiao (YQ) Coal Mine, Longdong (LD) Coal Mine, Xuzhuang (XZ) Coal Mine, Kongzhuang (KZ) Coal Mine, Zhangshuanglou (ZSL) Coal Mine, Sanhejian (SHJ) Coal Mine, Peicheng (PC) Coal Mine, and Longgu (LG) Coal Mine. The surface classification information is obtained from the global land cover dataset (Gong et al., 2019). Meanwhile, due to the rapid development of coal-mining operations, a lot of land resources were occupied, resulting in the reduction of traditional land resources. In recent years, with the closure of some coal mines such as SHJ coal mine and PC coal mine, the land was restored by the government, which increased the area of wetlands and waters (Zhang et al., 2016). The study region, with the temperate monsoon climate, is featured with very longer summer and winter. Generally, there is a large seasonal difference in land cover, especially in the region with bare land and sparse vegetation; most of them yield the similar characteristics such as the typical distributed targets, which would easily lead to incoherence in traditional SAR interferometry processing.

In this article, the surface deformation in Peibei mining area is measured with both L-band ALOS/PALSAR during 2007.2–2011.3 and C-band Sentinel-1A during 2017.1–2020.12 in an ascending orbit. The used dataset description is shown in **Table 1**. In order to avoid the serious incoherence phenomenon caused by the relative long temporal baseline and the adverse effects on the extraction of surface subsidence in the mining region, two periods were separated for research during 2017–2020 because of the large changes caused by mining operation and different surface coverage. In addition, the SRTM DEM with 30 m resolution provided by USGS is used for geocoding and topographic phase compensation for SAR data.

MATERIALS AND METHODS

For monitoring and identifying the land subsidence of mining areas, the improved DS-InSAR technology with combination of PS points and DS points was proposed and used in this article, which fully optimizes the phase quality with both region growing and T-EVD. The main data processing flowchart is shown as follows:

1) Statistically homogenous pixels (SHPs) identification and selection:

In order to process homogenous patches without the impact of PS targets, SHP should be identified from the beginning. Several statistical techniques have been used to detect SHP, such as the Kolmogorov–Smirnov test, Anderson–Darling test, generalized likelihood ratio test, fast SHP selection (Jiang et al., 2014), and two-sample *t*-test. All these methods are based on evaluating the similarity of the amplitude distribution of two image pixels. Hypothesis testing is used to analyze the similarity of sample

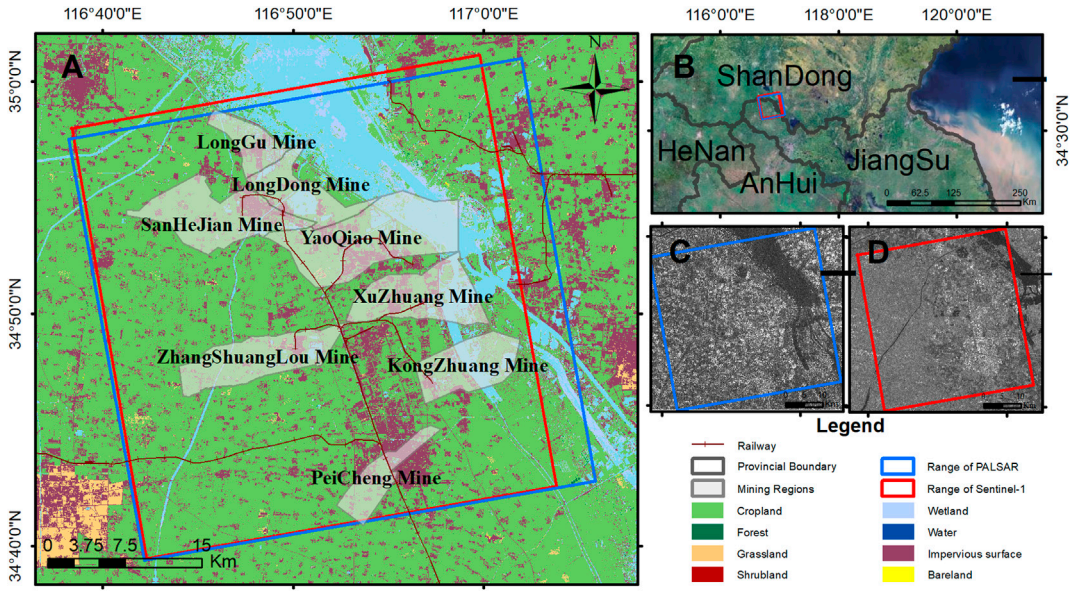

FIGURE 1 | Geographical elements and land cover in the Peibei mining area, Xuzhou city, China. **(A)** Land cover mapping based on Sentinel-2. **(B)** Google Maps. **(C)** Itensity map of ALOS/PALSAR. **(D)** Itensity map of Sentinel-1.

TABLE 1 | Basic information of data.

Type	ALOS/PALSAR	Sentinel-1A	Sentinel-1A
Band	L-band	C-band	C-band
Scenes	17	26	25
Period	2007.2–2011.3	2017.1–2018.12	2019.1–2020.12
Master image	20090225	20171210	20200105
Pass direction	Ascending	Ascending	Ascending
Polarization	HH	VV	VV

distribution characteristics, and adaptive multi-view processing is performed on points with the same statistical attributes as the target pixel. In this article, the two-sample *t*-test is used because of the high efficiency in identification and selection of SHPs (Shamshiri et al., 2018). The two-sample t-test is defined as:

$$H_0: \mu_1 = \mu_2 \qquad H_1: \mu_1 \neq \mu_2 ,$$

where μ_1 and $\mu 2$ are the averaged amplitudes of the populations. The corresponding test statistic for the same sample sizes is as follows:

$$t = \frac{\bar{A}(P_1) - \bar{A}(P_2)}{\sqrt{\frac{\sigma^2(P_1)+\sigma^2(P_2)}{N}}},$$

where N is the sample size, $\bar{A}(P_1)$ and $\bar{A}(P_2)$ are the sample means, and $\sigma^2(P_1)$ and $\sigma^2(P_2)$ are the sample variances. A pixel-centered estimation window (15 × 15) is defined for each pixel to select the homogenous statistical population. Then, the predefined significance level (0.05) is used to test the difference between the amplitude vector of the central pixel and that of all pixels within the window. Finally, pixels with the number of SHPs greater than 20 are used as distributed scatterers candidates (DSCs) (Ferretti et al., 2011; Jiang and Guarnieri, 2020), and the coherent values of SHPs below 20 are preserved as PS candidate points.

2) Optimized phase estimation:

The phase optimization plays an important key role in exploring the available DSC points. First, the coherent matrix is calculated based on the SHPs, and then the spatiotemporal phase optimization of DSC points is realized by using both the T-EVD and region growing method in this article, and the general data process flowchart is shown in **Figure 2**. With the help of combined filtering operation, the phase-optimized interferometry fringes have been largely improved, especially in low-coherent areas, where negative influence of incoherence noise has been effectively suppressed along with the DSC exploitation.

Assuming a homogenous point set Ω containing N_{SHPs} pixels with similar scattering properties, the coherence matrix for the homogenous point set can be expressed as:

$$\hat{T} = E[yy^T] = \frac{1}{N_{SHPs}} \sum_{y \in \Omega} yy^H,$$

where $y = [y_1\ y_2\ y_3 \ldots y_N]^T$ is the normalized complex observation of N SAR images. In addition, the interferometric phase and the estimated coherence value can be described in the coherence matrix,

$$\hat{T} = \begin{vmatrix} 1 & |\tilde{\gamma}_{1,2}|\exp(j\varphi_{1,2}) & \cdots & |\tilde{\gamma}_{1,N}|\exp(j\varphi_{1,N}) \\ |\tilde{\gamma}_{2,1}|\exp(j\varphi_{2,1}) & 1 & \cdots & |\tilde{\gamma}_{2,N}|\exp(j\varphi_{2,N}) \\ \vdots & \vdots & \ddots & \vdots \\ |\tilde{\gamma}_{N,1}|\exp(j\varphi_{N,1}) & |\tilde{\gamma}_{N,2}|\exp(j\varphi_{N,2}) & \cdots & 1 \end{vmatrix} = |\hat{T}| \circ \Phi,$$

where Φ represents the N×N matrix with the interferometric phases $\phi_{m,n}$ between the mth image and the nth image, $|\hat{T}|$

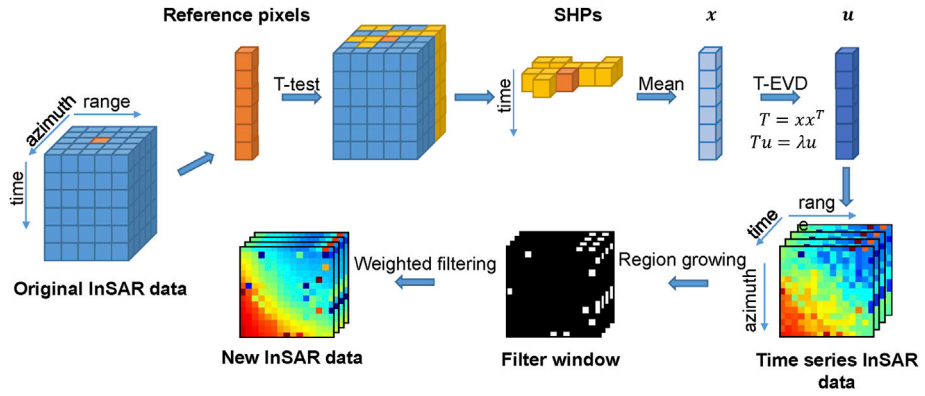

FIGURE 2 | Schematic diagram of phase optimization.

represents the N×N matrix with the estimation of the corresponding coherence $\tilde{\gamma}$, and ∘ is the Hadamard product.

Generally, there are multiple and undermined scattering mechanisms interacting with each other existing in the resolution unit, especially for the middle resolution SAR imagery. According to the characteristic of the coherence matrix, it can be written in the form of

$$\hat{T} = U\Lambda U^H = \sum_{i=1}^{N} \lambda_I \cdot u_i \cdot u_i^H,$$

where $\Lambda = [\lambda_1, \lambda_2, \ldots, \lambda_N]$ is a N×N diagonal matrix with the eigenvalues, and $U = [u_1, u_2, \ldots, u_N]$ corresponds to orthogonal eigenvectors. Generally, the eigenvalue $\boldsymbol{\lambda_i}$ is defined as the weight of different scattering mechanisms in the resolution unit. In reality, the number of dominant scattering mechanisms is unknown. Thus, the phase component of eigenvector $\boldsymbol{u_1}$, corresponding to the maximum eigenvalue $\boldsymbol{\lambda_1}$ in coherency matrix $\hat{\boldsymbol{T}}$, could be generally used as an optimized estimation of the interferometric phase (Cloude and Pottier, 1997). The corresponding phase optimization function is as follows:

$$\hat{\phi}_{T-EVD} = \arg\max_{\varphi} \left\{ \mathrm{Re}\left(\sum_{m=1}^{N} \sum_{n>m}^{N} \left[|u_1||u_1|^T \right]_{mn} |\hat{T}|_{mn} \exp\left(j\left(\varphi_{mn} - \left(\hat{\phi}_{om} - \hat{\phi}_{on} \right) \right) \right) \right) \right\},$$

where $\hat{\phi}_{om}$ and $\hat{\phi}_{on}$– represent the optimized phases of DS with a single master image, and ϕ_{mn} represents the adaptive multi-view interferometric phase.

However, in the process of constructing the coherence matrix by the T-EVD method, the spatial information between homogenous pixel points is lost, and the optimized phase value space is not sufficiently constrained. In order to eliminate acnode noise existing in the EVD-based optimized phase and further improve the quality of interferometry, the spatial filter window, generated by the region growing method relaying on the difference of interferometric phase differences, is used to realize the re-optimization of the DSC phase. Thus, the method fully utilizes the pixel connectivity in interferograms (Wang and Qin, 2009).

In this research, the center pixel of the preset window (15 × 15) is used as the initial seed point to select the pixels whose phase value could represent primary phase characteristics in the window. In order to preserve the fringe characteristics of the InSAR image, the phase difference threshold T of adjacent pixels is set at the growth criterion R, which is used to determine whether the selected window should continue to extend. Then, the final filter template can generate windows with various directions and sizes according to actual surface scenes, which would not be restricted by a regular shape.

$$R: \left| G(i,j) - G(i,j)_{(8)} \right| \le T,$$

where $G(i,j)$ represents the pixel phase value of point coordinates $(\boldsymbol{i},\boldsymbol{j})$, and point $(\boldsymbol{i},\boldsymbol{j})_{(8)}$ represents the pixel point within the eight neighborhoods of point $(\boldsymbol{i},\boldsymbol{j})$. In addition, the higher the coherence is, the more reliable the phase is. Therefore, the weighted average of the interferometric phase in the filter window is calculated, and the coherence is the weight ρ_i:

$$\bar{G}(i,j) = \frac{G_1\rho_1 + G_2\rho_2 + \cdots + G_k\rho_k}{n},$$

where $\boldsymbol{n}$ is the sum of the weights $\rho_i (i = 1, 2, \cdots, k)$, and $G_i (i = 1, 2, \cdots, k)$ represents the phase values of the corresponding points within the window.

3) Phase optimization quality evaluation:

In order to measure the extent of temporal incoherence on DSC and evaluate the quality of phase optimization, the temporal coherence γ_{DS} (Ferretti et al., 2011) is defined to make a fitting and comparison of the original phase and the optimized phase. The original interferometric phase would be replaced with the optimized phase value once the γ_{DS} is greater than the threshold, and then the corresponding SHP point is used as the DS point:

$$\gamma_{DS} = \frac{1}{N(N-1)} \sum_{n-1m \ne n}^{N} \sum^{N} \exp^{j\left(\phi_{mn} - \left(\hat{\phi}_{om} - \hat{\phi}_{on}\right)\right)}.$$

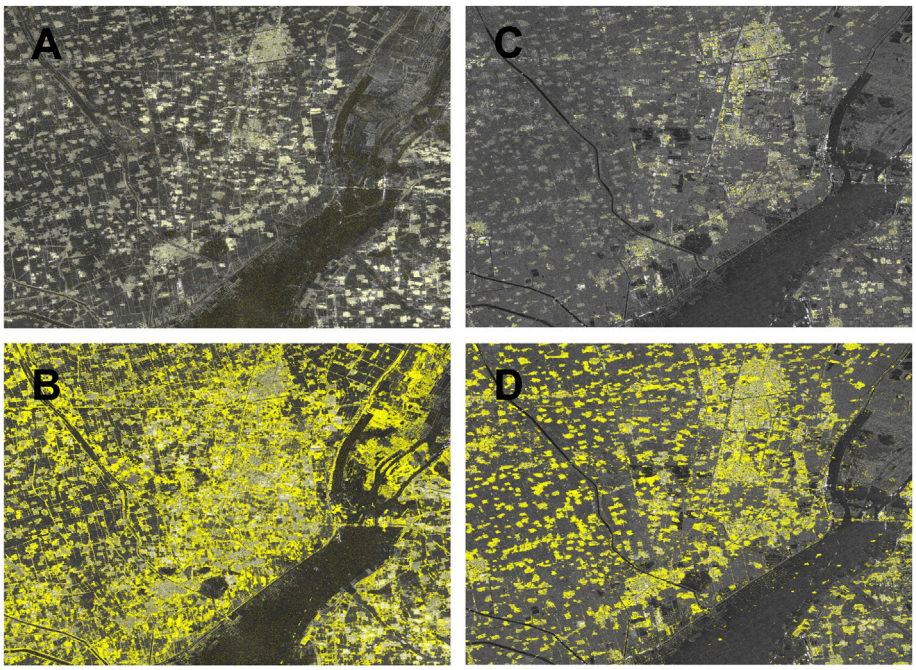

FIGURE 3 | Distribution of high coherent targets in the study area. **(A)** PSs distribution of ALOS/PALSAR. **(B)** Combination of PSs and DSs distribution of ALOS/PALSAR. **(C)** PSs distribution of Sentinel-1. **(D)** Combination of PSs and DSs distribution of Sentinel-1.

4) Observation targets fusion:

The selection of high-quality point targets is mainly based on high signal–noise ratio and stable phase scattering characteristics. The amplitude dispersion method and phase stability analysis are used in StaMPS to select high-quality point targets. Based on the amplitude deviation index, pixels greater than 0.4 are used as the initial permanent scatterer candidate (PSC). In addition, phase stability analysis is then further performed on each candidate point by calculating the temporal coherence coefficient to determine whether the PS points could satisfy the selection requirements (**Figures 3A,C**). Finally, along with the selected DS points in aforementioned (3), the observation targets could be obtained by the combination of PSs and DSs (**Figures 3B,D**).

5) TS-InSAR analysis:

Following this, analysis is performed in accordance with the traditional TS-InSAR data processing flow, such as residual terrain correction, phase unwrapping, and both GACOS-based (Yu et al., 2017) and temporal–spatial statistical-based atmospheric estimation and correction.

The entire process is shown in **Figure 4**.

RESULTS AND ANALYSIS

Spatial Distribution of Deformation Area

Compared with the results of traditional persistent scatterer interferometric synthetic aperture radar (PS-InSAR) (**Figure 5**), the negative influence of noise obtained from the deformation field was reduced, and then smooth results and clear boundary information of the subsidence region could be obtained by using the presented method. The improved method can increase the number of points by an average of about 14.3 times by comparing with the traditional PS-InSAR technology. By comparing the average coherence corresponding to the interferogram with the longest spatial baseline, it can be seen that the average coherence can be improved by about 1.63 times with the improved method.(**Table 2**). The subsidence results in Peibei mining area were calculated by the proposed method in this article along with both ALOS/PALSAR and Sentinel-1A data covering three periods from February 2007 to March 2011 (**Figure 6A**), January 2017 to December 2018 (**Figure 6B**), and January 2019 to December 2020 (**Figure 6C**). It can be seen that the spatial distribution and density of the measurement points were uniform during each period. But, the subsidence distribution was obviously yielded in Peibei mining area.

The comparison of monitoring results during different periods showed that there are different types in spatial evolution of deformation, such as expansion, offset, and reduction, and corresponding magnitude of subsidence also significantly varied. It can be seen that there were five obvious subsidence areas from 2007 to 2011 (**Figure 6A**). Among them, the region with the largest subsidence existed in ZSL Coal Mine, which included three obvious subsidence centers with the deformation ranging between −120 and −60 mm/year. In SHJ Coal Mine, there were two obvious subsidence areas with the deformation varying in the range between −90 and −70 mm/year. There are three

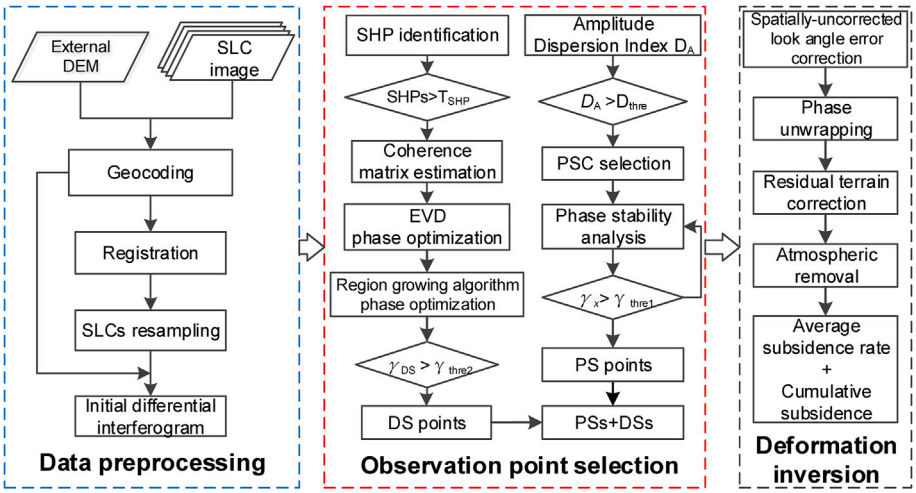

FIGURE 4 | Workflow of the study.

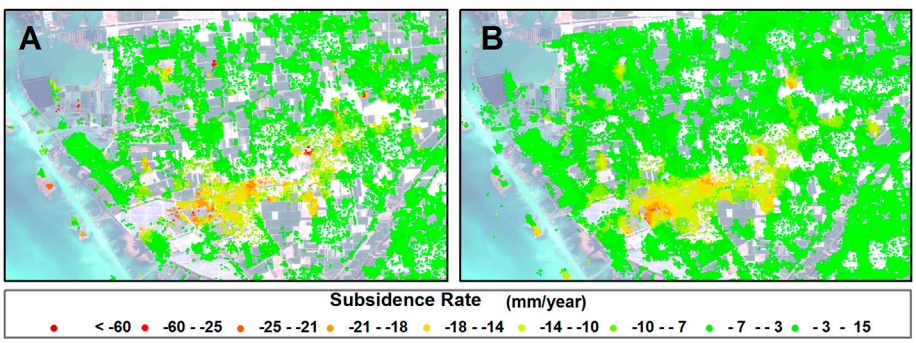

FIGURE 5 | Subsidence result obtained by DS-InSAR. **(A)** Tradition method. **(B)** Improved method.

TABLE 2 | Comparison of points and coherence of different methods.

Year/method	PS-InSAR (point number/coherence)	DS-InSAR (point number/coherence)	
		EVD method	Improved method
2007–2011	92954/0.26	975749/0.46	1697846/0.50
2017–2018	95390/0.25	781364/0.35	1553943/0.37
2019–2020	99264/0.24	568148/0.35	825417/0.36

obvious subsidence regions in PC Coal Mine with the subsidence value ranging from −60 to −30 mm/year, which were mainly located in the south of Peixian county and the west of Peicheng town. In addition, YQ Coal Mine had a comparatively small subsidence area as well.

During the period from 2017 to 2018 (**Figure 6B**), the surface was stable in LG and LD coal mines. However, there was localized subsidence in PC, KZ, and XZ coal mines, and large-scale subsidence in ZSL, YQ, and SHJ coal mines. Then, the surface of PC Coal Mine became stable between 2019 and 2020 (**Figure 6C**), and the deformation of the SHJ, YQ, ZSL, XZ, and KZ coal mines were significantly reduced at the same period.

In conclusion, the subsidence is mainly concentrated in ZSL, YQ, SHJ, and PC coal mines, where both the different deformation evolution patterns and serious large-scale subsidence could be observed.

Subsidence in Typical Mining Areas

In order to understand the evolution of goafs in different mining areas during different temporal periods, ZSL, YQ, SHJ, and PC coal mines were selected for further comparative analysis

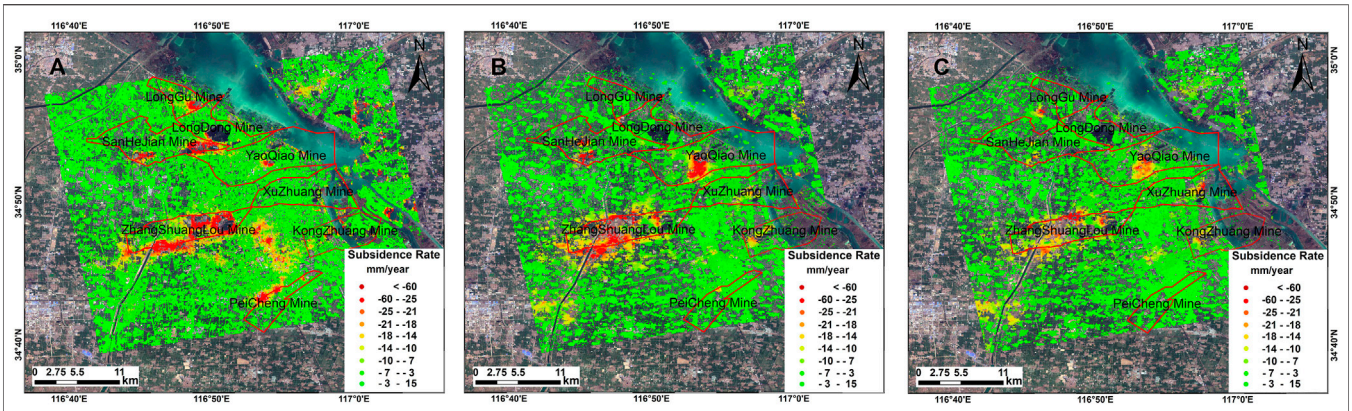

FIGURE 6 | Average deformation rate map of Peibei mining area. **(A)** 2007–2011. **(B)** 2017–2018. **(C)** 2019–2020.

TABLE 3 | Comparison of subsidence distribution during different periods in typical mining regions.

Name /Year	Zhangshuanglou Coal Mine	Yaoqiao Coal Mine	Sanhejian Coal Mine	Peicheng Coal Mine
Sentinel-2				
2007-2011				
2017				
2018				
2019				
2020				

Subsidence Rate (mm/year)

< -60 • -60 - -25 • -25 - -21 • -21 - -18 • -18 - -14 • -14 - -10 • -10 - -7 • -7 - -3 • -3 - 15

(**Table 3**). In addition, the cumulative subsidence curve of different research periods for the same location in each mine is given in **Figure 7**, which would be benefit for analyzing the evolution characteristics of each coal mine.

As shown in **Table 3**, three obvious subsidence centers could be found in ZSL Coal Mine during different monitoring periods. As data display, the mining was put into production in December 1986 and still in progress now. However, compared with the deformation results from 2007 to 2011, the results obtained from 2017 to 2020 yield that the subsidence center of R1 and R2 expanded gradually and then finally merged into a new large one, which was mainly caused by continuous underground mining operations in ZSL coal mines during corresponding periods. However, with the increase of the exploiting depth and the expansion of the mining range, the subsidence region was spatially expanding along with a comparative decrease in the magnitude of subsidence. Also, the subsidence occurred in R3, a excavate coal subside seeper area located in ZSL Coal Mine, was

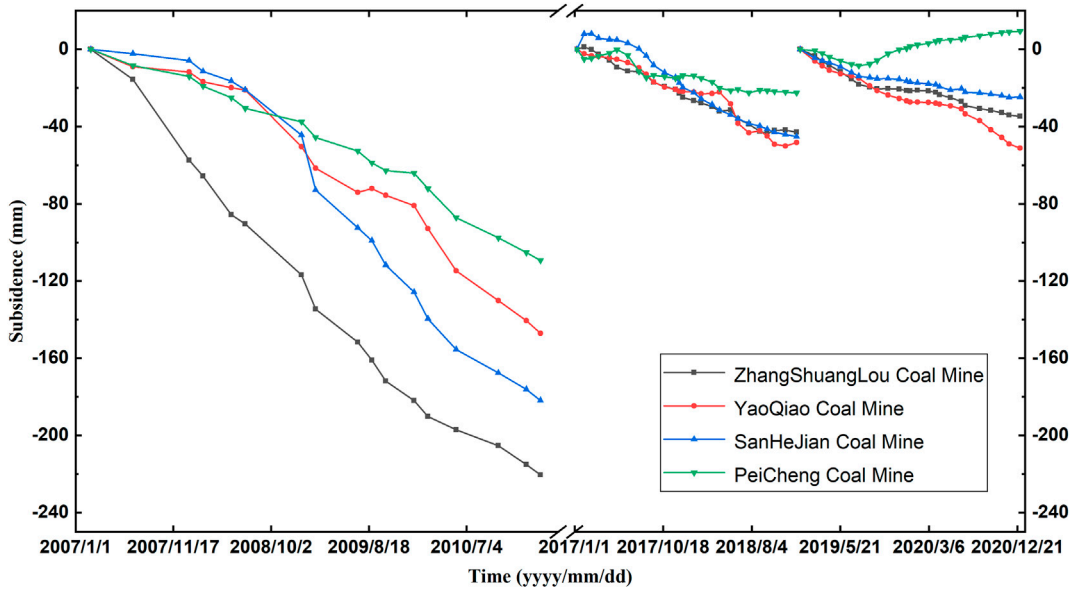

FIGURE 7 | Accumulated ground deformation of the coal mines deformation center in different time periods. The corresponding locations are indicated in **Table 3** with white stars.

reduced significantly, and the surrounding region became stable except for the northwest corner. It could be seen that the gradually stable surface status has mainly been brought by the goaf overburden strata compaction since the closure of the mining operation.

YQ Coal Mine was put into production in December 1976. Comparing the subsidence process in YQ Coal Mine (**Table 3**), the surface subsidence was evolved from partial to extensive during the period before 2020, while there was an expansion and offset to the southwest and the northeast in spatial evolution of deformation. Apparently, the subsidence range and magnitude of the mining area was reduced in 2020, but the operation is still in progress. Therefore, regular monitoring of YQ Coal Mine is needed to be carried out for improving the efficiency in development and utilization of the abandoned goaf. Furthermore, with the time series deformation obtained in the YQ mining region (**Figure 7**), it can be seen that the slope of the deformation curve during different monitoring periods had varied from steep to gentle, which is closely related to the comprehensive of multiple coal seams and the increase in exploiting depth.

The subsidence occurred in R2, located on the east side of SHJ Coal Mine, has slowed down significantly. The production of the mine started in August 1988. Due to the long-term natural compaction of the overburden in the goaf, the surface has been basically stable in recent years. However, there are still two obvious subsidence centers observed during the period from 2017 to 2019 on the south side of the SHJ Coal Mine, which corresponds to the actual mining activity at last. In addition, the surface subsidence caused by underground mining exhibits temporal hysteresis in SHL Coal Mine closed in May 2019, so that the surface instability is only often presented in the initial stage after mine closures. Furthermore, it can be seen that the region of R1 in SHJ coal mines tended to stabilize in 2020.

PC Coal Mine, which is nearest to the city, was established in 1971 and shut down earlier in August 2013. Compared with the three obvious subsidence centers during the period from 2007 to 2011, the surface subsidence of the goaf was weakened significantly in 2017, and there was no obvious subsidence during period from 2018 to 2020, which could be considered a stable goaf. The accumulated subsidence observed in **Figure 7** was mainly caused by the combination of overburden strata gravity and groundwater level. With the further compaction of the overburden layer and the rise of the groundwater level, the surface gradually stabilized with slight uplift.

In order to verify the results of this method, the subsidence rate of PS points obtained by the traditional PS-InSAR method was used as a reference value; the nearest point within 20 m was selected from the result of DS-InSAR as the point with the same name. In addition, correlation estimation is given on the points with the same name observed in both PS and DS-InSAR technology (**Figure 8**), and the corresponding difference could indicate the capability of the presented DS-InSAR in the mining region. There are 16,742 points with the same name in PALSAR data, and the average and standard deviation of those are 1.64 mm/year and 2.51 mm/year (**Figures 8A,C**), respectively. For Sentinel-1 data, a total of 12,404 points were selected with the average and standard deviation of 1.22 mm/year and 2.04 mm/year (**Figures 8B,C**), respectively. Moreover, referring to the ellipse shown in **Figure 8B**, large gradient subsidence in the mining region is much easier to be detected by the DS-InSAR method because of the improving accuracy of phase unwrapping along with the increasing observed points and interferometric phase optimization. The aforementioned analysis shows that the

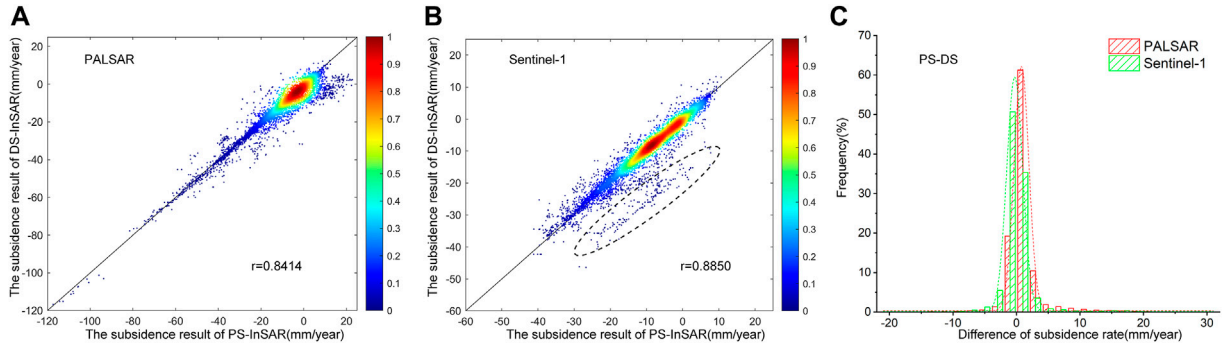

FIGURE 8 | Correlation diagram of the deformation rate and statistical histogram of the deformation rate difference of the same name between different monitoring results.

results of corresponding points obtained from the traditional PS-InSAR and DS-InSAR are congruous, which proves the consistency between the two monitoring methods.

DISCUSSION

Compared with the conventional PS-InSAR results, the DS-InSAR approach could largely increase the number and spatial distribution density of measurement points by fully exploiting PS and DS points in the mining region. According to the reduction of the distance between measurement points along with the increasing point density, the phase unwrapping operation could be partly improved by overcoming large distance between two adjacent points. Therefore, the deformation characteristics could be apparently reflected in the results obtained by the present method. In addition, the phase optimization processing of the DS target, filtering with both region growing and T-EVD algorithm, could improve the quality of the extracted deformation by weakening the negative influence of noise. The results obtained with DS-InSAR could provide a decision-making support for the land recycling in the abandoned mining region, which proved adaptability of the presented approach in surface activities analysis of the mining region.

Satellite imagery with C- and L-bands covering different temporal periods was only used for comparison and evolution analysis of subsidence in different mining stages owing to the limitation of data acquisition capability. In order to study the evolution of surface deformation fully in mining areas, it is necessary to use more abundant data to carry out a more in-depth and deliberate monitoring and analysis in the future. The comparison results of different periods indicate that the surface deformation during mining operation is mainly caused by underground mining activities. However, both the subsidence center and the deformation range changed along with the variation of the exploiting depth and actual mining. In recent years, some inefficiency and obsolete coal mines were closed gradually, and the phenomenon of surface rebound had been observed with DS-InSAR in some closed mines. In addition, affected by many factors such as the stability of the reserved coal pillars, the compaction of the stratum soil, and the restoration, small fluctuations in surface deformation would be occurring in the mining region. Along with an increase in the closure time, the surface of the mining region gradually became stabilized. In addition, the uplift or secondary subsidence of the surface might occur in some mining areas due to the changes in the groundwater level and the geological environment. Therefore, carrying out a comparative analysis of surface subsidence in Peibei mining area in the past 10 years is of great significance for understanding the surface deformation, stability evaluation, and development and utilization of mining areas.

CONCLUSION

An improved processing approach was proposed by combining region growing algorithm and T-EVD for phase optimization of distributed scatterers in this article. The number of measurement points could be largely increased, and the negative influence of noise can be weakened, which significantly improved the accuracy and reliability of PS-InSAR technology in surface deformation monitoring in the mining region. The long-term surface subsidence of mining areas in Peibei as well as 68 scenes of multi-source SAR data was calculated and analyzed with the proposed method in the past 10 years. Also, the deformation patterns over the mining region were comparatively studied during the different periods.

The results indicate that coal mines in operation were usually accompanied by the unstable surface with the subsidence. Obviously, with the deepening of the exploiting depth and the expansion of mining, the range of subsidence was expanding, while the mining intensity was decreasing. The surface gradually became stabilized along with the closure of the mining operation. However, the phenomenon of uplift or second subsidence could be sometime observed in the closed mine region, which might be brought by the variation of the groundwater level change along with the complex geological conditions. Thus, it is necessary to continuously carry out regular surface deformation monitoring in the mining area.

Generally, the proposed method is not only favorable for detecting the deformation position and influencing the range of goafs, but also promising for general survey of wide area and large gradient surface deformation and detection of subsidence in the mining area, which are vital for land restoration in mining areas and the prevention of related geological disasters.

DATA AVAILABILITY STATEMENT

The original contributions presented in the study are included in the article/Supplementary Material; further inquiries can be directed to the corresponding author.

AUTHOR CONTRIBUTIONS

YD designed and completed experiments and wrote the manuscript. SY contributed significantly to analysis and manuscript preparation. FZ contributed to the conception of the study. DC performed the experiment. HZ helped in performing the analysis with constructive discussions.

FUNDING

This work is funded by the National Natural Science Foundation of China (42004011), the Postgraduate Research and Practice Innovation Program of Jiangsu Province (KYCX21_2301), the Assistance Program for Future Outstanding Talents of China University of Mining and Technology (2021WLJCRCZL141), and the China Postdoctoral Science Foundation (2020M671646).

ACKNOWLEDGMENTS

The authors would like to express their gratitude to the European Space Agency (ESA) for providing the Sentinel-1 data and the Japan Aerospace Exploration Agency (JAXA) and ESA for providing the ALOS/PALSAR data.

REFERENCES

Ansari, H., De Zan, F., and Bamler, R. (2018). Efficient Phase Estimation for Interferogram Stacks. *IEEE Trans. Geosci. Remote Sensing* 56 (7), 4109–4125. doi:10.1109/tgrs.2018.2826045

Ao, M., Zhang, L., Shi, X., Liao, M., and Dong, J. (2019). Measurement of the Three-Dimensional Surface Deformation of the Jiaju Landslide Using a Surface-Parallel Flow Model. *Remote Sensing Lett.* 10 (7-9), 776–785. doi:10.1080/2150704X.2019.1608601

Chen, J., Wu, J., Zhang, L., Zou, J., Liu, G., Zhang, R., et al. (2013). Deformation Trend Extraction Based on Multi-Temporal InSAR in Shanghai. *Remote Sensing* 5 (4), 1774–1786. doi:10.3390/rs5041774

Cloude, S. R., and Pottier, E. (1997). An Entropy Based Classification Scheme for Land Applications of Polarimetric SAR. *IEEE Trans. Geosci. Remote Sensing* 35 (1), 68–78. doi:10.1109/36.551935

Dong, L. L., Ding, Z. Y., Liu, Y. W., Mao, M. Q., and Wang, Y. T. (2014). Ecaluation of Land Ecological Quality in Coal-Based Cities: a Case Study of Peixian County, Jiangsu Province. *Scientific Technol. Manag. Land Resour.* 31 (005), 34–40. doi:10.3969/j.issn.10-09-4210.2014.05.006

Dong, L., Wang, C., Tang, Y., Tang, F., Zhang, H., Wang, J., et al. (2021). Time Series InSAR Three-Dimensional Displacement Inversion Model of Coal Mining Areas Based on Symmetrical Features of Mining Subsidence. *Remote Sensing* 13 (11), 2143. doi:10.3390/RS13112143

Du, Z., Ge, L., Ng, A. H.-M., Zhang, Q., and Alamdari, M. M. (2018). Assessment of the Accuracy Among the Common Persistent Scatterer and Distributed Scatterer Based on SqueeSAR Method. *IEEE Geosci. Remote Sensing Lett.* 15, 1877–1881. doi:10.1109/LGRS.2018.2864274

Ferretti, A., Fumagalli, A., Novali, F., Prati, C., Rocca, F., and Rucci, A. (2011). A New Algorithm for Processing Interferometric Data-Stacks: SqueeSAR. *IEEE Trans. Geosci. Remote Sensing* 49 (9), 3460–3470. doi:10.1109/tgrs.2011.2124465

Fornaro, G., Verde, S., Reale, D., and Pauciullo, A. (2015). CAESAR: An Approach Based on Covariance Matrix Decomposition to Improve Multibaseline-Multitemporal Interferometric SAR Processing. *IEEE Trans. Geosci. Remote Sensing* 53 (4), 2050–2065. doi:10.1109/TGRS.2014.2352853

Gong, P., Liu, H., Zhang, M., Li, C., Wang, J., Huang, H., et al. (2019). Stable Classification with Limited Sample: Transferring a 30-m Resolution Sample Set Collected in 2015 to Mapping 10-m Resolution Global Land Cover in 2017. *Sci. Bull.* 64 (06), 370–373. doi:10.1016/j.scib.2019.03.002

Guarnieri, A. M., and Tebaldini, S. (2008). On the Exploitation of Target Statistics for SAR Interferometry Applications. *IEEE Trans. Geosci. Remote Sensing* 46, 3436–3443. doi:10.1109/TGRS.2008.2001756

Jiang, M., Ding, X., Hanssen, R. F., Malhotra, R., and Chang, L. (2015). Fast Statistically Homogeneous Pixel Selection for Covariance Matrix Estimation for Multitemporal InSAR. *IEEE Trans. Geosci. Remote Sensing* 53 (3), 1213–1224. doi:10.1109/TGRS.2014.2336237

Jiang, M., and Guarnieri, A. M. (2020). Distributed Scatterer Interferometry with the Refinement of Spatiotemporal Coherence. *IEEE Trans. Geosci. Remote Sensing* 58 (6), 3977–3987. doi:10.1109/tgrs.2019.2960007

Li, M., Zhang, L., Liao, M., and Shi, X. (2016). Detection of Coal-Mining-Induced Subsidence and Mapping of the Resulting Deformation Using Time Series of ALOS-PALSAR Data. *Remote Sensing Lett.* 7 (7-9), 855–864. doi:10.1080/2150704X.2016.1193794

Liu, L., Jiang, L., Jiang, H., Wang, H., Ma, N., and Xu, H. (2019). Accelerated Glacier Mass Loss (2011-2016) over the Puruogangri Ice Field in the Inner Tibetan Plateau Revealed by Bistatic InSAR Measurements. *Remote Sensing Environ.* 231, 111241. doi:10.1016/j.rse.2019.111241

Lu, Y. Y., Ke, C. Q., Chen, D. L., and He, M. (2016). Applocation of PS-InSAR in Pei County Mining Area Surface Subsidence Monitoring. *Geospatial Inf.* 14 (5), 96–99. doi:10.3969/j.issn.16724623.20-16.05.030

Mi, J. X., Zhang, S. L., Hou, H. P., Guo, S. C., and Shang, Z. M. (2017). Study on the Impact of Cutting Coal Overcapacity on Ecological Environment in Mining Area. *China Mining Mag.* (08), 86–92.

Ning Cao, N., Hyongki Lee, H., and Hahn Chul Jung, H. C. (2015). Mathematical Framework for Phase-Triangulation Algorithms in Distributed-Scatterer Interferometry. *IEEE Geosci. Remote Sensing Lett.* 12 (9), 1838–1842. doi:10.1109/LGRS.2015.2430752

Shamshiri, R., Nahavandchi, H., Motagh, M., and Hooper, A. (2018). Efficient Ground Surface Displacement Monitoring Using Sentinel-1 Data: Integrating Distributed Scatterers (DS) Identified Using Two-Sample T-Test with Persistent Scatterers (PS). *Remote Sensing* 10 (5), 794. doi:10.3390/rs10050794

Wang, T., Gu, L. J., Zhan, M. H., Wen, Y. M., Hong, S. Y., and He, F. H. (2013). Research on Ground Subsidence Monitoring of Tianjin Area Based on D-InSAR Technique. *Sci. Surv. Mapp.* 38 (06), 49–51. doi:10.16251/j.cnki.1009-2307.2013.06.008

Wang, Y. M., and Qin, Y. Y. (2009). Target Detection in SAR Images Based on Region Growing. *J. Comp. Appl.* 29 (01), 45–46. doi:10.3724/sp.j.1087.2009.00045

Yang, Z., Li, Z., Zhu, J., Yi, H., Hu, J., and Feng, G. (2017). Deriving Dynamic Subsidence of Coal Mining Areas Using InSAR and Logistic Model. *Remote Sensing* 9 (2), 125. doi:10.3390/rs9020125

Yu, C., Li, Z., and Penna, N. T. (2018). Interferometric Synthetic Aperture Radar Atmospheric Correction Using a GPS-Based Iterative Tropospheric Decomposition Model. *Remote Sensing Environ.* 204, 109–121. doi:10.1016/j.rse.2017.10.038

Zhang, Y., Wang, Y. J., and Yan, S. Y. (2016). Ground Subsidence Detection of Peibei Mining Area Based on Stacking InSAR Technology. *Coal Tech.* 35 (07), 102–105. doi:10.13301/j.cnki.ct.2016.07.042

Zhang, Z. J., Wang, C., Tang, Y. X., Fu, Q. Y., and Zhang, H. (2015). Subsidence Monitoring in Coal Area Using Time-Series InSAR Combining Persistent Scatterers and Distributed Scatterers. *Int. J. Appl. Earth Observations Geoinformation* 39 (99), 1–11. doi:10.1109/JSTARS.2019.294672910.1016/j.jag.2015.02.007

Zhao, S. Y. (2003). Destory of Ecological Environment Caused by Coal Over-mined and its Control Measures. *Shaanxi Coal* 1, 25–27. doi:10.3969/j.issn.1671-749X.2004.01.012

Conflict of Interest: The authors declare that the research was conducted in the absence of any commercial or financial relationships that could be construed as a potential conflict of interest.

frontiers in Ecology and Evolution

ORIGINAL RESEARCH
published: 08 March 2022
doi: 10.3389/fevo.2022.840464

A Lightweight Anchor-Free Subsidence Basin Detection Model With Adaptive Sample Assignment in Interferometric Synthetic Aperture Radar Interferogram

Yaran Yu, Zhiyong Wang, Zhenjin Li, Kaile Ye, Hao Li and Zihao Wang*

College of Geodesy and Geomatics, Shandong University of Science and Technology, Qingdao, China

The excessive exploitation of coal resources has caused serious land subsidence, which seriously threatens the lives of the residents and the ecological environment in coal mining areas. Therefore, it is of great significance to precisely monitor and analyze the land subsidence in the mining area. To automatically detect the subsidence basins in the mining area from the interferometric synthetic aperture radar (InSAR) interferograms with wide swath, a lightweight model for detecting the subsidence basins with an anchor-free and adaptive sample assignment based on the YOLO V5 network, named Light YOLO-Basin model, is proposed in this paper. First, the depth and width scaling of the convolution layers and the depthwise separable convolution are used to make the model lightweight to reduce the memory consumption of the CSPDarknet53 backbone network. Furthermore, the anchor-free detection box encoding method is used to deal with the inapplicability of the anchor box parameters, and an optimal transport assignment (OTA) adaptive sample assignment method is introduced to solve the difficulty of optimizing the model caused by abandoning the anchor box. To verify the accuracy and reliability of the proposed model, we acquired 62 Sentinel-1A images over Jining and Huaibei coalfield (China) for the training model and experimental verification. In contrast with the original YOLO V5 model, the mean average precision (mAP) value of the Light YOLO-Basin model increases from 45.92 to 55.12%. The lightweight modules of the model sped up the calculation with the one billion floating-point operations (GFLOPs) from 32.81 to 10.07 and reduced the parameters from 207.10 to 40.39 MB. The Light YOLO-Basin model proposed in this paper can effectively recognize and detect the subsidence basins in the mining areas from the InSAR interferograms.

Keywords: InSAR, subsidence basin detecting, YOLO V5, depthwise separable convolution, anchor-free, optimal transport assignment (OTA)

OPEN ACCESS

Edited by:
Yu Chen,
China University of Mining and Technology, China

Reviewed by:
Tao Li,
Ministry of Natural Resources of the People's Republic of China, China
Hongyu Liang,
Tongji University, China

****Correspondence:***
Zhiyong Wang
skd994177@sdust.edu.cn

Specialty section:
This article was submitted to Environmental Informatics and Remote Sensing, a section of the journal Frontiers in Ecology and Evolution

Received: *21 December 2021*
Accepted: *08 February 2022*
Published: *08 March 2022*

Citation:
Yu Y, Wang Z, Li Z, Ye K, Li H and Wang Z (2022) A Lightweight Anchor-Free Subsidence Basin Detection Model With Adaptive Sample Assignment in Interferometric Synthetic Aperture Radar Interferogram. Front. Ecol. Evol. 10:840464. doi: 10.3389/fevo.2022.840464

INTRODUCTION

Large-scale land subsidence resulting from coal mining has caused a series of ecological and environmental problems, including destroying farmlands, damaging buildings, and even inducing geological disasters (Wang et al., 2021a; Yuan et al., 2021). It threatens the lives and property of the local residents and restricts the economic sustainable development in mining areas (Fan et al., 2018;

Wang et al., 2020). Therefore, it is of great significance to continuously monitor and analyze the land subsidence in mining areas. Traditional geodetic surveying methods mainly include precise leveling, total station measurement, and global navigation satellite system (GNSS) (Fan et al., 2018). These methods have some limitations such as low spatial resolution, limited monitoring area, and low observation efficiency (Chen et al., 2015; Chen Y. et al., 2020; Shi M. Y. et al., 2021). Interferometric synthetic aperture radar (InSAR) technology has become a new means for monitoring the surface deformation in mining areas with the advantages of day/night data acquisition, all-weather imaging capability, and strong penetrability (Ng et al., 2017; Chen B. Q. et al., 2020; Wang et al., 2020).

Currently, the main research directions of InSAR technology for monitoring mine subsidence have evolved from acquiring single surface deformation information to three-dimensional deformation information or subsidence prediction based on deformation theory (Yang et al., 2017a,b, 2018a,b; Chen et al., 2021; Dong et al., 2021; Fan et al., 2021). Most of these works are targeted at one or more subsidence basins. However, the imaging mode of mainstream synthetic aperture radar (SAR) satellites, such as ALOS-2 and RadarSat-2, has an image width of more than 80 km. The image width of the interferometric wide swath (IW) mode of the Sentinel-1A satellite even reaches 250 km (Zheng et al., 2018). It is time-consuming and labor-intensive to search for subsidence basins with a radius of only a few hundred meters in a wide range of images. At present, there have been few studies on the automatic detection of subsidence basins from the InSAR interferogram. Hu et al. (2013) proposed a differential interferometric synthetic aperture radar (D-InSAR) based illegal-mining detection system, aiming to increase both accuracy and efficiency of underground-mining detection. The detection results are highly dependent on the quality of the phase unwrapping and subjective processing experience. By using the methods of D-InSAR technology, geographic information system (GIS), and mining subsidence, Xia et al. (2018) proposed a novel theory of effectively recognizing the subsidence basins. This method can detect subsidence basins without manual intervention. However, like the method proposed by Hu et al. (2013), the detection accuracy will also be affected by the quality of the phase unwrapping. Yang et al. (2018c) proposed a space-based method for recognizing the subsidence basins by relating the geometric parameters of subsidence basins to the InSAR derived line of sight deformation with the probability integral method (PIM). This method can determine the boundary of the subsidence basins, but it is not suitable for detecting subsidence basins in large-scale areas. Du et al. (2019) proposed a feature-point-based method for efficiently detecting subsidence basins. Du first used D-InSAR to monitor subsidence basins caused by mining and then used the PIM to determine the inflection and boundary points of the subsidence basins. Wang et al. (2021b) proposed a model for detecting the subsidence basin based on the histogram of oriented gradient features and support vector machine classifier. This method is limited by the feature detection operator and cannot effectively detect the subsidence basin with obscure edge features and too small scope. Bala et al. (2021) proposed a circlet transform method for detecting subsidence basins. This method reduces manual intervention, but the detection time is longer. Due to the long detection time, the above methods are difficult to carry out in a large-scale area. Furthermore, these methods conduct detection mostly based on the deformation gradient and the shape characteristics of the subsidence basin on the deformation map. The quality of the phase unwrapping is susceptible to atmospheric effects and noises, resulting in lower detection accuracy. Therefore, we propose a new method to detect subsidence basins from InSAR interferogram with large-scale areas.

After underground coal mining, a series of subsidence basins will appear in the mining area. Subsidence basins are scattered and large in number in the InSAR interferogram. It is difficult to identify these subsidence basins manually. The single subsidence basin of the mining area in the InSAR interferogram is approximately concentric circles or concentric ellipses, with a small scale and obvious edge features. Currently, the convolution neural network (CNN)-based objection detection method has been widely applied in many research fields (LeCun et al., 2015; Shi et al., 2020; Ren et al., 2021). For SAR images, it is mainly used to identify ships (Chang et al., 2019; Jiang et al., 2021; Wu Z. T. et al., 2021) and marine oil spills, etc. The CNN-based objection detection method can realize the automatic detection of subsidence basins. CNN-based objection detection frameworks primarily consist of three components, including backbone network, neck network, and detection head (Chen Q. S. et al., 2020; Fu K. et al., 2020). The backbone network mainly extracts the basic features of the input image, such as the ResNet (He et al., 2016; Xie et al., 2017) series and the DarkNet series. The main function of the neck network is to further strengthen the features extracted by the backbone network. For example, the feature pyramid network (FPN) combined features of different scales with lateral connections in a top-down manner to construct a series of scale-invariant feature maps, and multiple scale-dependent classifiers were trained on these feature pyramids (Lin et al., 2017a). The detection head network is responsible to predict and refine the bounding box, calculating the bounding box coordinates, confidence score, and classification score. According to the different head networks, object detection frameworks can be primarily divided into two categories. One is two-stage detectors that have high detection accuracy, mainly including R-CNN (Girshick et al., 2014), Fast-RCNN (Girshick, 2015), and Faster-RCNN (Ren et al., 2015), etc. Two-stage detectors first use a region proposal network to generate a sparse set of candidate object bounding boxes and then to extract features from each candidate bounding box for the following classification and bounding box regression tasks. The other is one-stage detectors that achieve high inference speed, mainly including the YOLO series (Redmon et al., 2016; Redmon and Farhadi, 2017, 2018; Bochkovskiy et al., 2020), SSD (Liu et al., 2016), and RetinaNet (Lin et al., 2017b), etc. One-stage detectors generate prediction boxes, confidence scores, and object classes concurrently.

At present, many CNN-based object detection methods have been proposed, most of which are designed to detect objects in natural images. However, there are two problems for recognizing the subsidence basins when directly using these methods. First,

due to the various object categories and shapes in natural images, big networks (such as DarkNet53, Resnet101) are often used as the backbone. However, the shape of the subsidence basin is relatively simple and the detection category is single, hence there is no need for a heavy network to detect subsidence basin. In addition, with the continuous development of SAR satellites, the image width is also increasing, then it will also increase the burden on the computer hardware when using heavy networks. Second, the anchor boxes obtained by clustering object structure in natural images are not suitable for the detection of subsidence basins.

The YOLO V5 model, a one-stage detector, has the advantages of high accuracy and fast speed. It has been widely used in various domains such as face recognition, text detection, and logo detection (Wu W. et al., 2021; Yan et al., 2021; Zhao et al., 2021). In order to automatically recognize and detect subsidence basins in large-scale mining areas with high accuracy, we proposed a lightweight detection model with adaptive sample assignment. The proposed model is based on the path aggregation network (PANet) of YOLO V5.

The main sections of this paper are organized as follows. In section "Data and Materials," the model proposed in this paper for detecting the subsidence basins from the InSAR interferogram is described. It mainly includes the depthwise separable convolution, anchor-free, and OTA adaptive sample assignment. The experimental results and quantitative evaluation are presented in Section "Method." Section "Results and Analysis" shows the discussions and the analysis of each module in the proposed model and the comparison results with the original YOLOV5 model. Finally, some valuable conclusions of this study are drawn in Section "Discussion."

DATA AND MATERIALS

Study Area

We selected the Jining and Huaibei mining areas in China as the study areas. The two mining areas are rich in coal resources and have a long mining history. There are many mines in the two areas with a complex distribution. The Jining mining area (115°50′–117°48′E, 34°58′–35°59′N) is located in the southwest of Shandong Province, China, with a cumulative proven coal reserve of nearly 15.1 billion tons. The Huaibei mining area (116°23′–117°12′E, 33°16′–34°14′N) is located in the north of the Huaihe River of Anhui Province, China, with a cumulative proven coal reserve of 13 billion tons. The locations of the study areas are shown in **Figure 1**.

Experimental Data

We used 24 Sentinel-1A images acquired from November 2017 to March 2020 over the Jining mining area and used 34 Sentinel-1A images acquired from November 2017 to March 2020 over the Huaibei mining area. The specific information of the partial interferometric pairs is shown in **Table 1**. The experimental Sentinel-1A data are interferometric wide swath imaging mode (Level 1 single-look complex images products) and in VV polarization with the 38.9° incidence angle. The revisit period of Sentinel-1A is 12 days and has a pixel size of about 2.33 × 13.91 m. Moreover, the shuttle radar topography mission digital elevation model (SRTM DEM) released by the National Aeronautics and Space Administration (NASA) was applied to remove both the flattening and terrain phases in D-InSAR data processing.

In order to obtain the differential interferograms of the two mining areas, we used the two-pass D-InSAR technology (Ou et al., 2018; Dai et al., 2020) to process these Sentinel-1A data. The procedures of D-InSAR technology mainly include interferogram generation, SAR simulation based on digital elevation model (DEM), differential processing between the real interferogram and the simulated interferogram, phase unwrapping, transformation from phase to deformation, and geocoding (Ilieva et al., 2019; Chen D. H. et al., 2020). **Figure 2** is a flow chart of the two-pass D-InSAR data processing. Interferograms with serious decoherence and large noise influence were excluded. We set the temporal baseline threshold of the interferogram to 36 days and the spatial baseline threshold to 200 m. The longest spatial baseline of the interferogram in this paper is 155.71 m. We obtained 62 interferograms in the Jining and Huaibei mining areas. The ratio of multi-looking is 1:5. The pixel size in the range direction is 18.54 m, and the pixel size in the azimuth direction is 13.89 m for the interferogram. The interferograms are too large to be used by the deep neural architecture, which generally accepts an image with a size of 416 × 416 as an input. Therefore, we segment the interferograms into smaller sub-images with a size of 416 × 416 according to the standard of the YOLO V5 model. The image data annotation software called "LabelImg" was used to draw the outer rectangular boxes of the subsidence basins on each sub-image, realizing the manual annotation of the border and labels of the ground truth box. The ground truth boxes were annotated according to the features of the subsidence basin. The subsidence basin on the InSAR interferogram is a series of approximately circular or elliptical interferometric fringes with a small scale and obvious edge features (Wang et al., 2021b). We have obtained a total of 1,160 sample images. In this study, 812 sample images were randomly selected from 1,160 images as the training samples; the remaining 30% were selected as the testing samples, which had a total of 348 images. The partial examples of the sample datasets are shown in **Figure 3**. In order to alleviate the over-fitting phenomenon during the training model incurred by limited sample datasets, rotation, translation, and flipping were used for data augmentation.

We selected two Sentinel-1A images acquired from December 2020 to January 2021 over the Jining mining area and two Sentinel-1A images acquired from January 2021 over the Huaibei mining area, constituting a total of two interferometric pairs to test the performance of the proposed model for detecting the subsidence basins from the interferograms. The parameters of the two interferometric pairs are listed in **Table 1**.

METHOD

To automatically detect the subsidence basins from the InSAR interferograms, a lightweight detection model with an adaptive

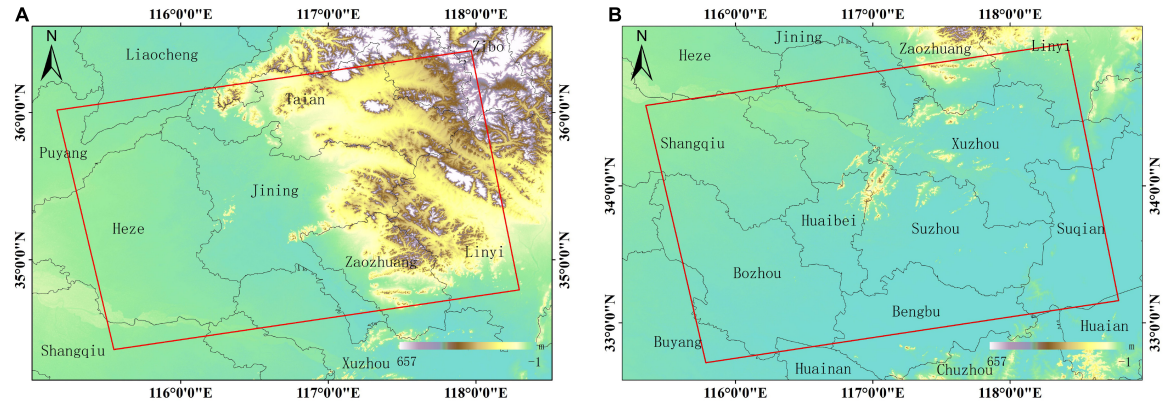

FIGURE 1 | Location of the study area. **(A)** The geographic location of the Jining mining area; **(B)** geographic location of the Huaibei mining area.

TABLE 1 | Sentinel-1A interferometric pairs for constructing the training/testing datasets and verifying the performance of the proposed model.

	Mining area	Master image	Slave image	Path	Frame	Temporal baseline/d	Perpendicular baseline/m
Datasets	Jining	28/11/2017*	22/12/2017	142	111	24	101.52
	Jining	11/11/2018	05/12/2018	142	111		22.76
	Jining	30/11/2019	24/12/2019	142	111		56.14
	Huaibei	10/12/2017	03/01/2018	142	106		81.53
	Huaibei	11/11/2018	05/12/2018	142	106		21.79
	Huaibei	18/11/2019	12/12/2019	142	106		115.70
Verifying data	Jining	30/12/2020	11/01/2021	142	111	12	25.10
	Huaibei	11/01/2021	23/01/2021	142	106		−22.02

**Date/month/year.*

sample assignment based on the YOLO V5 model was proposed. We first use the channel number scaling and depthwise separable convolution (Howard et al., 2017) to make the CSPDarknet53 network lightweight, and then model the prediction boxes as a width and height fit problem based on the center point like the anchor-free strategy in FCOS (Tian et al., 2019). In addition, we also introduced an OTA (Ge et al., 2021) that assigns positive and negative samples in an adaptive manner. The proposed model for detecting the subsidence basin was named the Light YOLO-Basin model. The network architecture of the Light YOLO-Basin model is shown in **Figure 4**.

YOLO V5 Network

The YOLO V5 model, as the basic framework for detecting the subsidence basins in this paper, mainly consists of three components: backbone network, neck network, and detection head. The backbone network is designed to extract the features of the subsidence basin, mainly composed of the CSPDarknet53 network and spatial pyramid pooling (SPP) (Purkait et al., 2017). The neck network adopts the path aggregation network instead of feature pyramid networks in YOLO V5. The detection head, as the final detection part of the model, is used to output the detection results of the subsidence basin. It utilizes the high-level semantic information outputted from the neck network to classify the category and regress the location of the objects.

The loss function of the YOLO V5 network mainly consists of three parts: bounding box regression loss, classification loss, and confidence loss (Shi P. F. et al., 2021). Since this paper only has the category of the subsidence basins, we only used confidence loss and bounding box regression loss, as shown in Formula (1).

$$Loss = L_{obj} + \lambda L_{DIoU} \tag{1}$$

where L_{obj} and L_{DIoU} mean confidence loss and bounding box regression loss, respectively. λ is the balancing factor and the value is 5 (Yan et al., 2021).

The Light YOLO-Basin model used the Focal Loss (Lin et al., 2017b) function confidence loss to alleviate the problem caused by the imbalanced number of hard and easy samples, as shown in Formula (2), in which the positive sample p with the high confidence is the easy sample and vice versa. Focal loss reduces the weight of easy samples so that the model can focus more on hard samples, ensuring that the contributions of all samples to model parameter updating are relatively balanced.

$$L_{obj} = \begin{cases} -\alpha\left(1-p\right)^{\gamma} log\left(p\right), y = 1 \\ -\left(1-\alpha\right) p^{\gamma} log\left(1-p\right), y = 0 \end{cases} \tag{2}$$

where $y = 1$ means positive samples and $y = 0$ means negative samples; the parameter α is used to balance the weight of the positive and negative samples during the model training; the parameter γ is used to balance the weight of the easy samples in the model; the parameter $p \in [0,1]$ is the model estimated probability for the confidence loss. The bounding box regression loss of the original YOLO V5 model adopts

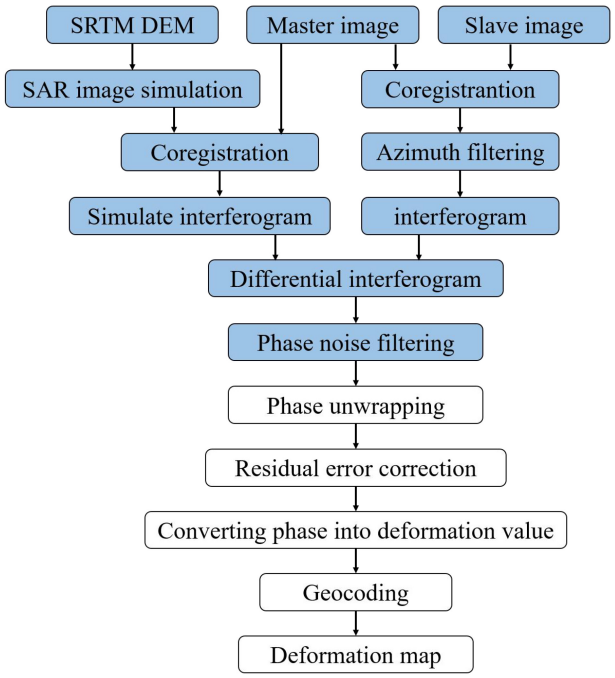

FIGURE 2 | The data processing flow of the two-pass differential interferometric synthetic aperture radar (D-InSAR). The blue part is the data processing implemented in the paper.

generalized intersection over union loss (GIoU Loss), but it only focuses on the overlapping areas and other non-overlapping areas, which ignores the impact of the bounding box on the IoU. The Light YOLO-Basin model used distance IoU loss (DIoU Loss) (Luo et al., 2020) as the bounding box regression loss. DIoU Loss is defined as Formula (3). It not only considers the distance of the center and the overlapping area between the ground truth box and prediction box, but also minimizes the center point distance.

$$\begin{aligned} IoU &= \frac{|A \cap B|}{|A \cup B|} \\ L_{DIoU} &= 1 - IoU + \frac{\rho^2(b, b^{gt})}{c^2} \end{aligned} \tag{3}$$

where A represents the area of the prediction box and B represents the area of the ground truth box; the parameter b and b^{gt} mean the center points of the prediction box A and ground truth box B, respectively; ρ^2 is the Euclidean Distance between b and b^{gt}; the parameter c represents the diagonal length of the smallest closed shape that includes the ground truth box A and the prediction box B.

The detection head module of the YOLO V5 model directly uses a single convolutional layer to calculate the classification loss, confidence loss, and bounding box regression loss. However, there is no classification loss in our study, the structure of the detection head requires to be changed. Some researches demonstrated that there is a conflict between classification and regression tasks (Song et al., 2020; Wu et al., 2020), so referencing the ideas of FCOS (Tian et al., 2019) and the literature (Song et al., 2020), the Light YOLO-Basin model used double-head as the detection head module. The Light YOLO-Basin model architecture after decoupling is shown in **Figure 4**. The double-head splits the output features of the subsidence basin into regression and confidence branches. The regression branch provides prediction box coordinates. Meanwhile, the confidence branch calculates the probability of positive samples.

The Lightweight of the CSPDarknet53 Network

At present, the YOLO V5 model has achieved great success in natural image datasets such as PASCAL VOC, ImageNet, and MS COCO. However, compared with objects in natural images, subsidence basins on the interferograms have more obvious edges and texture features and simpler shapes. Intuitively, the detection

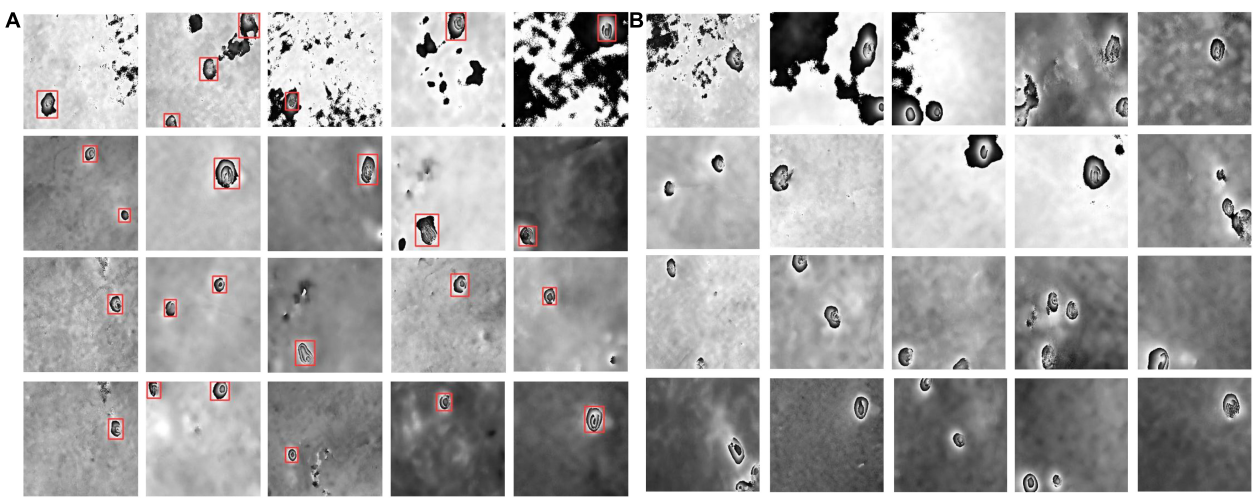

FIGURE 3 | Some examples of sample datasets. **(A)** Partial training data; **(B)** partial testing data. The red boxes represent the manual annotation of the ground truth box in panel **(A)**.

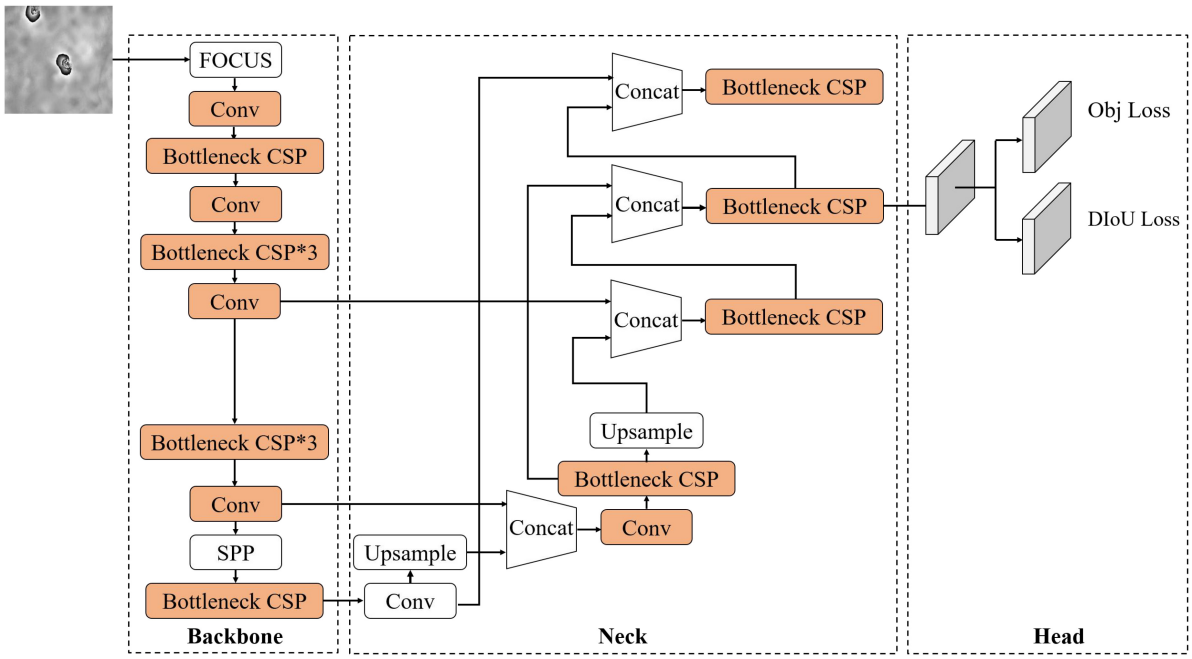

FIGURE 4 | Architecture of the Light YOLO-Basin network. SPP is spatial pyramid pooling. Upsample uses bilinear interpolation. Obj and distance intersection over union loss (DIoU) represent confidence loss and bounding box regression loss, respectively. In addition, convolution modules that can be lightweight are in orange.

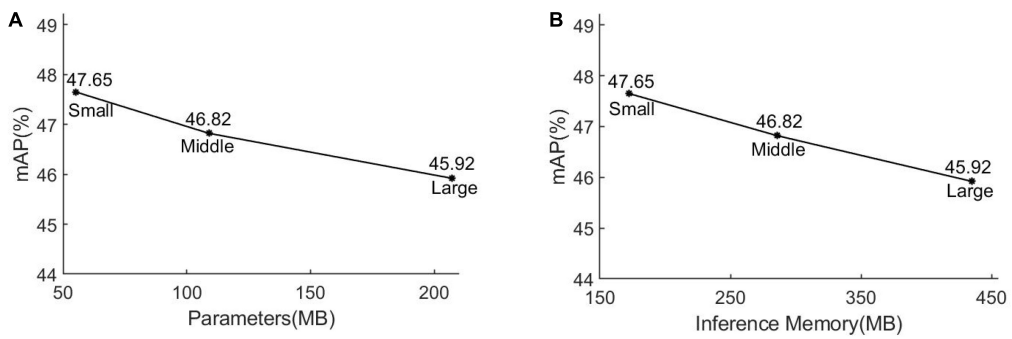

FIGURE 5 | Comparison results between the mean average precision (mAP) and parameters/inference memory of the three versions of YOLO V5 (Large, Middle, and Small) model. The abscissa in panel **(A)** represents the parameter amount of the model; the abscissa in panel **(B)** means the inference memory of the model for processing a 416 × 416 image. The numerical values of the mAP of the three versions of the YOLO V5 model.

of the subsidence basins on the interferogram from D-InSAR is simpler than the multi-category detection on natural images. This also leads to the conjecture of whether the heavy CSPDarknet53 network is necessary for detecting the subsidence basins. In order to verify that, we used the three versions of the YOLO V5 model (Large, Middle, and Small) to detect the subsidence basins from the interferograms. The variation of detection accuracy is shown in **Figure 5**. Experimental results show that as the number of parameters and computations of the model reduces, the detection accuracy of the model shows a rising trend instead of decreasing. The results demonstrate that the detection of subsidence basins does not require a heavy network. In addition, since the swath of SAR images is large wide, for example, the swath of Sentinel-1 is about 250 km, a lightweight model is used to detect subsidence basins from the interferograms to lighten the burden on the computer hardware. Therefore, we introduced depthwise separable convolutions to make the CSPDarknet53 network lightweight.

Compared with standard convolution, depthwise separable convolution generally sacrifices a small amount of detection accuracy to save the computations and parameters of the model. Depthwise separable convolution is a form of factorized convolutions that factorizes a standard convolution into a depthwise convolution and a pointwise convolution. Firstly, the depthwise convolution applies a single convolution to each channel feature map to extract feature information and keeps the number of feature maps unchanged. Secondly, the pointwise convolution applies multiple 1 × 1 convolutions to combine the

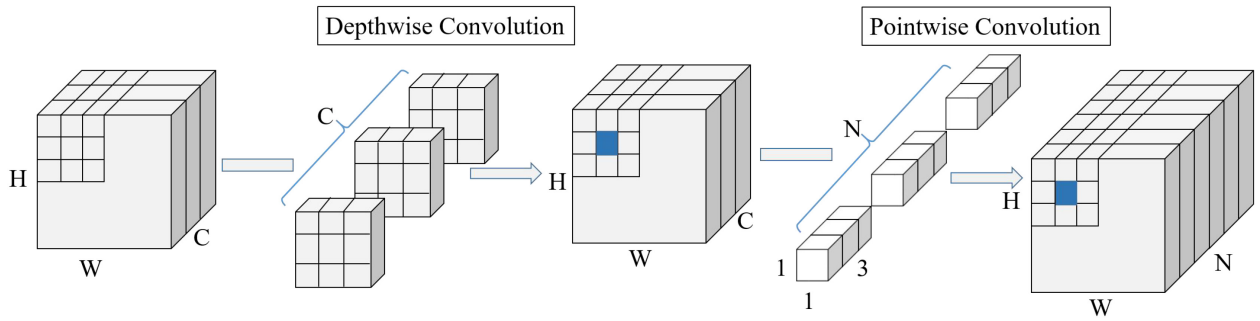

FIGURE 6 | The structure diagram of depthwise separable convolution. W and H are the spatial width and height of the feature map, respectively. C is the number of feature channels; N is the number of feature channels after depthwise separable convolution.

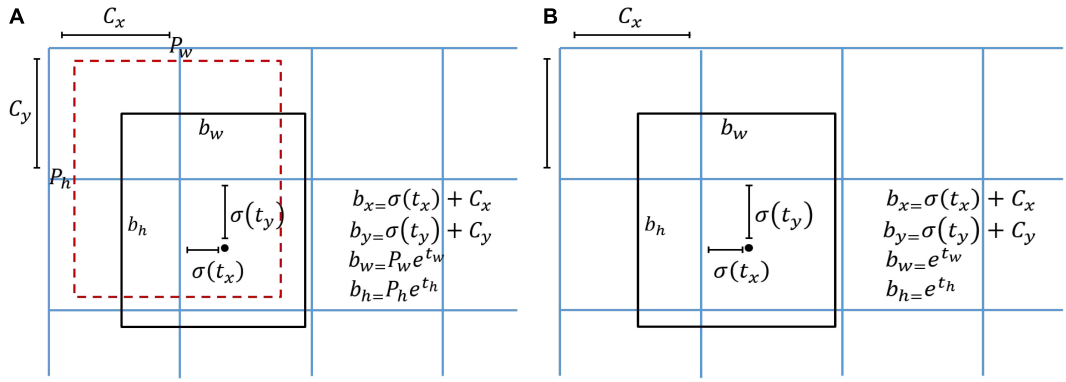

FIGURE 7 | Location encoding of bounding box in YOLO V5 and Light YOLO-Basin. **(A)** Location encoding of YOLO V5 bounding box. The red box denotes the anchor box and the black box denotes the prediction box. P_w and P_h mean the width and height of the anchor box, respectively; t_w and t_h are the predicted ratio of the width and height between the prediction box and anchor box. **(B)** Anchor-free location encoding of the bounding box. The black box denotes the prediction box; t_w and t_h directly predicted the width and height. b_x and b_y, respectively represent the coordinates of the center point x and y of the prediction box; b_w and b_h represent the width and height of the prediction box, respectively. t_x and t_y are the offsets between the center point of the prediction box and the top left corner of the cell computed by the model; σ is the Sigmoid function; C_x and C_y are the coordinates of the top left corner of the cell.

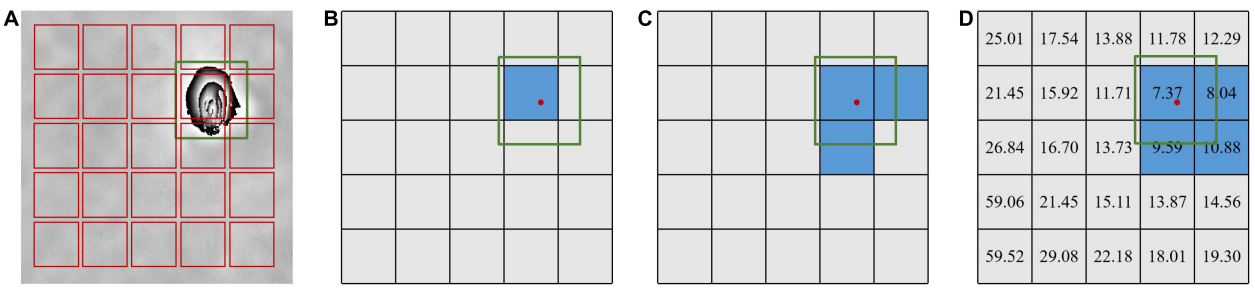

FIGURE 8 | Sample assignment of YOLO V3, YOLO V5, and optimal transport assignment (OTA). Panel **(A)** is the image with bounding box; panel **(B)** is the sample assignment of YOLO V3; panel **(C)** is the sample assignment of YOLO V5; panel **(D)** is the adaptive sample assignment of OTA. The value is the transporting cost value in panel **(D)**. The blue grid and the green box denote the positive sample and the ground truth box, respectively, and the red point is the center point of the ground truth.

feature maps obtained by the depthwise convolution. The process of performing depthwise separable convolution on a feature map with the size of W × H × C (W and H are the spatial width and height of the feature map, respectively, and C is the number of feature channels) is shown in **Figure 6**. The computation of the standard convolution is 3 × 3 × C × N × W × H, while the computation of the depthwise separable convolution is 3 × 3 × C × W × H+1 × 1 × C × N × W × H = (3 × 3+N) × (C × W × H), which is approximately 1/N + 1/(3 × 3) of the standard convolution. The parameter of the standard convolution is 3 × 3 × C × N, while the parameter of the depthwise separable convolution is 3 × 3 × C + 1 × 1 × C × N,

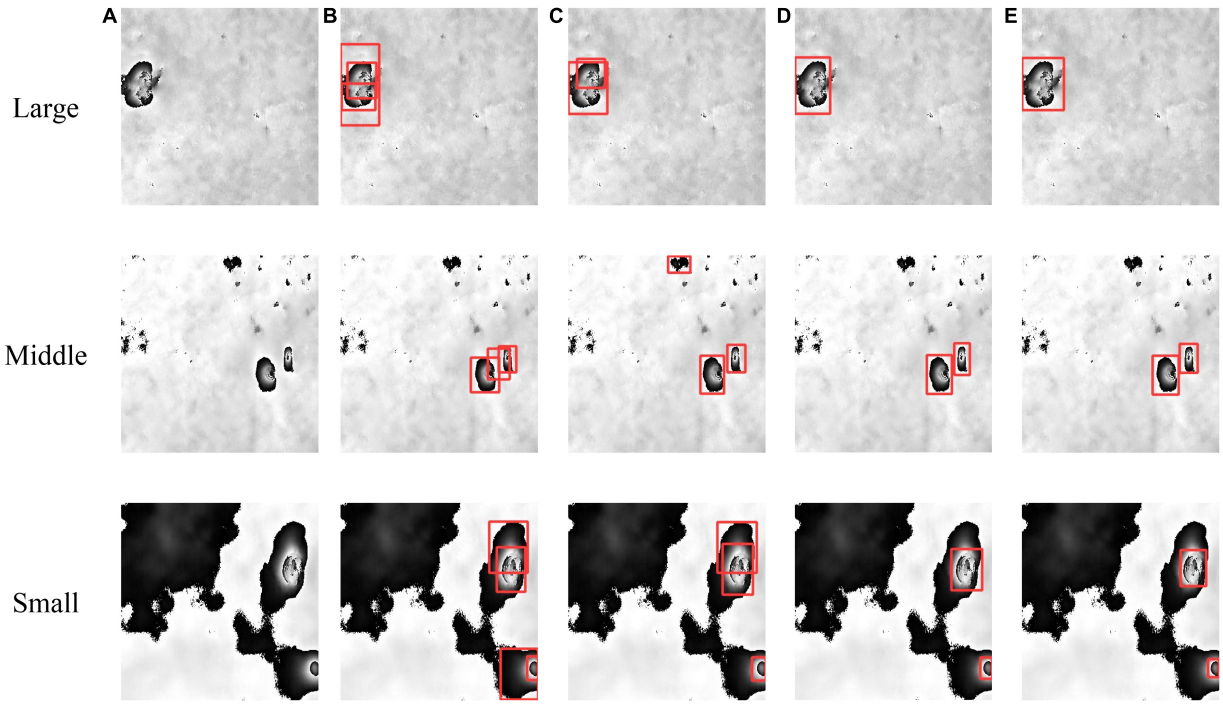

FIGURE 9 | Results of qualitative comparison experiment. Large, Middle, and Small mean the three models produced by scaling, respectively. **(A)** Cropped original image; **(B)** detection results of subsidence basins using YOLO V5 model; **(C)** detection results of subsidence basins using YOLO-Basin model; **(D)** detection results of subsidence basins using Light YOLO-Basin. **(E)** Ground truth box.

which is about $1/N + 1/(3 \times 3)$ of the standard convolution. The depthwise separable convolution has the effect of drastically reducing the computation and model size. In this study, the depthwise separable convolution is introduced into the CSPDarknet53 network, which is combined with the scaling of the depth (the number of convolutional layers) and the width (the number of channels of the convolution kernel) to realize the lightweight of the model, as shown in the orange part of **Figure 4**.

Anchor-Free and Adaptive Sample Assignment

YOLO V5, an anchor-based method, predicts boxes by fitting the deviation of the anchor boxes, where the anchor boxes have a preset width and height. Although anchor-based methods improve the detection accuracy to a certain extent, there are still some drawbacks (Fu J. M. et al., 2020). First, a large number of anchor boxes are used in the model, resulting in excessive redundant computation and slowing down the detection speed of the model. Second, only a tiny fraction of the anchor boxes is labeled as positive samples, resulting in a huge imbalance between positive and negative samples. Third, fixed anchor boxes cannot be applied to various data, which increases the difficulty of model optimization. Anchor boxes generally require to be reset according to different data. Currently, the anchor boxes obtained by clustering objects in natural images are quite different from the features of the subsidence basins in the InSAR interferograms. In addition, since the training data cannot represent all the subsidence basins, the anchor-boxes obtained by clustering the characteristics of the subsidence basins cannot guarantee their versatility. Therefore, we used an anchor-free method to detect the subsidence basins from interferograms.

The location of the prediction box in the original YOLO V5 model is determined by the center point and the width and height of the anchor box, as shown in **Figure 7A**. The coordinate value of the center point is represented by the offset from the top left corner of the cell, and the width and height are the scaling ratios of the corresponding anchor box. However, if the anchor box is abandoned, the width and height cannot be expressed. Hence, the Light YOLO-Basin model directly fits the width and height instead of the ratio of the anchor box and keeps the computation of the center point unchanged to achieve anchor-free (Law and Deng, 2018; Duan et al., 2019), as shown in **Figure 7B**.

The lack of the constraint of anchor boxes in the anchor-free method increases the degree of freedom of the model and also increases the difficulty of optimizing the prediction box. Adopting IoU at a certain threshold as positive and negative assignment criterion, which is commonly used in anchor-based detection methods, is usually not suitable for the anchor-free method. For example, the two-stage Faster R-CNN network labels the prediction box with an IoU value greater than 0.7 as a positive sample and less than 0.3 as a negative sample; the one-stage YOLO V3 model labels the prediction box with the highest IoU value as a positive sample, as shown in **Figure 8B**. Moreover, based on the anchor-free method, using a certain IoU threshold

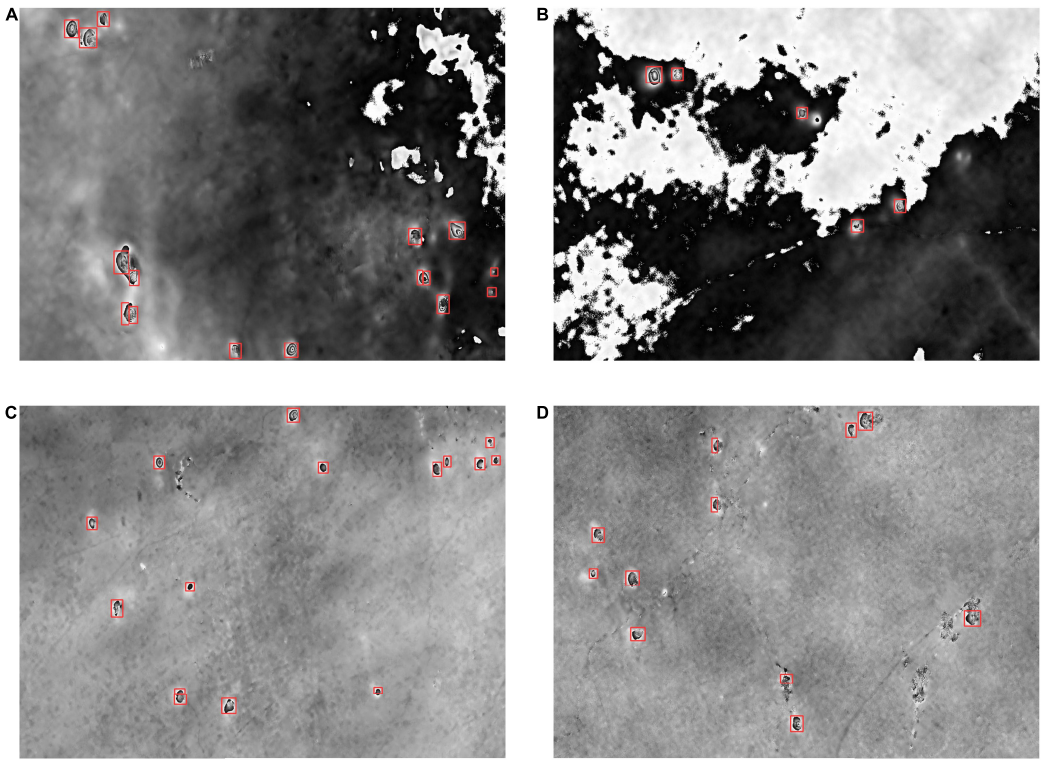

FIGURE 10 | Detection results of partial subsidence basins in the Interferometric synthetic aperture radar (InSAR) interferogram with wide swath. We select two differential interferograms obtained from the experimental data in **Table 1** to test the performance of the Light YOLO-Basin model. Panels **(A,B)** are representative areas selected from the detection results of the Jining mining area; panels **(C,D)** are representative areas selected from the detection results of the Huaibei mining area.

to assign prediction boxes will cause a large number of useful prediction boxes to be discarded. To increase the number of positive samples, the YOLO V5 model expands the selection range of positive samples to the surrounding pixels, reducing the difficulty of model optimization, as shown in **Figure 8C**. However, the YOLO V5 model still selects a fixed number of positive samples with a certain IoU threshold, and it cannot adaptively determine the number and assignment of hard and easy positive samples. Therefore, we used the OTA (Ge et al., 2021) to model the positive and negative samples assignment as an optimal transmission problem, which selects and balances positive and negative samples in an adaptive manner.

The OTA method treats the ground truth box as the supplier in the optimal transport theory, and the prediction box in the model training as the demander. The unit transportation cost between each demander and supplier is defined as the weighted summation of losses between the ground truth box and prediction box. If a demander receives enough goods from the supplier, this demander becomes one positive sample. The model needs the best positive and negative samples assignment solution to minimize the global transportation cost. Concretely, assuming that there are m ground truth boxes and n prediction boxes for image I, the ground truth box, namely supplier, holds k units of goods, while the prediction box, namely demander, needs d units of goods. $c_{i,j}$ represents the transporting cost of each unit of good from the i-th supplier to the j-th demander. The positive and negative sample assignment problem can be defined as finding an optimal transmission strategy $\pi = \{\pi_{i,j} | i = 1, 2, \ldots, m, j = 1, 2, \ldots, n\}$ to minimize the transportation cost, as shown in Formula (4). The formula behind s.t. is a condition that needs to be satisfied during optimization.

$$\min_{\pi} \sum_{i=1}^{m} \sum_{j=1}^{n} c_{i,j} \pi_{i,j}$$

$$s.t. \sum_{i=1}^{m} \pi_{i,j} = d_j, \sum_{j=1}^{n} \pi_{i,j} = k_i \tag{4}$$

$$\sum_{i=1}^{m} k_i = \sum_{j}^{n} d_j$$

$$\pi_{i,j} = 0, i = 1, 2, \cdots m, j = 1, 2, \cdots n$$

The key of the OTA is how to define the transportation cost. The original OTA method defines transportation cost between the ground truth box and the prediction box as the weighted summation of their regression loss and classification loss. Since there is only the category of subsidence basin in our study, the transporting cost was defined as the weighted summation of confidence loss and bounding box regression loss.

The computation equation is as follow:

$$c_{i,j} = L_{obj}\left(P_j^{obj}, G_i^{\mathbf{obj}}\right) + \alpha L_{reg}(P_j^{box}, G_i^{box}) \quad (5)$$

where L_{obj} and L_{reg} represent the binary cross-entropy and bounding box regression loss; P_j^{obj} and G_i^{obj} denote the confidence score of the model prediction box and ground truth box, respectively; P_j^{box} and G_i^{box}, respectively, represent the coordinates of the prediction box and the ground truth box. α is the balanced coefficient with the value of 3. The visualization result of transporting cost value is shown in **Figure 8D**.

The original OTA method uses Sinkhorn-Knopp Iteration (Cuturi, 2013) to solve the optimal transmission problem, but the multiple iteration optimization of the Sinkhorn-Knopp greatly reduces the training efficiency of the model. Hence, the Light YOLO-Basin adopted an approximate method to solve the optimal transmission problem. The OTA solution mainly consists of two parts: (1) *k* value, which is the number of positive samples of each ground truth box; (2) the assignment of the *k* value, that is, how the positive samples are assigned to the prediction box. Since the cost matrix has been determined, the assignment solution of *k* can be simplified to assign *k* of each ground truth box to the prediction box with the lowest cost in turn, as shown in the blue grid in **Figure 8D**. The determination of the value of *k* for each ground truth box is simplified to a statistical problem: first, sorting all the prediction boxes in the model according to the IoU value, and then adding up the cost value of the prediction box with the top Z (default 10) IoU value to round to get the estimated value of k, as shown in Formula (6).

$$k_i = sum\left(TopZ_{IoU}\left(\lambda^* c_{i,j}\right)\right), j = 1, 2, \cdots n \quad (6)$$

where k_i means the *k* value of the i-th ground truth box; λ is set to 0.1 derived from experiments.

RESULTS AND ANALYSIS

Experimental Setting

Accuracy Evaluation Index

The average precision (AP) and mAP (Li et al., 2017; Sun et al., 2021) were used to evaluate the performance of the Light YOLO-Basin model proposed in this study. The detection results mainly include four categories: true-positive (TP) and false-positive (FP)are the numbers of positive samples that are correctly predicted and incorrectly predicted, respectively; true-negative (TN) and false-negative (FN) mean the number of negative samples that are correctly predicted and incorrectly predicted, respectively. Precision refers to the proportion of all detected samples that are correct, and recall refers to the proportion of the objects recognized by the model among all the objects that require to be recognized. The precision (P) and recall (R) are defined in Formula (7). The P-R curve takes the precision as the ordinate and the recall as the abscissa.

$$P = \frac{TP}{TP + FP}$$

$$R = \frac{TP}{TP + FN} \quad (7)$$

The AP measures the detection performance of a single category, as shown in Formula (8). The evaluation indicators of the Light YOLO-Basin model proposed in this paper are AP_{50} : AP_{95}. AP_{50} : AP_{95} is the value of AP at different IoU thresholds that the IoU ranges from 0.5 to 0.95 and the step size is 0.05. The mAP measures the detection performance of all the categories. Since there is only the category of subsidence basin in this paper, mAP is defined as the average AP at different IoU thresholds, as shown in Formula (9).

$$AP = \int_0^1 P(R)\, dR \quad (8)$$

$$mAP = \frac{\sum_{i=0}^{9} AP_{50+i*5}}{10} \quad (9)$$

Training Settings

The experiment was conducted using the Microsoft Windows, 64-bit operating system. The central processing unit (CPU) is Intel Core i5-8300H. The graphics processing unit (GPU) is NVIDIA GeForce GTX 1050 Ti (4GB video memory). The deep learning framework is Facebook PyTorch 1.8. In this study, all subsidence basin detection models in this paper were trained by the adaptive moment estimation (Adam) optimization method (Kingma and Ba, 2014). The initial learning rate is set to 0.001 and decayed according to the formula $0.001*(1 - (iter/max\_iter)^{0.9})$, where *iter* is the current number of iterations and the maximum number of iterations (*max_iter*) is set to 60,000.

Results

According to the standard of the YOLO V5 model, we divided the Light YOLO-Basin into three versions: Large (L), Middle (M), and Small (S). The three versions are distinguished by three scaling ratios of the depth (the number of convolutional layers) and the width (the number of channels of the convolution kernel), which are (1.0, 1.0), (0.67, 0.75), and (0.33, 0.50), respectively. The model that does not introduce depthwise separable convolution in this paper is called YOLO-Basin. Examples of the qualitative comparison results of the Light YOLO-Basin model and the YOLO V5 model are shown in **Figure 9**. It can be seen that the Light YOLO-Basin model can detect the subsidence basin misdetected by the YOLO V5 model. Importantly, in order to verify the performance of the Light YOLO-Basin model in the actual scene, we selected two representative InSAR interferograms with the size of 7,636 × 8,205 and 8,127 × 10,338, respectively. We first cut the whole images regularly to obtain a large number of sub-images with a size of 416 × 416, then used the Light YOLO-Basin model to detect the subsidence basins for each sub-image, and finally stitched the detection results of each sub-image. **Figure 10** exhibits part of the detection results of subsidence basins using the Light YOLO-Basin model. It can be seen that most subsidence basins have been correctly detected. 42 and 40 subsidence basins were detected in Jining and Huaibei mining areas, respectively. Regardless of the time consumption on image segmenting and

TABLE 2 | Quantitative experiment comparison between the Light YOLO-Basin model and the YOLO V5 model.

Method	Backbone	mAP (%)	AP_{50} (%)	AP_{60} (%)	AP_{70} (%)	AP_{80} (%)
YOLO V5-L	CSPDarknet-53	45.92	88.33	80.76	61.91	21.94
YOLO V5-M	CSPDarknet-53	46.82	86.57	78.43	63.15	28.31
YOLO V5-S	CSPDarknet-53	47.65	89.78	84.36	65.70	20.12
YOLO-Basin-L	CSPDarknet-53	49.96	87.45	82.79	69.21	30.89
YOLO-Basin-M	CSPDarknet-53	51.77	89.08	84.23	69.18	36.21
YOLO-Basin-S	CSPDarknet-53	51.92	90.03	85.12	71.24	35.32
Light YOLO-Basin-L	Light CSPDarknet-53	53.46	88.95	84.02	71.68	40.53
Light YOLO-Basin-M	Light CSPDarknet-53	54.61	90.37	**86.48**	**75.29**	41.96
Light YOLO-Basin-S	Light CSPDarknet-53	**55.12**	**90.64**	86.21	75.20	**43.17**

Light CSPDarknet-53 represents the CSPDarknet-53 backbone network after introducing the depthwise separable convolution. L, M, and S represent the three versions of YOLO V5, YOLO-Basin, and Light YOLO-Basin model Large, Middle, and Small, respectively. The bold values is the maximum value of each column.

TABLE 3 | The experiment for test the accuracy and efficiency of lightweight module.

Method	Backbone	mAP (%)	Parameters (MB)	GFLOPs	Inference memory (MB)
YOLO-Basin-L	CSPDarknet-53	49.96	207.10	32.81	434.96
YOLO-Basin-M	CSPDarknet-53	51.77	108.99	19.25	285.76
YOLO-Basin-S	CSPDarknet-53	51.92	55.08	11.99	**172.22**
Light YOLO-Basin-L	Light CSPDarknet-53	53.46	92.09	16.63	559.73
Light YOLO-Basin-M	Light CSPDarknet-53	54.61	60.12	12.54	352.60
Light YOLO-Basin-S	Light CSPDarknet-53	**55.12**	**40.39**	**10.07**	198.95

The bold values is the maximum value of each column.

TABLE 4 | Roadmap of the Light YOLO-Basin model in terms of mAP and average precision (AP) (%).

	mAP (%)	AP_{50} (%)	AP_{60} (%)	AP_{70} (%)	AP_{80} (%)
YOLOV5-S	47.65	89.78	84.36	65.70	20.12
+Depthwise	46.98	86.77	79.19	66.01	24.34
+Anchor-free and OTA	54.84	**91.52**	**86.82**	**75.85**	40.88
+Double-head	54.62	88.62	86.17	75.48	42.75
+Focal Loss	**55.12**	90.64	86.21	75.20	**43.17**

The bold values is the maximum value of each column.

TABLE 5 | Ablation study for loss function.

Loss	mAP (%)	AP_{50} (%)	AP_{60} (%)	AP_{70} (%)	AP_{80} (%)
IoU loss	54.91	90.28	87.40	74.70	41.41
GIoU loss	54.08	89.67	85.73	74.89	42.01
DIoU loss	**55.12**	90.64	86.21	**75.20**	**43.17**
CIoU loss	54.89	**91.27**	**87.86**	75.05	40.98

The bold values is the maximum value of each column.

TABLE 6 | Ablation study of Z in optimal transport assignment (OTA).

Z	mAP (%)	AP_{50} (%)	AP_{60} (%)	AP_{70} (%)	AP_{80} (%)
5	54.12	90.33	**86.81**	74.62	38.63
10	**55.12**	90.64	86.21	75.20	**43.17**
15	54.47	**90.70**	88.43	**75.91**	37.43
20	54.15	90.01	85.15	74.52	42.31

The bold values is the maximum value of each column.

stitching, the Light YOLO-Basin model only consumed 16.28 s to detect the whole image. We made statistics on the deformation values of the detected subsidence basins from the Jining and Huaibei mining areas, among which, the deformation value of the subsidence basin with the smallest deformation is 1.5 cm.

Quantitative Evaluation

The detection accuracy of the Light YOLO-Basin model and the YOLO V5 model are shown in **Table 2**. The experimental results demonstrate: (1) with the same experimental method, the smaller the scaling ratio of the model is, the higher the detection accuracy is. The value of mAP increased from 45.92% of the YOLO V5-L model to 47.65% of the YOLO V5-S model. This further verified the hypothesis proposed above that the detection of subsidence basins does not require a heavy network. (2) Benefiting from the introduction of the anchor-free detection box encoding method and OTA, the mAP value of the YOLO-Basin-S model has greatly improved compared to the YOLO V5-L model which was 6% higher than that of the original YOLO V5-L model. By comparing the detection accuracy in **Table 2**, it can be found that the improvement of the YOLO-Basin model detection accuracy is mainly manifested by the strict evaluation indicators such as AP_{70} and AP_{80}. The AP_{70} value increased from 65.70 to 71.24%, and the AP_{80} value increased by 15.20%. (3) The detection accuracy of the Light YOLO-Basin model is further improved, benefiting from the introduction of the depthwise separable convolution. Similarly, the improvement of the Light YOLO-Basin model detection accuracy is also mainly manifested by the evaluation indicators

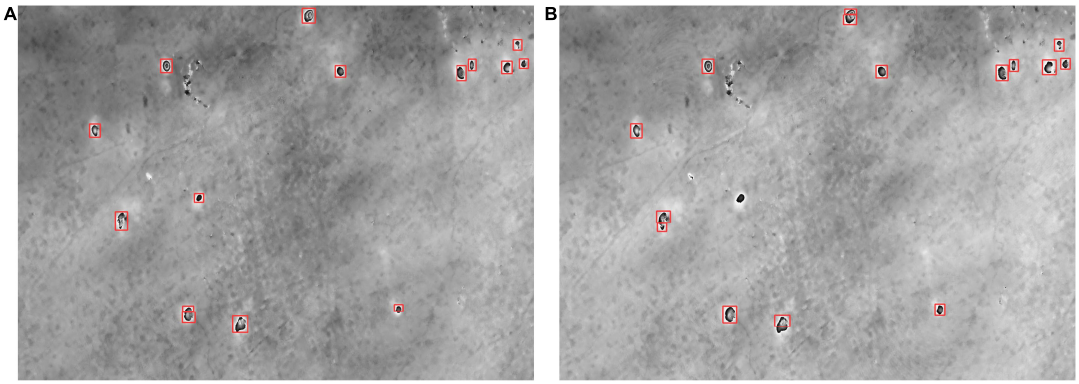

FIGURE 11 | The detection results using different spatial resolutions of DEM. Panel **(A)** is the result using DEM data with a spatial resolution of 30 m; panel **(B)** is the result using DEM data with a spatial resolution of 90 m.

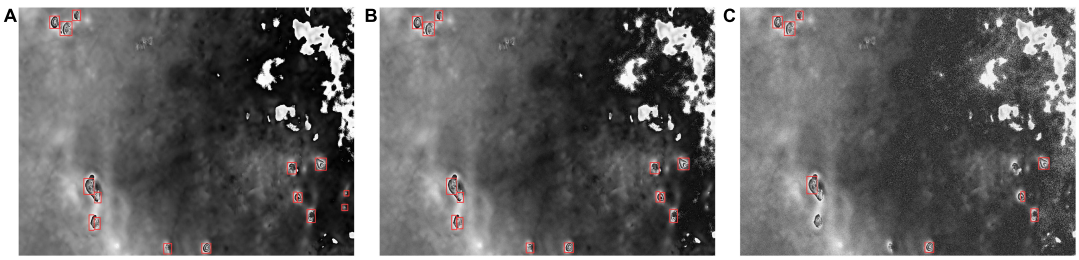

FIGURE 12 | The influence of noise on the detection results. Panel **(A)** is the detection result of this paper to remove noise; panels **(B,C)** are the detection results under Gaussian complex noise with the variance of 0.001 and 0.01, respectively.

such as AP_{70} and AP_{80}. The AP_{70} value improved from 71.24 to 75.20%, and the AP_{80} value increased by 7.85% compared to the non-lightweight model. In summary, on the one hand, the experimental results prove the effectiveness of anchor-free and OTA methods in detecting the subsidence basins. On the other hand, depthwise separable convolution can improve the detection accuracy of the Light YOLO-Basin model with less model parameters.

DISCUSSION

Efficiency Experiment of the Lightweight Module

The lightweight module of the Light YOLO-Bain model mainly includes scaling and depthwise separable convolution. The lightweight detection model needs to pay attention to two aspects: (1) whether the lightweight module can improve model computing efficiency and reduce memory utilization; (2) whether the lightweight module affects detection accuracy. We used network parameters, GFLOPs, and inference memory as the evaluation indicators of model efficiency and mAP as the evaluation indicator of model accuracy. The results are shown in **Table 3**. The image size is set to 416 × 416 and the batch size is set to 1 when training the model.

Firstly, by analyzing the values of the evaluation indicators of model efficiency in **Table 3**, introducing depthwise separable convolution and scaling can exponentially decrease the number of model parameters and speed up model training. The improvement of model efficiency by depthwise separable convolution is mainly reflected in the number of model parameters and detection speed. Note that the smaller the model is, the smaller the effect of the depthwise separable convolution is. In addition, since the depthwise separable convolution factorizes a standard convolution into two parts, the computation memory utilization of the model increases. **Table 3** indicates the use of scaling and depthwise separable convolution has a better lightweight effect on the model. Secondly, observing the model accuracy evaluation indicators data in **Table 3**, compared with the detection method of natural images, the lightweight of the model can improve the accuracy of the detection of subsidence basins rather than reducing the accuracy. Compared with the YOLO-Basin-S model, the Light YOLO-Basin-S model increases the mAP value from 51.92 to 55.12%.

Ablation Study for Detection Head and Loss Function

To address the problem caused by the anchor boxes, the Light YOLO-Basin model introduces the anchor-free method and the OTA method. In addition, we also changed the neck network and loss function of the YOLO V5 model, as seen in Section "YOLO V5 Network." We used mAP and AP_{50} : AP_{95} as the evaluation indicators of model accuracy in **Table 4**, showing the accuracy changes of the modules added to the YOLO V5-S model.

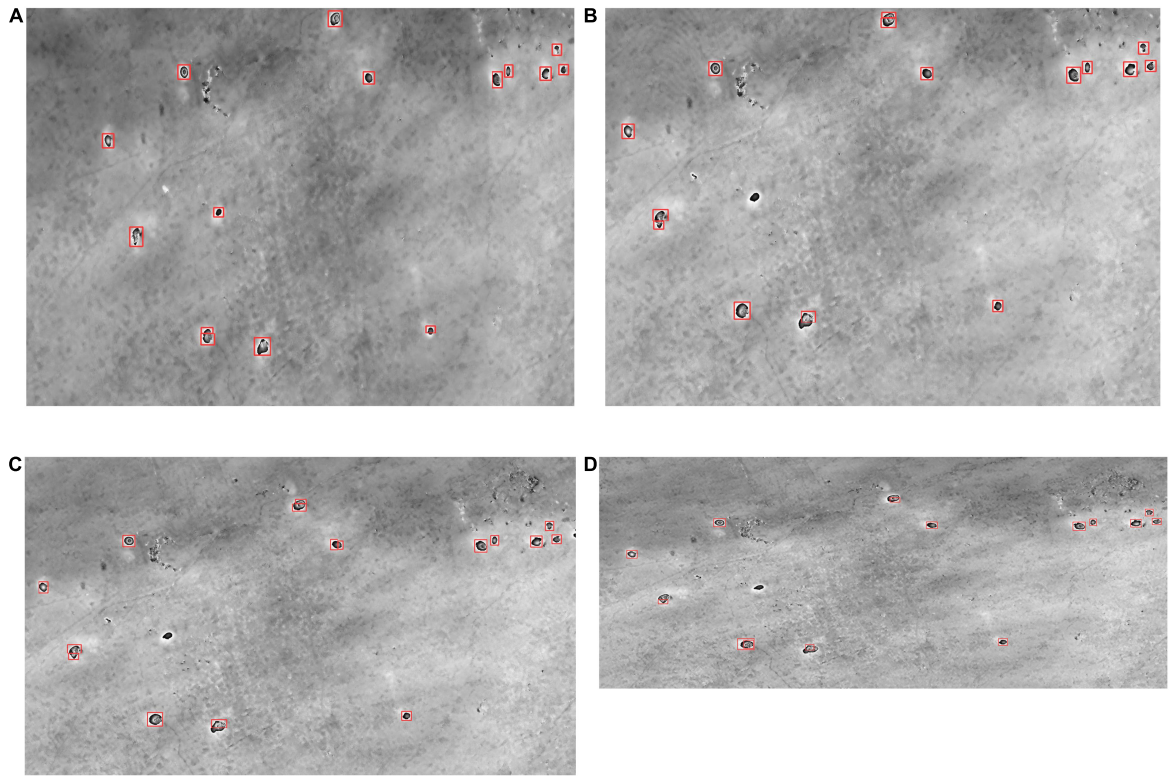

FIGURE 13 | Detection results of different multi looking numbers of the interferogram. Panels **(A–D)** are the detection results with multi looking ratios of 1:5, 1:4, 1:3, and 1:2, respectively.

It visually shows the change of model accuracy with added different modules in **Table 4**. By analyzing the changes in model accuracy, we can draw the following three conclusions: (1) The anchor-free detection box encoding method and OTA have the greatest effect on improving the detection accuracy of the model, greatly increasing the value of AP_{70} and AP_{80}. The accuracy evaluation indicators mAP has also been significantly improved, increasing from 47.65 to 55.12%. (2) The introduction of depthwise separable convolution did not improve the detection accuracy of the YOLO V5 model. However, it can improve the accuracy of the Light YOLO-Basin model, perhaps benefiting from the combined effects of depthwise separable convolution and OTA. (3) Compared with the OTA, the double-head and Focal loss only less improve the accuracy.

We also analyzed the influence of different IoU loss functions on the Light YOLO-Bain model accuracy, as shown in **Table 5**. It can be seen from **Table 5** that the detection accuracy is the highest when we used the DIoU loss function. Hence, we used DIoU loss as the bounding box regression loss function.

Ablation Study for Optimal Transport Assignment

To avoid the inefficient iterative computation of Sinkhorn-Knopp Iteration, we used statistical methods to estimate the k value corresponding to the ground truth box in the Light YOLO-Bain model, each of which represents the number of corresponding positive samples. The k value is obtained by adding up the cost value of the prediction box of the top Z in the IoU value and rounding it. Hence, the number of Z determines the size of the k value to a certain extent. According to Formula (6), the larger the value of Z is, the larger the corresponding k value is. That is, each ground truth box is assigned more positive samples. However, too many positive samples will divide the poorly optimized prediction boxes into positive samples, resulting in incorrect detection of the Light YOLO-Bain model. Too few positive samples will cause the imbalance of positive and negative samples, increasing the difficulty of model optimization. Therefore, it is important to choose a suitable Z. **Table 6** shows the effect of different values of Z on the accuracy of the Light YOLO-Basin model. It can be seen that the detection accuracy of the model is highest when the value of Z is 10.

Robustness of Light YOLO-Basin Model

To test the robustness of the model, we, respectively, tested the effects of DEM, decorrelation noise, and the number of interferogram multi looking on detection. We first conducted a set of comparative experiments using DEM with a spatial resolution of 30 and 90 m. The detection results of subsidence basins using different levels of DEM are shown in **Figure 11**. Since the DEM does not affect the features of the subsidence basins, it has little influence on the detection results where 14 and 13 subsidence basins were detected using DEM with

a spatial resolution of 30 and 90 m, respectively. Note that the spatial resolution of DEM used in this paper is 30 m. Then, to test the effect of decorrelation noise on detection, the Gaussian complex noise was used to simulate the decorrelation noise. **Figure 12** gives the influence of noise on the detection results. It can be seen that noise has a greater influence on the detection results. Hence, we used the Goldstein filtering method to remove image noise in this paper. Finally, we conducted a set of comparative experiments with different numbers of multi-looking. The comparison of the detection results is shown in **Figure 13**. It can be seen that the number of interferogram multi-looking changes the aspect ratio of the subsidence basin but has little effect on the detection result of the subsidence basin. We adopted a more appropriate ratio of multi looking is 1: 5.

CONCLUSION

Based on the YOLO V5 network architecture, the Light YOLO-Basin model for automatically detecting subsidence basins from interferograms was proposed in this paper. The Light YOLO-Basin model uses depthwise separable convolution as the lightweight module and introduces the anchor-free detection box encoding method and OTA to solve the problem caused by fixed anchor boxes. Through experiment, the valuable conclusions can be obtained as follows:

1. Depthwise separable convolution generally sacrifices a small amount of accuracy to improve the detection efficiency. The depthwise separable convolution of the Light YOLO-Basin model can improve the detection speed and reduce the model parameters from 207.10 to 40.39 MB. More importantly, the detection accuracy of the Light YOLO-Basin model has also been significantly improved. The value of mAP is increased by 3.2% compared with the non-lightweight model, which verifies the assumption that it does not require a heavy network when detecting the subsidence basins from interferograms.
2. It can effectively detect the subsidence basins through combined anchor-free and OTA adaptive sample assignment methods. The ablation experiments in this study indicate that anchor-free and OTA methods in the Light YOLO-Basin model increase the value of mAP from 46.98 to 54.84%, and the value of AP_{50}, AP_{60}, and AP_{70} increase by 4.75, 7.63, and 9.84%, respectively.
3. We introduce the Focal Loss function in the Light YOLO-Basin model when computing the confidence loss to balance the weight of the hard and easy samples during model training, increasing the value of mAP from 54.62 to 55.12% and AP_{50} from 88.62 to 90.64%.

The Light YOLO-Basin model proposed in this paper has good performance to detect subsidence basins from InSAR interferograms with wide swaths. This study also has some limitations. When making sample datasets, the labeling of training samples has a greater impact on the detection accuracy of the model. For subsidence basins with poor visual interpretation, the Light YOLO-Basin model also has false detection or missing detection in the poor interferogram. In addition, the reason why the depthwise separable convolution improves the detection accuracy of the subsidence basin may be related to the shape of the subsidence basin on the InSAR interferogram. We will solve these above problems in future works. We will propose a better detection model by analyzing the difference in morphological characteristics between the subsidence basin on the InSAR interferogram and the object in the natural image.

DATA AVAILABILITY STATEMENT

The original contributions presented in the study are included in the article/supplementary material, further inquiries can be directed to the corresponding author.

AUTHOR CONTRIBUTIONS

YY collected and analyzed the data, and wrote the manuscript. ZYW proposed the method, designed its structure, and revised the manuscript. ZL and KY helped in collecting and analyzing the data. HL and ZHW critically revised the manuscript. All authors contributed to the article and approved the submitted version.

FUNDING

This research was funded by the Major Science and Technology Innovation Projects of Shandong Province (No. 2019JZZY020103). This research was supported by funding from the National Natural Science Foundation of China (No. 41876202).

ACKNOWLEDGMENTS

We thank the European Space Agency (ESA) for providing the Sentinel-1A remote sensing data. We also thank NASA for providing the SRTM DEM data. We want to thank the reviewers for their valuable suggestions and comments which improved the quality of the manuscript.

REFERENCES

Bala, J., Dwornik, M., and Franczyk, A. (2021). Automatic subsidence troughs detection in SAR interferograms using circlet transform. *Sensors* 21:1706. doi: 10.3390/s21051706

Bochkovskiy, A., Wang, C. Y., and Liao, H. Y. M. (2020). Yolov4: optimal speed and accuracy of object detection. *arXiv* [Preprint] arXiv: 2004.10934,

Chang, Y. L., Anagaw, A., Chang, L. N., Wang, Y. C., Hsiao, C. Y., and Lee, W. H. (2019). Ship detection based on YOLOv2 for SAR imagery. *Remote Sens.* 11:786. doi: 10.3390/rs11070786

Chen, B. Q., Deng, K. Z., Fan, H. D., and Yu, Y. (2015). Combining SAR interferometric phase and intensity information for monitoring of large gradient deformation in coal mining area. *Eur. J. Remote Sens.* 48, 701–717. doi: 10.5721/EuJRS20154839

Chen, B. Q., Li, Z. H., Yu, C., Fairbairn, D., Kang, J. R., Hu, J. S., et al. (2020). Three-dimensional time-varying large surface displacements in coal exploiting areas revealed through integration of SAR pixel offset measurements and mining subsidence model. *Remote Sens. Environ.* 240:111663. doi: 10.1016/j.rse.2020.111663

Chen, B. Q., Mei, H., Li, Z. H., Wang, Z. S., Yu, Y., and Yu, H. (2021). Retrieving three-dimensional large surface displacements in coal mining areas by combining SAR pixel offset measurements with an improved mining subsidence model. *Remote Sens.* 13:2541. doi: 10.3390/rs13132541

Chen, D. H., Chen, H. E., Zhang, W., Cao, C., Zhu, K. X., Yuan, X. Q., et al. (2020). Characteristics of the residual surface deformation of multiple abandoned mined-out areas based on a field investigation and SBAS-InSAR: a case study in Jilin, China. *Remote Sens.* 12, 3752. doi: 10.3390/rs12223752

Chen, Q. S., Fan, C., Jin, W. Z., Zou, L., Li, F. Y., Li, X. P., et al. (2020). EPGNet: enhanced point cloud generation for 3D object detection. *Sensors* 20:6927. doi: 10.3390/s20236927

Chen, Y., Tong, Y. X., and Tan, K. (2020). Coal mining deformation monitoring using SBAS-InSAR and offset tracking: a case study of yu county, china. *IEEE J. Sel. Topics Appl. Earth Observ.* 13, 6077–6087. doi: 10.1109/JSTARS.2020.3028083

Cuturi, M. (2013). Sinkhorn distances: lightspeed computation of optimal transport. *Adv. Neural Inf. Process. Syst.* 26, 2292–2300.

Dai, Y. W., Ng, A. H. M., Wang, H., Li, L. Y., and Tao, T. Y. (2020). Modeling-assisted InSAR phase-unwrapping method for mapping mine subsidence. *IEEE Geosci. Remote Sens. Lett.* 18, 1059–1063. doi: 10.1109/LGRS.2020.2991687

Dong, L. K., Wang, C., Tang, Y. X., Tang, F. Q., and Duan, W. (2021). Time series InSAR three-dimensional displacement inversion model of coal mining areas based on symmetrical features of mining subsidence. *Remote Sens.* 13, 2143–2159. doi: 10.3390/rs13112143

Du, S., Wang, Y. J., Zheng, M. N., Zhou, D. W., and Xia, Y. P. (2019). Goaf locating based on InSAR and probability integration method. *Remote Sens.* 11:8. doi: 10.3390/rs11070812

Duan, K. W., Bai, S., Xie, L. X., Qi, H. G., Huang, Q. M., and Tian, Q. (2019). "Centernet: keypoint triplets for object detection," in *Proceedings of the 2019 IEEE International Conference on Computer Vision (ICCV)*, Seoul, 6569–6578.

Fan, H. D., Lu, L., and Yao, Y. H. (2018). Method combining probability integration model and a small baseline subset for time series monitoring of mining subsidence. *Remote Sens.* 10:1444. doi: 10.3390/rs10091444

Fan, H. D., Wang, L., Wen, B. F., and Du, S. (2021). A new model for three-dimensional deformation extraction with single-track InSAR based on mining subsidence characteristics. *Int. J. Appl. Earth Obs.* 94:102223. doi: 10.1016/j.jag.2020.102223

Fu, J. M., Sun, X., Wang, Z. R., and Fu, K. (2020). An anchor-free method based on feature balancing and refinement network for multiscale ship detection in SAR images. *IEEE Trans. Geosci. Remote Sens.* 59, 1331–1344. doi: 10.1109/TGRS.2020.3005151

Fu, K., Chang, Z. H., Zhang, Y., Xu, G. L., Zhang, K. S., and Sun, X. (2020). Rotation-aware and multi-scale convolutional neural network for object detection in remote sensing images. *ISPRS J. Photogramm.* 161, 294–308. doi: 10.1016/j.isprsjprs.2020.01.025

Ge, Z., Liu, S. T., Li, Z. M., Yoshie, O., and Sun, J. (2021). "OTA: optimal transport assignment for object detection," in *Proceedings of the 2021 IEEE Conference on Computer Vision and Pattern Recognition (CVPR)*, Nashville, TN, 303–312.

Girshick, R. (2015). "Fast R-CNN," in *Proceedings of the 2015 IEEE International Conference on Computer Vision (ICCV)*, Santiago, 1440–1448. doi: 10.1109/ICCV.2015.169

Girshick, R., Donahue, J., Darrell, T., and Malik, J. (2014). "Rich feature hierarchies for accurate object detection and semantic segmentation," in *Proceedings of the 2014 IEEE Conference on Computer Vision and Pattern Recognition (CVPR)*, Columbus, OH, 580–587. doi: 10.1109/cvpr.2014.81

He, K., Zhang, X., Ren, S., and Sun, J. (2016). "Deep residual learning for image recognition," in *Proceedings of the 2016 IEEE Conference on Computer Vision and Pattern Recognitionn (CVPR)*, Las Vegas, NV, 770–778. doi: 10.1109/CVPR.2016.90

Howard, A. G., Zhu, M., Chen, B., Kalenichenko, D., Wang, W., Weyand, T., et al. (2017). Mobilenets: efficient convolutional neural networks for mobile vision applications. *arXiv* [Preprint] arXiv: 1704.04861,

Hu, Z., Ge, L. L., Li, X. J., Zhang, K., and Zhang, L. (2013). An underground-mining detection system based on DInSAR. *IEEE Trans. Geosci. Remote Sens.* 51, 615–625. doi: 10.1109/TGRS.2012.2202243

Ilieva, M., Polanin, P., Borkowski, A., Gruchlik, P., Smolak, K., Kowalski, A., et al. (2019). Mining deformation life cycle in the light of InSAR and deformation models. *Remote Sens.* 11:745. doi: 10.3390/rs11070745

Jiang, J. H., Fu, X. J., Qin, R., Wang, X. Y., and Ma, Z. F. (2021). High-speed lightweight ship detection algorithm based on YOLO-V4 for three-channels RGB SAR image. *Remote Sens.* 13:1909. doi: 10.3390/rs13101909

Kingma, D. P., and Ba, J. (2014). Adam: a method for stochastic optimization. *arXiv* [Preprint] arXiv: 1412.6980,

Law, H., and Deng, J. (2018). "Cornernet: detecting objects as paired keypoints," in *Proceedings of the 2018 European Conference on Computer Vision (ECCV)*, Munich, 734–750. doi: 10.1007/s11263-019-01204-1

LeCun, Y., Bengio, Y., and Hinton, G. (2015). Deep learning. *Nature* 2015, 436–444. doi: 10.1038/nature14539

Li, K., Cheng, G., Bu, S. H., and You, X. (2017). Rotation-insensitive and context-augmented object detection in remote sensing images. *IEEE Trans. Geosci. Remote Sens.* 56, 2337–2348. doi: 10.1109/TGRS.2017.2778300

Lin, T. Y., Dollár, P., Girshick, R., He, K. M., Hariharan, B., and Belongie, S. (2017a). "Feature pyramid networks for object detection," in *Proceedings of the 2017 IEEE Conference on Computer Vision and Pattern Recognition (CVPR)*, Honolulu, HI, 2117–2125. doi: 10.1109/CVPR.2017.106

Lin, T. Y., Goyal, P., Girshick, R., He, K. M., and Dollar, P. (2017b). "Focal loss for dense object detection," in *Proceedings of the 2017 IEEE International Conference on Computer Vision (ICCV)*, Venice, 2980–2988. doi: 10.1109/TPAMI.2018.2858826

Liu, W., Anguelov, D., Erhan, D., Szegedy, C., Reed, S., Fu, C. Y., et al. (2016). "SSD: single shot multibox detector," in *Proceedings of the 2016 European Conference on Computer Vision (ECCV)*, Amsterdam, 21–37. doi: 10.1007/978-3-319-46448-0_2

Luo, Z., Yu, H. L., and Zhang, Y. Z. (2020). Pine cone detection using boundary equilibrium generative adversarial networks and improved YOLOv3 model. *Sensors* 20:4430. doi: 10.3390/s20164430

Ng, A. H. M., Ge, L. L., Du, Z. Y., Wang, S. R., and Ma, C. (2017). Satellite radar interferometry for monitoring subsidence induced by longwall mining activity using Radarsat-2, Sentinel-1 and ALOS-2 data. *Int. J. Appl. Earth Obs.* 61, 92–103. doi: 10.1016/j.jag.2017.05.009

Ou, D. P., Tan, K., Du, Q., Chen, Y., and Ding, J. W. (2018). Decision fusion of D-InSAR and pixel offset tracking for coal mining deformation monitoring. *Remote Sens.* 10:1055. doi: 10.3390/rs10071055

Purkait, P., Zhao, C., and Zach, C. (2017). SPP-Net: deep absolute pose regression with synthetic views. *arXiv* [Preprint]. arXiv: 1712.03452.

Redmon, J., and Farhadi, A. (2017). "YOLO9000: better, faster, stronger," in *Proceedings of the 2017 IEEE Conference on Computer Vision and Pattern Recognition (CVPR)*, Honolulu, HI, 7263–7271. doi: 10.1109/CVPR.2017.690

Redmon, J., and Farhadi, A. (2018). Yolov3: an incremental improvement. *arXiv* [Preprint] arXiv: 1804.02767,

Redmon, J., Divvala, S., Girshick, R., and Farhadi, A. (2016). "You only look once: unified, real-time object detection," in *Proceedings of the 2016 IEEE Conference on Computer Vision and Pattern Recognition (CVPR)*, Las Vegas, NV, 779–788. doi: 10.1109/CVPR.2016.91

Ren, C. J., Jung, H. J., Lee, S. H., and Jeong, D. W. (2021). Coastal waste detection based on deep convolutional neural networks. *Sensors* 21:7269. doi: 10.3390/s21217269

Ren, S. Q., He, K. M., Girshick, R., and Sun, J. (2015). Faster R-CNN: towards real-time object detection with region proposal networks. *IEEE Trans. Pattern Anal. Mach. Intell.* 39:6. doi: 10.1109/TPAMI.2016.2577031

Shi, G., Zhang, J., Liu, J., Zhang, C., and Yang, S. (2020). Global context-augmented objection detection in VHR optical remote sensing images. *IEEE Trans. Geosci. Remote Sens.* 59, 10604–10617. doi: 10.1109/tgrs.2020.3043252

Shi, M. Y., Yang, H. L., Wang, B. C., Peng, J. H., and Zhang, B. (2021). Improving boundary constraint of probability integral method in SBAS-InSAR for deformation monitoring in mining areas. *Remote Sens.* 13,:1497. doi: 10.3390/rs13081497

Shi, P. F., Jiang, Q. G., Shi, C., Xi, J., Tao, G. F., Zhang, S., et al. (2021). Oil well detection via large-scale and high-resolution remote sensing images based on improved YOLO v4. *Remote Sens.* 13:3243. doi: 10.3390/rs13163243

Song, G. L., Liu, Y., and Wang, X. G. (2020). "Revisiting the sibling head in object detector," in *Proceedings of the 2020 IEEE Conference on Computer Vision and Pattern Recognition (CVPR)*, Seattle, WA, 11563–11572.

Sun, X., Wang, P. J., Wang, C., Liu, Y. F., and Fu, K. (2021). PBNet: Part-based convolutional neural network for complex composite object detection in remote sensing imagery. *ISPRS J. Photogramm.* 173, 50–65. doi: 10.1016/j.isprsjprs.2020.12.015

Tian, Z., Shen, C. H., Chen, H., and He, T. (2019). "Fcos: Fully convolutional one-stage object detection," in *Proceedings of the in 2019 IEEE International Conference on Computer Vision (ICCV)*, Seoul, 9627–9636. doi: 10.1109/ICCV.2019.00972

Wang, L. Y., Deng, K. Z., and Zheng, M. N. (2020). Research on ground deformation monitoring method in mining areas using the probability integral model fusion D-InSAR, sub-band InSAR and offset-tracking. *Int. J. Appl. Earth Obs.* 85:101981. doi: 10.1016/j.jag.2019.101981

Wang, Z. Y., Li, L., Yu, Y. R., Wang, J., Li, Z. J., and Liu, W. (2021a). A novel phase unwrapping method used for monitoring the land subsidence in coal mining area based on U-Net convolutional neural network. *Front. Earth Sci.* 9:761653. doi: 10.3389/feart.2021.761653

Wang, Z. Y., Li, L., Wang, J., and Liu, J. (2021b). A method of detecting the subsidence basin from InSAR interferogram in mining area based on HOG features. *J. China Univ. Mining Technol.* 50, 404–410. doi: 10.13247/j.cnki.jcumt.001264

Wu, W., Liu, H., Li, L., Long, Y., Wang, X., Wang, Z., et al. (2021). Application of local fully convolutional neural network combined with YOLO v5 algorithm in small target detection of remote sensing image. *PLoS One* 16:e0259283. doi: 10.1371/journal.pone.0259283

Wu, Y., Chen, Y. P., Yuan, L., Liu, Z. C., Wang, L. J., Li, H. Z., et al. (2020). "Rethinking classification and localization for object detection," in *Proceedings of the 2020 IEEE Conference on Computer Vision and Pattern Recognition (CVPR)*, Seattle, WA, 10186–10195. doi: 10.1109/CVPR42600.2020.01020

Wu, Z. T., Hou, B., Ren, B., Ren, Z. L., Wang, S., and Jiao, L. C. (2021). A deep detection network based on interaction of instance segmentation and object detection for SAR images. *Remote Sens.* 13:2582. doi: 10.3390/rs13132582

Xia, Y., Wang, Y., Du, S., Liu, X., and Zhou, H. (2018). Integration of D-InSAR and GIS technology for identifying illegal underground mining in Yangquan District, Shanxi Province, China. *Environ.Earth Sci.* 77, 1–19.

Xie, S. N., Girshick, R., Dollár, P., Tu, Z. W., and He, K. M. (2017). "Aggregated residual transformations for deep neural networks," in *Proceedings of the 2017 IEEE Conference on Computer Vision and Pattern Recognition (CVPR)*, Honolulu, HI, 1492–1500. doi: 10.1109/CVPR.2017.634

Yan, B., Fan, P., Lei, X. Y., Liu, Z. J., and Yang, F. Z. (2021). A real-time apple targets detection method for picking robot based on improved YOLOv5. *Remote Sens.* 13:1619. doi: 10.3390/rs13091619

Yang, Z. F., Li, Z. W., Zhu, J. J., Feng, G. C., Wang, Q. J., Hu, J., et al. (2018a). Deriving time-series three-dimensional displacements of mining areas from a single-geometry InSAR dataset. *J. Geodesy* 92, 529–544. doi: 10.1007/s00190-017-1079-x

Yang, Z. F., Li, Z. W., Zhu, J. J., Preusse, A., Hu, J., Feng, G. C., et al. (2018b). An InSAR-based temporal probability integral method and its application for predicting mining-induced dynamic deformations and assessing progressive damage to surface buildings. *IEEE J. Sel. Topics Appl. Earth Observ.* 11, 472–484. doi: 10.1109/JSTARS.2018.2789341

Yang, Z. F., Li, Z. W., Zhu, J. J., Feng, G. C., Hu, J., Wu, L. X., et al. (2018c). Locating and defining underground goaf caused by coal mining from space-borne SAR interferometry. *ISPRS J. Photogramm.* 135, 112–126. doi: 10.1016/j.isprsjprs

Yang, Z. F., Li, Z. W., Zhu, J. J., Preusse, A., Yi, H. W., Wang, Y. J., et al. (2017a). An extension of the InSAR-based probability integral method and its application for predicting 3-D mining-induced displacements under different extraction conditions. *IEEE Trans. Geosci. Remote Sens.* 55, 3835–3845. doi: 10.1109/TGRS.2017.2682192

Yang, Z. F., Li, Z. W., Zhu, J. J., Yi, H. W., Hu, J., and Feng, G. C. (2017b). Deriving dynamic subsidence of coal mining areas using InSAR and logistic model. *Remote Sens.* 9, 125–143. doi: 10.3390/rs9020125

Yuan, M. Z., Li, M., Liu, H., Lv, P. Y., Li, B., and Zheng, W. B. (2021). Subsidence monitoring base on SBAS-InSAR and slope stability analysis method for damage analysis in mountainous mining subsidence regions. *Remote Sens.* 13:3107. doi: 10.3390/rs13163107

Zhao, J. Q., Zhang, X. H., Yan, J. W., Qiu, X. L., Yao, X., Tian, Y. C., et al. (2021). A wheat spike detection method in UAV images based on improved YOLOv5. *Remote Sens.* 133095. doi: 10.3390/rs13163095

Zheng, M. N., Deng, K. Z., Fan, H. D., and Du, S. (2018). Monitoring and analysis of surface deformation in mining area based on InSAR and GRACE. *Remote Sens.* 10, 1392–1411. doi: 10.3390/rs10091392

Conflict of Interest: The authors declare that the research was conducted in the absence of any commercial or financial relationships that could be construed as a potential conflict of interest.

Publisher's Note: All claims expressed in this article are solely those of the authors and do not necessarily represent those of their affiliated organizations, or those of the publisher, the editors and the reviewers. Any product that may be evaluated in this article, or claim that may be made by its manufacturer, is not guaranteed or endorsed by the publisher.

frontiers in Environmental Science

ORIGINAL RESEARCH
published: 09 March 2022
doi: 10.3389/fenvs.2022.857739

Coseismic Displacement and Slip Distribution of the 21 May 2021 Mw 6.1 Earthquake in Yangbi, China Derived From InSAR Observations

Yongsheng Li[1,2], Yujiang Li[1], Kuan Liang[1], Hao Li[1] and Wenliang Jiang[1]*

[1]National Institute of Natural Hazards, Ministry of Emergency Management of China, Beijing, China, [2]Key Laboratory of Landslide Risk Early-warning and Control, Ministry of Emergency Management of China, Chengdu, China

On 21 May 2021, a Mw 6.1 earthquake struck Yangbi County, Yunnan Province, China. In this study, InSAR data from Sentinel-1 SAR images were processed to image the coseismic deformation fields of the Yangbi earthquake. Then, the optimal slip model was obtained by applying the particle swarm optimization method. The interferometry results revealed that the earthquake triggered obvious surface deformation near the epicenter, while the earthquake did not produce an obvious surface rupture zone from field investigation. The optimal slip model suggests that the strike of the seismogenic fault responsible for this event is 139°, the dip angle is 81°, and the average rake angle is -170°. Additionally, the slip was concentrated mainly at depths of 2–8 km, the maximum dip-slip amount was 0.5 m, and the cumulative seismic moment reached 1.43×10^{18} N·m, equivalent to a Mw 6.1 earthquake. The geodetic and geophysical inversion results demonstrate that the Yangbi earthquake was dominated by a steeply dipping dextral strike-slip rupture. The rupture fault generally strikes NNW-SSE, which is consistent with that of the Weixi-Qiaohou fault, and may be a relatively new fault formed by an E-W-oriented extension of the western boundary of the Sichuan-Yunnan block. Finally, based on the InSAR results in combination with the spatial distribution characteristics of ground fissures and the strong historical earthquakes, we analyzed the tectonic background preceding the Yangbi earthquake and analyzed the relationship between the Yangbi earthquake and strong historical earthquakes in the region, thereby providing empirical evidence for analyzing seismic risk and fault rupture parameters, interpreting seismic deformation characteristics, and better understanding the seismogenic background of the western boundary of the Sichuan-Yunnan block.

Keywords: Yangbi Mw 6.1 earthquake, InSAR, slip distribution, focal mechanism inversion, stress change background

OPEN ACCESS

Edited by:
Chen Yu,
Newcastle University, United Kingdom

Reviewed by:
Lingyun Ji,
China Earthquake Administration, China
Chisheng Wang,
Shenzhen University, China
Wu Zhu,
Chang'an University, China

****Correspondence:***
Yujiang Li
yujiangli@ninhm.ac.cn

Specialty section:
This article was submitted to Environmental Informatics and Remote Sensing, a section of the journal Frontiers in Environmental Science

Received: *19 January 2022*
Accepted: *11 February 2022*
Published: *09 March 2022*

Citation:
Li Y, Li Y, Liang K, Li H and Jiang W (2022) Coseismic Displacement and Slip Distribution of the 21 May 2021 Mw 6.1 Earthquake in Yangbi, China Derived From InSAR Observations. Front. Environ. Sci. 10:857739. doi: 10.3389/fenvs.2022.857739

INTRODUCTION

According to the China Seismic Network, on 21 May 2021, a Mw 6.1 earthquake struck Yangbi County, Yunnan Province, at (25.67°E, 99.87°N), the depth of hypocenters was 8 km (Li C. et al., 2021; Hu et al., 2021). Different research institutions have provided focal mechanism solutions for this earthquake using the global or regional network data (**Table 1**). This earthquake is generally characterized as a dextral strike-slip event (Liu et al., 2021). Based on the earthquake epicenter, this event occurred along the western boundary of the Sichuan–Yunnan block, which is consistent with the movement properties and

TABLE 1 | Focal mechanisms and fault parameters from different studies.

Source	Epicenter		Focal mechanisms	Mag (Mw/Ms)	Depth (km)	References
	Lon (°E)	Lat (°N)				
Regional seismic network	99.87	25.67	138°/82°/-161°	Mw 6.0	5	http://www.cea-igp.ac.cn/kydt/278248.html
P-wave	99.87	25.67	141°/68°/-153°	Ms 6.4	-	http://www.cea-igp.ac.cn/kydt/278248.html
Far-field body wave	100.008	25.67	135°/82°/-	Mw6.1	11	http://www.cea-igp.ac.cn/kydt/278248.html
USGS	100.016	25.744	135°/82°/-165°	Mw 6.1	9	https://earthquake.usgs.gov/earthquakes/eventpage/us7000e532/executive
InSAR	99.934	25.644	139°/81°/-170°	Mw 6.1	6	Yang Z. et al., 2021
InSAR	99.87	25.67	316°/86°/-	Mw 6.14	3–13	Zhang K. et al., 2021
InSAR	99.93	25.64	139°/81°/-171°	Mw 6.1	6	This Study

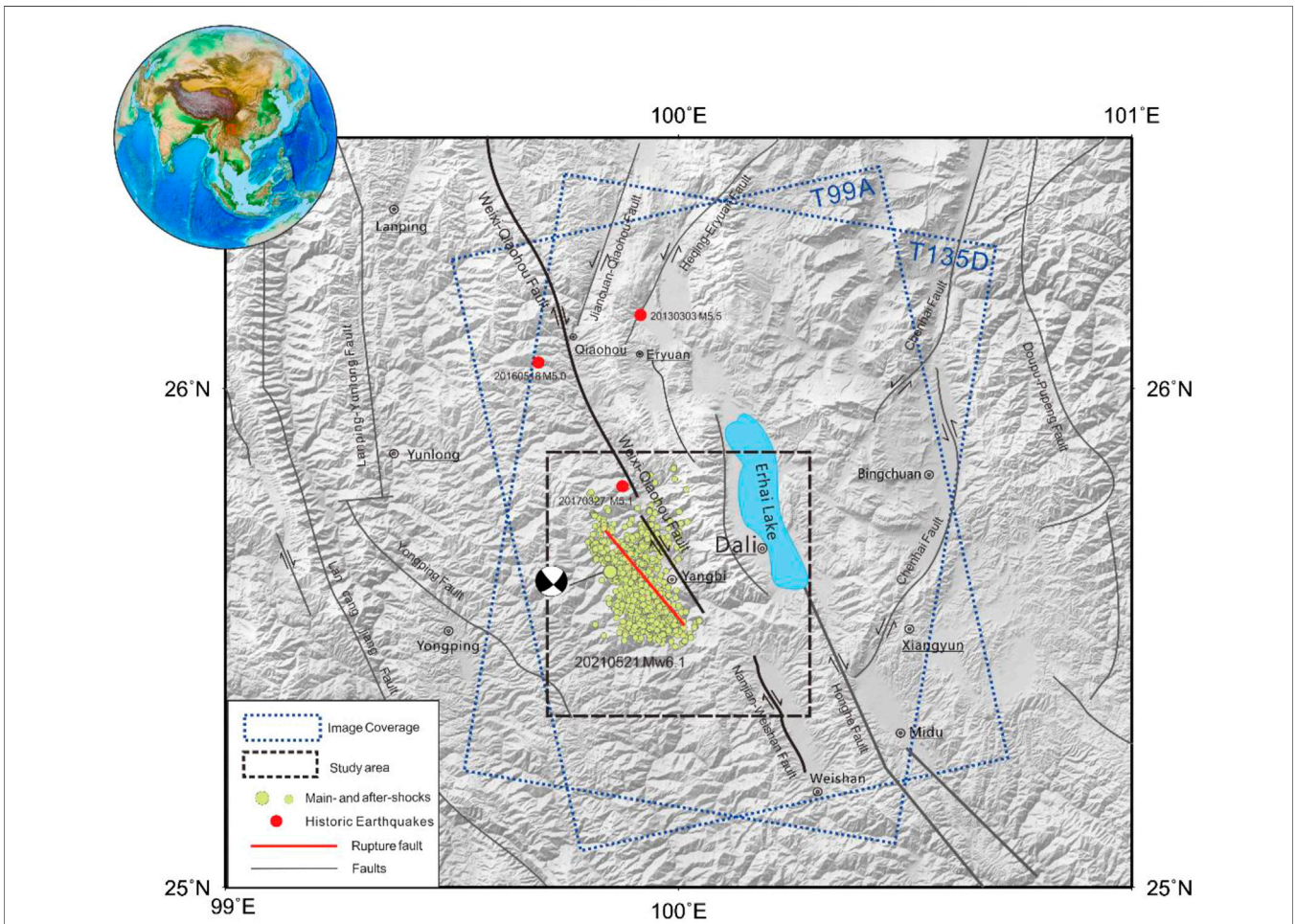

FIGURE 1 | Active faults and seismotectonic background of the region surrounding the Yangbi earthquake. The China Earthquake Networks Center provided the locations of historical earthquakes. The yellow dots denote the Yangbi Mw 6.1 mainshock and aftershock (Su et al., 2021).

trends of the Red River and Weixi–Qiaohou fault zones (**Figure 1**), the latter of which has been characterized by dextral strike-slip movement since the late Quaternary (Chang et al., 2016a; Zhang K. et al., 2021). There are no obvious surface ruptures that have been found in field investigations. Consequently, the identity and geometric characteristics of the seismogenic fault responsible for the Yangbi earthquake need to be further clarified. In particular, intensive research must be conducted to ascertain whether the Weixi–Qiaohou fault zone, which represents the closest fault to the epicenter of the Yangbi event or an unknown hidden fault, was responsible for this earthquake, and the characteristics of such a hidden fault must be thoroughly investigated.

In recent years, earth observation technologies such as interferometric synthetic aperture radar (InSAR) have been

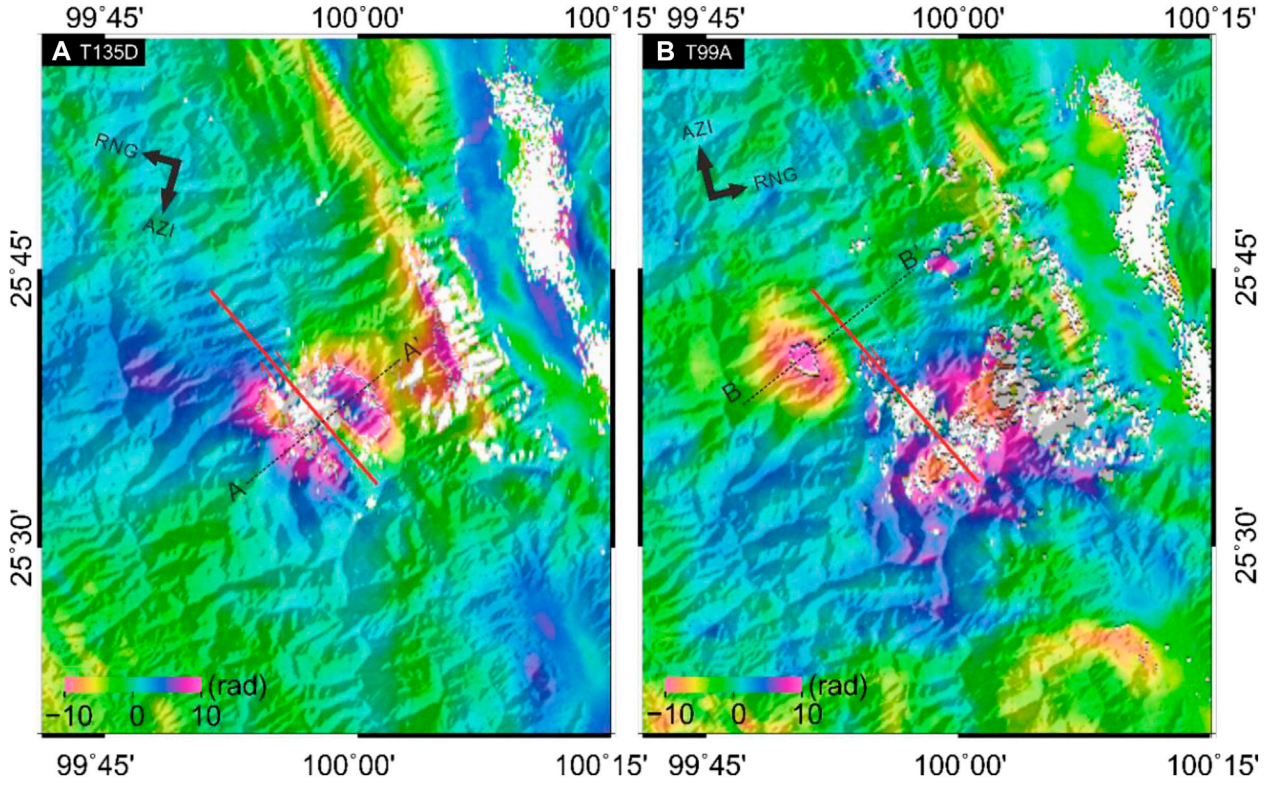

FIGURE 2 | (A) Coseismic deformation fields of the Yangbi earthquake are calculated from Sentinel-1 descending track 163. **(B)** Coseismic deformation fields calculated from ascending track 99. The red line represents the inferred ruptured fault, and the black dotted lines indicate the cross-sections perpendicular to the inferred fault.

employed to remotely monitor the Earth's surface to quantify global surface microdeformation globally with high precision (Li et al., 2020; Li K. et al., 2021; Li B. et al., 2020). In this paper, the InSAR coseismic deformation fields of the Yangbi earthquake were mapped using Sentinel-1 images acquired in terrain observation with progressive scans (TOPS) mode, and the focal mechanism and fault slip distribution were calculated and discussed. Analyzing the focal mechanism of the Yangbi Mw6.1 earthquake has essential theoretical and practical significance for fundamentally understanding the seismotectonic background, the structural deformation mechanism, and the activities along the block boundary in NW Yunnan. In particular, studying the seismotectonic activity in this region is crucial to understanding the tectonic background of the southeastern Qinghai–Tibet Plateau.

TECTONIC SETTING

The Yangbi earthquake occurred along the southwestern boundary of the rhombic Sichuan–Yunnan block (**Figure 1**), which has been forming since the early Cenozoic as a result of the eastward extrusion of the Qinghai–Tibet Plateau. During this time, the southeastward motion of the Sichuan–Yunnan block resulted in the development of a series of active right-lateral, oblique NW-trending faults in this region, obstructed by the South China block. The Sichuan–Yunnan block shifted toward the SE and rotated clockwise around the East Himalayan tectonic junction. Consequently, the Sichuan–Yunnan block is the most representative active block (featuring the strongest lateral extrusion) along the eastern margin of the Qinghai–Tibet Plateau (Long et al., 2021) and, being a research hotspot for studying the movement and tectonic deformation of rigid blocks, is the focus of many investigations on active tectonics and earthquake monitoring and prediction (Chang et al., 2016b). The northeastern and eastern boundaries of the Sichuan-Yunnan block are controlled by the Ganzi-Yushu, Xianshuihe-Anninghe-Zemuhe, and Xiaojiang fault segments and other fault zones, all of which are characterized by sinistral strike-slip and high slip rates. In particular, the eastern boundary of this block has a clear structure and frequently experiences earthquakes (Ren et al., 2007).

The Yangbi earthquake occurred in an active fault zone traversing the western boundary of the Sichuan-Yunnan block and is where the Weixi-Qiaohou-Weishan fault connects with the Red River fault, both of which are NW-trending dextral strike-slip faults. The main well-known active segments are situated near the epicenter of the 2021 Yangbi event. As major faults, the Weixi-Qiaohou-Weishan fault and Red River fault control the crustal deformation along the southwestern boundary of the Sichuan-Yunnan block (Wang S. et al., 2021). Using the cut-and-paste (CAP) waveform inversion method (Wang Y. et al., 2021a), the epicenter of the Yangbi

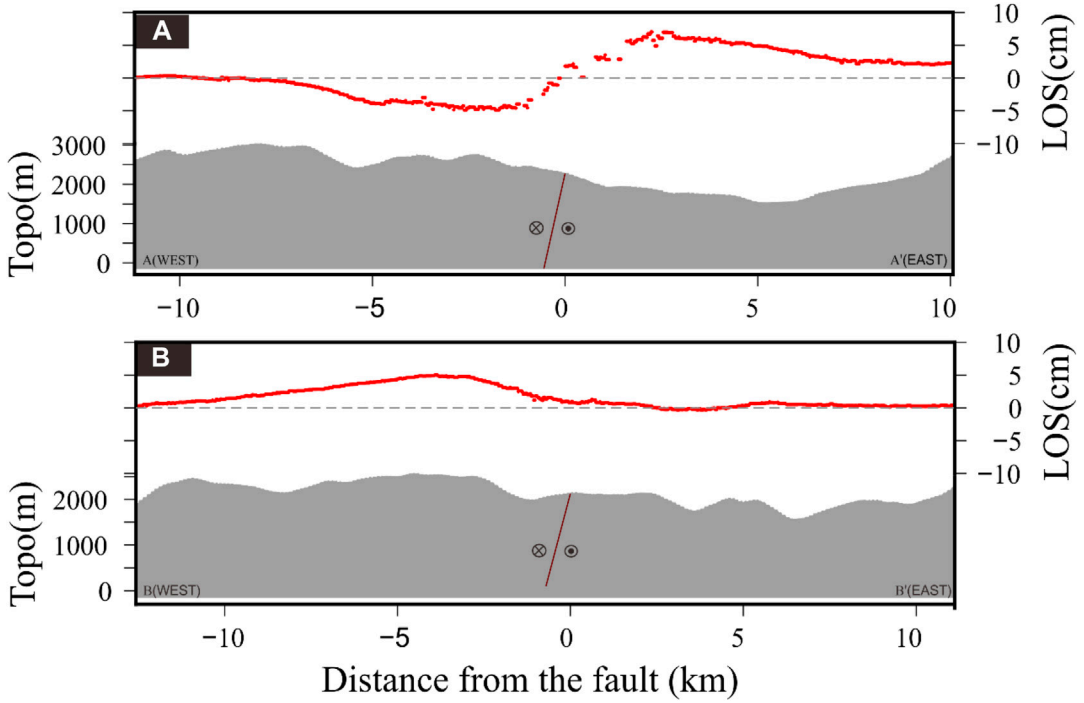

FIGURE 3 | (A) Profile of the coseismic LOS deformation along line A-A′ in Figure 2A. **(B)** Profile of the coseismic LOS deformation changes along line B-B′ in **Figure 2B**.

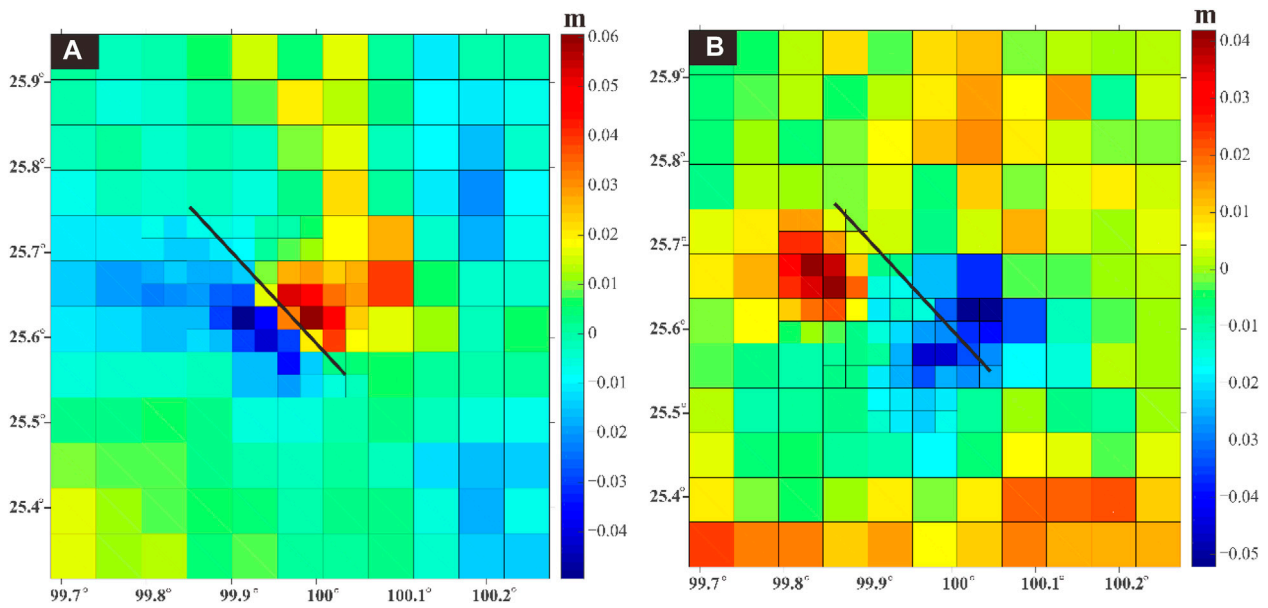

FIGURE 4 | Quadtree downsampling results of the coseismic deformation fields corresponding to **(A)** descending track 163 in Figure 2A and **(B)** ascending track 99 in Figure 2B.

earthquake sequence was shown to be approximately 3–10 km SW along the Weixi–Qiaohou fault and the long axis of the aftershock area was reported to trend NW–SE.

The Weixi–Qiaohou fault is a large-scale boundary fault that starts in northwestern Weixi County and connects with the Red River fault in southern Weishan, spanning approximately 280 km

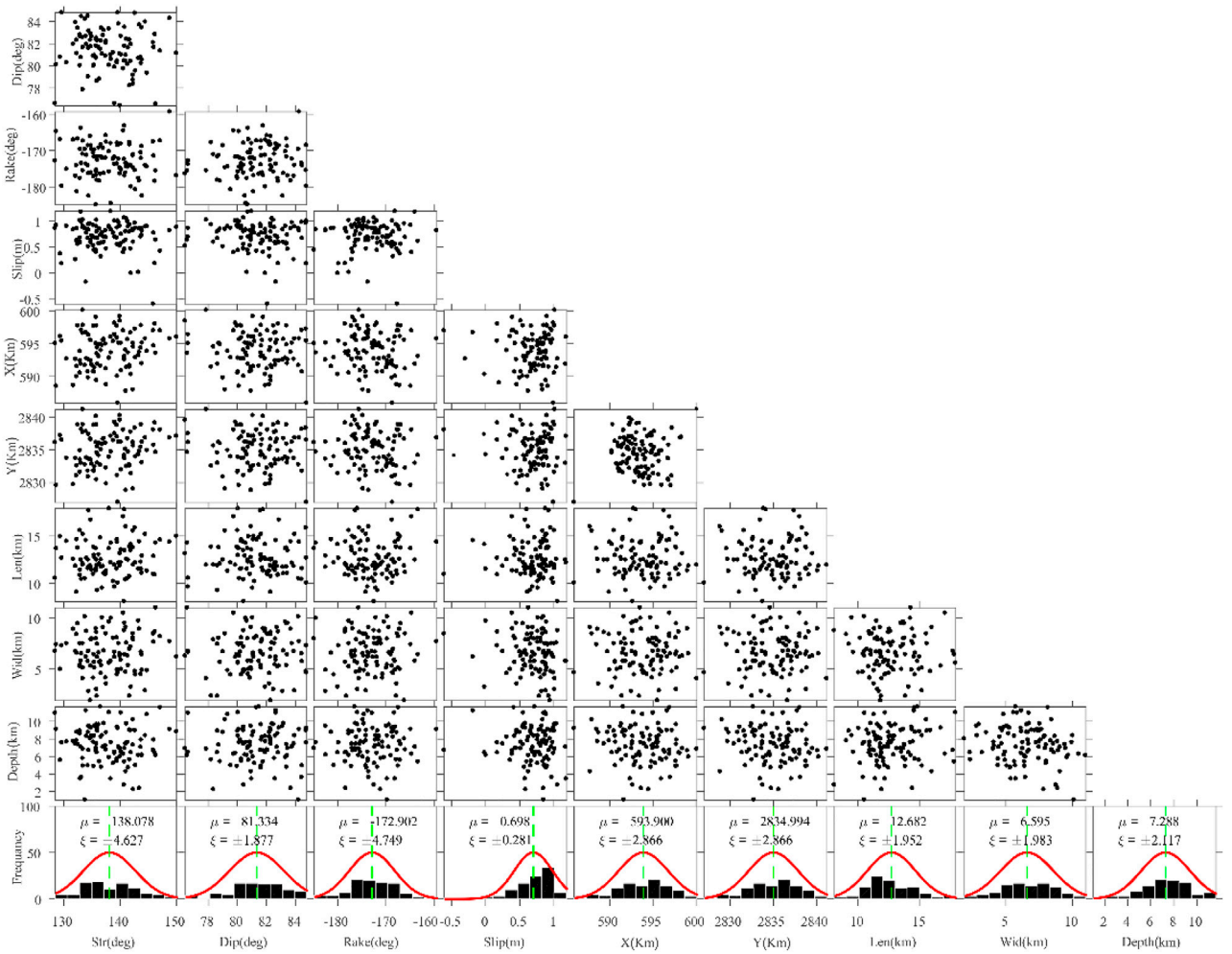

FIGURE 5 | Uncertainties and trade-offs for the nonlinear inversion computed using Monte Carlo analysis.

with a general strike of NNW–SSE (**Figure 1**). The fault shows strong late Quaternary activity, which has manifested in new active landforms such as straight fault troughs, clear fault triangles, and fault scarps (Ren et al., 2007; Duan et al., 2021). The fault is dominated by dextral strike-slip with a minor normal slip component, and ridges and water systems show apparent synchronous dextral dislocations along the fault (Li D. et al., 2021). Because the historical records of earthquakes in this region are not noteworthy, this area has received little attention for many years. However, many moderately strong earthquakes have recently occurred, such as the 2017 Yangbi Ms5.1 earthquake (25 km from the epicenter of the 2021 Yangbi Mw6.1 earthquake), the 2016 Yunlong Ms5.0 earthquake (59 km from the epicenter), and the 2013 Eryuan Ms5.5 earthquake (31 km away from the epicenter) (**Figure 1**). These phenomena suggest that the tectonic activity in this region is gradually increasing.

INSAR COSEISMIC DEFORMATION

The focal mechanisms and waveform inversion results reported by previous studies show that the seismogenic fault that produced the Yangbi earthquake exhibited dextral strike-slip motion (Ye et al., 2021; Yang Z. et al., 2021). However, the overall deformation amplitude is small from field investigation, and there are almost no signs of rupture on the surface. To image the coseismic deformation field generated by this earthquake, the Sentinel-1 satellite equipped with C-band SAR launched by the European Space Agency was employed in this paper. Sentinel-1 descending track 135 and ascending track 99 data with interferometric wide swath (IW) mode were obtained (**Figure 1**). Using an automatic seismic deformation monitoring system for Sentinel-1 SAR data (Li Y. et al., 2021), the ascending and descending InSAR coseismic deformation fields were obtained, as shown in **Figure 2**. The Advanced

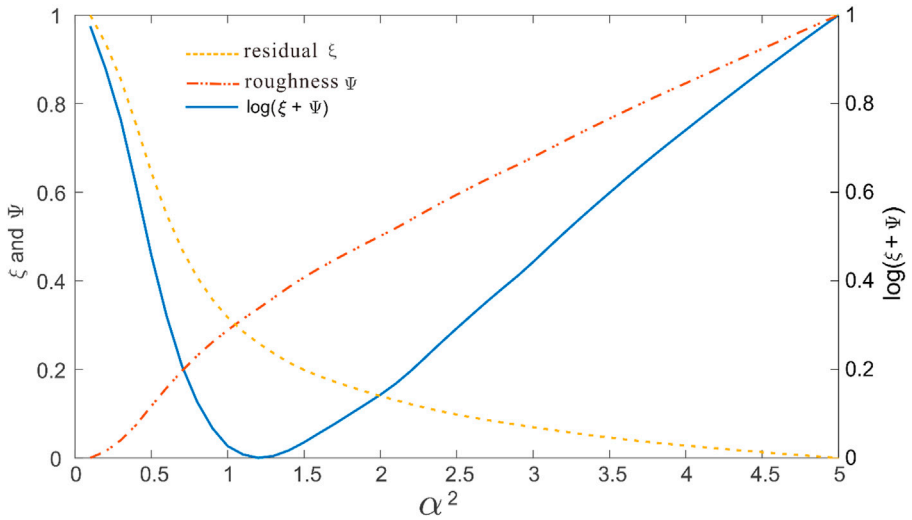

FIGURE 6 | Trade-off curves line the residuals (ξ) and roughness (ψ). The solid line represents the normalized log ($\psi + \xi$).

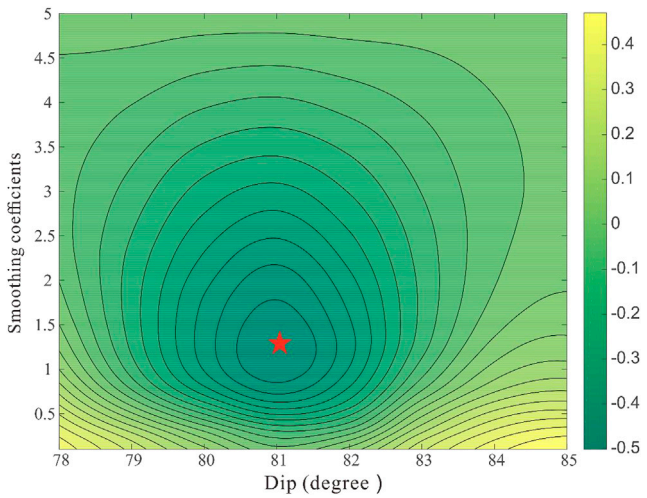

FIGURE 7 | Contour map of the log function with variations in the dip and smoothing coefficients (α2). The red star indicates the global minimum.

Land Observing Satellite Global Digital Surface Model (ALOS World 3D) with a 30-m resolution was used as external digital elevation model (DEM) data to eliminate the phase contribution of undulating terrain (Tadono et al., 2014). Additionally, an adaptive Goldstein filtering algorithm was applied to filter the original interferograms (Goldstein et al., 1988), and the minimum cost flow algorithm was used for phase unwrapping (Chen and Zebker, 2000). The atmospheric delay error was preliminarily corrected by the Generic Atmospheric Correction Online Service for InSAR (GACOS) method (Yu et al., 2018), and the residual orbit was fitted by linear fitting.

The resulting coseismic deformation field based on Sentinel-1 satellite data can clearly describe the spatial distribution and magnitude of deformation caused by the Yangbi earthquake (**Figure 2**). The results predominantly indicate that the strike of the fault is NNW–SSE, which is consistent with recent aftershock location findings (Su et al., 2021). After correcting the atmospheric contribution, the coseismic interferogram of the descending track in **Figure 2A** reflects a clear deformation pattern. The long axis is distributed in the NW–SE direction. There are obvious deformation signals distributed on both sides of the inferred fault (the surface to the SW of the fault is moving away from the satellite, while that to the NE is moving toward the satellite). Cross sections perpendicular to the inferred fault were selected to conduct a profile analysis (**Figure 3A**), revealing that the maximum deformation in the line-of-sight (LOS) direction on the NE side reached approximately 8 cm, while that on the SW side was approximately 5 cm. The ascending coseismic interferogram (**Figure 2B**) shows an obvious deformation pattern moving toward the satellite in the epicenter area, reaching 5 cm in the LOS direction (**Figure 3B**). However, the deformation field cannot accurately describe the coseismic deformation characteristics of this strike-slip earthquake, mainly because the azimuth of the ascending track is nearly consistent with the fault strike. Therefore, the SAR sensor is not sensitive enough to capture the deformation signal parallel to the surface movement direction.

FOCAL MECHANISM INVERSION

After unwrapping the InSAR interferograms, the data were downsampled using the quadtree method constrained by the data resolution (Lohman and Simons 2005; Feng et al., 2018; 2019). The large deformation gradients in the downsampled interferograms are mainly in the areas with large surface deformation, while the deformation gradients are low in the far field (**Figure 4**). This downsampled measurement ensures the inversion accuracy and dramatically reduces the

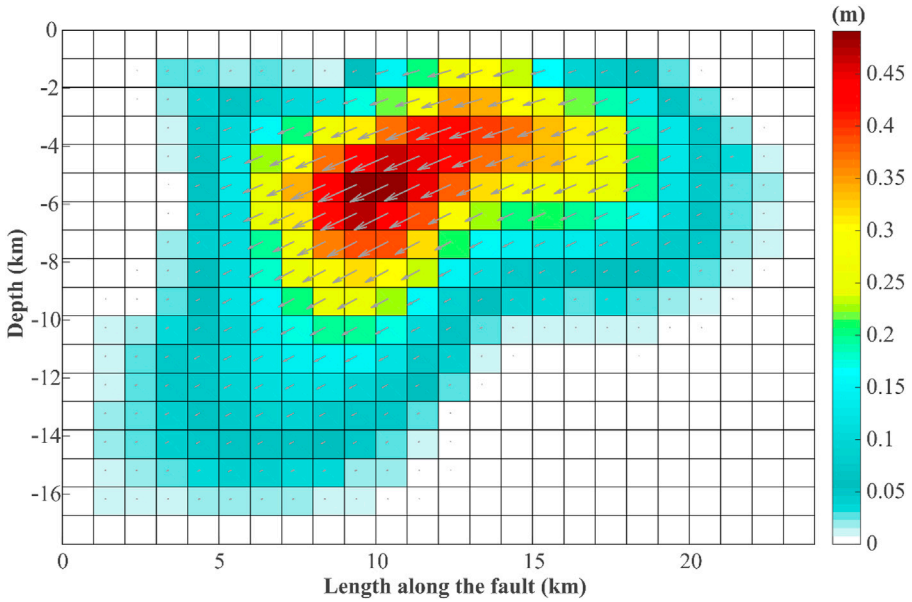

FIGURE 8 | Optimal slip distribution of the Yangbi earthquake. The gray arrows represent the hanging wall's motion direction relative to the footwall.

computational cost of the inversion. Then, the downsampled deformation fields were employed as inversion constraints, and the geometric parameters and slip distribution of the fault were estimated by a two-step inversion method (Feng et al., 2013). The fault parameters and slip mechanism of the Yangbi earthquake were studied as described below.

Uniform Slip

We assumed a uniform slip model to determine the fault's geometric parameters of the fault, including epicenter location (latitude/longitude), strike, dip, and top and bottom depths. Then, the rupture slip distribution on the rectangular fault plane was estimated by a nonlinear inversion algorithm (Feng et al., 2013; Li B. et al., 2020; Yang J. et al., 2021). We used the Particle Swarm Optimization and okada inversion package (PSOKINV) (Feng et al., 2013) to ensure that the source parameters could be successfully retrieved under relatively few parameter constraints. The adaptive function is defined as

$$\sigma = \sqrt{\frac{(W(D - GS))^2}{N}}, \quad (1)$$

where G is Green's function, with the coefficient matrix representing the surface motion in response to 1 m of dip-slip on a uniform fault, S is the slip vector at each patch, W is the weight matrix, D is the observed surface deformation, and N is the number of observed deformations (Feng et al., 2013).

To evaluate the reliability of the nonlinear inversion of source parameters, we added Gaussian-distributed error to the original observations to generate 100 perturbed datasets. Then, we performed a Monte Carlo test to estimate the uncertainties and trade-offs for the geometric parameters during the nonlinear inversion (Parsons et al., 2006). The test results (Fig. 5) revealed that the uncertainties are small and that the trade-offs are strong enough to indicate that the nonlinear inversion estimates are reliable.

The nonlinear inversion results suggest that the major seismogenic fault is a dextral strike-slip fault with a strike of ~139°, a dip of ~81°, and an average rake angle of approximately -173°. Moreover, the optimal inverted slip model suggests that coseismic slip was concentrated at a depth of 7.2 km with a maximum slip of ~0.7 m.

Distributed Slip

We then conducted a linear inversion to estimate the slip distribution during the Yangbi earthquake and fixed the optimal geometry of the fault plane determined from the uniform slip solution. The fault plane was extended to 24 km long and 18 km wide, and the size of each slip patch was set to 1 km × 1 km. To prevent physically impossible oscillatory slip and determine the optimal fitting solution, we applied a log function $f(\delta, a^2) = \log(\psi + \xi)$ to find the optimal dip angle and smoothing factor for the distributed slip model. ξ and ψ represent the residual and slip roughness, respectively, and a^2 and δ represent the smoothing factor and dip angle, respectively (Burgmann et al., 2002). According to the literature, the above log function can effectively determine the optimal dip and smoothness coefficient simultaneously (Feng et al., 2013).

With normalization, the residual curve is a monotonically decreasing function, while the roughness is a monotonically increasing function. The optimal smoothing factor was determined to be $a^2 \approx 1.2$ (**Figure 6**). We set the dip angle in the range of [78°, 85°] and the smoothing factor in the domain of [0.1 5] and then iterated the dip angle and smoothing factor to perform an additional grid search for the optimal dip. The

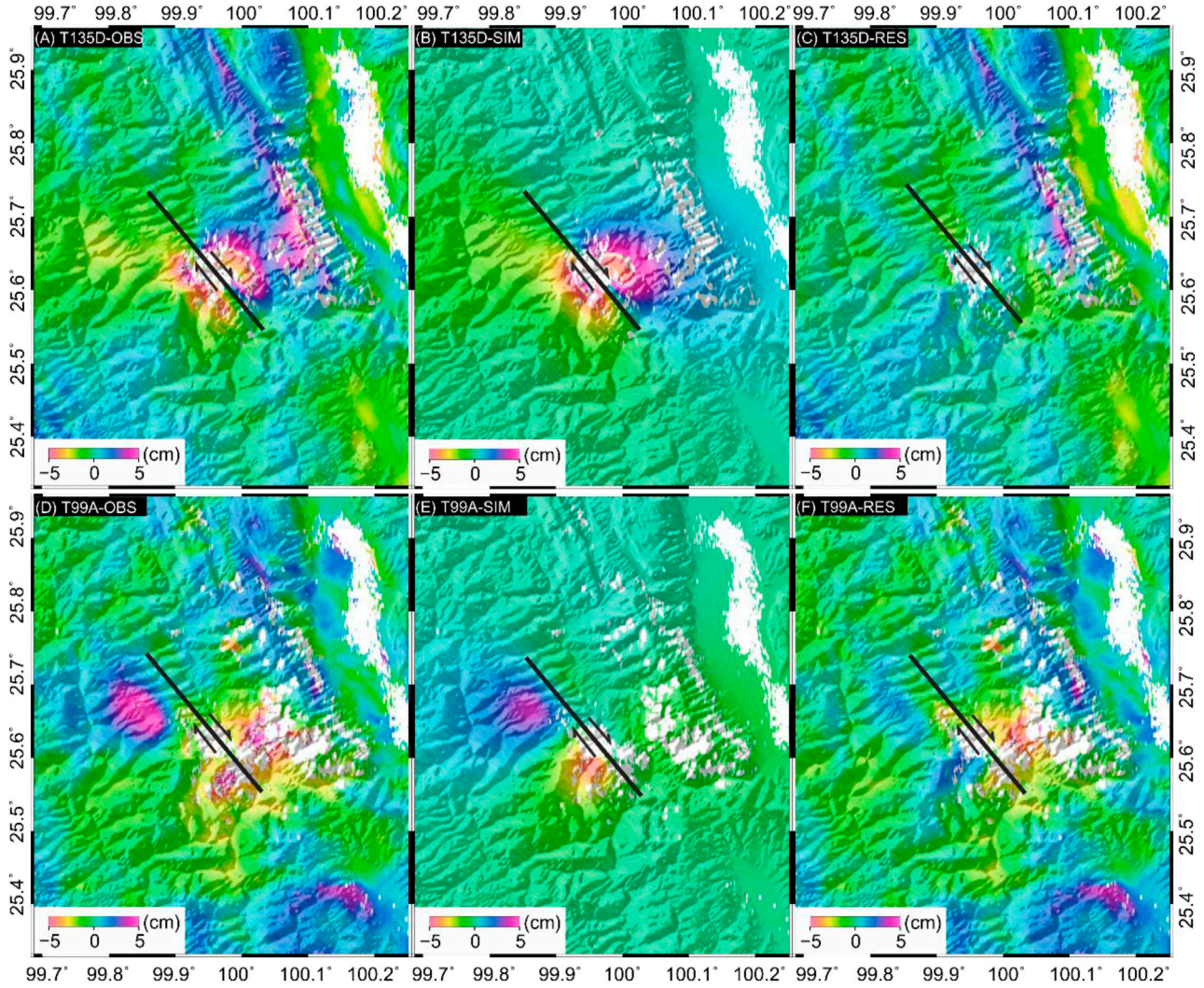

FIGURE 9 | (A) and **(D)** Observed coseismic deformation fields for descending track 135 and ascending track 99, respectively. **(B)** and **(E)** Corresponding simulated deformation. **(C)** and **(F)** Corresponding residuals. Positive values represent movement toward the satellite, while negative values represent movement away from the satellite.

optimal dip angle and smoothing coefficients were determined by obtaining global minima of 81° and 1.2, respectively (**Figure 7**).

Finally, we obtained the best-fitting slip model shown in **Figure 8**, suggesting that this event ruptured on a dextral strike-slip fault with a strike of ~139°, a dip of ~81°, and an average rake angle of -170°. A slip was concentrated mainly at depths of 2–8 km and spanned a distance of 20 km. The maximum amount of slip reached 0.5 m at a depth of 6 km, and the corresponding moment magnitude was Mw 6.1. **Figure 9** represents the observed displacements, simulated results derived from the optimal slip model, and residuals between the observation and simulation. Our distributed slip model can sufficiently explain the general deformation pattern from both tracks. There are no notable residual fringes except for some contributions from the atmospheric disturbance in the far field (**Figures 9C,F**), which suggest that the inversion results are stable and reliable.

DISCUSSION

Verification of the Field Investigation Results

Seismic activity produces ground fissures due to either shear or tensile stresses that alter the stress state of rock and soil masses near the Earth's surface (Li C. et al., 2021). To accurately map and quantitatively measure the surface rupture associated with the Yangbi earthquake, we carried out a field investigation around the epicenter of this event. No obvious surface rupture was found, but we discovered that many fresh cracks had formed during the earthquake. By measuring the trends of

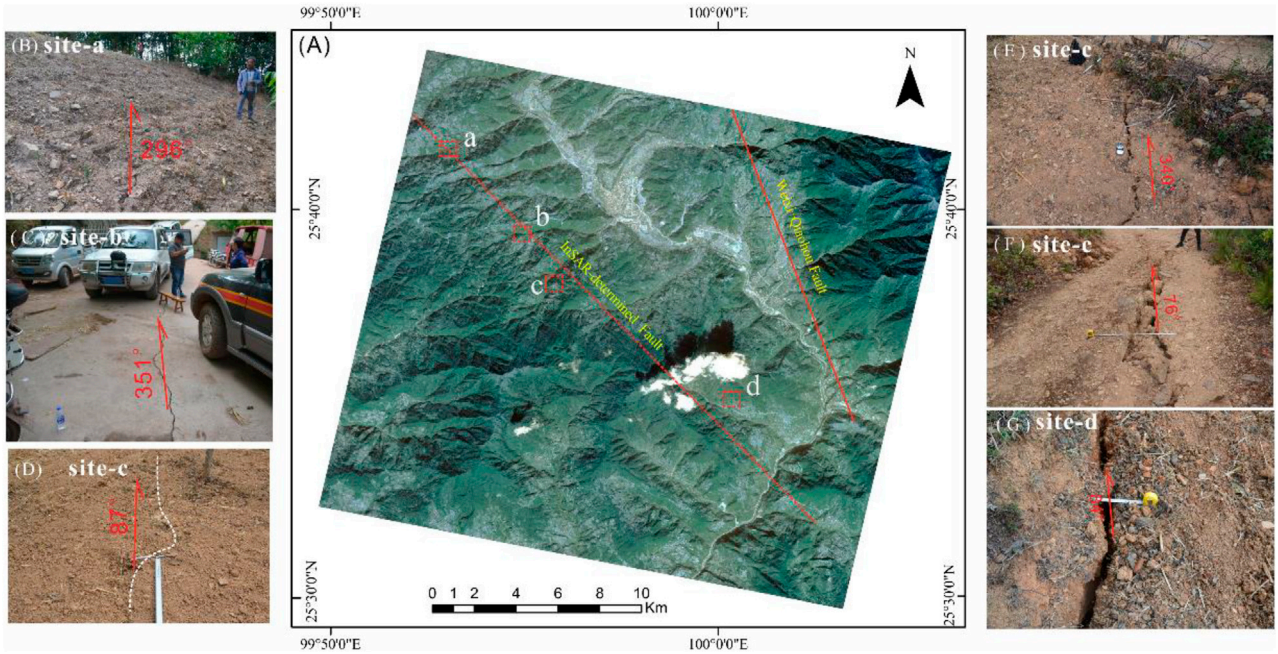

FIGURE 10 | Remote sensing images of the epicenter of the Yangbi earthquake and its on-site photos of ground fissures. **(A)** Optical image of the earthquake epicenter acquired on 19 November 2020, by the Gaofen-2 sensor, The red dotted line indicates the estimated fault of this event. The solid red line represents the Weixi-Qiao fault **(B)** Field photo of the ground fissure at point a, **(C)** reveals point b **(D)**, **(E)**, **(F)** represent point c, and **(G)** indicates point d.

these fissures in the field, we determined that these fissures trend mostly NW–SE, and the fissures show the characteristics of dextral strike-slip. The spatial distribution of crack locations illustrates that the fissured area is roughly distributed in a NW–SE strip that is completely consistent with the fault determined from InSAR (**Figure 10**). These ground fissures have obvious directionality, and their strikes are consistent with that of the rupturing fault. Therefore, we infer that their locations are controlled by the fault. We selected several representative points for analysis. At points a and b in **Figure 10A**, the spatial orientations of the ground fissures are basically consistent with those of the inferred fault (**Figures 10B,C**). In contrast, those of the ground fissures at points c and d are disordered, with the ground fissures distributed in all directions (**Figures 10D–G**). We stipulate that this irregular distribution results from slope and terrain influences. There are no obvious surface cracks near the Weixi–Qiaohou fault, which has a low earthquake intensity. Therefore, the field investigation further verified that the seismogenic structure of the earthquake was a new NW-trending blind fault.

Rupture Structure and Seismogenic Mechanism

The Weixi–Qiaohou, Red River, Jinshajiang, and Deqin–Zhongdian–Daju faults constitute the western boundary of the active Sichuan–Yunnan block. They, therefore, play essential roles in the formation, evolution, and movement of the block (Li et al., 2021). Specifically, the southwestern boundary of the Sichuan–Yunnan block exhibits a high strike-slip rate in response to the lateral extrusion of crustal material from the Qinghai–Tibet Plateau. The boundary of the block is not a single fault but rather a group of dispersed and complex dextral strike-slip faults (Long et al., 2021). The evolutionary history of these faults reflects mutual structural transformation, stress generation, and strain weakening between them. The tectonic interactions, stresses, and deformation among these faults may constitute the main mechanism of absorbing the eastward extrusion of the Qinghai–Tibet Plateau. In this process, some fault activities weaken, and new faults arise with the expansion of existing major faults.

The fault location determined by InSAR and the spatial distribution of relocated aftershocks show that the seismogenic fault of the Yangbi earthquake is far from known active faults and is approximately 4–10 km from the nearest segment of the Weixi–Qiaohou–Weishan fault zone (Fig. 11). According to the characteristics of coseismic deformation, the seismogenic segment belongs to a branch fault at the junction between the Weixi–Qiaohou–Weishan fault and Red River fault zones and may be a secondary fault of the Weixi–Qiaohou–Weishan fault (Chang et al., 2016b; Yang J. et al., 2021). The seismogenic fault is associated with and parallel to the Weixi–Qiaohou fault. The formation of this structure may be related to the southeastward motion of the Sichuan–Yunnan block and the clockwise rotation in SW Yunnan (Fig. 11). The clockwise rotation in SW Yunnan exerts a drag force on the SW wall of the NW-SE-trending

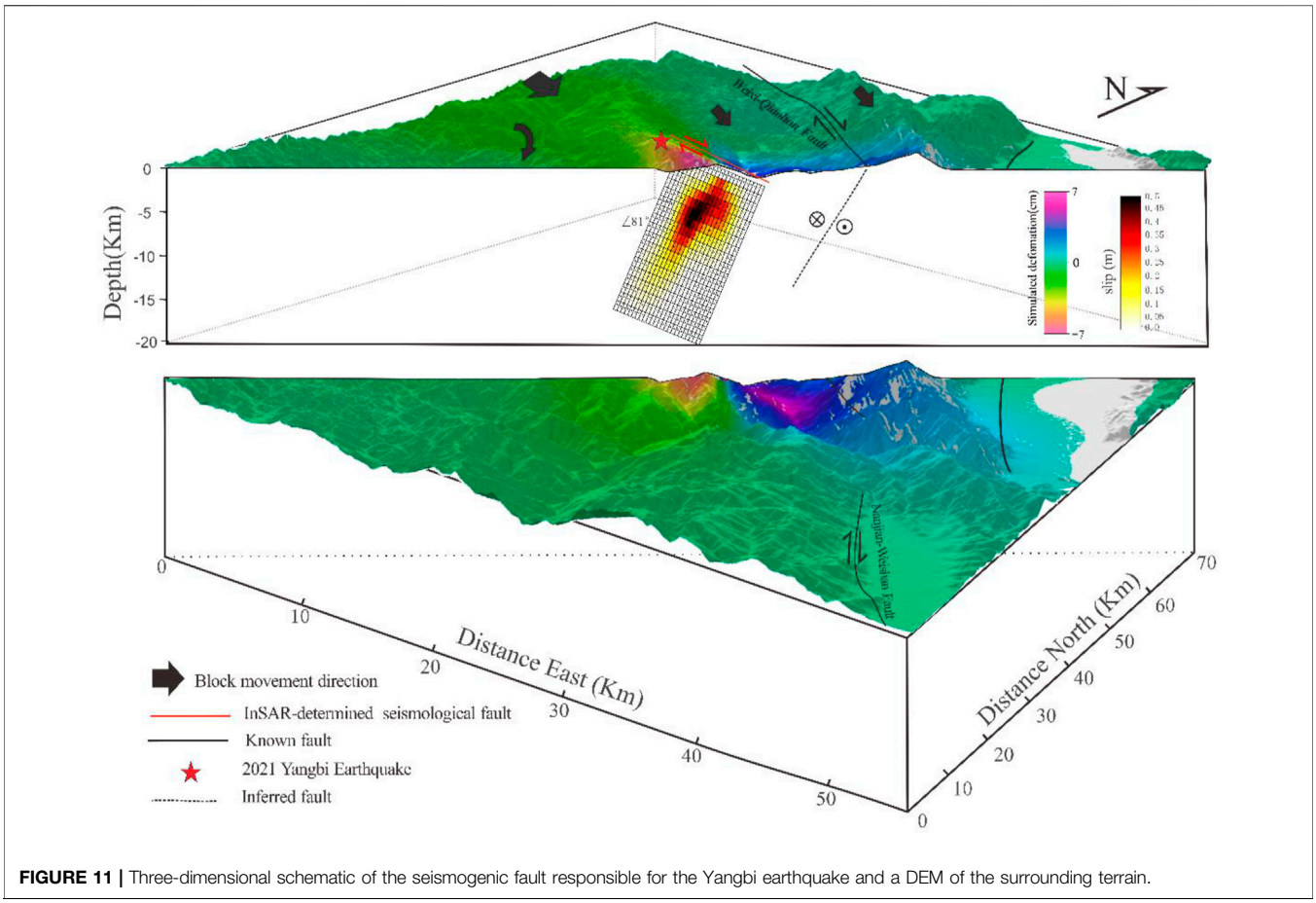

FIGURE 11 | Three-dimensional schematic of the seismogenic fault responsible for the Yangbi earthquake and a DEM of the surrounding terrain.

seismogenic fault. This may be the main dynamic cause of this quake event. In addition, the EW extension results in the dip component of the fault (Chang et al., 2016a; Long et al., 2021).

Stress Change Background of Earthquake Occurrence

The Yangbi event was a strong earthquake that occurred on a secondary fault in the Sichuan–Yunnan block. The characteristics of the regional stress field are critical to understanding its seismogenic mechanism. Thus, the focal mechanism solutions of 27 strong historical earthquakes (Mw > 6.5) in this region (Li et al., 2020; Zhang et al., 1989) were utilized to estimate the stress tensor (Gephart and Forsyth, 1984; Wan, 2015), and then we obtained the three principal stress directions and stress shape factors on a 0.1°×0.1° grid (Angelier, 1979).

Using the optimal stress tensor obtained from the method of Li et al. (2020), the potential rupture plane of future strong earthquakes in the region was determined (**Figure 12**). The NW–SE-trending seismogenic faults in the vicinity of the Yangbi earthquake epicenter are characterized by dextral strike-slip, which is consistent with the InSAR inversion results (139°/81°/-170°), the focal mechanism parameters derived from seismological data (Long Y. et al., 2021; Wang Y. et al., 2021b), and the fault motion characteristics implied by the

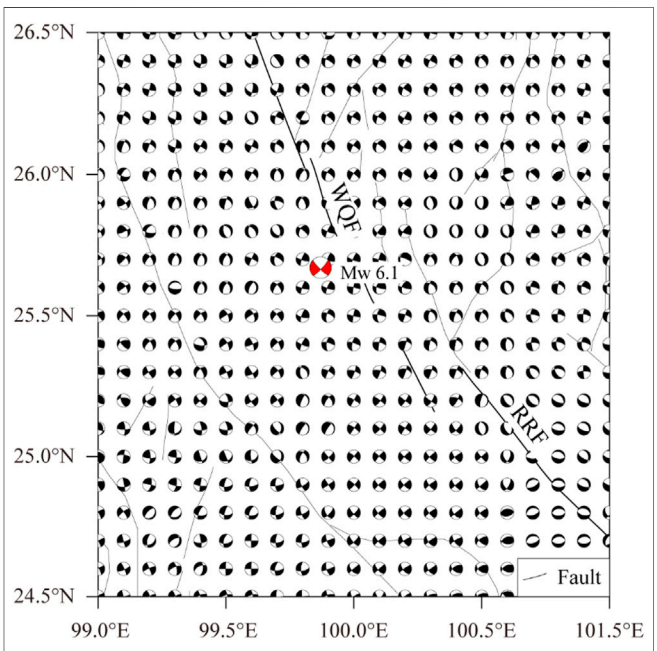

FIGURE 12 | The potential rupture plane of future strong earthquakes in the region is determined based on historical earthquake focal mechanisms (WQF: Weixi-Qiaohou fault; RRF: Red River fault).

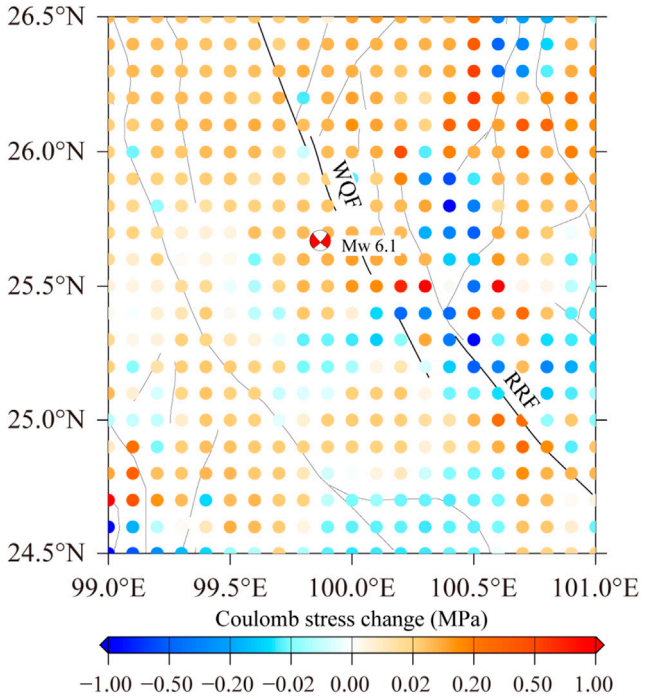

FIGURE 13 | Coulomb stress changes in the area surrounding the Yangbi earthquake epicenter and potential rupture planes caused by strong historical earthquakes (WQF: Weixi–Qiaohou fault; RRF: Red River fault).

focal mechanisms of aftershocks (Zhang et al., 2022). The direction of the maximum principal compressive stress and principal compressive strain in the region is NNW–SSE (Hu et al., 2017; Wang and Shen, 2020), which can effectively explain the seismogenesis of the Yangbi earthquake and the earthquakes in the surrounding area dominated by dextral strike-slip.

Since the occurrence of the Yangbi earthquake, many studies have focused on the impact of the earthquake on the future seismic risk of the surrounding faults (Yang Z. et al., 2021; Zhang B. et al., 2021), although few studies have addressed the possible relationship between the Yangbi earthquake and strong historical earthquakes in the region. Based on the potential rupture planes of future strong earthquakes shown in **Figure 13**, the optimal and auxiliary rupture planes were used as the receiving fault for a stress tensor projection. The maximum Coulomb stress was selected to represent the stress change at the source (Toda and Enescu, 2011) to analyze the changes in the Coulomb stress on the seismogenic fault caused by strong historical earthquakes. The historical earthquake source model and medium model are referred to Li Y. et al. (2020). According to the resulting Coulomb stress changes (**Figure 12**), strong historical earthquakes produced an obvious stress increase at the epicenter of the Yangbi earthquake, and the stress increment exceeded the stress trigger threshold of 0.1 bar, which promoted the occurrence of the Yangbi earthquake. In addition, we found the northwestern RRF is also within the influence scope of positive Coulomb stress changes, which inferred that the northwestern RRF is an area requiring special attention.

CONCLUSION

In this study, the coseismic deformation field produced by the Yangbi earthquake that occurred on 21 May 2021, was derived from Sentinel-1 ascending and descending track data. Taking the deformation fields as constraints, a two-step inversion strategy was applied to estimate the geometric structure and slip distribution of the rupture plane. The PSOKINV method was employed to find the best solution that minimizes the fitting function in the whole parameter domain. The inferred optimal slip model suggests that the rupture surface of the earthquake trends NNW–SSE and is predominantly a steeply dipping dextral strike-slip fault. This reveals that the coseismic slip distribution was controlled by secondary faults west of the Weixi–Qiaohou fault. The earthquake nucleated at a shallow depth on the rupture plane, and the major seismogenic fault was a dextral strike-slip fault with a strike of ~139°, a dip of ~81° to the southwest, and an average rake angle of -170°. A maximum slip of ~0.5 m was achieved at a depth of 6 km. The cumulative seismic moment reached up to 1.43×10^{18} N·m, equivalent to a magnitude of Mw 6.1. According to the resulting Coulomb stress changes, the strong historical earthquakes produced an obvious stress increase at the epicenter of the Yangbi earthquake and promoted the occurrence of the Yangbi earthquake. The efficient and accurate analysis of the focal mechanism of the Yangbi earthquake is of great significance for interpreting coseismic deformation characteristics and facilitating the rapid deployment of earthquake emergency rescue personnel. Moreover, this work is expected to benefit further research on the geological structure and kinematic mechanism of the Weixi–Qiaohou fault and the active prediction of geological disasters.

DATA AVAILABILITY STATEMENT

The original contributions presented in the study are included in the article/Supplementary Material, further inquiries can be directed to the corresponding author.

AUTHOR CONTRIBUTIONS

YL contributed to the conception of the study, performed the experiment and writen YL contributed to the conception of the study, performed the data analyses and wrote the manuscript KL performed the field inverestment and analyses HL contributed significantly to analysis and manuscript preparation WJ helped perform the analysis with constructive discussions.

FUNDING

This research is partly supported by research grants from the National Institute of Natural Hazards, MEMC (grant

numbers No. ZDJ 2019-17); the National Natural Science Foundation of China (no. 41704051,41772219); National Key Research and Development Program of China (2021YFC3001903) and Gaofen earthquake monitoring and emergency application demonstration (phase II) (31_Y30F09-9001-20/22).

REFERENCES

Angelier, J. (1979). Determination of the Mean Principal Directions of Stresses for a Given Fault Population. *Tectonophysics* 56, T17–T26. doi:10.1016/0040-1951(79)90081-7

Burgmann, R., Ayhan, M. E., Fielding, E. J., Wright, T. J., McClusky, S., Aktug, B., et al. (2002). Deformation during the 12 November 1999 Duzce, Turkey, Earthquake, from GPS and InSAR Data. *Bull. Seismological Soc. America* 92, 161–171. doi:10.1785/0120000834

Chang, Z., Chang, H., and Dai, B. (2016b). Recent Active Features of Weixi-Qiaohou Fault and its Relationship with the Honghe Fault. *Journal geomechanics* 22 (3), 517

Chang, Z., Chang, H., Li, J., Dai, B., Zhou, Q., Zhu, J., et al. (2016a). The Characteristic of Active Normal Faulting of the Southern Segment of Weixi-Qiaohou Fault. *Joural Seismological Res.* 39 (4).

Chen, C. W., and Zebker, H. A. (2000). Network Approaches to Two-Dimensional Phase Unwrapping: Intractability and Two New Algorithms. *J. Opt. Soc. Am. A.* 17 (3), 401–414. doi:10.1364/josaa.17.000401

Duan, M., Zhao, C., Zhou, L., Zhao, C., and Zuo, K. (2021). Seismogenic Structure of the May 21 2021 MS6.4 Yunnan Yangbi Earthquake Sequence. *Chin. J. Geophys.* 64 (9), 3111–3125. doi:10.6038/cjg2021P0423

Feng, W., Li, Z., Elliott, J. R., Fukushima, Y., Hoey, T., Singleton, A., et al. (2013). The 2011 MW 6.8 Burma Earthquake: Fault Constraints provided by Multiple SAR Techniques. *Geophys. J. Int.* 195, 650–660. doi:10.1093/gji/ggt254

Feng, W., Samsonov, S., Almeida, R., Yassaghi, A., Li, J., Qiu, Q., et al. (2018). Geodetic Constraints of the 2017 M W 7.3 Sarpol Zahab, Iran Earthquake, and its Implications on the Structure and Mechanics of the Northwest Zagros Thrust-Fold Belt. *Geophys. Res. Lett.* 45 (14), 6853–6861. doi:10.1029/2018gl078577

Feng, W., Samsonov, S., Liang, C., Li, J., Charbonneau, F., Yu, C., et al. (2019). Source Parameters of the 2017Mw 6.2 Yukon Earthquake Doublet Inferred from Coseismic GPS and ALOS-2 Deformation Measurements. *Geophys. J. Int.* 216 (3), 1517–1528. doi:10.1093/gji/ggy497

Gephart, J. W., and Forsyth, D. W. (1984). An Improved Method for Determining the Regional Stress Tensor Using Earthquake Focal Mechanism Data: Application to the San Fernando Earthquake Sequence. *J. Geophys. Res.* 89, 9305–9320. doi:10.1029/jb089ib11p09305

Goldstein, R. M., Zebker, H. A., and Werner, C. L. (1988). Satellite Radar Interferometry: Two-Dimensional Phase Unwrapping. *Radio Sci.* 23 (4), 713–720. doi:10.1029/RS023i004p00713

Hu, J., Zhao, T., Bai, C., Guo, H., Wang, Y., Li, X., et al. (2021). Three-dimensional P and S Wave Velocity Structure and Earthquake Relocation of the May 21, 2021 Yangbi MS6.4 Source Region. *Chin. J. Geophys.* 64 (12), 4488–4509. doi:10.6038/cjg2021P0456

Hu, X., Zang, A., Heidbach, O., Cui, X., Xie, F., and Chen, J. (2017). Crustal Stress Pattern in China and its Adjacent Areas. *J. Asian Earth Sci.* 149, 20–28. doi:10.1016/j.jseaes.2017.07.005

Li, B., Li, Y., Jiang, W., Su, Z., and Shen, W. (2020). Conjugate Ruptures and Seismotectonic Implications of the 2019 mindanao Earthquake Sequence Inferred from Sentinel-1 InSAR Data. *Int. J. Appl. Earth Observation Geoinformation* 90, 102127. doi:10.1016/j.jag.2020.102127

Li, Y., Shi, F. Q., Zhang, H., Wei, W. X., Xu, J., and Shao, Z. G. (2020). Coulomb Stress Change on Active Faults in Sichuan-Yunnan Region and its Implications for Seismic hazard. *Seismol. Geol.* 42, 526

Li, C., Zhang, J., Wang, W., Sun, K., and Shan, X. (2021). The Seismogenic Fault of the 2021 Yunnan Yangbi Ms6.4 Earthquake. *Seismology Geology.* 43 (3), 706

Li, D., Ding, Z., Wu, P., Liu, S., Deng, P., Liu, S., et al. (2021). The Characteristics of Crustal Structure and Seismogenic Background of Yangbi MS6.4 Earthquake on May 21, 2021 in Yunnan Province, China. *Chin. J. Geophys.* 64 (9), 3083–3100. doi:10.6038/cjg2021P0405

Li, K., Li, Y., Tapponnier, P., Xu, X., Li, D., and He, Z. (2021). Joint InSAR and Field Constraints on Faulting during the Mw 6.4, July 23, 2020, Nima/Rongma Earthquake in central Tibet. *J. Geophys. Res. Solid Earth* 126, e2021JB022212. doi:10.1029/2021jb022212

Li, Y., Jiang, W., Zhang, J., Li, B., Yan, R., and Wang, X. (2021). Sentinel-1 SAR-Based Coseismic Deformation Monitoring Service for Rapid Geodetic Imaging of Global Earthquakes. *Nat. Hazards Res.* 1 (1), 11–19. doi:10.1016/j.nhres.2020.12.001

Liu, J., Gan, W., Wang, G., Wang, Z., Zhang, Y., and Cai, H., L. (2021). Seismic Moment Tensor and Seismogenic Structure of the Yangbi MS6.4 Earthquake Sequence on May 21, 2021 in Yunnan. *Chin. J. Geophys.* 64 (12), 4475–4487. doi:10.6038/cjg2021P0559

Lohman, R. B., and Simons, M. (2005). Some Thoughts on the Use of InSAR Data to Constrain Models of Surface Deformation: Noise Structure and Data Downsampling. *Geochem. Geophys. Geosyst.* 6, a–n. doi:10.1029/2004GC000841

Long, F., Qi, Y. P., Yi, G. X., Wu, W. W., Wang, G. M., Zhao, X. Y., et al. (2021). Relocation of the Ms 6.4 Yangbi Earthquake Sequence on May 21, 2021 in Yunnan Province and its Seismogenic Structure Analysis. *Chin. J. Geophys.* 64, 263

Parsons, B., Wright, T., Rowe, P., Andrews, J., Jackson, J., Walker, R., et al. (2006). The 1994 Sefidabeh (Eastern Iran) Earthquakes Revisited: New Evidence from Satellite Radar Interferometry and Carbonate Dating about the Growth of an Active Fold above a Blind Thrust Fault. *Geophys. J. Int.* 164, 202–217. doi:10.1111/j.1365-246x.2005.02655.x

Ren, J., Zhang, S., Hou, Z., and Liu, X. (2007). Study of Late Quaternary Slip Rate in the Mid-segment of the Tongdian-Weishan Fault. *Seismology Geology.* 29 (4), 756

Su, J., Liu, M., Zhang, Y., Wang, W., Li, H., Yang, J., et al. (2021). High Resolution Earthquake Catalog Building for the May 21 2021 Yangbi, Yunnan, MS6.4 Earthquake Sequence Using Deep-Learning Phase Picker. *Chin. J. Geophys* 64 (8), 2647–2656. doi:10.6038/cjg2021O0530

Tadono, T., Ishida, H., Oda, F., Naito, S., Minakawa, K., and Iwamoto, H. (2014). Precise Global DEM Generation by ALOS PRISM. *ISPRS Ann. Photogramm. Remote Sens. Spat. Inf. Sci.* II-4, 71–76. doi:10.5194/isprsannals-ii-4-71-2014

Toda, S., and Enescu, B. (2011). Rate/state Coulomb Stress Transfer Model for the CSEP Japan Seismicity Forecast. *Earth Planet. Sp* 63, 171–185. doi:10.5047/eps.2011.01.004

Wan, Y. G. (2015). A Grid Search Method for Determination of Tectonic Stress Tensor Using Qualitative and Quantitative Data of Active Faults and its Application to the Urumqi Area. *Chin. J. Geophys.* 58, 3144

Wang, M., and Shen, Z.-K. (2020). Present-Day Crustal Deformation of Continental China Derived from GPS and its Tectonic Implications. *J. Geophys. Res.* 125, e2019JB018774. doi:10.1029/2019jb018774

Wang, S., Liu, Y., and Shan, X. (2021). Coseismic Surface Deformation and Slip Models of the 2021 Ms6.4 Yangbi (Yunnan, China) Earthquake. *Seismology Geology.* 43 (3), 692

Wang, Y., Chen, K., Shi, Y., Zhang, X., Chen, S., Li, P. e., et al. (2021b). Source Model and Simulated Strong Ground Motion of the 2021 Yangbi, China Shallow Earthquake Constrained by InSAR Observations. *Remote Sensing* 13, 4138. doi:10.3390/rs13204138

Wang, Y., Hu, S., He, X., Guo, K., Xie, M., Deng, S., et al. (2021a). Relocation and Focal Mechanism Solutions of the May 21 2021 MS6.4 Yunnan Yangbi Earthquake Sequence. *Chin. J. Geophys.* 64 (12), 4510–4525. doi:10.6038/cjg2021P0401

Yang, J., Wen, Y., and Xu, C. (2021). The May 21 2021 MS6.4 Yangbi (Yunnan) Earthquake: A Shallow Strike-Slip Event Rupturing in a Blind Fault. *Chin. J. Geophys.* 64 (9), 3101–3110. doi:10.6038/cjg2021P0408

Yang, Z., Liu, J., Liu, J., Zhang, X.-M., Deng, W., Du, G., et al. (2021). A Preliminary Report of the Yangbi, Yunnan, MS6.4 Earthquake of May 21, 2021. *Earth Planet. Phys.* 5 (4), 1–3. doi:10.26464/epp2021036

Ye, T., Chen, X., Huang, Q., and Cui, T. (2021). Three-dimensional Electrical Resistivity Structure in Focal Area of the Yangbi Ms6.4 Earthquake and its Possible Seismogenic Mechanism. *Chin. J. geophys.* 64 (7), 2267–2276. doi:10.6038/cjg2021O0523

Yu, C., Li, Z., Penna, N. T., and Crippa, P. (2018). Generic Atmospheric Correction Model for Interferometric Synthetic Aperture Radar Observations. *J. Geophys. Res. Solid Earth* 123 (10), 9202–9222. doi:10.1029/2017jb015305

Zhang, C., Cao, X., and Qu, K. (1989). *Earthquake Focal Mechanism in China*. Beijing: Academic Books Press.

Zhang, Y., An, Y., Long, F., Zhu, G., Qin, M., Zhong, Y., et al. (2022). Short-Term Foreshock and Aftershock Patterns of the 2021 Ms 6.4 Yangbi Earthquake Sequence. *Seismological Soc. America* 93, 21–32. doi:10.1785/0220210154

Zhang, B., Xu, G., Lu, Z., He, Y., Peng, M., and Feng, X. (2021). Coseismic Deformation Mechanisms of the 2021 Ms 6.4 Yangbi Earthquake, Yunnan Province, Using InSAR Observations. *Remote Sensing* 13, 3961. doi:10.3390/rs13193961

Zhang, K., Gan, W., Liang, S., Xiao, G., Dai, C., Wang, Y., et al. (2021). Coseismic Displacement and Slip Distribution of the 2021 May 21, Ms6.4, Yangbi Earthquake Derived from GNSS Observation. *Chin. J. geophys.* 64 (7), 2053–2266. doi:10.6038/cjg2021O0524

Conflict of Interest: The authors declare that the research was conducted in the absence of any commercial or financial relationships that could be construed as a potential conflict of interest.

frontiers | Frontiers in Environmental Science

ORIGINAL RESEARCH
published: 28 April 2022
doi: 10.3389/fenvs.2022.883427

Automatic Identification of Slope Active Deformation Areas in the Zhouqu Region of China With DS-InSAR Results

Yuanjian Wang[1], *Ximin Cui*[1]*, *Yuhang Che*[1], *Peixian Li*[1], *Yue Jiang*[2] *and Xiaozhan Peng*[1]

[1]School of Geoscience and Surveying Engineering, China University of Mining and Technology (Beijing), Beijing, China, [2]School of Environment Science and Spatial Informatics, China University of Mining and Technology, Xuzhou, China

Zhouqu has narrow terrain and steep mountains on both sides of the Bailong River. It is one of the most serious landslide disaster areas in China due to the fracture development of rock and complex geological conditions. To identify the slope active deformation areas (SADAs) in the region accurately, the Distributed Scatter Interferometric Synthetic Aperture Radar (DS-InSAR) technique was used based on the process of the sentinel ascending and descending orbit data. Deformation results of the region from January 2019 to February 2021 were obtained. A new method for automatically identifying SADA while accounting for radar geometric distortion was established to quickly and efficiently identify SADA from the large-scale deformation results in the region. The SADA identified by this method can eliminate the region affected by geometric distortion. Based on the method, 62 SADAs including 12 in the upstream and 50 in the downstream of Zhouqu County were identified. Compared with 12 typical landslide areas in the study area, 9 typical landslides match with the detected SADA. The SADA is mainly concentrated in the section from the downstream of Zhouqu County to Lianghekou, and statistical analysis showed that the vegetation coverage and topographic slope angle are two main reasons for this difference. At the same time, the analysis of the typical landslide time-series deformation reveals that the slope deformation activity mainly takes place during the rainy season. It has high correlation with precipitation. These results of the study provided an important reference for geological disaster prevention in the Zhouqu region.

Keywords: DS-InSAR, slope active deformation areas, automatic identification, geometric distortion, temporal and spatial characteristics

OPEN ACCESS

Edited by:
Chen Yu,
Newcastle University, United Kingdom

Reviewed by:
Yang Liu,
Wuhan University, China
Fatma Canaslan Çomut,
Ministry of Interior Disaster and Emergency Management Presidency, Turkey
Elena Nikolaeva,
Serco (United Kingdom), United Kingdom

***Correspondence:**
Ximin Cui
cxm@cumtb.edu.cn

Specialty section:
This article was submitted to Environmental Informatics and Remote Sensing, a section of the journal Frontiers in Environmental Science

Received: *25 February 2022*
Accepted: *30 March 2022*
Published: *28 April 2022*

Citation:
Wang Y, Cui X, Che Y, Li P, Jiang Y and Peng X (2022) Automatic Identification of Slope Active Deformation Areas in the Zhouqu Region of China With DS-InSAR Results. Front. Environ. Sci. 10:883427. doi: 10.3389/fenvs.2022.883427

1 INTRODUCTION

The process and phenomenon of slope geotechnical body sliding downward with a certain acceleration along the continuous penetrating damage surface is called landslide (Aleotti and Chowdhury 1999). As the global population continues to grow and the interaction between man and nature intensifies, the landslide has become one of the serious natural disasters threatening human survival and development, and especially under the influence of heavy rainfall and earthquake, the damage caused by landslide disaster is more serious (Schuster and Highland 2007; Zhang et al., 2020). The movement of landslides is sliding rather than tipping or rolling. Slow landslide movements last longer, usually not catastrophically and suddenly, and do not

terminate the movement immediately (Sun et al., 2016; Kavoura et al., 2020; Novellino et al., 2021). Slope angle, height, rock weathering, fissures, geological structure, hydrogeological conditions, etc. are all factors that cause landslides (Dai et al., 2002; Vilímek et al., 2021). Quickly identifying the deformation of slope areas can provide help for landslide investigation and interpretation. The Zhouqu region is a typical geological disaster-prone area, and there have been many geological disaster events in the history of the area. Several large mudslide disasters occurred around the Zhouqu region in 1978, 1989, 1992, and 2010, which caused great loss of life and property (Zhang et al., 2018; Dai et al., 2021). The Xieliupo landslide, which was in the downstream of the county, has continued to deform, and a large landslide occurred in 1981, causing blockage of the river and inundation of villages (Sun et al., 2015). The Suoertou landslide located in the upstream of Zhouqu County, with its landslide volume of tens of millions of cubic meters, has been in the creeping slip deformation stage since the last century after the resurrection. On 8 August 2010, a mudslide formed in the northern mountainous area of the Zhouqu region due to heavy rainfall, causing most of the Zhouqu region to be destroyed and death of 1,765 people, and on 12 July 2018, a large-scale destabilization occurred in the landslide of Jiangdingya in Nanyu Township, blocking the Bailong River to form a weir, making the issue of landslide stability in the region once again attract great attention from all walks of life (Wang 2013; Zhang et al., 2016). Therefore, early identification of the SADA in the region is important to protect the lives and properties of local residents and infrastructure safety.

In the past decade, landslides in the Zhouqu region have become a hot spot for geological hazard research. Numerous scholars have conducted research from the perspectives of landslide genesis, hazard evaluation, and detection methods. Bai et al. (2012) evaluated the landslide susceptibility of the Zhouqu area using GIS and logistic regression models. Cui et al. (2013) studied the influence of complex topography and landscape on the scale of landslide and debris flow disasters in the Zhouqu region. Jiang et al. (2016) discussed the activity mechanism of the Xieliupo landslide using GPS monitoring data. Zhang et al. (2018) used InSAR technology to identify the slow landslides in the Zhouqu region and analyzed the patterns of the movements of typical landslides. Dai et al. (2021) used InSAR technology to identify landslides around Zhouqu county. InSAR is increasingly used by researchers in landslide monitoring, and although the technology is limited in sudden landslide monitoring, it has a promising future in the fields of wide-area potential landslide identification and slow landslide activity pattern research.

Traditional surface deformation monitoring techniques and means, such as level measurement and GPS measurement, are characterized by high monitoring accuracy and flexibility. However, with the increasing requirements of deformation monitoring, these point-based surface deformation monitoring techniques and means have the shortcomings of large workload, high cost, and low spatial sampling rate, which can hardly meet the requirements of a long-time and large-scale surface deformation monitoring. With the development of space geodesy technology, Interferometric Synthetic Aperture Radar (InSAR), which is an important method for deformation monitoring, has gradually matured and is widely used in deformation monitoring (Hilley et al., 2004; Zhao et al., 2012; Wild et al., 2018). The Differential InSAR (D-InSAR) is susceptible to the influence of atmospheric and spatio-temporal decoherence factors. In order to overcome the disadvantages of the D-InSAR technique, Ferretti et al. (2001) proposed the Persistent Scatterer InSAR (PS-InSAR) algorithm in 2001, which can effectively weaken the effects of atmospheric delay and spatio-temporal decoherence by detecting and calculating the features (such as buildings, concrete dikes, rocks, and artificial corner reflectors) that can maintain strong and stable characteristics to radar waves in long time sequences. Compared with persistent scatterers, the unstable phase of radar echoes of concrete, fields, and other surface features targets limits the PS-InSAR point target extraction and reduces the spatial sampling rate of deformation information. To compensate for the disadvantage of the PS-InSAR technique in the poorly coherent region with small point density, Ferretti et al. (2011)proposed a method to combine PS points and Distributed Scatter (DS) points for solving, which is based on the feature that similar DS points have the same statistical properties, and the density of points is increased by screening DS points with specific thresholds to obtain more detailed surface deformation information, which is suitable for natural scenes such as landslides in mountainous areas. InSAR technology can not only capture landslide signals on a large scale from the spatial scale but also orbit the movement of landslides in a longer period from the temporal scale, which has unique monitoring advantages such as long time, large range, fast acquisition, and accuracy.

In the high mountain canyon area, due to the characteristics of synthetic aperture radar and side-view imaging, SAR images inevitably show geometric distortion phenomena (including shadow, layover, and foreshortening), resulting in a decrease in the resolution, and the monitoring accuracy becomes low or even cannot be monitored (Cigna et al., 2014; Liu et al., 2018; Ren et al., 2021). Carrying out accurate qualitative and quantitative geometric distortion analysis can help to correctly judge the reliability of InSAR deformation monitoring results and improve the accuracy of SADA identification.

Conventional ground survey methods to identify potential landslides are time consuming and laborious, and numerous studies have been conducted using automatic and semi-automatic methods to identify Active Deformation Areas (ADAs) and then determine whether the target is a landslide. Barra et al. (2017) proposed a method to automatically identify ADA based on PS-InSAR results and update the geohazard database in real time; Luo et al. (2021) proposed a method for automatic identification and evaluation of geological hazards based on spatial and temporal characteristics of deformation. The automatic identification method can efficiently and accurately identify and separate potential landslide hazard areas from large-scale data.

In this study, the Sentinel-1A ascending and descending data covering the study area are processed by a time-series InSAR processing method that takes into account the DS points to obtain the deformation results of the study area. Based on previous

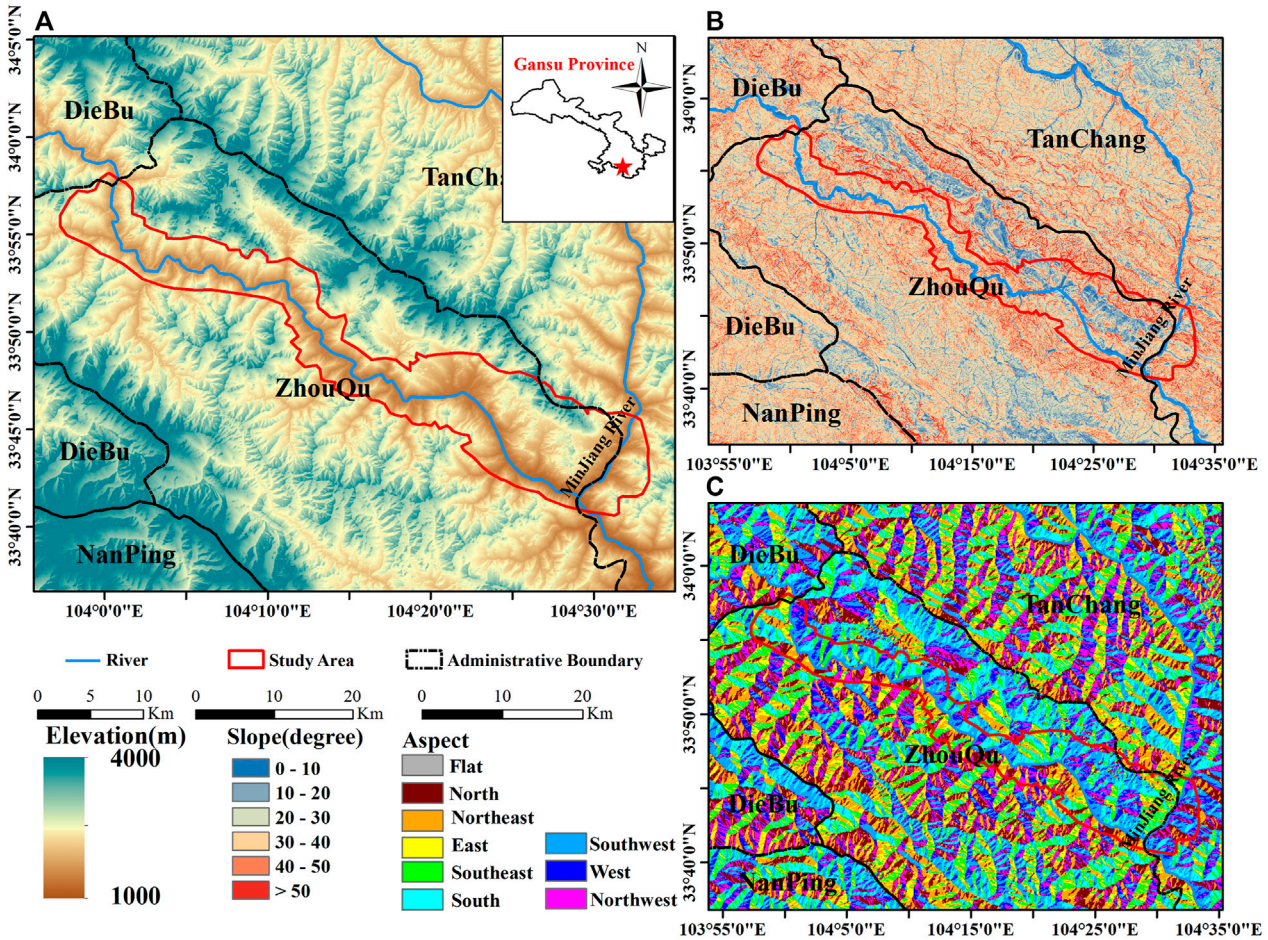

FIGURE 1 | Location map of the study area. **(A)** Elevation map. **(B)** Slope angle map. **(C)** Aspect map.

studies, an automatic identification method of SADA based on InSAR deformation results and terrain visibility is proposed. The method not only considers the spatial distribution of deformation in the monitoring area but also takes into account the visibility of SAR satellites in the monitoring area, which improves the accuracy of potential SADA identification and judgment. Based on the results of automatic identification and optical images and other information, this study analyzes the spatial and temporal characteristics of deformation of typical landslides in the study area. This study will provide a reference for automatic identification of deformation areas and active landslide prevention in complex terrain.

2 Study Area

The Bailong River Basin is located in the transition zone between the first and second terraces of China's landforms and is the intersection of three major geomorphic units: the Loess Plateau, the Sichuan Basin, and the Qinghai–Tibet Plateau. Affected by tectonic movements, concentrated rainfall, and human activities, landslides and mudslides are frequent and widespread in the basin, making it one of the four major geological disaster-prone areas in China (Ma et al., 2020). The Zhouqu region is located in the middle reaches of the Bailong River Basin in southern Gansu. The Bailong River enters from the northwest of the Zhouqu region and passes through the city in the southeast. The terrain is high in the west and low in the east. The elevation, slope, and aspect of the study area are shown in **Figure 1**. From the figure, it can be seen that the region has large mountains, deep ditches, and broken terrain, and the relative height difference between the valley peaks reaches more than 1,000 m, and the slope of the ditch is large, which is conducive to the development of gravity geological phenomena such as collapse (Zhang et al., 2016).

The average annual precipitation in the study area is 434 mm, which is low, but because the rain falls mostly from May to September and the rainfall is mostly in the form of continuous rain and heavy rainfall, this concentrated rainfall provides hydrodynamic conditions for the formation of landslide and debris flow geological disasters (Zhang and Matsushima, 2016). At the same time, due to the loose geological structure in the area, engineering activities such as slope reclamation, water conservancy, highway construction, and hydroelectric power

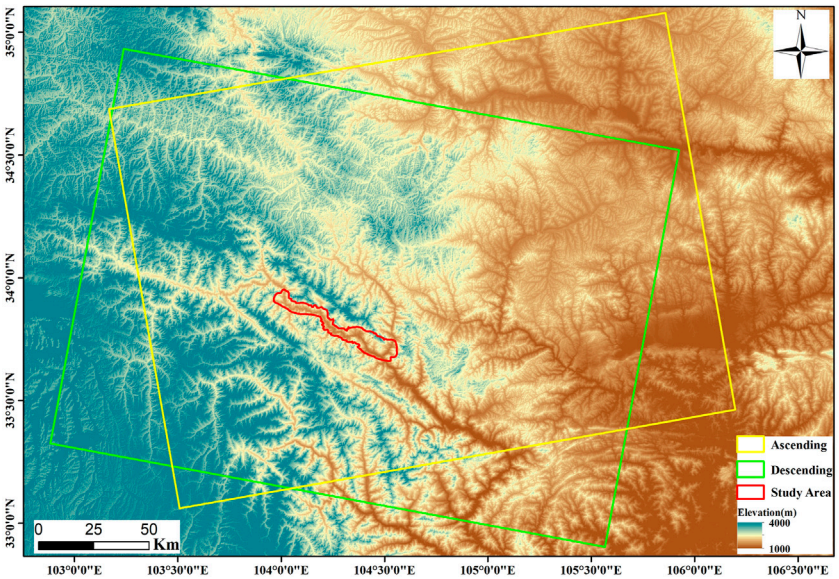

FIGURE 2 | The spatial coverage of the images used in the study.

TABLE 1 | SAR data parameters.

Satellite	Direction	Time	Angle of incidence	Heading	Resolution
Sentinel-1A	Ascending	20190104–20210210	36.26°	−10.44°	5m*20m
Sentinel-1A	Descending	20190104–20210210	39.15°	−169.85°	5m*20m

station construction directly destroy the rock structure of the slope and reduce the stability of the slope, even directly lead to landslides and landslides, coupled with the narrow terrain in the mountainous area, the unreasonable piling or random dumping of construction debris, etc., and deteriorate the already fragile ecological environment. In addition, the vegetation cover of the section from Zhouqu County to Lianghekou along the Bailong River is poor, and it is mainly debris landslides, most of which are rocky landslides re-activated, large in scale, mostly large and giant landslides, and large in number, mainly medium and deep landslides, which are the key areas of concern in this study.

3 DATA AND METHODS

3.1 Data

This study uses the 45 Sentinel-1A ascending images and 43 Sentinel-1A descending images covering the study area from January 2019 to February 2021 for estimating the deformation rate in the study area, and the data coverage is shown in **Figure 2**. The external reference DEM is required for terrain phase removal, geocoding, during the InSAR data processing. The DEM is also required for terrain visibility calculation, and the ALOS 12.5 m DEM provided by JAXA is used in this study. The basic parameters of Sentinel-1A data used are shown in **Table 1**.

3.2 Data Process

3.2.1 DS-InSAR

Compared with other monitoring targets, the surface of the slope is mostly covered with natural features and fewer artificial structures. PS-InSAR mostly monitors man-made feature targets, which is suitable for urban ground settlement monitoring, and it is difficult to obtain detailed and accurate deformation information for the monitoring of distributed scatterer targets such as grass and bare ground with fewer points extracted. Because the DS-InSAR method can improve the distribution density of points and obtain richer and more reliable deformation information for targets such as landslides, we use this method.

The DS-InSAR method to obtain the deformation mainly consists of the following steps:

(1) Selecting a master image: the temporal and spatial baselines between all image pairs are calculated, a temporal and spatial baseline distribution map is generated, and an image with the centered temporal and spatial baseline is selected as the master image.

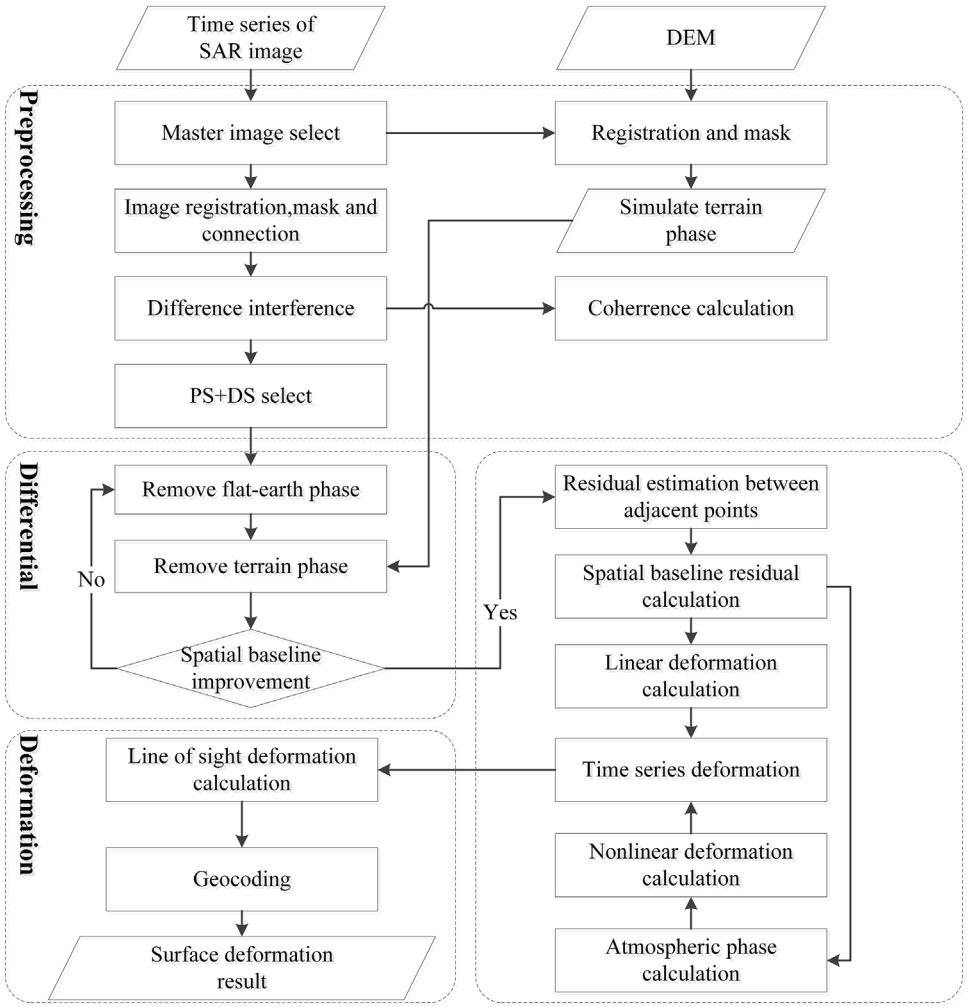

FIGURE 3 | DS-InSAR processing chain used in the study.

(2) Image coregistration: the SAR image is coregistered with the master image. The coregistration accuracy is greater than 0.001 pixels.
(3) Calculating the interferogram phase: all the coregistered images are combined with the master image in pairs according to the time series. The interferometric phase is calculated pixel by pixel to generate a time-series interferogram set.
(4) Selecting PS and DS: the selection of the DS consists of two main steps: homogeneous time dimensional filtering and phase optimization estimation. They are described in detail in the following.
(5) The flat earth phase and topographic phase are removed.
(6) From the differential interferometric phase, the spatio-temporal deformation is estimated and the time-series deformation phase of each point target is obtained.
(7) Deformation calculation: based on the radar wavelength parameters, the unwrapping phase is converted into millimeter-scale deformation variables in the line-of-sight direction.

Two key steps of the DS-InSAR technique are homogeneous pixel identification and phase reconstruction, respectively (Goel and Adam 2014; Fornaro et al., 2015; Cao et al., 2016). Distributed targets are usually represented as neighboring pixels with homogeneous scattering characteristics and obey the same statistical distribution on the time-series SAR magnitude images. Therefore, spatial adaptive filtering of the interferometric phase is generally performed first, and then, a statistical test is used to determine statistically homogeneous pixels for each pixel to extract distributed targets (Jiang et al., 2015). Since the spatial adaptive filtering causes the interferometric phases to not strictly satisfy the phase consistency, it is necessary to adopt a certain phase optimization algorithm to construct a set of single master image optimized phase values under the condition of phase consistency and obtain a set of best-fit phases after the adaptive multi-look process to minimize the effect of the decoherence phenomenon of the distributed targets.

In this study, spatial adaptive filtering based on the KS hypothesis testing method is used to identify homogeneous pixels, and phase triangulation is used to estimate the optimal phase. The KS

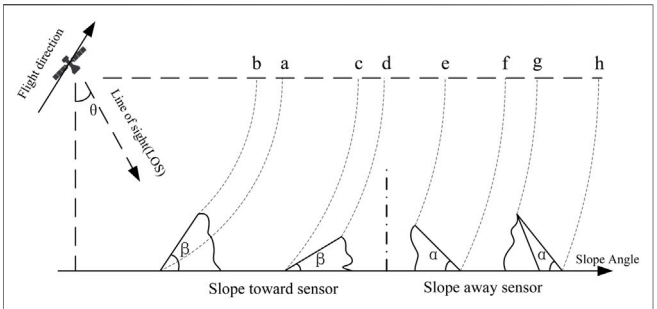

FIGURE 4 | Geometric distortion diagram of radar side-view imaging. When illuminated towards the satellite, foreshortening **(C–D)** occurs when the slope angle is less than or equal to, and layover **(B–A)** occurs when the slope angle is greater than. When backward facing the satellite, shadowing **(G–H)** occurs when the slope angle is greater.

hypothesis test is based on the cumulative distribution function and is used as a method to test whether a distribution conforms to a certain theoretical distribution or to compare whether two empirical distributions are significantly different from each other. In the time-series SAR image set, the backscattered intensity information of homogeneous pixels is similar in the time dimension, and when the test statistic of the intensity information in the time dimension of two pixels is less than the critical value at the significant level, the two pixels are considered to be homogeneous pixels. The DS-InSAR processing flow chart is shown in **Figure 3**.

3.2.2 Decomposition of Deformation Along the Aspect

In mountainous areas with complex topography, the surface deformation information is complicated, and it is difficult to obtain accurate surface deformation using single orbit data, especially for slope areas, where the deformation has a high correlation with slope angle and aspect. Therefore, this study adopts a combination of ascending and descending orbits and external DEM to obtain the deformation information along the aspect in the Nanyu landslide, and the results can more truly reflect the motion of unstable slopes. The relationship between the line-of-sight (LOS) deformation (D_{los}) and the three-dimensional motion can be shown as follows (Zhao et al., 2016):

$$D_{\mathrm{los}} = D_{\mathrm{u}} \cos\theta - D_n \sin\theta \cos\left(\alpha - \frac{3}{2}\pi\right) - D_e \sin\theta \sin\left(\alpha - \frac{3}{2}\pi\right), \tag{1}$$

where θ and α represent the radar incidence angle and satellite heading angle, D_n, D_e, and D_u represent the north–south direction deformation, the east–west direction deformation, and the vertical direction deformation, respectively.

Since the horizontal motion of a slope generally points along the aspect, it can be assumed that the deformation of a slope can be decomposed into two directions, D_{hor} and D_u, and then, the functional relationship for solving the joint ascending and descending can be expressed as follows:

$$\begin{pmatrix} D_u \\ D_{hor} \end{pmatrix} = \begin{pmatrix} \cos\theta_A, -\sin\theta_A \cos\left(\beta - \alpha_A + \frac{3}{2}\pi\right) \\ \cos\theta_D, -\sin\theta_D \cos\left(\beta - \alpha_D + \frac{3}{2}\pi\right) \end{pmatrix} \begin{pmatrix} D^A_{los} \\ D^D_{los} \end{pmatrix}, \tag{2}$$

where θ_A and θ_D are the radar incidence angles from the ascending and descending orbits, respectively; α_A and α_D are the satellite heading angles from the ascending and descending orbits, respectively; and β represents the aspect of the point. The final deformation along the aspect of the slope (D_f) can be expressed as

$$D_f = \sqrt{(D_{hor})^2 + (D_u)^2}. \tag{3}$$

3.2.3 Automatic Identification Method of SADA

The method of automatic identification SADA is divided into four steps:

(1) The DS-InSAR deformation results are read in a shapefile format. The data are spatially filtered by sliding window point

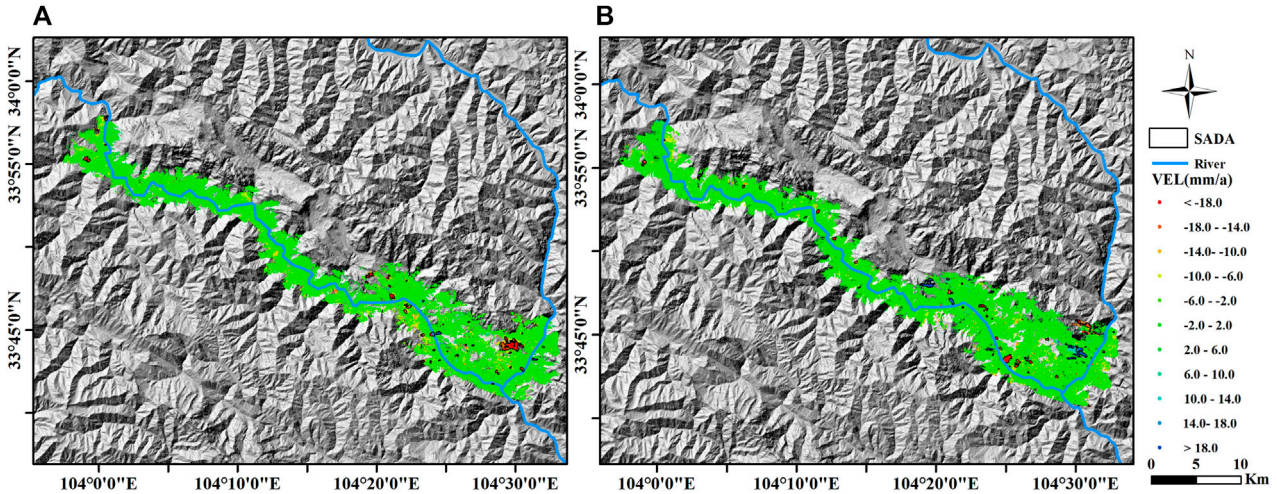

FIGURE 5 | Average deformation velocities in the LOS direction are derived from **(A)** ascending images and **(B)** descending images. The black boundary is the extent of each SADA.

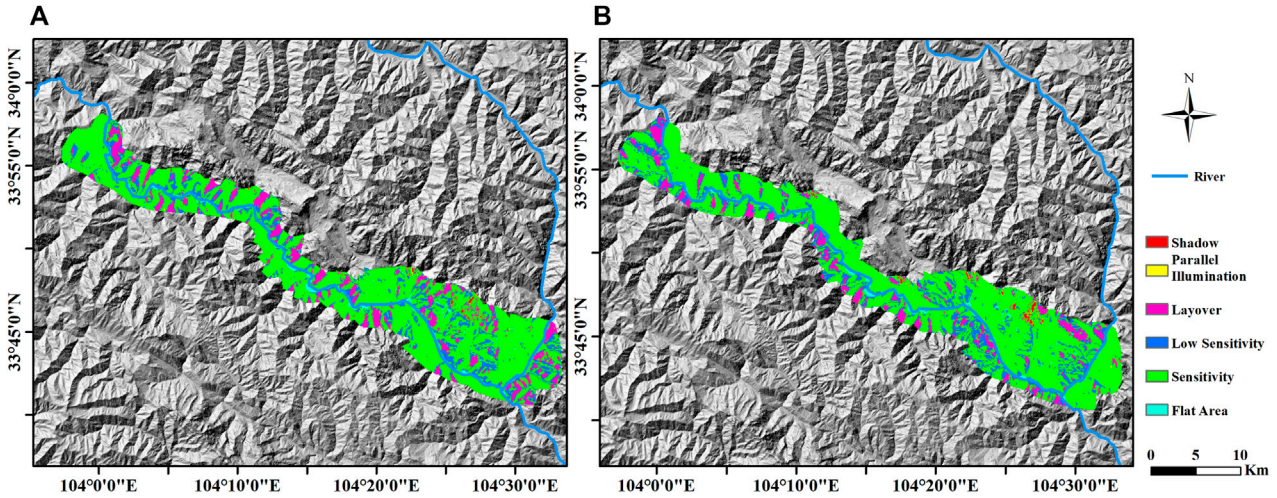

FIGURE 6 | Visibility results of sentinel-1A from the **(A)** ascending orbit and **(B)** descending orbit.

TABLE 2 | SAR data observation information ratio.

Type	Ascending (%)	Descending (%)	Ascending and descending
Shadow	0.2	0.4	0
Parallel Illumination	0.1	0.1	0
Layover	11.8	9	0.2%
Low sensitivity	14.1	15.0	0.7%
Sensitivity	71.2	72.7	96.4%
Flat area	2.6	2.6	2.7%

by point to remove outliers and isolated points from the data. The radius of the sliding window is set to two times the spatial resolution of the data, and 40 m is used. Z-score normalization is used to determine the outliers, and the outliers are determined when the normalized value of the deformation rate is greater than 3 or less than −3. If the number of adjacent points in the sliding window is less than one, it is considered as an isolated point.

(2) The absolute value of the deformation rate threshold is set to filter out the obvious deformation points. All deformation points are constructed into Delaunay triangulation irregular net, and edges larger than the radius of clustering are eliminated to form numerous isolated triangulation irregular net clusters. A recursive approach is used to cluster the deformation points and generate polygonal active deformation areas. Combined with the experience of previous studies, the absolute value of the rate threshold adopted is 15 mm/a, and the clustering radius is set to three times the image resolution, i.e., 60 m.

(3) Combined with the DEM data, the slope of each ADA is calculated, and the ADA with a slope greater than 10° is considered as SADA.

(4) The obtained SADA is overlaid with the terrain visibility map, and unreliable areas such as overlay and shadow areas are removed to obtain the final accurate SADA.

The abovementioned process involves the following main parameters:

(1) Denoising radius: this parameter is mainly used to remove noise points; when the number of PS + DS points in the radius of influence of a point is small, the point is deleted.

(2) Number of neighboring points: it is determined whether PS or DS points are isolated points; when the number in the influence radius is less than this value, they are isolated points.

(3) Rate threshold: this parameter is used to determine the points where deformation occurs. Unlike other studies where the rate threshold is determined based on the standard deviation of the rate, this method takes into account the monitoring accuracy of the conventional time-series InSAR method and the flexibility of the actual operation process and directly gives the upper and lower limits of the rate threshold, automatically extracts the deformation points with a certain step size several times, and generates multiple ADA results for judging potential landslides.

(4) Clustering radius: points within this radius are considered as the same deformation area.

(5) Minimum number of PS + DS points within the ADA: the number of PS + DS points within each ADA must be greater than this value; otherwise, it is not considered as an ADA.

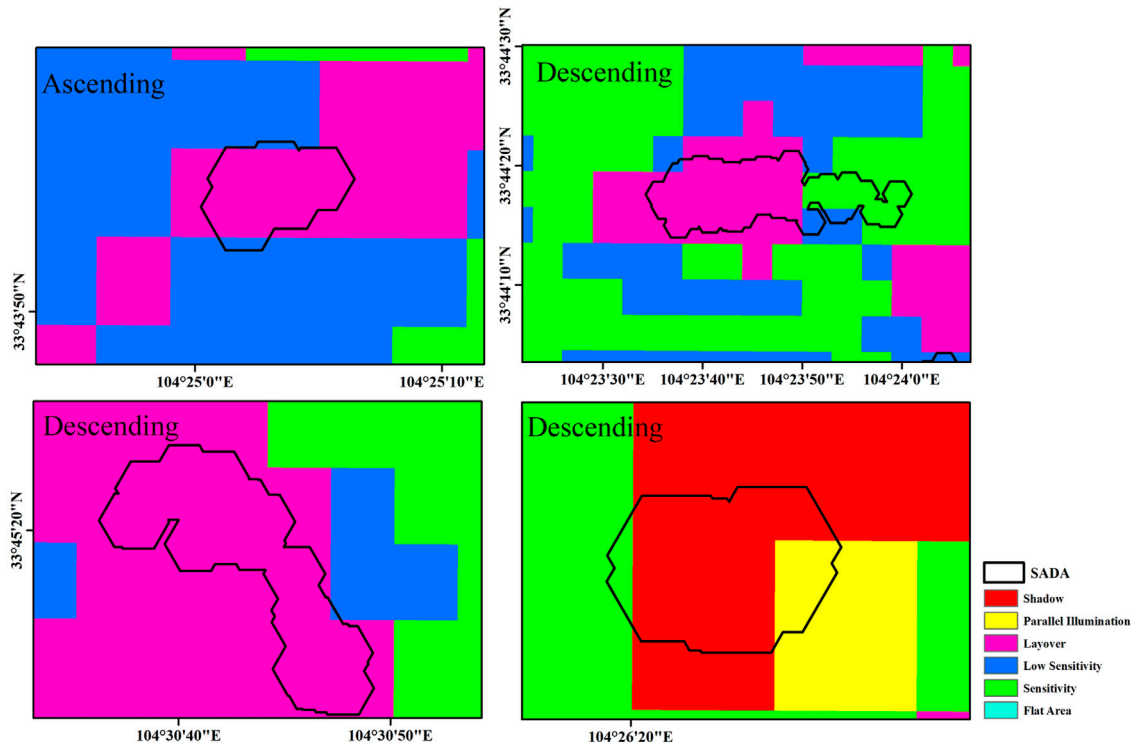

FIGURE 7 | The distribution map of unreliable SADA. The image shows one SADA in the geometric distortion area from ascending data, and three SADA in the geometric distortion area from descending data.

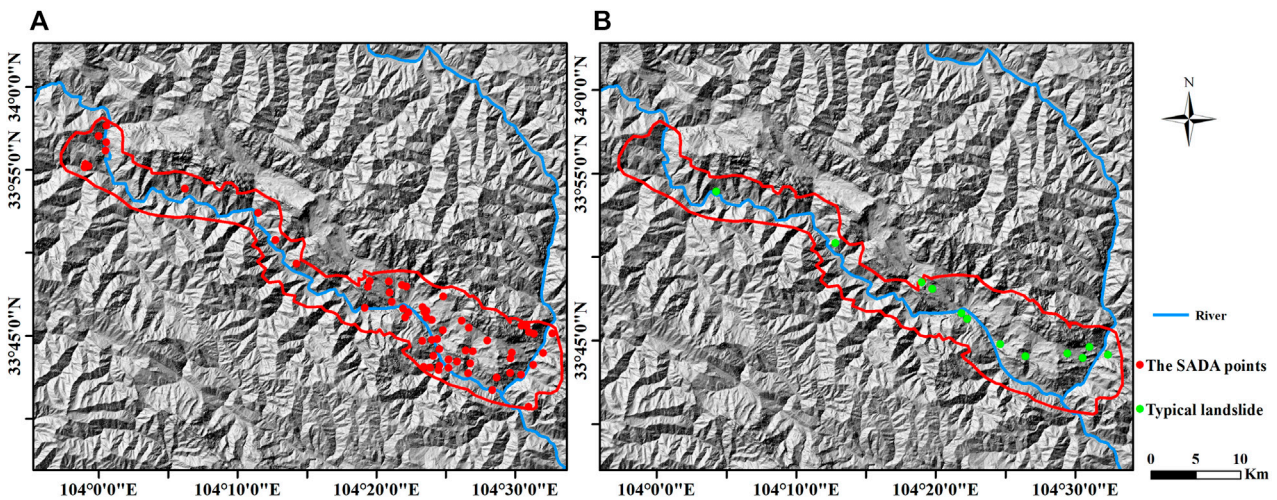

FIGURE 8 | SADA and landslide maps. **(A)** Final result of the SADA distribute and **(B)** typical landslide distribute.

(6) Slope angle: the slope angle of the ADA is greater than this threshold value, and then, it is considered as a SADA.

3.3 Terrain Visibility

The distortion on the SAR images is mainly of the types of layover, shadow, and foreshortening, depending on the geometric parameters of the radar satellite acquisition data, the angle of the LOS direction, and the slope angle and aspect of the terrain. **Figure 4** shows the geometric distortion of radar side view imaging. When illuminated towards the satellite, foreshortening (c–d) occurs when the slope angle is less than or equal to θ, and layover (b–a) occurs when the slope angle is greater than θ. When backward facing the satellite, shadowing (g–h) occurs when the slope angle is greater than $90 - \alpha$ (Dun et al., 2021).

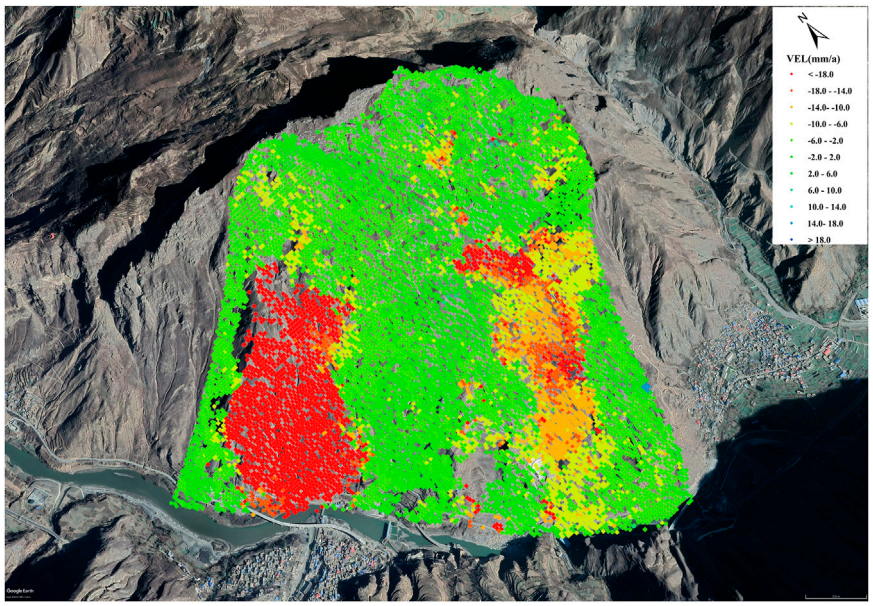

FIGURE 9 | Deformation from the descending orbit data.

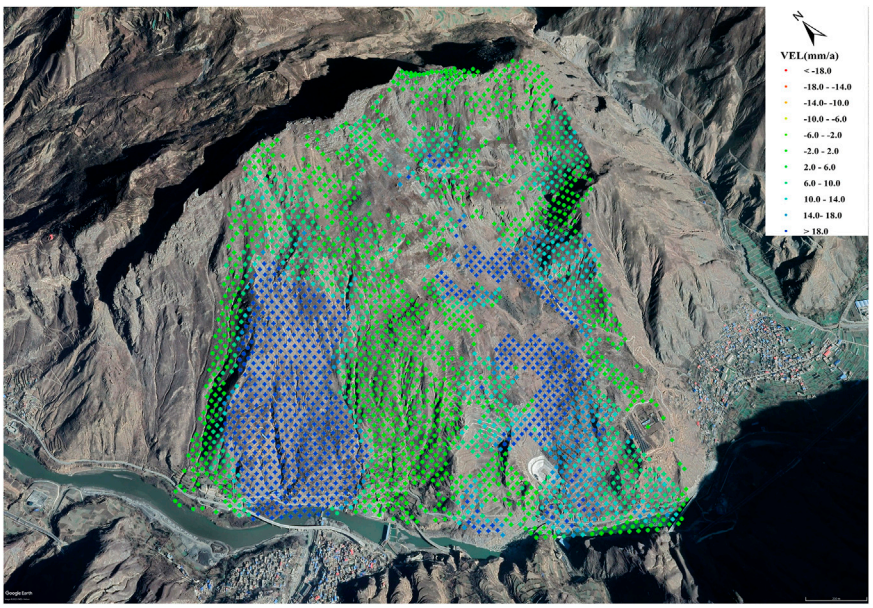

FIGURE 10 | The deformation along the aspect.

4 RESULTS AND ANALYSIS

4.1 Deformation Identification Results

The LOS direction surface deformation results for the study area obtained using the DS-InSAR method are shown in **Figure 5**. The annual average deformation rate in the LOS direction of the ascending orbit ranges from −79 to 47 mm/a, and the absolute value of the large deformation rate exceeds 20 mm/a. The annual average deformation rate in the LOS direction of the descending orbit ranges from −66–79 mm/a. The larger deformation areas obtained from the descending orbit coincide with the ascending orbit, which are mainly distributed on both sides of the gully from Zhouqu County to Lianghekou.

Based on the results of surface deformation in the study area, combined with previous research results and experience, the SADA was detected with the absolute value of deformation

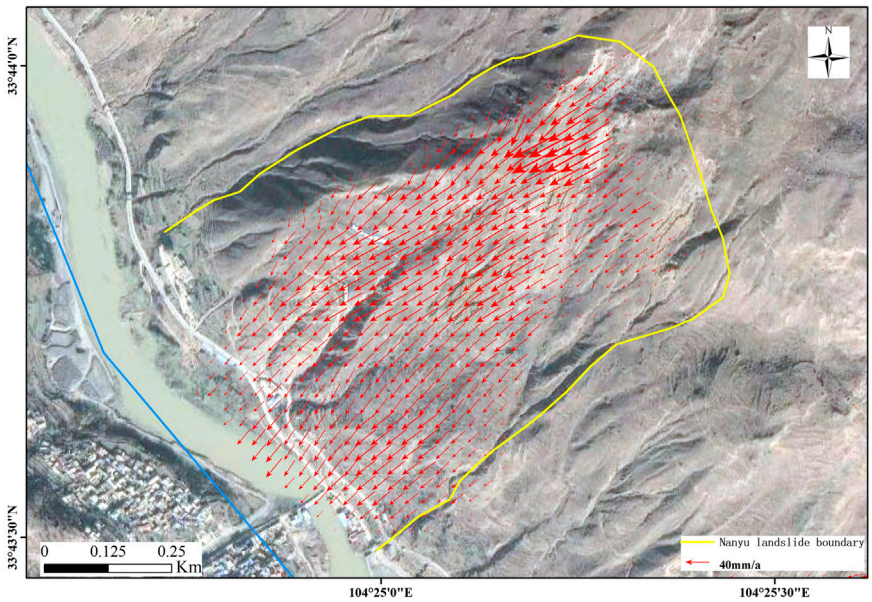

FIGURE 11 | Motion direction map of Nanyu landslide.

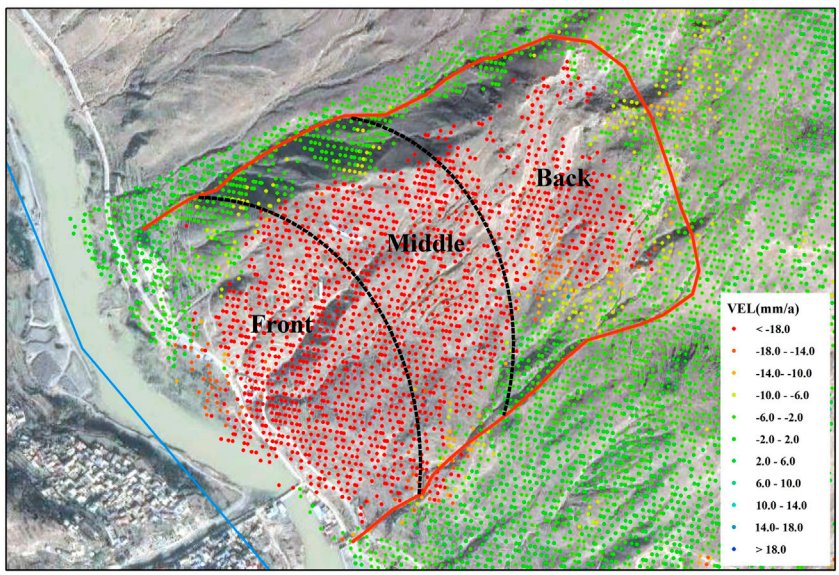

FIGURE 12 | Landslide body division map.

rate greater than 15 mm/a as the threshold value. Through the automatic identification program, 40 SADA were identified in the ascending orbit data, covering an area of about 5.37 km^2, and 48 SADA were identified in the descending orbit data, covering an area of about 6.32 km^2. Comparing the results of the ascending and descending orbit identification, a total of 16 SADA were found to overlap, but the specific extent was not exactly the same, and the results of the SADA identification for the ascending and descending orbits are shown in **Figure 5**.

4.2 Identifying the Results of SADA With Terrain Visibility

Due to the special of radar side view imaging, geometric distortion such as layover and shadow may be produced according to the angle of incidence and different terrain features. In mountainous areas with large topographic relief, the aspect and slope angle characteristics are decisive factors for generating geometric distortion, and the topography needs to be fully considered first. In this study area, there are several

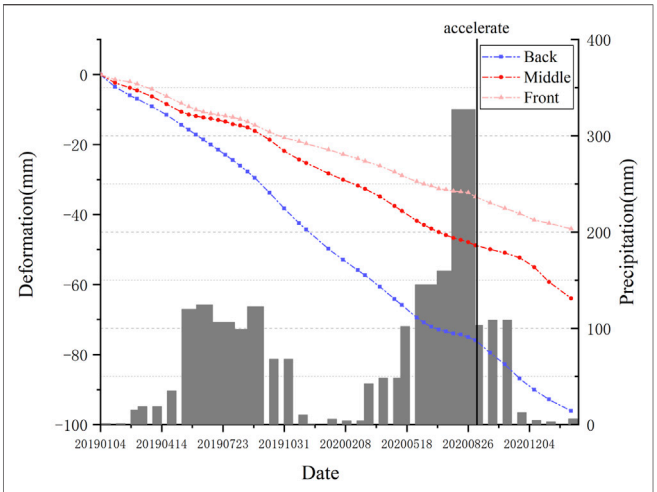

FIGURE 13 | Time-series deformation and precipitation of three parts.

geometric distortions on SAR images along the undulating sides of the river. In order to improve the accuracy of identification, the relationship between the location of SADA and geometric distortion must be considered comprehensively, the areas that may be inaccurate are eliminated, and the results are refined. Based on the incidence angle, heading angle, and external DEM data of the satellite, the terrain visibility results of the ascending and descending orbit SAR satellites in the study area were obtained, and the results are shown in **Figure 6**. The percentage of each visibility type for ascending and descending orbits were counted, and the results are shown in **Table 2**. From the results, it can be seen that there are many geometric distortion areas in the single orbit data, among which the percentage of layover and shadow areas in the ascending orbit data is 12.0%, and the percentage of stacked and shadowed areas in the descending orbit data is 9.4%. For most of the layover and shadow areas, the ascending and descending orbit data can complement each other, and after the combination of ascending and descending orbit, the area of stacked and shadowed areas is only 0.2%.

As shown in **Figure 7**, based on the aboveobtained visibility results, geometric distortion analysis and verification were performed on the SADA identified from this study area, among which one SADA on the ascending orbit was located in the geometric distortion area, and three SADAs on the descending orbit were located in the geometric distortion area. It should be noted that the purpose of our automatic extraction method is to obtain the deformation area more efficiently, and the deformation area obtained after eliminating the geometric distortion area is the result we like to obtain, and the abovementioned process is automatic.

To count the total number identified, optical images are needed to assist. For the same landslide, different parts of the deformation may be identified in the ascending and descending results, so it is necessary to combine the optical images to determine whether the identified deformation areas are located on the same slope to avoid double counting. After combining the integrated identify SADA with the GoogleEarth long time-series optical images and eliminating the unreliable areas located in geometric distortion, the final statistics obtained a total of 62 SADA found in this study area, and the study area was divided into two sections with the Zhouqu County as the boundary, of which there were 10 upstream and 52 downstream, and the final result of the SADA is shown in **Figure 8A**. By comparing with 12 typical landslides in the study area, 9 typical landslides match with the detected SADA, which indicates the high accuracy of this method. In addition, Sun et al. (2016) used InSAR to identify four typical deformation areas, all of which are located in the identified 62 SADAs. Dai et al. (2021) used SBAS-InSAR to detect 23 active landslides around Zhouqu County, which are highly consistent with the SADA obtained in this paper.

4.3 Nanyu Landslide Deformation Analysis

The Nanyu landslide is located on a large paleo-landslide body which includes two large landslides: the Nanyu landslide and the Jiangdingya landslide. Due to many repeated activities, the surface of the Nanyu landslide is undulating and part of the area has been artificially transformed into an arable land. The trailing edge of the landslide is steep, forming a chert ridge. The longitudinal gully of the landslide is developed, and the deep gully of erosion on the east and west sides is the boundary of the landslide (Zhang et al., 2018). The landslide body has a loose structure, and the main components are gravel and loess.

4.3.1 Spatial Characteristics of Deformation

As shown in **Figure 9** and **Figure 10**, the deformation of the whole Nanyu landslide obtained from the descending orbit data and the deformation along the aspect obtained from the decomposition of the ascending and descending orbit are shown, respectively. From the monitoring results, it can be seen that there is obvious deformation of the Nanyu landslide located on the northwest side of the landslide body. From the aspect deformation rate diagram, the deformation rate of the top of the landslide is more than 70 mm/a, and the maximum can reach 102 mm/a, while the deformation rate of the middle and lower part is about 20 mm/a~40 mm/a. The rate of the trailing edge of the landslide is much larger than the front edge, which indicates that the movement mode of the landslide is pushing type. The direction of movement of each point of the Nanyu landslide is shown in **Figure 11**. The landslide belongs to the overall decline, and the bottom of the slope slides into the river after the rapid decline, so there is no obvious siltation phenomenon on the slope.

4.3.2 Temporal Characteristics of the Deformation

As shown in **Figure 12**, to study the temporal characteristics of landslide deformation, the landslide body was divided into three parts, front, middle, and back, and the average deformation of each part was calculated separately. The calculation was carried out only for the points where the deformation rate was greater than 15 mm/a. The cumulative deformation curves of the three parts are shown in **Figure 13**. The average deformation rate of the

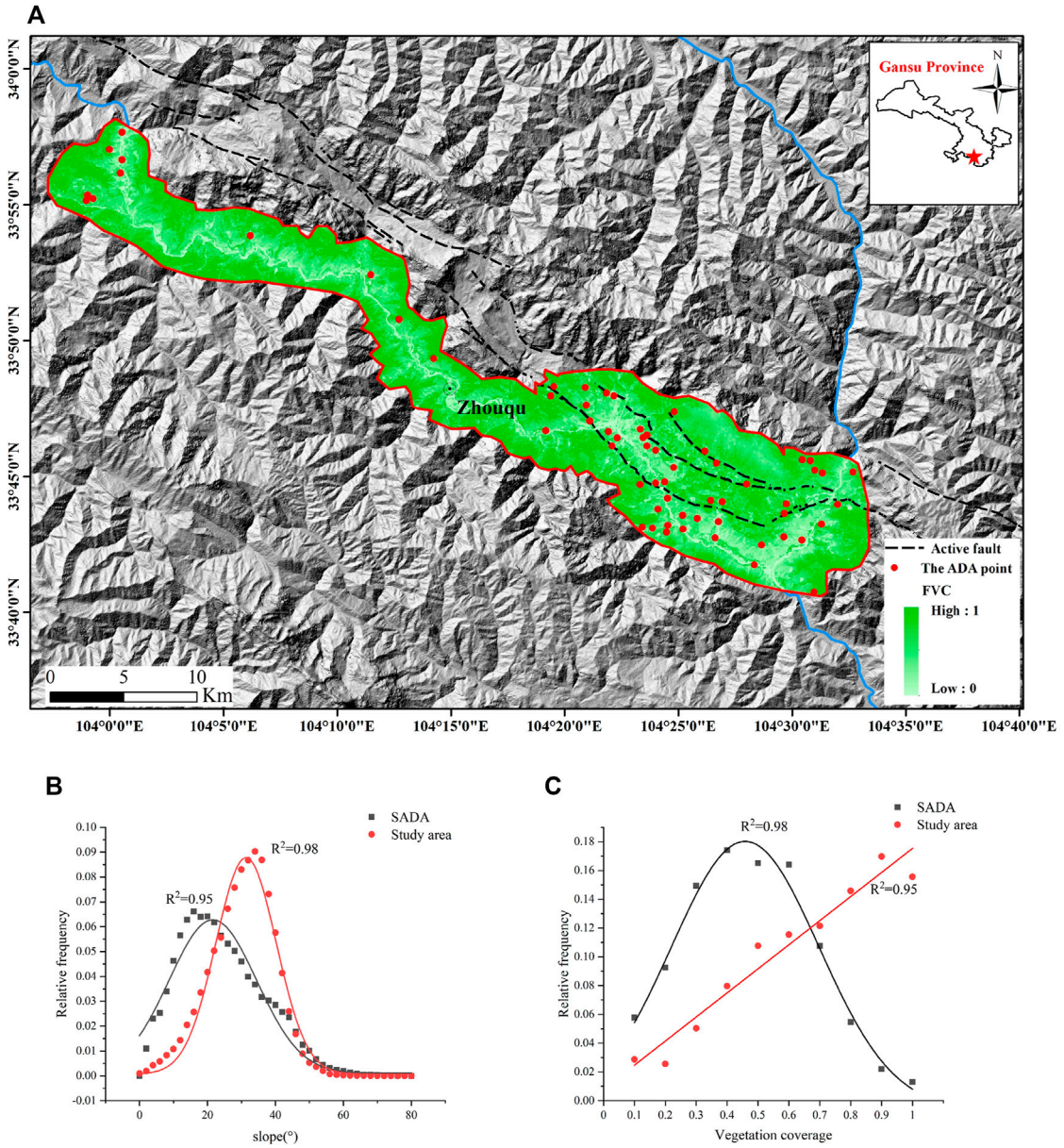

FIGURE 14 | Factors influencing landslides. **(A)** Vegetation coverage and fault distribution map of study area, **(B)** relative frequency distributions of slope angle, **(C)** relative frequency distributions of vegetation coverage.

front part is −21 mm/a, and the cumulative deformation is −44 mm; the average deformation rate of the middle part is −30 mm/a, and the cumulative deformation is −64 mm; the average deformation rate of the back part is −48 mm/a, and the cumulative deformation is −96 mm. During the monitoring time period, the deformation trend of the three parts is more consistent, and all of them show the deformation away from the satellite direction.

As shown in **Figure 13**, the landslide deformation did not accelerate immediately with the increase in precipitation at the beginning of the rainy season in June each year but began to accelerate when the precipitation reached its peak in August. This indicates that the accelerated deformation of the landslide is related to the high intensity of intensive precipitation. When the rainfall is not enough to make the landslide unstable, the accelerated deformation of the landslide body lags behind the rainfall, and the accelerated deformation of the landslide body continues after each cycle of rainfall. This phenomenon is highly consistent with the study results of Yang et al. (2014) and Ma et al. (2020). Significantly, the acceleration of landslide deformation in 2019 is less than in 2020, which correlates well with the magnitude of the rainfall peak, suggesting that more intense precipitation triggers faster deformation.

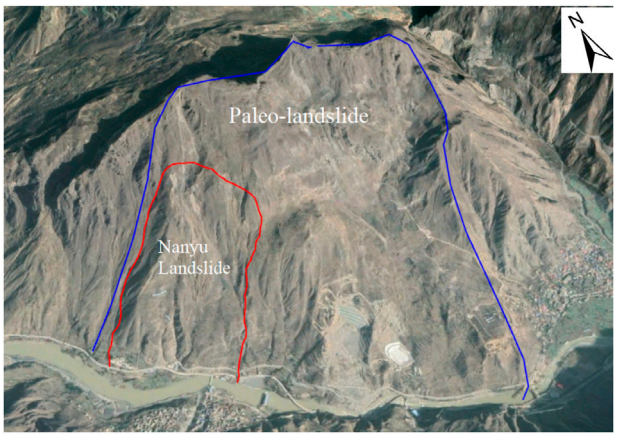

FIGURE 15 | Optical image of Nanyu landslide.

5 DISCUSSION

Landslides occur as a result of coupled internal and external dynamics. Fault distribution, slope, vegetation coverage, precipitation, and human activities can all affect landslides.

5.1 Active Faults and Slope

Fault is the basic factor controlling the formation and development of landslides. Fault activity causes slope fragmentation and changes in the regional tectonic stress field so that landslides are distributed along major active fault zones. As shown in **Figure 14A**, the spatial distribution of the identified SADA is highly correlated with the distribution of active faults, which indicates that faults are one of the important factors affecting landslides in the area. As shown in **Figure 14B**, the slope of the SADA and the whole study area were counted separately, and the maximum frequency slope of the SADA area is 15°, which is smaller than the maximum frequency slope of the whole study area of 38°, which indicates that the landslides in this area are mostly developed on smaller slopes, which is consistent with the study of Zhang et al. (2018). The focus should be on the gentle slopes within the influence of faults in future disaster control.

5.2 Vegetation Coverage

As an important factor in the surface evolution, vegetation is constantly influencing the surrounding soil evolution, hydrological evolution, and geomorphological evolution, which are all closely related to the formation of landslides. As shown in **Figure 14A** and **Figure 14C**, the vegetation coverage of the study area was calculated based on Landsat8 images. The vegetation coverage of SADA and the whole study area were counted separately, the average vegetation coverage of SADA was 0.42, and the average vegetation coverage of the whole study area was 0.66. The distribution of SADA in this study area was negatively related to the vegetation coverage, and the higher the vegetation coverage in this study area, the less likely landslides occurred.

5.3 Precipitation

Continuous and concentrated rainfall plays an important role in inducing landslide damage (Qiu et al., 2020). The spatial and temporal distribution of precipitation in the study area is uneven. As shown in **Figure 13**, 70% of precipitation is distributed from June to September, with more localized and concentrated heavy precipitation. Higher precipitation was seen in the southeastern part of the study area than in the northwestern part (Li et al., 2015). This precipitation characteristic leads to landslide susceptibility in the southeastern part of the study area.

5.4 Human Activities

The population in this study area is distributed along the river valley, and there is very little land available for development. Therefore, human activities that are not conducive to slope stability, such as excavating the foot of the slope and filling the ditch to create land, occur frequently. **Figure 15** shows the presence of numerous traces of human activities on the Nanayu landslide. There are trails and roads on the landslide, which destroy the slope structure and reduce the stability of the landslide. In addition, most of the transportation routes were built along the river valleys, and human engineering activities were particularly intense (Ma et al., 2020).

In this study, the DS-InSAR technology is used to process SAR data, and the results monitored by different orbit data are slightly different, which is due to the fact that SAR satellites are side-view imaging systems, and the use of ascending and descending orbit data can play a complementary effect. Since the SAR satellite flies along the north–south direction, it is not sensitive to the deformation in the north–south direction for either the ascending or descending orbit data, so the subsequent introduction of Pixel Offset Tracking or Multiple Aperture InSAR methods can be considered to assist in the deformation area identification. Since C-band sentinel data are used in this study, compared with L-band SAR data, the penetration ability of this band is weaker for vegetation, which may lead to difficulties in obtaining valid and reliable observations on slopes partially covered with vegetation. Otherwise, for areas with more vegetation cover, it is necessary to use high-resolution optical images, stratigraphic lithology and other data, and ground investigation to make interpretations and judgments.

The proposed identification method relies on the validity of InSAR monitoring results, and for low-coherence regions, accurate InSAR monitoring results cannot be obtained, and the SADA cannot be identified by this method. In addition, it is worth noting that the accuracy of terrain visibility depends on the accuracy of DEM, which is also the limitation of the method.

6 CONCLUSION

Based on the DS-InSAR deformation monitoring results, this study proposes a method for automatic identification of SADA. Compared with previous studies, the method can identify SADA from large-scale deformation data efficiently and rapidly; also, the accuracy of identification can be improved by considering the

influence of SAR image geometric distortion in the high mountain canyon area.

The method was used to identify the areas on both sides of the Bailong River in the Zhouqu region. The study showed that landslide hazard detection using single orbit radar satellite data could lead to the leakage of landslide hazards easily, and a total of 62 SADA were identified in the study area by integrating the deformation results obtained from ascending and descending orbit images and SAR visibility analysis results. It is proven that the results of deformation area identification have high accuracy.

The deformation of the Nanayu landslide began to accelerate when the precipitation reached its peak and lasted for a period of time. The deformation of this landslide has a high correlation with rainfall.

DATA AVAILABILITY STATEMENT

The original contributions presented in the study are included in the article/Supplementary Material, further inquiries can be directed to the corresponding author.

AUTHOR CONTRIBUTIONS

All authors listed have made a substantial, direct, and intellectual contribution to the work and approved it for publication.

FUNDING

This research was funded by the National Natural Science Foundation of China (51474217), the Ecological Smart Mine Joint Fund of the Natural Science Foundation of Hebei Province (E2020402086) and the Fundamental Research Funds for the Central Universities (2022YQDC01).

ACKNOWLEDGMENTS

The DEM, Sentinel-1 data, and Landsat8 images were provided by the Japan Aerospace Exploration Agency (JAXA), European Space Agency (ESA), and United States Geological Survey(USGS), respectively.

REFERENCES

Aleotti, P., and Chowdhury, R. (1999). Landslide hazard Assessment: Summary Review and New Perspectives. *Bull. Eng. Geol. Env* 58, 21–44. doi:10.1007/s100640050066

Bai, S., Wang, J., Zhang, Z., and Cheng, C. (2012). Combined Landslide Susceptibility Mapping after Wenchuan Earthquake at the Zhouqu Segment in the Bailongjiang Basin, China. *Catena* 99, 18–25. doi:10.1016/j.catena.2012.06.012

Barra, A., Solari, L., Béjar-Pizarro, M., Monserrat, O., Bianchini, S., Herrera, G., et al. (2017). A Methodology to Detect and Update Active Deformation Areas Based on sentinel-1 SAR Images. *Remote Sensing* 9, 1002. doi:10.3390/rs9101002

Cao, N., Lee, H., and Jung, H. C. (2016). A Phase-Decomposition-Based PSInSAR Processing Method. *IEEE Trans. Geosci. Remote Sensing* 54, 1074–1090. doi:10.1109/TGRS.2015.2473818

Cigna, F., Bateson, L. B., Jordan, C. J., and Dashwood, C. (2014). Simulating SAR Geometric Distortions and Predicting Persistent Scatterer Densities for ERS-1/2 and ENVISAT C-Band SAR and InSAR Applications: Nationwide Feasibility Assessment to Monitor the Landmass of Great Britain with SAR Imagery. *Remote Sensing Environ.* 152, 441–466. doi:10.1016/j.rse.2014.06.025

Cui, P., Zhou, G. G. D., Zhu, X. H., and Zhang, J. Q. (2013). Scale Amplification of Natural Debris Flows Caused by Cascading Landslide Dam Failures. *Geomorphology* 182, 173–189. doi:10.1016/j.geomorph.2012.11.009

Dai, C., Li, W., Wang, D., Lu, H., Xu, Q., and Jian, J. (2021). Active Landslide Detection Based on sentinel-1 Data and InSAR Technology in Zhouqu County, Gansu Province, Northwest china. *J. Earth Sci.* 32, 1092–1103. doi:10.1007/s12583-020-1380-0

Dai, F. C., Lee, C. F., and Ngai, Y. Y. (2002). Landslide Risk Assessment and Management: an Overview. *Eng. Geology.* 64, 65–87. doi:10.1016/S0013-7952(01)00093-X

Dun, J., Feng, W., Yi, X., Zhang, G., and Wu, M. (2021). Detection and Mapping of Active Landslides before Impoundment in the Baihetan Reservoir Area (China) Based on the Time-Series InSAR Method. *Remote Sensing* 13, 3213. doi:10.3390/rs13163213

Ferretti, A., Fumagalli, A., Novali, F., Prati, C., Rocca, F., and Rucci, A. (2011). A New Algorithm for Processing Interferometric Data-Stacks: SqueeSAR. *IEEE Trans. Geosci. Remote Sensing* 49, 3460–3470. doi:10.1109/TGRS.2011.2124465

Ferretti, A., Prati, C., and Rocca, F. (2001). Permanent Scatterers in SAR Interferometry. *IEEE Trans. Geosci. Remote Sensing* 39, 8–20. doi:10.1109/36.898661

Fornaro, G., Verde, S., Reale, D., and Pauciullo, A. (2015). CAESAR: An Approach Based on Covariance Matrix Decomposition to Improve Multibaseline-Multitemporal Interferometric SAR Processing. *IEEE Trans. Geosci. Remote Sensing* 53, 2050–2065. doi:10.1109/TGRS.2014.2352853

Goel, K., and Adam, N. (2014). A Distributed Scatterer Interferometry Approach for Precision Monitoring of Known Surface Deformation Phenomena. *IEEE Trans. Geosci. Remote Sensing* 52, 5454–5468. doi:10.1109/TGRS.2013.2289370

Hilley, G. E., Bürgmann, R., Ferretti, A., Novali, F., and Rocca, F. (2004). Dynamics of Slow-Moving Landslides from Permanent Scatterer Analysis. *Science* 304, 1952–1955. doi:10.1126/science.1098821

Jiang, M., Ding, X., Hanssen, R. F., Malhotra, R., and Chang, L. (2015). Fast Statistically Homogeneous Pixel Selection for Covariance Matrix Estimation for Multitemporal InSAR. *IEEE Trans. Geosci. Remote Sensing* 53, 1213–1224. doi:10.1109/TGRS.2014.2336237

Jiang, S., Wen, B.-P., Zhao, C., Li, R.-D., and Li, Z.-H. (2016). Kinematics of a Giant Slow-Moving Landslide in Northwest China: Constraints from High Resolution Remote Sensing Imagery and GPS Monitoring. *J. Asian Earth Sci.* 123, 34–46. doi:10.1016/j.jseaes.2016.03.019

Kavoura, K., Konstantopoulou, M., Depountis, N., and Sabatakakis, N. (2020). Slow-moving Landslides: Kinematic Analysis and Movement Evolution Modeling. *Environ. Earth Sci.* 79, 1–11. doi:10.1007/s12665-020-8879-7

Li, Z. H., Wen, B. P., Jia, G. Y., Zhang, Y. J., Dong, K. J., and Yang, Y. B. (2015). Characteristics of the Landslide Distribution along the Bailongjiang River basin and its Controlling Factors. *J. Lanzhou University(Natural Sciences)* 51 (06), 768–776. doi:10.13885/j.issn.0455-2059.2015.06.002

Liu, X., Zhao, C., Zhang, Q., Peng, J., Zhu, W., and Lu, Z. (2018). Multi-Temporal Loess Landslide Inventory Mapping with C-, X- and L-Band SAR Datasets-A Case Study of Heifangtai Loess Landslides, China. *Remote Sensing* 10, 1756. doi:10.3390/rs10111756

Luo, S., Feng, G., Xiong, Z., Wang, H., Zhao, Y., Li, K., et al. (2021). An Improved Method for Automatic Identification and Assessment of Potential Geohazards Based on MT-InSAR Measurements. *Remote Sensing* 13, 3490. doi:10.3390/rs13173490

Ma, S., Qiu, H., Hu, S., Yang, D., and Liu, Z. (2020). Characteristics and Geomorphology Change Detection Analysis of the Jiangdingya Landslide on July 12, 2018, China. *Landslides* 18, 383–396. doi:10.1007/s10346-020-01530-3

Novellino, A., Cesarano, M., Cappelletti, P., Di Martire, D., Di Napoli, M., Ramondini, M., et al. (2021). Slow-moving Landslide Risk Assessment Combining Machine Learning and InSAR Techniques. *Catena* 203, 105317. doi:10.1016/j.catena.2021.105317

Qiu, H., Cui, Y., Pei, Y., Yang, D., Hu, S., Wang, X., et al. (2020). Temporal Patterns of Nonseismically Triggered Landslides in Shaanxi Province, China. *Catena* 187, 104356. doi:10.1016/j.catena.2019.104356

Ren, T., Ma, S., Bowa, V. M., Tang, H., Chen, J., and Zhao, F. (2021). An Improved R-Index Model for Terrain Visibility Analysis for Landslide Monitoring with InSAR. *Remote Sensing* 13, 1938. doi:10.3390/rs13101938

Schuster, R. L., and Highland, L. M. (2007). The Third Hans Cloos Lecture. Urban Landslides: Socioeconomic Impacts and Overview of Mitigative Strategies. *Bull. Eng. Geol. Environ.* 66, 1–27. doi:10.1007/s10064-006-0080-z

Sun, Q., Hu, J., Zhang, L., and Ding, X. (2016). Towards Slow-Moving Landslide Monitoring by Integrating Multi-Sensor InSAR Time Series Datasets: The Zhouqu Case Study, China. *Remote Sensing* 8, 908. doi:10.3390/rs8110908

Sun, Q., Zhang, L., Ding, X. L., Hu, J., Li, Z. W., and Zhu, J. J. (2015). Slope Deformation Prior to Zhouqu, China Landslide from InSAR Time Series Analysis. *Remote Sensing Environ.* 156, 45–57. doi:10.1016/j.rse.2014.09.029

Vilímek, V., Wang, F., and Strom, A. (2021). Catastrophic Landslides and Frontiers of Landslide Science. *Landslides* 18, 3733–3735. doi:10.1007/s10346-021-01765-8

Wang, G. L. (2013). Lessons Learned from Protective Measures Associated with the 2010 Zhouqu Debris Flow Disaster in China. *Nat. Hazards* 69, 1835–1847. doi:10.1007/s11069-013-0772-1

Wild, C. T., Marsh, O. J., and Rack, W. (2018). Unraveling InSAR Observed Antarctic Ice-Shelf Flexure Using 2-D Elastic and Viscoelastic Modeling. *Front. Earth Sci.* 6. doi:10.3389/feart.2018.00028

Yang, W. M., Huang, X., Zhang, C. S., and Si, H. B. (2014). Deformation Behavior of Landslides and Their Formation Mechanism along Pingding Huama Active Fault in Bailongjiang River Region. *J. Jilin University(Earth Sci. Edition)* 44 (02), 574–583. doi:10.13278/j.cnki.jjuese.201402201

Zhang, N., and Matsushima, T. (2016). Simulation of Rainfall-Induced Debris Flow Considering Material Entrainment. *Eng. Geology.* 214, 107–115. doi:10.1016/j.enggeo.2016.10.005

Zhang, Y., Meng, X., Chen, G., Qiao, L., Zeng, R., and Chang, J. (2016). Detection of Geohazards in the Bailong River basin Using Synthetic Aperture Radar Interferometry. *Landslides* 13, 1273–1284. doi:10.1007/s10346-015-0660-8

Zhang, Y., Meng, X., Jordan, C., Novellino, A., Dijkstra, T., and Chen, G. (2018). Investigating Slow-Moving Landslides in the Zhouqu Region of China Using InSAR Time Series. *Landslides* 15, 1299–1315. doi:10.1007/s10346-018-0954-8

Zhang, Y., Meng, X. M., Dijkstra, T. A., Jordan, C. J., Chen, G., Zeng, R. Q., et al. (2020). Forecasting the Magnitude of Potential Landslides Based on InSAR Techniques. *Remote Sensing Environ.* 241, 111738. doi:10.1016/j.rse.2020.111738

Zhao, C., Lu, Z., Zhang, Q., and de la Fuente, J. (2012). Large-area Landslide Detection and Monitoring with ALOS/PALSAR Imagery Data over Northern California and Southern Oregon, USA. *Remote Sensing Environ.* 124, 348–359. doi:10.1016/j.rse.2012.05.025

Zhao, C. Y., Kang, Y., Zhang, Q., Zhu, W., and Li, B. (2016). "Landslide Detection and Monitoring with InSAR Technique over Upper Reaches of Jinsha River, China," in Proceedings of the IGARSS 2016, Beijing, China, 10–15 July 2016. doi:10.1109/igarss.2016.7729744

Conflict of Interest: The authors declare that the research was conducted in the absence of any commercial or financial relationships that could be construed as a potential conflict of interest.

Publisher's Note: All claims expressed in this article are solely those of the authors and do not necessarily represent those of their affiliated organizations, or those of the publisher, the editors and the reviewers. Any product that may be evaluated in this article, or claim that may be made by its manufacturer, is not guaranteed or endorsed by the publisher.

frontiers | Frontiers in Environmental Science

ORIGINAL RESEARCH
published: 30 May 2022
doi: 10.3389/fenvs.2022.885346

Predicting the Settlement of Mine Waste Dump Using Multi-Source Remote Sensing and a Secondary Consolidation Model

Reza Tabish[1,2], Zefa Yang[1,2], Lixin Wu[1,2], Zhihua Xu[3], Zhanpeng Cao[1,2], Kaihui Zheng[4] and Yanqing Zhang[5]*

[1]School of Geosciences and Info-Physics, Central South University, Changsha, China, [2]Key Laboratory of Metallogenic Prediction of Nonferrous Metals and Geological Environment Monitoring (Central South University), Ministry of Education, Changsha, China, [3]College of Geoscience and Surveying Engineering, China University of Mining and Technology, Beijing, China, [4]North Weijiamao Power and Coal Co., Ltd., Ordos, China, [5]North United Electric Power Co., Ltd., Hohhot, China

The settlement (or subsidence) of mine waste dump is likely to cause landslides, thereby imposing threats on the safety of human beings and other local properties. Hence, it is essential to accurately predict the settlement for the early-warning of settlement-induced geohazards. Traditional mechanical methods require *in situ* mechanical parameters and the geological structure of mine waste dump, narrowing their practical applications. In this paper, we proposed a remote sensing-based method for predicting the settlement of mine waste dump without the requirement for field observations. Firstly, the historical settlement and thickness of mine waste dump were measured by space-borne interferometric synthetic aperture radar (InSAR) and photogrammetry techniques, respectively. Secondly, the temporal evolution of the settlement of mine waste dump was described by a secondary consolidation model. Thirdly, the parameters of the secondary consolidation model were inverted based on the InSAR-measured historical settlements and photogrammetry-estimated thickness. Finally, the evolution trend of the settlement of the mine waste dump was predicted with the secondary consolidation model and its inverted parameters. The proposed method was tested over a mine waste dump in Weijiamao open-pit mine, China. The result shows that the root mean square error of the predicted time-series settlement is about 0.8 cm. The presented method will be beneficial to the assessment and early-warning of the settlement-related geohazards of mine waste dumps over a large area.

Keywords: mine waste dump, InSAR, ground deformation analysis, consolidation settlement, secondary consolidation model

OPEN ACCESS

Edited by:
Yu Chen,
China University of Mining and Technology, China

Reviewed by:
Yunmeng Cao,
GNS Science, New Zealand
Wu Zhu,
Chang'an University, China
Bingqian Chen,
Jiangsu Normal University, China

***Correspondence:**
Zefa Yang
yangzf@csu.edu.cn

Specialty section:
This article was submitted to Environmental Informatics and Remote Sensing, a section of the journal Frontiers in Environmental Science

Received: *28 February 2022*
Accepted: *12 April 2022*
Published: *30 May 2022*

Citation:
Tabish R, Yang Z, Wu L, Xu Z, Cao Z, Zheng K and Zhang Y (2022) Predicting the Settlement of Mine Waste Dump Using Multi-Source Remote Sensing and a Secondary Consolidation Model. Front. Environ. Sci. 10:885346. doi: 10.3389/fenvs.2022.885346

1 INTRODUCTION

For open-pit mining activities, earth materials (e.g., rock and soil) overlying ore deposits have to be mined. These materials are usually placed in heaps or fills (referred to as mine waste dump) over an area where they will not restrict the exploration of underground ore. Mine waste dump, especially associated with large open-pit mining activities, is possibly one type of the largest man-made structure in terms of volume and mass. For instance, a mine waste dump located in the Elk Valley

region of British Columbia, Canada associated with a large coal open-pit mining has a cumulative height of up to 400 m and a mass of 8.5 billion tons of earth materials (Hawley and Cunning 2017). Since mine waste dump generally consists of soil and/or disaggregated rock (Lianhuan et al., 2018; Cho and Song 2014), the weak and loose structure of mine waste dump would cause settlement (or subsidence). The settlement potentially causes geohazards like landslides and further impose threats on the safety of human beings, mine's equipment, and other infrastructures around the mine (Pinto et al., 2014). Therefore, it is essential to accurately predict the settlement of mine waste dump for assessing and controlling the settlement-related geohazards.

The numerical analysis is one of the most common methods for predicting the settlement of mine waste dump and further assessing the geohazard risks (Behera et al., 2016; Verma et al., 2013; Ashutosh et al., 2013). In the numerical analysis, the geotechnical parameters and material samples of the concerned mine waste dumps are firstly *in situ* collected. Then, the material properties of the collected samples (e.g., unit weight, cohesion, internal friction angle, and Young's modulus) are analyzed by laboratory tests. Finally, numerical methods (e.g., finite element method and limit equilibrium method) are utilized to predict the potential settlement and assess the risk of settlement-related geohazards. The numerical analysis methods can take the complex and irregular geometries, various types of material properties of mine waste dumps into a model, thus it usually could reliably assess the geohazard risks, if the geotechnical and material parameters are accurate (Kainthola et al., 2013). However, this, in return, implies that the numerical analysis methods rely on the geotechnical properties and material parameters of mine waste dump that need to be field surveyed or laboratory tested. Limited by the high cost, labor-intensive, and time-consuming characteristics of field surveying or laboratory tests, the numerical analysis methods are usually used in a local mine waste dump, rather than in numerous dumps in a large area simultaneously.

Interferometric synthetic aperture radar (InSAR) is a useful remote sensing technique, which is able to monitor ground surface displacements over a wide coverage (e.g., with a swath width of 250 km for Sentinel-1) with a high spatial resolution (e.g., 0.25 m for TerraSAR-X) (Gabriel et al., 1989; Massonnet et al., 1993; Massonnet and Feigl 1998; Bürgmann et al., 2000). It has become an important alternative to terrestrial surveying techniques for monitoring surface deformation relating to various geohazard events, including landslides (Pierluigi et al., 2019; Carlà et al., 2019; Li et al., 2020), earthquakes (Atzori et al., 2019; Yu et al., 2020), volcanic eruptions (Suwarsono et al., 2019), land settlement associated with mining activities (Chen et al., 2020; Yuan et al., 2021; Qingsong et al., 2021), and consolidation processing over mine waste dumps (Gong et al., 2021; Williams et al., 2021; Juan et al., 2021). If we can predict the settlement trend of mine waste dump based on InSAR observations of historical settlement, the geotechnical and material parameters required by the numerical analysis methods will be unnecessary. In other words, the settlement of numerous mine waste dumps over a large area can be predicted without the requirement for field observations in theory. This cannot be achieved by numerical analysis methods. However, to the best of our knowledge, it is rather rare to do that to date Roland et al., 2020.

In this paper, we proposed a new method for predicting the settlement of mine waste dump based on multi-source remote sensing techniques and a secondary consolidation model. More specifically, the historical settlement and thickness of the concerned mine waste dump were then estimated by space-borne InSAR and high-resolution photogrammetry techniques. A secondary consolidation model was then utilized to model the settlement evolution of mine waste dump on a basis of pixel-by-pixel. Thirdly, the parameters of the secondary consolidation model were inverted in the least-square sense. Finally, the settlement trend of the concerned mine waste dump was predicted based on the inverted model parameters and the secondary consolidation model. The proposed method is theoretically able to predict ground surface settlement of mine waste dump in a long time due to soil consolidation without *in situ* surveying. Therefore, it offers a new tool for assessing the stability risk of waste dump over a wide area (e.g., thousands of square kilometers) that cannot be achieved by traditional numerical analysis methods.

2 STUDY AREA AND DATASETS

2.1 Study Area

In this study, a mine waste dump located in Weijiamao open-pit mine, China (marked by the red star in **Figure 1**), was selected to test the proposed method. The mine waste dump started to normally operate in the year of 2012 and ceased the operation in the year 2017. Since the mine waste dump is located above the loess plateau, and some infrastructures (e.g., industry buildings and roads) are nearby it (see **Figure 1D**). Therefore, it is essential to predict the settlement of the mine waste dump for assessing its stability and assessing geohazards (e.g., landslides).

2.2 Datasets

Ninety SAR images spanning from 30 May 2017 to 14 May 2020 over the study area were firstly collected for monitoring the historical settlement. These 90 SAR images were acquired by the Terrain Observation with Progressive Scan imaging mode of the C-band Sentinel-1A satellite in an ascending orbit (track 113 and frame 126). The pixel spacing of the collected Sentinel-1 SAR images is about 2.3 and 14.1 m in the range and azimuth directions, respectively. The mean temporal separation of the collected SAR images is about 12 days.

In addition, two pairs of ZiYuan-3 (ZY-3) stereo images were collected for extracting high-resolution digital elevation models (DEMs) and further estimating terrain elevation and its changes pattern in this study. The ZY-3 surveying satellite was launched on 9 January 2012, and it can acquire images from nadir, forward, and backward viewing angles with spatial resolutions of 2.5, 3.5, and 3.5 m, respectively (Zhang et al., 2014). In this study the collected ZY-3 image pairs were

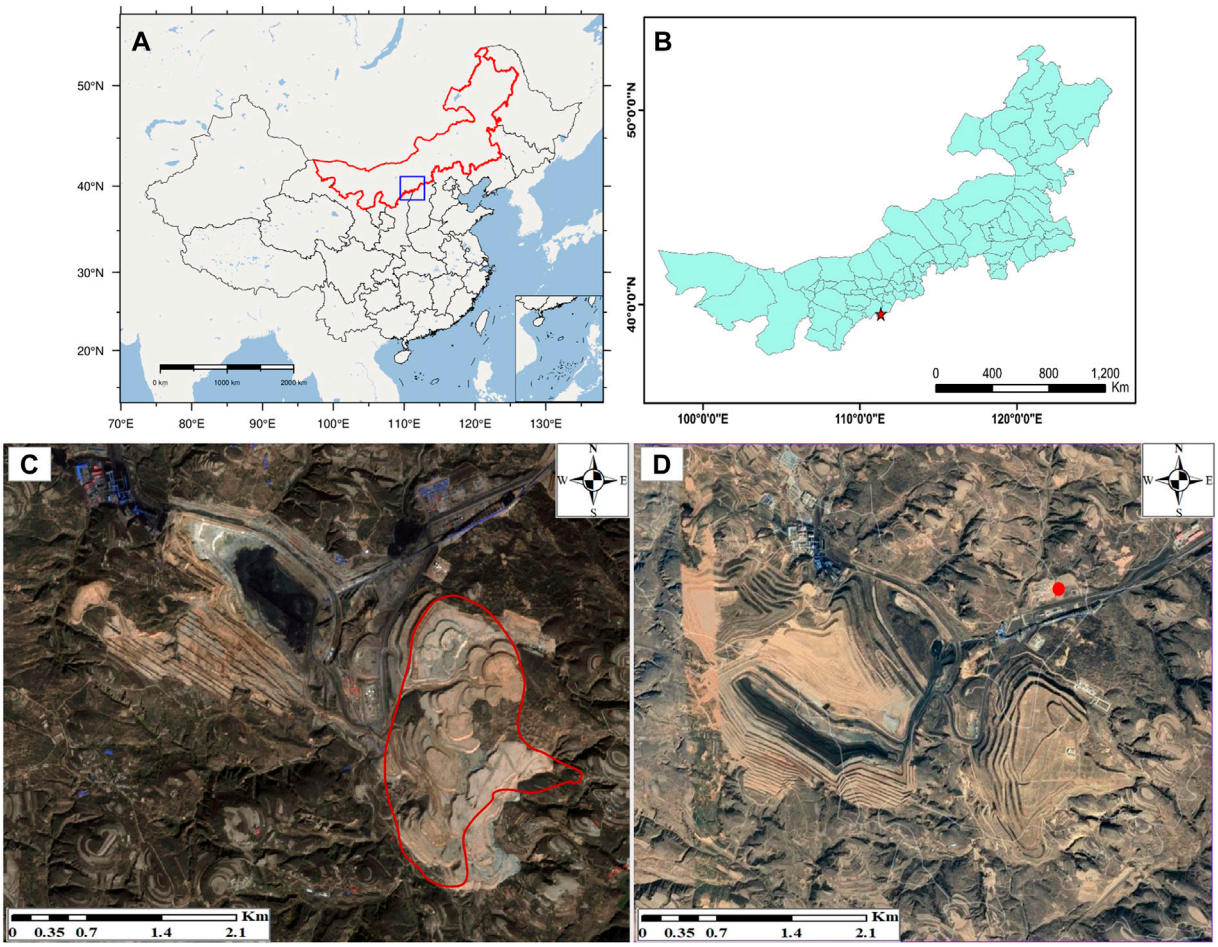

FIGURE 1 | (A,B) Location of the study area; **(C,D)** are optical images of the focused mine waste dump in the years of 2012 and 2019, respectively. The red circle in **(D)** represents the location of the selected reference pixel for InSAR processing.

acquired on 10 October 2012 (close to the date of the normal operation of the concerned mine waste dump), and 5 May 2019 (after the cease date of dumping operation), respectively.

3 METHODOLOGY

3.1 Retrieving Historical Settlement Using Time-Series InSAR

Time-series InSAR techniques can observe historical displacements of Earth's surface over time based on a series of co-registered SAR acquisitions. In the past decades several algorithms or toolbox have been developed for time series InSAR processing (Osmanoğlu et al., 2016), e.g., Interferometric Point Target Analysis (IPTA) (Werner et al., 2003), Small Baseline Subset (SBAS) (Berardino et al., 2002), Permanent Scatterer InSAR (PSInSAR) (Ferretti et al., 2001), SqueeSAR (Ferretti et al., 2011), and so on. In this section, we take the IPTA toolbox as an example to briefly review the main processing steps to generate time-series displacements.

The IPTA processing begins with the stack of co-registered SAR images for the construction of interferometric pairs. Firstly, point targets are selected based on some indicators such as low temporal variability of the backscatter and high coherence. Then, the stacks of interferometric phases on those point targets are processed by traditional differential InSAR chains (e.g., differential interferogram generation, adaptive filtering, and phase unwrapping). Thirdly, a stepwise iteration is conducted to estimate linear deformation phases, height error phases, and non-linear deformation phases at those point targets. Finally, time-series displacements at those point targets along the line-of-sight (LOS) direction are obtained by transforming the linear and non-linear deformation phases. Since mine waste dump is primarily made of soft soil, and the settlement generally dominates the deformation; that is, the horizontal component of deformation is generally much smaller than the settlement.

Consequently, we neglected the contribution of horizontal movements on InSAR LOS deformation and further convert the LOS deformation to settlement by:

$$d_v(i,j,\boldsymbol{t}_{obs}) = d_{LOS}(i,j,\boldsymbol{t}_{obs})/\cos\theta(i,j) \quad (1)$$

where d_v is a settlement at an arbitrary point target (i, j), $\boldsymbol{t}_{obs} = [\, t_{obs1} \quad t_{obs2} \quad \cdots \quad t_{obsM} \,]$ is a vector of acquisition dates of the collected M SAR images; d_{LOS} is the deformation in the LOS direction (positive towards the satellite, and negative away from the satellite), and θ is the incidence angle of SAR sensor.

3.2 Modeling and Predicting Time-Series Settlement With a Consolidation Model

The gradual reduction in the volume of soil under sustained load is called consolidation (Terzaghi et al., 1996). Commonly, the consolidation settlement is divided into the primary stage which is normally expected load applied on the soil by the dissipation of pore pressure, and the secondary consolidation stage which is continuing under constant effective stress (Hanrahan and Barden 1968). In soft soil such as mine waste dump clearly, the primary consolidation usually occurs in the operation period, and the secondary consolidation will continue after the operation. Consequently, InSAR-measured subsidence is mainly due to the secondary consolidation, if we neglect other factors potentially causing subsidence (e.g., rainfall) (Zhang et al., 2019). According to (EBMEG 2006), the secondary consolidation can be modeled by:

$$d_v(t) = c \cdot \Delta H \cdot \log_{10}\frac{t}{T_p} \quad (2)$$

where $d_v(t)$ is the time-series settlement due to secondary consolidation, c is the coefficient of secondary consolidation, ΔH is the thickness of mine waste dump, t is the entire estimation time (including the primary and secondary consolidation), and T_p is the main consolidation completion time. Note that the settlement is defined as positive, and uplift is defined as negative in **Eq. 2**.

In **Eq. 2**, the T_p and t can be determined based on the operation procedure and the expected period that will predict. Consequently, the key issue for predicting time-series settlement of mine waste dump using **Eq. 2** is determining the coefficient of secondary consolidation (namely c). As stated in *Introduction Section*, the historical settlement of the mine waste dump can be obtained using time-series InSAR. In addition, the parameter c can be generally considered as constant during the secondary consolidation. Thus, for a point target (i, j), the coefficient of secondary consolidation can be estimated based on InSAR observations of historical time-series settlement using a least-square sense, i.e.,

$$\hat{c}(i,j) = (\boldsymbol{A}^{\mathrm{T}}\boldsymbol{P}\boldsymbol{A})^{-1}\boldsymbol{A}\boldsymbol{P}\boldsymbol{L} \quad (3)$$

Where

$$\boldsymbol{A} = \left[\, \Delta H(i,j)\cdot\log_{10}\frac{t_{obs1}}{T_p} \quad \Delta H(i,j)\cdot\log_{10}\frac{t_{obs2}}{T_p} \quad \cdots \quad \Delta H(i,j)\cdot\log_{10}\frac{t_{obsM}}{T_p} \,\right]^{\mathrm{T}}$$

$\boldsymbol{L} = [\, d_v(i,j,t_{obs1}) \quad d_v(i,j,t_{obs2}) \quad \cdots \quad d_v(i,j,t_{obsM}) \,]^{\mathrm{T}}$; $\boldsymbol{P}$ is a weighting matrix. Having obtained the coefficient of secondary consolidation, the settlement in the future could be predicted based on **Eq. 2**. The general methodology workflow is shown in **Figure 2**.

4 RESULTS

4.1 Historical Time-Series Displacements Retrieval Using IPTA Toolbox

In this study, the collected 90 C-band ascending Sentinel-1A images from 30 May 2017 to 14 May 2020, were processed using the IPTA InSAR toolbox. More specifically, the image acquired on December 10, 2019, was selected to be the master image, and the remaining images were co-registered with it. Then, a threshold of the maximum perpendicular baseline of 200 m and the longest temporal separation of 90 days was designated to select small baseline interferograms (whose temporal-spatial baselines are shown in **Figure 3**). Then, the IPTA was used to process the formed small baseline interferograms to generate time-series LOS displacements from 30 May 2017 and 14 May 2020 (see **Supplementary Figure S1** in **Supplementary Material**). In which, a pixel located in a factory that is considered to be stable (marked by a red circle in **Figure 1D**) nearby the focused mine waste dump was selected to be the reference pixel, in order to reduce error propagation as much as possible (Cao et al., 2021). In addition, the phase errors due to uncertainties of the used external digital elevation model was iteratively estimated in the IPTA processing chain. Finally, the historical time-series settlement of the mine waste dump was estimated using **Eq. 1**.

Figure 4 shows the estimated accumulative settlement and the annual settlement velocity of the concerned mine waste dump from 30 May 2017 to 14 May 2020. Owing to the bare surface, the mine waste dump was monitored with dense InSAR observations (a total of 4658 coherent points). As is seen in **Figure 4**, the settlement on the edge of the mine waste dump is smaller than that on the central part. In addition, the maximum settlement rate and accumulative settlement in the mine waste dump, which occurred in the middle toward the south-west part of the mine waste dump, are −0.103 m/yr and −0.369 m, respectively. Such a large settlement is likely to cause geohazards. To analyze the temporal evolution of mine waste dump settlement intuitively, we plotted the time-series settlement at randomly selected three points (P1- P3, marked by black triangles in **Figure 4A**). The results are plotted in **Figure 5**. As is seen, the time-series settlement from 30 May 2017 to 14 May 2020 at these three points approximately follows an exponential growth. This is a typical pattern associated with secondary consolidation of soil.

4.2 Estimating the Parameters of the Secondary Consolidation Model Using InSAR Observations and ZY-3 DEMs

4.2.1 Estimating Soil Thickness of the Mine Waste Dump Based on ZY-3 Images

Prior to the parameter estimation of the secondary consolidation model, the soil thickness of the mine waste dump was estimated using

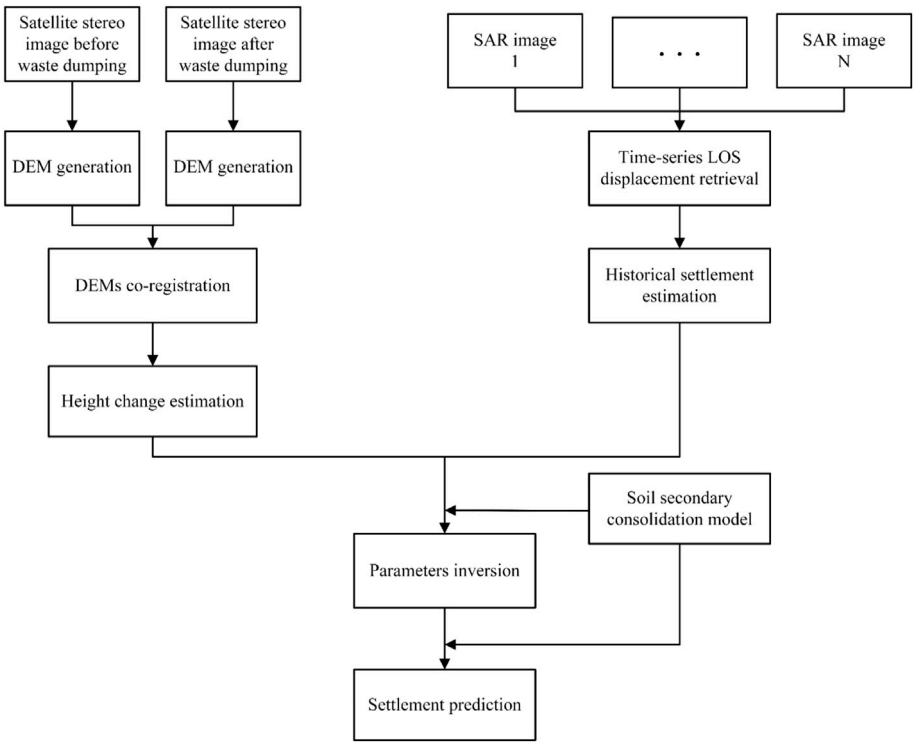

FIGURE 2 | The workflow of the presented method.

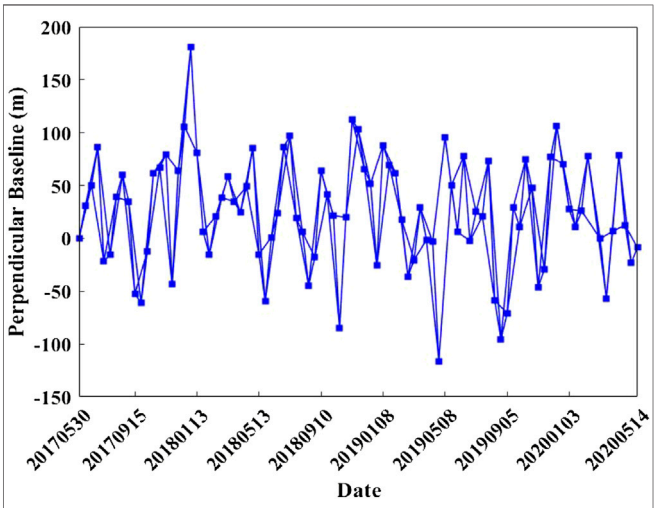

FIGURE 3 | The temporal and perpendicular baseline of the formed small baseline interferograms.

photogrammetry technique based on ZY-3 stereo images. The main procedure for generating DEMs with ZY-3 stereo pairs are three steps. Firstly, ground control points (GCPs) and tie points are manually and/or automatically be collected from a different image view. The block adjustment is then conducted based on the collected GCPs and tie points. Finally, DEM is generated based on the ZY-3 stereo pairs. Readers can refer to (Yanan et al., 2012; Guo et al., 2015) for the more detailed processing of DEM generation using stereo images. As stated in *Datasets Section*, the ZY-3 satellite can acquire stereo images from nadir, forward, and backward viewing angles. Generally, the accuracy of the generated DEMs using the stereo pair formed with the forward and backward viewing images is higher than that with other views (Cai et al., 2015; Liu et al., 2021). Thus, we generated DEMs of the mine waste dump using the ZY-3 forward and backward stereo pairs in the years of 2012 and 2019 for estimating the dump soil thickness.

More specifically, to associate projection coordinates with the location on a raw image, 20 well-distributed GCPs were manually collected. With the increase in the number of GCPs, it can improve the accuracy and quality of DEMs (Shen et al., 2017). The GCPs were selected on the stable area, such as road intersections, the corner of the road, the building, etc. The tie points were automatically obtained by the Fast Fourier Transform Phase matching method on overlap area in the stereo images and achieved sub-pixel accuracy. The block adjustment model was used based on the rational function model. Note that, before calculating the soil thickness of the mine waste dump, the slope and aspect-based method (Nuth and Kääb 2011) was used to co-register the two DEMs in the years 2012 and 2019 (shown in **Figures 6A,B**), in order to ensure that the corresponding pixels in the two DEMs represent the same geo-location.

Figure 6C shows the soil thickness of the mine waste dump estimated by calculating the difference of these two co-registered DEMs in the years of 2012 and 2019. In which, the positive value

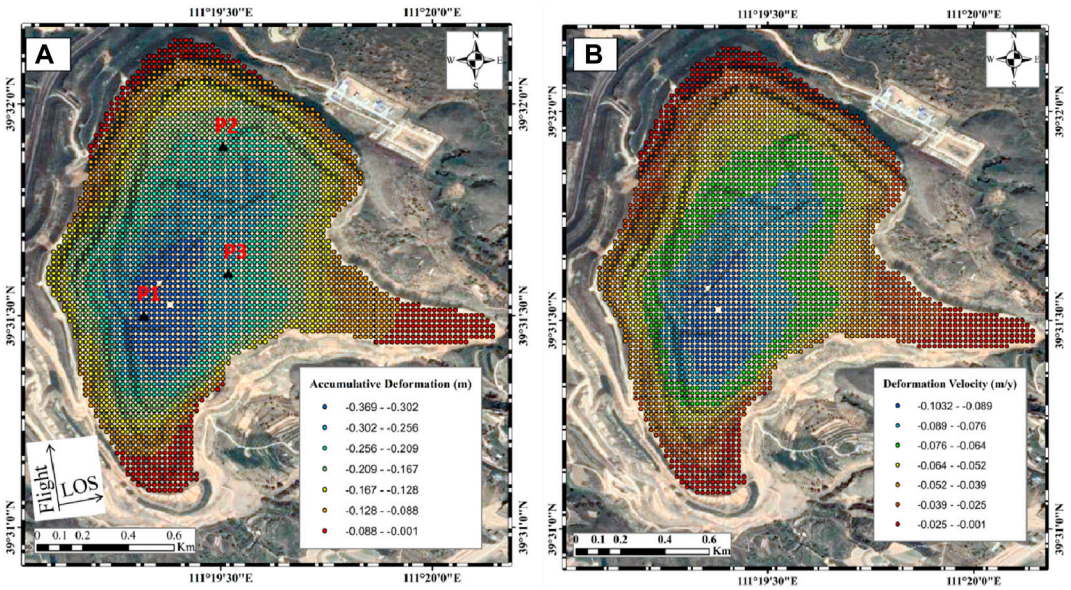

FIGURE 4 | Accumulative settlement **(A)** and the annual settlement velocity **(B)** over the focused mine waste dump in the period from 30 May 2017 to 14 May 2020.

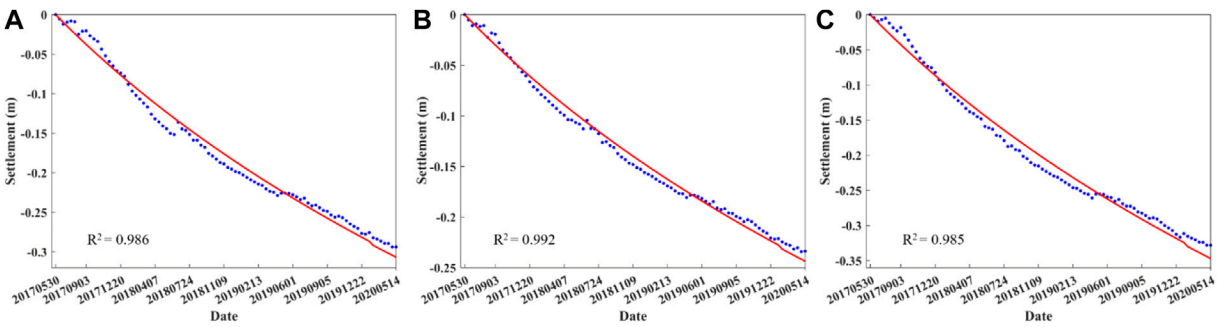

FIGURE 5 | (A–C): Time-series settlement at the points P1-P3 whose locations are marked by black triangles in **Figure 4**.

indicates increased elevation, and the negative value indicates decreased elevation. As can be seen from **Figure 6C**, the maximum thickness of the mine waste dump by May 2019 is about 85 m, which occurs in the center-south and west-east parts. The location of the maximum thickness that occurred is spatial coincidence with the maximum settlement occurred. This validates again that the settlement of mine waste dumps is related to soil thickness.

4.2.2 Estimating the Parameters of the Secondary Consolidation Model

Since the coefficient of the secondary consolidation could be considered as constant at the same point, we could theoretically estimate it using the thickness of the mine waste dump and historical settlement in any period of the secondary consolidation. It should be pointed out that the mine waste would be tamped using tools like road rollers after putting them in the dump site, thus the primary consolidation of the mine waste dump has been completed during the tamping operation. This implies that the time-series settlement obtained by InSAR from 2017 to 2020 were mainly caused by soil secondary consolidation. Hence, we estimated the coefficient of the secondary consolidation model at each target point of the IPTA processing using **Eq. 3** based on the estimated soil thickness and the InSAR observations of time-series settlement from 30 May 2017 to 5 May 2019 (near to the acquisition date of 14 May 2019 of the lastest ZY-3 images in this study). Note that the time-series InSAR observations of settlement from 5 May 2019 and 14 May 2020 were used to validate the accuracy of the predicted settlement due to the unavailability of *in situ* settlements. The estimated coefficients of the secondary consolidation model of the mine waste dump were plotted in **Figure 6D**.

4.3 Predicting Settlement Trends Using the Secondary Consolidation Model

Having obtained the coefficients of the mine waste dump, settlement in the future can be predicted using **Eq. 2**. **Figure 7**

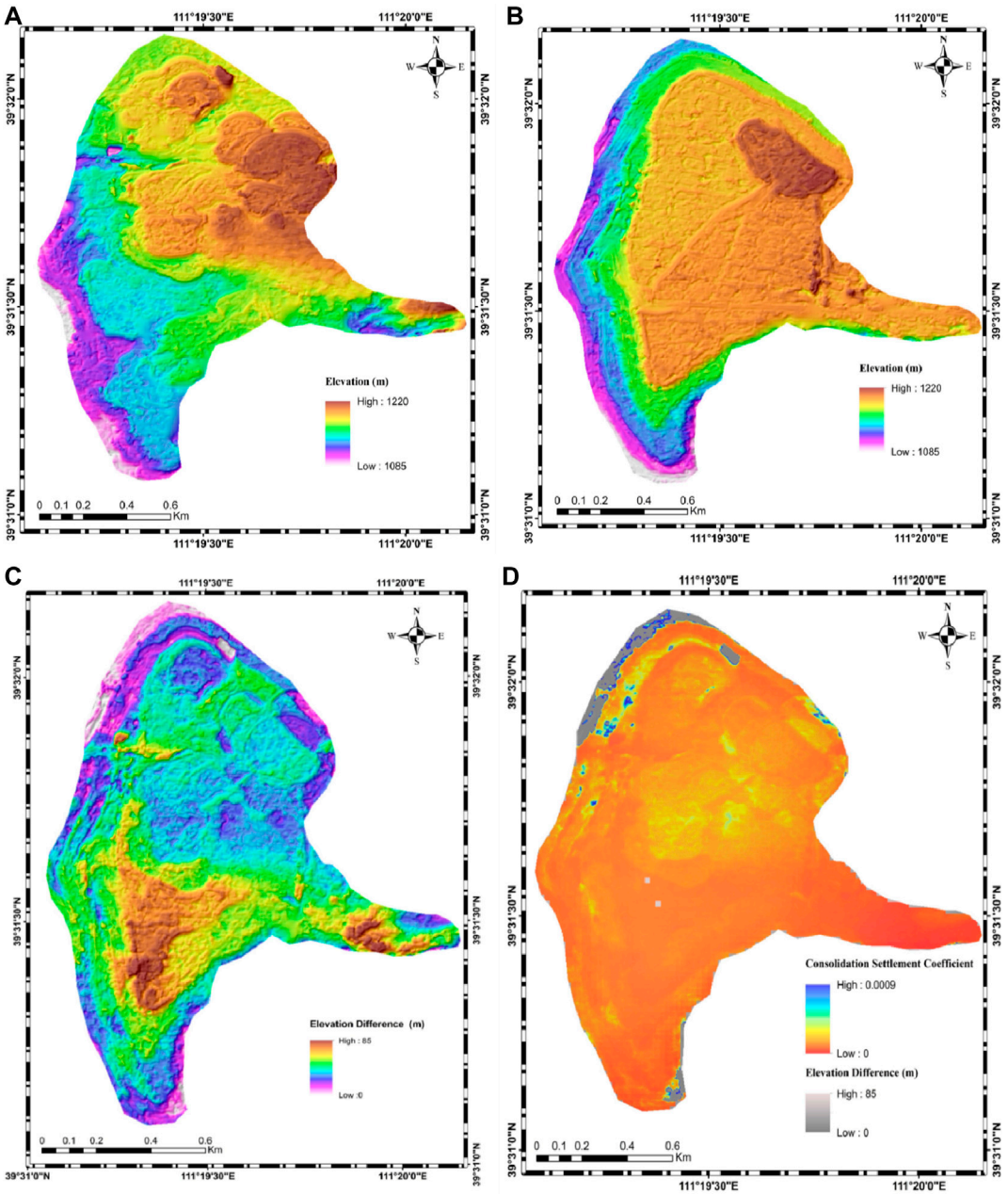

FIGURE 6 | (A,B) are the generated DEMs in the years 2012 and 2019; **(C)** Soil thickness of the mine waste dump estimated by calculating the difference of the two co-registered ZY-3 DEMs in the years of 2012 and 2019, respectively; **(D)** Estimated parameters of the secondary consolidation model and its background is the elevation difference between the years 2012 and 2019.

shows the predicted settlement of the mine waste dump in the years 2025, 2030, and 2035 (i.e., after 5, 10, and 15 years). As can be seen, the secondary consolidation significantly increased with increasing the timescale. The maxim secondary consolidations after 5, 10, and 15 years of primary consolidations are –0.4575, –0.6045, and –0.7241 m, respectively. This, in return, suggests that the focused mine waste dump has not been stable by now, a significant large settlement may occur in the future, and the governor should pay more attention to the potential geohazards.

4.4 Accuracy Evaluation of the Predicted Settlement

As stated previously, the InSAR observations of time-series settlement from 5 May 2019 and 14 May 2020, which did not

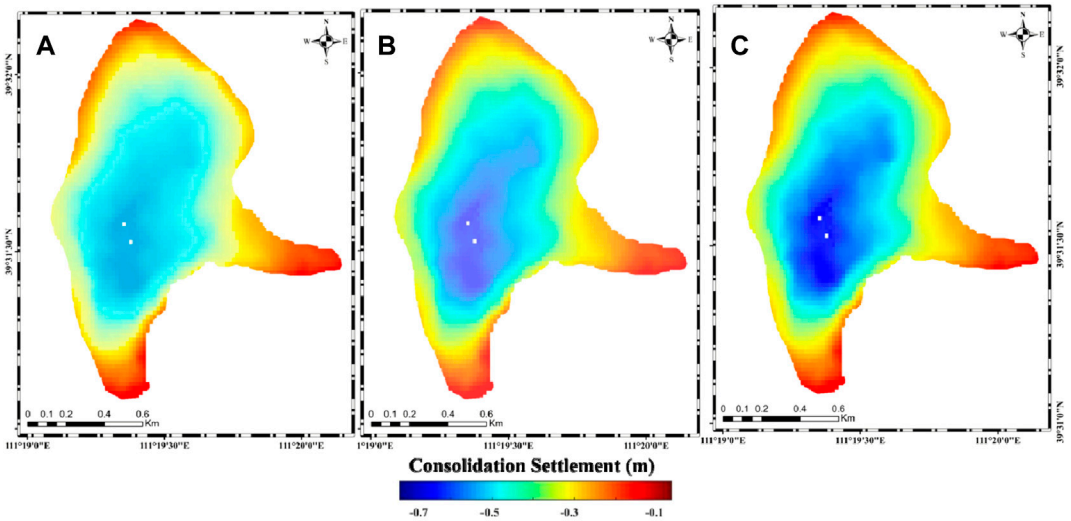

FIGURE 7 | Predicted settlement of the mine waste dump in 2025 **(A)**, 2030 **(B)**, and 2035 **(C)**, respectively, using the secondary consolidation model and its inverted parameters.

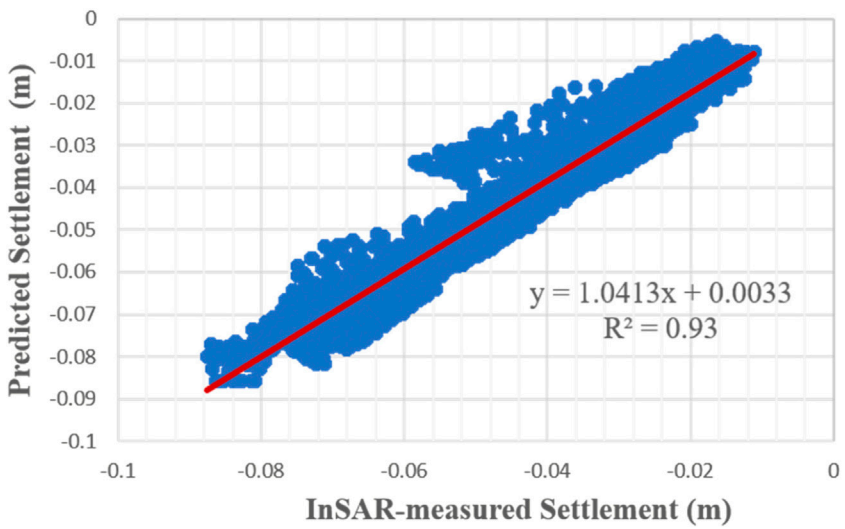

FIGURE 8 | Scatter plot between the InSAR-measured and the predicted cumulative settlement from 5 May 2019 to 14 May 2020. The red line is the fitted linear trend between the both.

be used to invert the parameters of the secondary consolidation, were used for accuracy evaluation in this section, due to the lack of the *in situ* settlement measurements. More specifically, we first predicted the time-series settlement at the acquisition dates of the collected Sentinel-1 images from 5 May 2019 to 14 May 2020 using the inverted coefficients and the secondary consolidation model. Then, the time-series InSAR settlements in the same epochs were considered as references for assessing the reliability of the predicted settlements.

Figure 8 shows a scatterplot between the InSAR-measured and the predicted settlements from 5 May 2019 and 14 May 2020. As is seen, most of them both settlements agree well with each other with a root mean square error (RMSE) of 0.008 m. In addition, we fitted the relationship between both of them with a linear function (marked by a red line in **Figure 8**). The results show that the slope and intercept of the fitted line are about 1.04 and 0.003, respectively, and the R-square is around 0.93. These results suggest that the predicted settlement using the presented method is reliable. In order to intuitively demonstrate the differences between the InSAR-measured and the predicted settlement of the mine waste dump, we added the predicted time-series settlements at the points P1, P2, and P3 in **Figure 5**, where the InSAR-measured time-series settlement between 30 May 2017 and 14 May 2020 are plotted. As is shown, the InSAR-

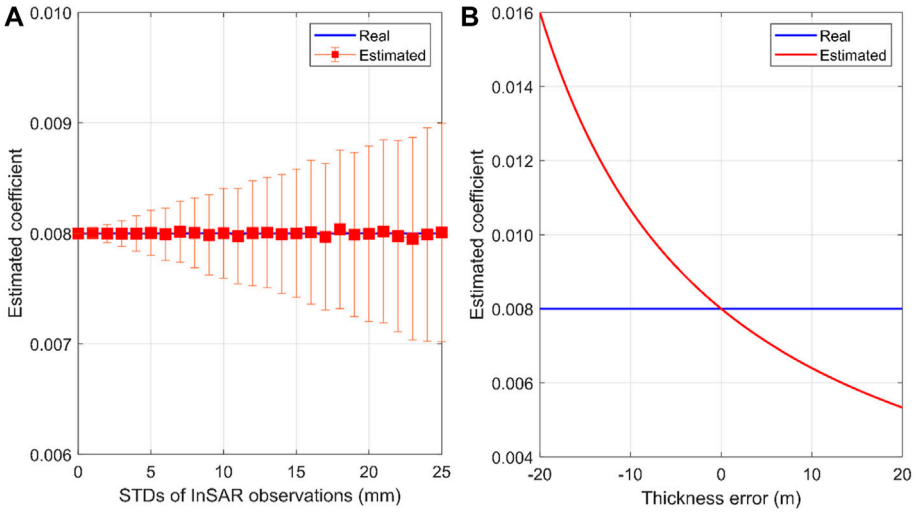

FIGURE 9 | Influences of InSAR observation errors **(A)** and dump thickness errors on the estimated coefficients of secondary consolidation **(B)**.

measured and the predicted settlements (red line) have a good agreement with each other. This further indicates that the presented method in this study is feasible.

5 DISCUSSION

5.1 Influence of InSAR and DEM Errors on the Parameter Estimation of the Secondary Consolidation Model

In this study, the coefficient of the secondary consolidation model was estimated with historical InSAR observations of time-series settlement and ZY-3 DEMs. Since errors are inevitably contained in InSAR observations and ZY-3 DEMs, the accuracy of the estimated coefficient of the secondary consolidation model would be degraded. Simulation analyses were conducted to illustrate this issue in detail in this section.

5.1.1 Influence of InSAR Errors on the Parameter Estimation

We firstly assumed a real coefficient of $c = 0.008$ (the mean of its common range from 0.004 to 0.012 for soil) and a dump thickness of $\triangle H = 40$ m. Then, the real time-series settlement of secondary consolidation was simulated using **Eq. 1** based on the real coefficient and dump thickness. Thirdly, InSAR observations of the settlement were generated by adding different level Gaussian noise (with the same mean of zero and different standard deviations (STDs) from zero to 25 mm) to the real time-series settlement. Finally, the InSAR observations with different error levels were used to estimate the coefficient of the secondary consolidation. To reduce the influence of the generation of Gaussian errors, the above steps were repeated 1000 times. The results are plotted in **Figure 9A**. Note that, Gaussian noise may well not simulate the real error of InSAR displacement observations due to its complex error sources (e.g., decorrelation noise, unwrapping errors, and atmospheric phase screen) (Zebker and Villasenor 1992; Li et al., 2019; Yunjun et al., 2019; Cao et al., 2021). However, the main aim of using Gaussian noise simulation in this section is to analyze the influence of InSAR error magnitude on the accuracy of the estimated coefficient. In this regard, it is unnecessary to simulate the errors of InSAR displacement observations accurately.

It can be seen from **Figure 9A** that, with the error increasing of InSAR observations, the STDs of the estimated coefficient (calculating with the results of the 1000 repeated simulation) are increased but below 0.001 in this simulated case. In addition, the mean of the coefficient estimate approximately equals the real one (i.e., 0.008), although the STD of InSAR observations increases from zero to 25 mm. This result indicates that the errors of InSAR observations have an insignificant influence on the coefficient estimation of the secondary consolidation. This conclusion is theoretically expectable. According to **Eq. 3**, the error propagation of InSAR observations into the estimated coefficient is inversely proportional to the thickness of the mine waste dump. Generally, the thickness of the mine waste dump is much larger than the error magnitude of InSAR observations. This implies that the errors of InSAR observations will be dramatically mitigated when they propagate into the estimated coefficient. Based on InSAR observation samples over a far-field and stable area nearby the focused mine waste dump in the real data experiment, we observed that the statistical mean and STD of the far-field InSAR observations were about −0.001 and 0.005 m. Such an error level has an insignificant influence on the estimated coefficient of the focused mine waste dump in this case.

5.1.2 Influence of Dump Thickness Errors on the Parameter Estimation

A simulation analysis was carried out to show the influence of dump thickness errors on the parameter estimation in this section. More specifically, the parameters of the secondary consolidation model were the same as those in *Influence of*

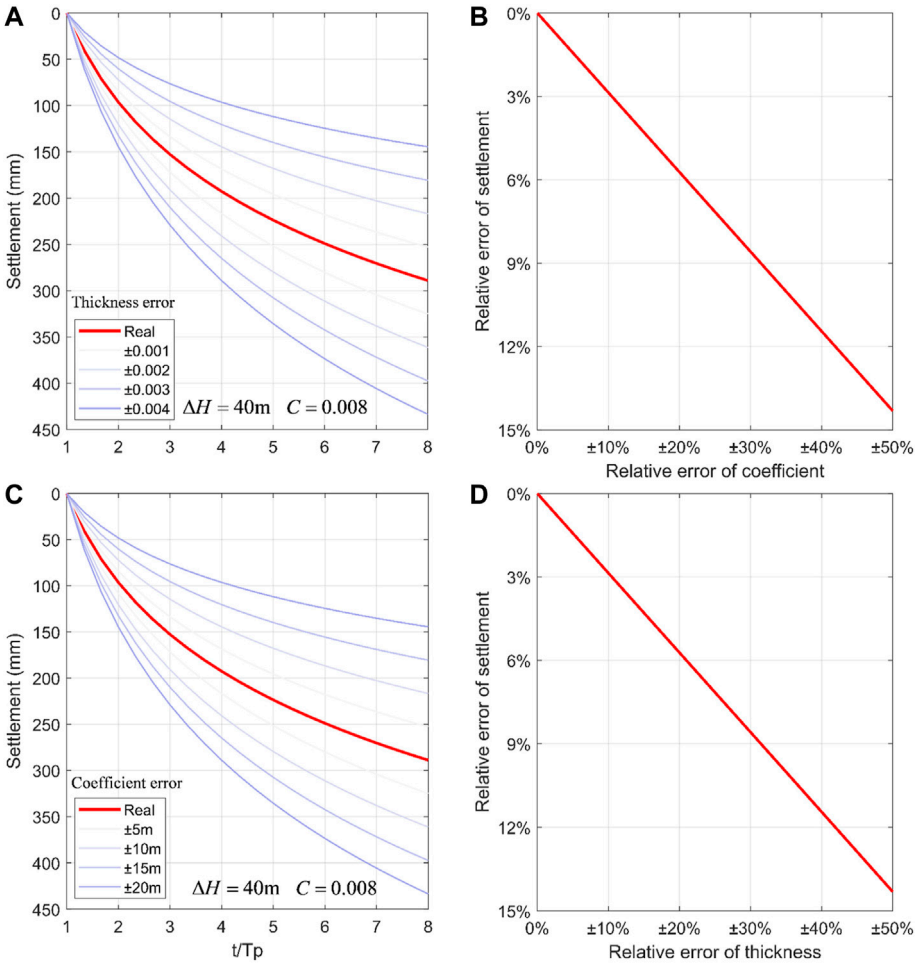

FIGURE 10 | (A,C): Examples of the influence of thickness errors and coefficient errors on the predicted settlement, respectively; **(B,D)**: Relationship of the predicted settlement relative errors with thickness and coefficient relative errors, respectively.

InSAR Errors on the Parameter Estimation Section. However, InSAR observations were assumed to be error-free and the estimation of dump thickness was designated by a range from 20 to 60 m (indicating a relative error to the real one from −50 to 50%). Then, the estimation of dump thickness with different error levels were used to inverted the model parameters using **Eq. 3**, respectively, and the result is plotted in **Figure 9B**.

As can be seen from **Figure 9B**, the dump thickness errors have a significant influence on the accuracy of the estimated coefficient of secondary consolidation. For instance, about 50% of errors would be caused when the uncertainty of the dump thickness reaches up to 50% (i.e., −20 m in this study). According to the comparison of the ZY-3-derived DEMs with ICESat-2 elevation observations (with error levels of centimeters, see **Supplementary Figure S2** in **Supplementary Material**), the accuracies of the ZY-3 DEM products in the years 2012 and 2019 are about 6.4 and 5.3 m, respectively. Such an error level would cause a maximum error of about 0.0016 (occupying 20% of the real coefficient) in this simulation case.

5.2 Error Influence of the Secondary Consolidation Model Parameters on the Accuracy of the Predicted Settlement

The settlement of the mine waste dump was modeled and further predicted using the secondary consolidation model in **Eq. 2** in this study. As can be seen from **Eq. 2**, besides the model inaccuracy, the reliability of the predicted settlement primarily depends on two factors, i.e., the errors of dump thickness and the estimated coefficient of secondary consolidation. In this section, simulation analyses were conducted to demonstrate the error influence of these two parameters on the accuracy of the predicted settlement.

5.2.1 Influence of the Coefficient Errors on the Accuracy of the Predicted Settlement

Similar to the simulation in *Influence of InSAR and DEM Errors on the Parameter Estimation of the Secondary Consolidation Model Section*, we firstly simulated the real time-series settlement of the mine waste dump (see red line in **Figure 10A**) by assuming that c =

0.008 and $\triangle H$ = 40 m. Then, we assumed that the estimated coefficients were 0.004–0.012, which indicates error levels from −50 to 50%. Finally, the estimated coefficients with different error levels were used to predict time-series settlement, and the results are plotted in **Figure 10A** for comparison. It can be seen from **Figure 10A** that the error of the estimated coefficient significantly affects the reliability of the predicted settlement using the secondary consolidation model. The larger the error of the estimated coefficient is, the lower the reliability of the predicted settlement, and vice versa. Even for the same error in the estimated coefficient, the error magnitude of the predicted settlement would be increased with the increase of the predicted time.

Figure 10B plots a comparison between the relative errors of the predicted settlement to the maximum predicted one (referred to as relative error of settlement) and the relative errors of the estimated coefficient to the real one (referred to as relative error of coefficient). As is shown, the settlement relative error is linearly proportional to the coefficient relative errors with an intercept of zero and a slope of about 16° in the simulation case. In addition, it can be seen from **Figure 10B** that the maximum relative error of the predicted settlement is about 14.3% when the maximum relative error of the coefficient reaches up to 50%.

5.2.2 Influence of the Dump Thickness Errors on the Accuracy of the Predicted Settlement

Figure 10C shows a comparison of the dump thickness errors on the accuracy of the predicted settlement. In which, the real parameters of the secondary consolidation model were given as c = 0.008 and $\triangle H$ = 40 m, and the estimated dump thicknesses were 20–40 m (indicating relative errors of −50–50% of the real thickness). As can be seen from **Figure 10C**, the error of the estimated dump thickness imposes a significant effect on the accuracy of the predicted settlement. The larger the error is, the lower the accuracy is, and vice versa. In addition, as is shown in **Figure 10D** where the relationship between the relative errors of the predicted settlement and the dump thickness, both the relative errors are linearly proportional with each other. When the maximum relative error of the coefficient reaches up to 50%, the error of 14.3% of the maximum predicted settlement will be caused.

6 CONCLUSION

In this study, a remote sensing-based method was proposed to predict the time-series settlement of mine waste dump. The test over Weijiamao open-pit mine, China, shows that the presented method can reliably predict the time-series settlement of the mine waste dump, with an accuracy of 0.008 m. In this presented method the coefficient estimation of the secondary consolidation is sensitive to the error of thickness estimation but is insensitive to the error of InSAR observations. In addition, both the errors of thickness estimation and the estimated coefficient have a significant influence on the predicted settlement of mine waste dump using the secondary consolidation model. Therefore, it is important to obtain the thickness of the concerned mine waste dumps at a high accuracy level. In addition, it should be pointed out that the contribution of horizontal movements of mine waste dump was neglected when we estimated settlement from single-track InSAR observations of LOS displacements. Such a strategy would cause errors in the estimated settlement, and further degrading the accuracy of the predicted settlement. This issue will be our future research topic.

DATA AVAILABILITY STATEMENT

The original contributions presented in the study are included in the article/**Supplementary Material**, further inquiries can be directed to the corresponding author.

AUTHOR CONTRIBUTIONS

ZY contributed to conception and design of the study. ZX and ZC organized the database. TR, ZY, and LW performed the statistical analysis. TR wrote the first draft of the manuscript. TR and ZY wrote sections of the manuscript. All authors contributed to manuscript revision, read, and approved the submitted version.

FUNDING

This work was partly supported by the National Natural Science Foundation of China (Grant No. 41904005); the Basic Science Center of the National Natural Science Foundation of China (Grant No. 72088101); The Science and Technology Innovation Program of Hunan Province (2021RC3008); the Natural Science Foundation of Hunan Province, China (Grant No. 2020JJ4699); and the Research Foundation of Education Bureau of Hunan Province, China (Grant No. 20K134), the Science and Technology Plan of Department of Natural Resources of Hunan Province, China (2021-17).

ACKNOWLEDGMENTS

We also thank the reviewers for the constructive suggestions. The Sentinel-1 data used in this study were provided by ESA/Copernicus (https://scihub.copernicus.eu).

SUPPLEMENTARY MATERIAL

The Supplementary Material for this article can be found online at: https://www.frontiersin.org/articles/10.3389/fenvs.2022.885346/full#supplementary-material

Supplementary Figure S1 | InSAR observations of time-series displacements from 30 May 2017 (denoting by 20170530 in the figure) to 14 May 2020.

Supplementary Figure S2 | (A, B): ZY-3 generated DEMs in the years of 2012 and 2019, respectively. The red circles denote the location of ICESat-2 data which is used to validate the accuracy of the ZY-3 DEMs.

Supplementary Table S1 | Accuracy of the ZY-3 generated DEMs with respect to ICESat-2.

REFERENCES

Ashutosh, K., Verma, D., Thareja, R., and Singh, T. N. (2013). A Review on Numerical Slope Stability Analysis. *Int. J. Sci. Eng. Tech. Res.* 2, 1315–1320.

Atzori, S., Antonioli, A., Tolomei, C., De Novellis, V., De Luca, C., and Monterroso, F. (2019). InSAR Full-Resolution Analysis of the 2017-2018 M>6 Earthquakes in Mexico. *Remote Sensing Environ.* 234, 111461. doi:10.1016/j.rse.2019.111461

Behera, P. K., Sarkar, K., Singh, A. K., Verma, A. K., and Singh, T. N. (2016). Dump Slope Stability Analysis - A Case Study. *J. Geol. Soc. India* 88, 725–735. doi:10.1007/s12594-016-0540-4

Berardino, P., Fornaro, G., Lanari, R., and Sansosti, E. (2002). A New Algorithm for Surface Deformation Monitoring Based on Small Baseline Differential SAR Interferograms. *IEEE Trans. Geosci. Remote Sensing* 40, 2375–2383. doi:10.1109/tgrs.2002.803792

Bürgmann, R., Rosen, P., and Fielding, J. E. (2000). Synthetic Aperture Radar Interferometry to Measure Earth's Surface Topography and its Deformation. *Annu. Rev. Earth Planet. Sci.* 28, 169–209. doi:10.1146/annurev.earth.28.1.16

Cai, G., Huan, J., Liu, Y., and Du, M. (2015). DEM Generation and Accuracy Assessment Using ZY-3 Stereo Image Pairs. *Appl. Mech. Mater.* 738–739, 613–617. doi:10.4028/www.scientific.net/AMM.738-739.613

Cao, Y., Jónsson, S., and Li, Z. (2021). Advanced InSAR Tropospheric Corrections from Global Atmospheric Models that Incorporate Spatial Stochastic Properties of the Troposphere. *JGR Solid Earth* 126, e2020JB020952. doi:10.1029/2020JB020952

Carlà, T., Intrieri, E., Raspini, F., Bardi, F., Farina, P., Ferretti, A., et al. (2019). Perspectives on the Prediction of Catastrophic Slope Failures from Satellite InSAR. *Sci. Rep.* 9, 14137. doi:10.1038/s41598-019-50792-y

Chen, Y., Tong, Y., and Tan, K. (2020). Coal Mining Deformation Monitoring Using SBAS-InSAR and Offset Tracking: A Case Study of Yu County, China. *IEEE J. Sel. Top. Appl. Earth Observations Remote Sensing* 13, 6077–6087. doi:10.1109/JSTARS.2020.3028083

Cho, Y.-C., and Song, Y.-S. (2014). Deformation Measurements and a Stability Analysis of the Slope at a Coal Mine Waste Dump. *Ecol. Eng.* 68, 189–199. doi:10.1016/j.ecoleng.2014.03.005

Confuorto, P., Diego, D. M., Infante, D., Novellino, A., Papa, R., Calcaterra, D., et al. (2019). Monitoring of Remedial Works Performance on Landslide-Affected Areas through Ground- and Satellite-Based Techniques. *Catena* 178, 77–89. doi:10.1016/j.catena.2019.03.005

EBMEG (2006). *Manual of Engineering Geology*. China: Chinese Architectural Industry Press Beijing.

Ferretti, A., Fumagalli, A., Novali, F., Prati, C., Rocca, F., and Rucci, A. (2011). A New Algorithm for Processing Interferometric Data-Stacks: SqueeSAR. *IEEE Trans. Geosci. Remote Sensing* 49 (9), 3460–3470. doi:10.1109/TGRS.2011.2124465

Ferretti, A., Prati, C., and Rocca, F. (2001). Permanent Scatterers in SAR Interferometry. *IEEE Trans. Geosci. Remote Sensing* 39, 8–20. doi:10.1109/36.898661

Gabriel, A. K., Goldstein, R. M., and Zebker, H. A. (1989). Mapping Small Elevation Changes over Large Areas: Differential Radar Interferometry. *J. Geophys. Res.* 94, 9183–9191. doi:10.1029/JB094iB07p09183

Gong, C., Lei, S., Bian, Z. F., Tian, Y., Zhang, Z., Guo, H., et al. (2021). Using Time Series InSAR to Assess the Deformation Activity of Open-Pit Mine Dump Site in Severe Cold Area. *J. Soils Sediments* 21, 3717–3732. doi:10.1007/S11368-021-03040-8

Guo, C., Huan, J., Liu, Y., and Du, M. (2015). DEM Generation and Accuracy Assessment Using ZY-3 Stereo Image Pairs. *Appl. Mech. Mater.* 738-739, 613–617. doi:10.4028/www.scientific.net/AMM.738-739.613

Hanrahan, E. T., and Barden, L. (1968). Primary and Secondary Consolidation of Clay and Peat. *Géotechnique* 183, 387–388. doi:10.1680/geot.1968.18.3.387

Hawley, P. M., and Cunning, J. (2017). *Guidelines for Mine Waste Dump and Stockpile Design*. Vic: ClaytonCSIRO.

Juan, L. V., Fernandez-Merodo, J. A., Ezquerro, P., López-Davalillo, J. C., Sarro, R., Reyes-Carmona, C., et al. (2021). Combining Satellite InSAR, Slope Units and Finite Element Modeling for Stability Analysis in Mining Waste Disposal Areas. *Remote Sensing* 13 (10), 2008. doi:10.3390/rs13102008

Kainthola, A., Verma, D., Thareja, R., and Singh, T. N. (2013). A Review on Numerical Slope Stability Analysis. *Int. J. Sci. Eng. Tech. Res* 2, 1315–1320. doi:10.3390/rs13102008

Li, M., Zhang, L., Ding, C., Li, W., Luo, H., Liao, M., et al. (2020). Retrieval of Historical Surface Displacements of the Baige Landslide from Time-Series SAR Observations for Retrospective Analysis of the Collapse Event. *Remote Sensing Environ.* 240, 111695. doi:10.1016/j.rse.2020.111695

Li, Z., Cao, Y., Wei, J., Duan, M., Wu, L., Hou, J., et al. (2019). Time-series InSAR Ground Deformation Monitoring: Atmospheric Delay Modeling and Estimating. *Earth-Science Rev.* 192, 258–284. doi:10.1016/j.earscirev.2019.03.008

Lianhuan, W., Zhang, Y., Zhao, Z., Zhong, X., Liu, S., Mao, Y., et al. (2018). Analysis of Mining Waste Dump Site Stability Based on Multiple Remote Sensing Technologies. *Remote Sensing* 10, 2025. doi:10.3390/rs10122025

Liu, Z., Han, L., Yang, Z., Cao, H., Guo, F., Guo, J., et al. (2021). Evaluating the Vertical Accuracy of DEM Generated from ZiYuan-3 Stereo Images in Understanding the Tectonic Morphology of the Qianhe Basin, China. *Remote Sensing* 13, 1203. doi:10.3390/rs13061203

Lopez-Vinielles, J. V., Fernandez-Merodo, J. A., Ezquerro, P., López-Davalillo, J. C., Sarro, R., Reyes-Carmona, C., et al. (2021). Combining Satellite InSAR, Slope Units and Finite ElementModeling for Stability Analysis in MiningWaste Disposal Areas. *Remote Sensing* 13 10, 2008. doi:10.3390/rs13102008

Massonnet, D., and Feigl, K. L. (1998). Radar Interferometry and its Application to Changes in the Earth's Surface. *Rev. Geophys.* 36 (4), 441–500. doi:10.1029/97RG03139

Massonnet, D., Rossi, M., Carmona, C., Adragna, F., Peltzer, G., Feigl, K., et al. (1993). The Displacement Field of the Landers Earthquake Mapped by Radar Interferometry. *Nature* 364 (6433), 138–142. doi:10.1038/364138a0

Nuth, C., and Kääb, A. (2011). Co-registration and Bias Corrections of Satellite Elevation Data Sets for Quantifying Glacier Thickness Change. *The Cryosphere* 5, 271–290. doi:10.5194/tc-5-271-2011

Osmanoğlu, B., Sunar, F., Wdowinski, S., and Cabral-Cano, E. (2016). Time Series Analysis of InSAR Data: Methods and Trends. *ISPRS J. Photogrammetry Remote Sensing* 115, 90–102. doi:10.1016/J.ISPRSJPRS.2015.10.003

Pierluigi, C., Diego, D. M., Infante, D., Novellino, A., Papa, R., Calcaterra, D., et al. (2019). Monitoring of Remedial Works Performance on Landslide-Affected Areas through Ground- and Satellite-Based Techniques. *Catena* 178, 77–89. doi:10.1016/j.catena.2019.03.005

Pinto, C., Paradella, W. R., Mura, J. C., Gama, F. F., Santos, A. D., and Silva, G. G. (2014). "Results of the Application of Persistent Scatterers Interferometry for Surface Displacements Monitoring in the Azul Open Pit Manganese Mine (Carajás Province, Amazon Region) Using TerraSAR-X Data," in Proc. SPIE 9245, Earth Resources and Environmental Remote Sensing/GIS Applications V, Amsterdam, Netherlands (SPIE Remote Sensing), 92451K. doi:10.1117/12.2067233

Qingsong, Q., Li, G., Zhou, Y., Chai, M., Chen, D., Qi, S., et al. (2021). Deformation Monitoring in an Alpine Mining Area in the Tianshan Mountains Based on SBAS-InSAR Technology. *Adv. Mater. Sci. Eng.* 2021, 1–15. doi:10.1155/2021/9988017

Roland, B., Rosen, P., and Fielding, J. E. (2000). Synthetic Aperture Radar Interferometry to Measure Earth's Surface Topography and its Deformation. *Annu. Rev. Earth Planet. Sci.* 28, 169–209. doi:10.1146/annurev.earth.28.1.169

Shen, X., Liu, B., and Li, Q.-Q. (2017). Correcting Bias in the Rational Polynomial Coefficients of Satellite Imagery Using Thin-Plate Smoothing Splines. *ISPRS J. Photogrammetry Remote Sensing* 125, 125–131. doi:10.1016/j.isprsjprs.2017.01.007

Suwarsono, S., Prasasti, I., Nugroho, J. T., Sitorus, J., Arief, R., Rahmi, K. I. N., et al. (2019). Detecting Deformation Due to the 2018 Merapi Volcano Eruption Using Interferometric Synthetic Aperture Radar (INSAR) From Sentinel-1 TOPS. *IJReSES* 16, 45. doi:10.30536/j.ijreses.2019.v16.a3145

Terzaghi, K., Peck, R. B., and Mesri, G. (1996). *Soil Mechanics in Engineering Practice*. New York: John Wiley & Sons, Inc.

Verma, D., Kainthola, A., Gupte, S. S., and Singh, T. N. (2013). A Finite Element Approach of Stability Analysis of Internal Dump Slope in Wardha Valley Coal Field, India, Maharashtra. *Am. J. Mining Metall.* 1, 1–6. doi:10.12691/ajmm-1-1-1

Wei, L., Zhang, Y., Zhao, Z., Zhong, X., Liu, S., Mao, Y., et al. (2018). Analysis of Mining Waste Dump Site Stability Based on Multiple Remote Sensing Technologies. *Remote Sensing* 10, 2025. doi:10.3390/rs10122025

Werner, C., Wegmuller, U., Strozzi, T., and Wiesmann, A. (2003). Interferometric point Target Analysis for Deformation Mapping. *Proceedings (IEEE Cat. No.03CH37477)* 7, 4362–4364. doi:10.1109/IGARSS.2003.1295516

Williams, C., Ross, B., Zebker, M., Leighton, J., Gaida, M., Morkeh, J., et al. (2021). Assessment of the Available Historic RADARSAT-2 Synthetic Aperture Radar Data Prior to the Manefay Slide at the Bingham Canyon Mine Using Modern InSAR Techniques. *Rock Mech. Rock Eng.* 54, 3469–3489. doi:10.1007/s00603-021-02483-2

Yanan, Z., Fuguang, D., and Changqing, Z. (2012). DEM Extraction and Accuracy Assessment Based on ZY-3 Stereo Images. *IEEE*, 1439–1442. doi:10.1109/iccsnt.2012.6526191

Yu, C., Li, Z., and Penna, N. T. (2020). Triggered Afterslip on the Southern Hikurangi Subduction Interface Following the 2016 Kaikōura Earthquake from InSAR Time Series with Atmospheric Corrections. *Remote Sensing Environ.* 251, 112097. doi:10.1016/j.rse.2020.112097

Yuan, M., Li, M., Liu, H., Lv, P., Li, B., and Zheng, W. (2021). Subsidence Monitoring Base on SBAS-InSAR and Slope Stability Analysis Method for Damage Analysis in Mountainous Mining Subsidence Regions. *Remote Sensing* 13 (16), 3107. doi:10.3390/rs13163107

Yunjun, Z., Fattahi, H., and Amelung, F. (2019). Small Baseline InSAR Time Series Analysis: Unwrapping Error Correction and Noise Reduction. *Comput. Geosciences* 133, 104331. doi:10.1016/j.cageo.2019.104331

Zebker, H. A., and Villasenor, J. (1992). Decorrelation in Interferometric Radar Echoes. *IEEE Trans. Geosci. Remote Sensing* 30, 950–959. doi:10.1109/36.175330

Zhang, Y., Huang, H., Liu, Y., Liu, Y., and Bi, H. (2019). Spatial and Temporal Variations in Subsidence Due to the Natural Consolidation and Compaction of Sediment in the Yellow River delta, china. *Mar. Georesources Geotechnology* 37, 152–163. doi:10.1080/1064119X.2017.1414903

Zhang, Y., Zheng, M., Xiong, J., Lu, Y., and Xiong, X. (2014). On-Orbit Geometric Calibration of ZY-3 Three-Line Array Imagery with Multistrip Data Sets. *IEEE Trans. Geosci. Remote Sensing* 52, 224–234. doi:10.1109/TGRS.2013.2237781

Conflict of Interest: KZ was employed by the company North Weijiamao Power and Coal Co., Ltd., and YZ was employed by the company North United Electric Power Co., Ltd.

The remaining authors declare that the research was conducted in the absence of any commercial or financial relationships that could be construed as a potential conflict of interest.

frontiers | Frontiers in Environmental Science

ORIGINAL RESEARCH
published: 13 July 2022
doi: 10.3389/fenvs.2022.929958

Time Series Multi-Sensors of Interferometry Synthetic Aperture Radar for Monitoring Ground Deformation

Chuanguang Zhu[1]*, *Sichun Long*[1]*, *Jixian Zhang*[2], *Wenhao Wu*[1] and *Liya Zhang*[1]

[1]School of Earth Sciences and Geospatial Information Engineering, Hunan University of Science and Technology, Xiangtan, China, [2]National Quality Inspection and Testing Center for Surveying and Mapping Products, Ministry of Natural Resources of the People's Republic of China, Beijing, China

A stack of images is a prerequisite for the multi-temporal interferometric synthetic aperture radar (MT-InSAR) due to the wrapped nature of the interferometric phase. Although the SBAS technique can relieve the requirement of the amount of SAR data, dozens of SAR acquisitions could be regarded as the minimum requirement. However, due to the limitation of the imaging capability of the spaceborne SAR system, the amount of available SAR data acquired from only one SAR sensor is often not enough to satisfy the requirement for phase unwrapping based on the Nyquist sampling assumption. Fortunately, there sometimes may be more than one SAR stack, that is, stacks of SAR data acquired from different SAR systems. In this study, we propose a methodology to detect ground deformation by combining multiple SAR images acquired from different satellite systems for MT-InSAR analysis. First, the low-pass deformation is estimated based on time series SAR acquisitions with low spatial resolution and long wavelengths such as ENVISAT ASAR (ASAR). This information is then incorporated into the processing of time series of SAR acquisitions with high spatial resolution and short wavelength, such as TerraSAR-X (TSX). Specifically, the low-pass deformation will be subtracted from each differential interferogram generated from short-wavelength SAR images, and the rest of the MT-InSAR analysis will be based on the double-differentiation interferograms. Then, the residual deformation will be calculated from these double-differentiation interferograms and together with the low-pass deformation forms the full deformation. As the principal component of deformation has already been subtracted, the phase gradient of those double-differentiated interferograms will be smooth enough to facilitate the phase unwrapping. Between January 2009 and September 2010, 14 ASAR images and 11 TSX images acquired from Tianjin, China are selected as the test data. A root means square error (RMSE) of 9.1 mm/year is achieved from 11 TSX images, while a root means square error of 3.7 mm/year is achieved from 14 ASAR images. However, an RMSE of 1.6 mm/year is achieved when integrating 11 TSX images and 14 ASAR images for MT-InSAR analysis. The experiments show that the proposed method can effectively detect ground deformation.

Keywords: multitemporal interferometric synthetic aperture radar, ground deformation, Nyquist sampling, multiple satellite systems, spaceborne SAR

OPEN ACCESS

Edited by:
Yu Chen,
China University of Mining and Technology, China

Reviewed by:
Chaoying Zhao,
Chang'an University, China
Maged Marghany,
Syiah Kuala University, Indonesia

***Correspondence:**
Chuanguang Zhu
zhuchuanguang@163.com
Sichun Long
sclong@hnust.edu.cn

Specialty section:
This article was submitted to Environmental Informatics and Remote Sensing, a section of the journal Frontiers in Environmental Science

Received: *27 April 2022*
Accepted: *07 June 2022*
Published: *13 July 2022*

Citation:
Zhu C, Long S, Zhang J, Wu W and Zhang L (2022) Time Series Multi-Sensors of Interferometry Synthetic Aperture Radar for Monitoring Ground Deformation. Front. Environ. Sci. 10:929958. doi: 10.3389/fenvs.2022.929958

INTRODUCTION

Land subsidence, caused by mining and excessive extraction of groundwater, is a common hazard in contemporary society (Marghany, 2021; Marghany, 2022). Moreover, in coastal areas with low topography, land subsidence can cause more risky damages such as flooding and even inundation (Hu et al., 2009). Measurement of the magnitude of deformation is required to study the land subsidence and control its development.

Differential Synthetic Aperture Radar (DInSAR), a newly emerging space geodetic technique developed in the 1980s (Gabriel et al., 1989; Massonnet et al., 1993), has been proven as a powerful technique for mapping ground deformation caused by earthquake, landslide, and excessive extraction of underground water with high precision and spatial resolution over a large area. Nevertheless, DInSAR may fail due to low correlation caused by spatiotemporal baselines and atmospheric artifacts (Zebker and Villasenor, 1992; Zebker et al., 1997; Bamler and Hartl, 1998; Massonnet and Feigl, 1998; Hanssen et al., 1999; Li et al., 2004), particularly in vegetated areas. Marghany (Marghany, 2013 and Marghany, 2014) have presented two approaches to eliminate the temporal decorrelation to reduce phase unwrapping error.

Fortunately, it was found that some ground targets can maintain the characteristics of stable scattering over long intervals of time (Sousa et al., 2011). With the advantage of these coherent targets, several advanced approaches to multi-temporal InSAR (MT-InSAR) have been presented to overcome the technical limitations of DInSAR since the late 1990s (Ferretti et al., 2000; Ferretti et al., 2001; Berardino et al., 2002; Hooper et al., 2004; Lanari et al., 2004; Wegmüller et al., 2010).

These MT-InSAR approaches differ primarily in the algorithms of coherent target selection and deformation estimation. In some MT-InSAR algorithms, *a priori* information is required to model the deformation (Hooper et al., 2007). Only this scatterer, whose behavior of deformation is close to the predetermined model, will be identified as a coherent target, also referred to as a permanent scatterer (PS). In contrast, the Stanford Method for PS (StaMPS) algorithm, developed by Hooper et al., uses the spatial correlation of the interferogram phase to identify coherent targets, and it does not require prior knowledge of the variations of deformation in time series (Hooper et al., 2007). Moreover, it is found that the density of coherent targets identified by StaMPS is significantly increased in rural areas with few buildings (Sousa et al., 2011). Therefore, in this study, the StaMPS approach is used while the suburb of Tianjin is chosen as the study area.

The crucial limitation of the MT-InSAR, including the StaMPS, is the wrapped nature of the interferometric phase, which will introduce 2π-ambiguities to the unknown parameters to be estimated. Adding more information, such as an explicit functional model and prior information, to the MT-InSAR is one way to solve this impasse (Heuff and Hanssen, 2020). Dehghani et al. (2013) presented a method that combines DInSAR and Persistent Scatterer InSAR (PSI) to monitor severe ground subsidence. The linear term of subsidence was estimated using DInSAR based on the interferograms with small temporal baselines and then subtracted from all interferograms used for PSI analysis (Dehghani et al., 2013). However, lack of availability of SAR data with high coherent interferograms is mainly the limitation of this method (Sadeghi et al., 2013). In order to overcome this limitation, the periodogram approach is used to estimate the principal component of deformation (Sadeghi et al., 2013). This approach strongly depends on the discretization of the parameter in solution space. However, it is difficult to yield a unique solution as there are alternative solutions based on a different distribution of the unknown parameters (Kampes and Hanssen, 2004). Pawluszek-Filipiak and Borkowski (Pawluszek-Filipiak and Borkowski, 2020) present a method that adopts PSI and DInSAR to estimate the subsidence in the surrounding and central subsidence basins based on the same SAR dataset. Then, the PSI and DInSAR results are merged based on regularized spline functions, yielding the final ground deformation.

The objective of adding more information is to reduce the spatiotemporal variability of the interferometric phase. The interferometric phase will be smooth enough, and the phase gradients are small if the revisit time is short enough. In other words, the deformation can be accurately estimated by MT-InSAR without any additional information if the available SAR images are acquired with high temporal sampling. However, the number of available SAR images is often not enough to satisfy the requirement due to limited capability of the spaceborne sensor to collect SAR acquisitions.

Until now, many spaceborne SAR satellites, such as Envisat, ALOS-1/2, TSX, Tandem-X (TDX), COSMO-SkyMed (CSK), Radarsat-1/2, and Sentinel-1, have been launched, which allows us to observe the Earth with different wavelength, repeat time, spatial resolution, and incidence angle. With the advantage of an increasing number of SAR satellites, there may be more than one SAR stack, for example, several stacks of SAR datasets acquired from several SAR systems covering the same area.

In order to reduce the likelihood of ambiguity errors caused by severe deformation based on finite SAR data, we have developed a new methodology to integrate two different datasets, for example, ASAR with longer and TSX with shorter wavelength, for MT-InSAR analysis. First, the low-pass deformation pattern is estimated based on the time-series ASAR dataset, which represents an initial estimation (that is, the principal component) of the ground deformation. Then, this result will be subtracted from each interferogram generated from the TSX dataset to reduce the phase gradients and meet the Nyquist sampling criterion, and the rest of the MT-InSAR analysis will be based on these double-differentiated TSX interferograms. As the principal component of deformation has already been subtracted, the phase gradient of those double-differentiated TSX interferograms will be smooth enough to better facilitate the phase unwrapping. Therefore, the residual deformation could then be estimated more accurately and reliably from the time-series TSX dataset. As the final step, the residual deformation derived from TSX, together with that from ASAR, forms the full

deformation. Through the synergic use of multi-frequency SAR images, the process of deriving ground deformation from time series InSAR analysis can be improved in terms of accuracy and robustness. In addition, the algorithm is capable of extending the applications of achieved SAR data on ground deformation monitoring, especially in the case that considering the historical deformation information. The experiments show that the proposed method can effectively detect the ground deformation with an accuracy of mm/yr by combining multi-sensor SAR data to reduce the phase unwrapping errors.

METHODOLOGY

StaMPS was designed by Hooper et al. (Hooper et al., 2007) to overcome the limitation of the absence of man-made buildings on most of the Earth's surface and prior knowledge of the temporal behavior of the ground deformation, and it has been successfully applied in many cases lacking in anthropogenic features (Costantini et al., 2016; Tiwari et al., 2016; Dwivedi et al., 2017).

The small baseline method implemented in the standard StaMPS software, referred to as StaMPS-SB for simplicity, is used in the following study as there are only a few SAR acquisitions with irregular gaps. StaMPS-SB focuses on these pixels that show a slowly decorrelating filtered phase (SDFP) over a short interval of time to mitigate atmospheric effects and improve the coherence (Hooper, 2008). According to the way that StaMPS-SB selects SDFP pixels, some candidates will be first chosen based on amplitude dispersion with a relatively low threshold. Then, the final SDFP pixels will be selected through an iterative procedure calculating the noise level of each candidate.

As shown in (Hooper et al., 2007), the wrapped interferometric phase, $\varphi_{x,i}$, of the xth in the ith flatted and topographically corrected interferogram can be expressed as the wrapped sum of five terms,

$$\varphi_{x,i} = w\left\{\phi_{D,x,i} + \phi_{A,x,i} + \phi_{S,x,i} + \phi_{\theta,x,i} + \phi_{N,x,i}\right\}, \quad (1)$$

where $\phi_{D,x,i}$ is the phase contribution due to the movement along the line-of-sight (LoS) direction, $\phi_{A,x,i}$ is the phase caused by changes in atmospheric delay between two SAR acquisitions, $\phi_{S,x,i}$ is the residual phase due to inaccuracies of satellite position, $\phi_{\theta,x,i}$ is the residual phase due to the look angle error mainly caused by the inaccuracy of DEM such as SRTM-DEM which is usually used to correct the topographic phase, $\phi_{N,x,i}$ is the phase noise term due to variability in scattering, thermal, decorrelation, etc., and $w\{\cdot\}$ is the wrapping operator.

The absolute phase difference between adjacent SDFP pixels may be larger than π due to the spatially uncorrelated component of the signal. Therefore, the spatially uncorrelated portion of $\phi_{\theta,x,i}$ should be estimated and subtracted from $\varphi_{x,i}$ before phase unwrapping. The three-dimensional phase unwrapping algorithm adopted by StaMPS-SB contains two steps. First, the differential phase between adjacent pixels is unwrapped in the temporal domain under the Nyquist assumption that the differential phase is less than π. Then, the unwrapped differential phase is used to build *a priori* probability density functions (PDFs) in each interferogram. Also, these PDFs will be converted into cost functions and fed into the optimization routines of a two-dimensional statistical-cost network-flow algorithm to obtain the final unwrapped results (Hooper, 2010).

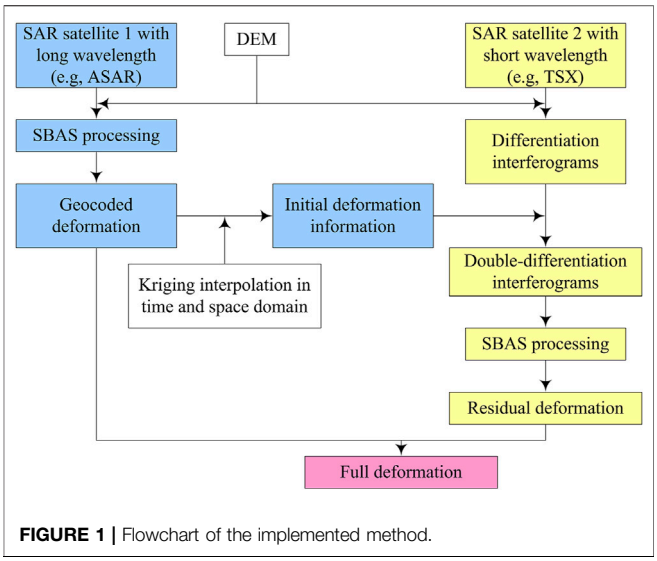

FIGURE 1 | Flowchart of the implemented method.

After unwrapping, the spatially correlated portion of $\phi_{\theta,x,i}$ can be estimated using the least squares solution. Then, the atmosphere $\phi_{A,x,i}$ and the orbit errors $\phi_{S,x,i}$ will be estimated by high-pass filtering in the temporal domain followed by low-pass filtering in the spatial domain. Finally, subtracting these nuisance terms leaves the deformation phase $\phi_{D,x,i}$and the spatially uncorrelated errors which can be regarded as random noise.

The phase-unwrapping algorithm adopted by StaMPS-SB is typically based on the Nyquist sampling assumption that the differential phase between adjacent SDFP pixels is less than π. In order to satisfy this condition, the spatially uncorrelated portion of $\phi_{\theta,x,i}$ should be estimated and subtracted from the original signal before unwrapping. However, the deformation phase $\phi_{D,x,i}$, if too large, can also lead to the differential phase being greater than π, especially when only a few SAR acquisitions are available.

Fortunately, many spaceborne SAR satellites, such as Envisat, ALOS-1/2, TSX, and Sentinel-1., have been launched, which allows us to observe the Earth using multiple SAR sensors with different wavelength, repeat time, spatial resolution, and incidence angle. With the advantage of an increasing number of SAR satellites, there may be more than one SAR stack, for example, several stacks of SAR datasets acquired from different SAR systems covering the same area. In this study, we have developed a new StaMPS-SB procedure to integrate two different SAR datasets, that is, ASAR with longer and TSX with shorter wavelength for MT-InSAR analysis. The flowchart applied in this study is shown in **Figure 1**.

In the proposed method, the deformation $\phi_{D,x,i}$ can be expressed as

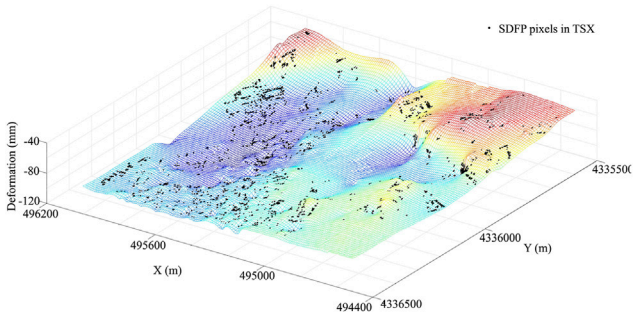

FIGURE 2 | Extracting the deformation rate of SDFP pixels in TSX by Kriging interpolation in space. The mesh grid is generated from the deformation rate derived from ASAR images. The black dots denote the SDFP pixels selected from TSX acquisitions.

$$\phi_{D,x,i} = \phi^{lp}_{D,x,i} + \phi^{res}_{D,x,i}, \tag{2}$$

where $\varphi^{lp}_{D,x,i}$ is the low-pass (that is, principal) component deformation and $\phi^{res}_{D,x,i}$ is the residual deformation.

First, $\phi^{lp}_{D,x,i}$ is estimated based on the time-series ASAR dataset, which represents an initial estimation (that is, the principle component) of the ground deformation. Then, this information will be subtracted from each differential interferogram generated from the TSX dataset to fulfill the Nyquist sampling criterion.

It should be noted that the date of ASAR and TSX acquisitions is inconsistent. Also, the location of SDFPs selected from ASAR and TSX is also different from each other. Therefore, the deformation retrieved from ASAR has been first interpolated in time to match the date of TSX data. The quadratic polynomial was used to model the evolution of deformation in time. Then, the time-interpolated deformation was interpolated in the space domain using the Kriging method (**Figure 2**).

After interpolation processing in time and space followed by conversion of LoS direction, the low-pass deformation derived from ASAR can be incorporated into the processing of the TSX dataset according to the longitude and latitude of each SDFP. The matching error based on the geographical coordinates is about a few meters, which is acceptable as the deformation is spatially correlated.

Once subtracting the low-pass deformation, further analysis will be based on the double-differentiated TSX interferograms. As the principal component of ground deformation has already been subtracted, the double-differentiated phase will be smooth enough (**Figure 3**) to facilitate phase unwrapping. Therefore, the residual deformation could then be estimated more accurately and reliably from the time-series TSX dataset using the standard StaMPS-SB procedure. As the final step, the residual deformation derived from TSX, together with that from ASAR, forms the final deformation.

STUDY AREA AND AVAILABLE DATA

The suburb of western Tianjin, shown in **Figure 4**, is chosen as the study area. Tianjin, one of the four municipalities in China, is located in the North China Plain (Liu et al., 2014). Tianjin lies in a semi-arid and semi-humid climate region and suffers from water shortage as the annual precipitation is less than 500 mm. Due to the shortage of surface water sources and small amount of precipitation, the groundwater has been extracted to meet the agricultural and industrial needs for decades, which leads to severe ground subsidence with maximum cumulative subsidence of 3.22 m in history (Yi et al., 2011). The rates of ground subsidence have visibly increased since the 1950s, reaching 80–100 mm/year from 1967 to 1985 (He et al., 2006a; He et al., 2006b). After the 1980s, some measures, such as injection and restricting exploitation of groundwater, have been taken to reduce the subsidence rate. However, the ground subsidence rate is still very high (approximately 137 mm/year), and the phenomenon of subsidence has even worsened since 2010 (Zhu et al., 2015).

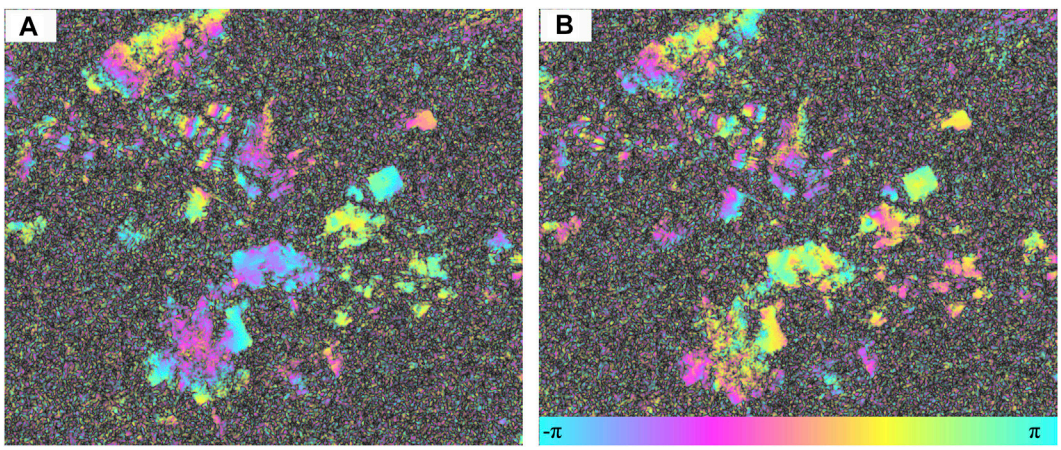

FIGURE 3 | TSX interferogram **(A)** before and **(B)** after subtracting the initial deformation derived from ASAR acquisitions. The temporal and perpendicular baselines are 429 days and 25 m, respectively.

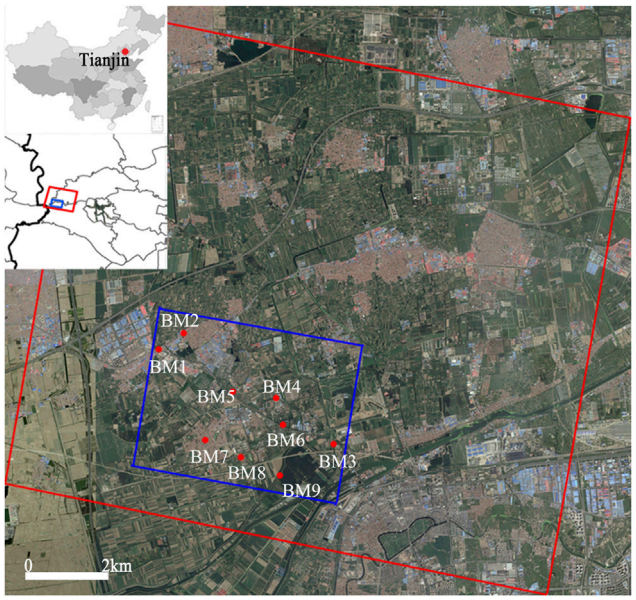

FIGURE 4 | Location of the study area. The two insets depict the geographical location of Tianjin in China and the ground coverage of ASAR (red rectangle) and TSX (blue rectangle). The 22 BMs are used to evaluate the results derived from different methods.

The performance of the presented method will be investigated using ASAR and TSX images with the ground coverage represented by red and blue rectangles, respectively, in **Figure 4**. The ASAR dataset, which consisted of 14 acquisitions spanning the intervals of time from 23 January 2009 to 10 September 2010 (see **Table 1**), was acquired in Stripmap mode with an incidence angle of 23° along descending orbit path direction. The ASAR acquisitions have a longer wavelength of about 5.6 cm and a coarser spatial resolution of approximately 5 m in the azimuth direction and 20 m in the ground range direction. The TSX dataset, which consisted of 11 acquisitions spanning the interval time from 27 March 2009 to 6 September 2010 (see **Table 1**), was acquired in Stripmap mode, with an incidence angle of 41° along descending orbit path direction. The TSX acquisitions have a shorter wavelength of about 3.1 cm and a higher spatial resolution of approximately 3.3 m in the azimuth direction and 2.7 m in the ground range direction.

There are nine leveling bench-marks (BM1-BM9) that are denoted by red dots in **Figure 4**, located within the study area. The subsidence rate, derived from the leveling data with high-level precision, can be used to evaluate the accuracy of the presented method.

EXPERIMENTAL RESULTS AND DISCUSSION

Due to the irregular gaps in SAR acquisitions and serious ground deformation, the StaMPS-SB approach is used in the following experiments. Using the multi-master SBAS approach, only these interferograms with smaller geometric and temporal baselines than the predefined threshold are used for MT-InSAR analysis, which can improve the interferometric coherence by minimizing the decorrelation effects caused by geometric and temporal baselines.

It should be noted that the ground deformation, retrieved from the InSAR technique, is along the LoS direction and composed of the horizontal and uplifted components. However, previous studies (Yi et al., 2011; Zhu et al., 2015) have suggested that the deformation is dominated by vertical components as the ground displacement is mainly caused by over-extraction of groundwater in this study area. Therefore, the ground deformation along the vertical direction is simply obtained by dividing the cosine of the incidence angle.

Results From the Standard StaMPS-SB Approach Based on 11 TSX Acquisitions

In this section, the standard StaMPS-SB approach is used to estimate the ground deformation based on a few SAR acquisitions (i.e., 11 TSX images).

TABLE 1 | Envisat ASAR and TerraSAR-X dataset.

Envisat ASAR				TerraSAR-X			
No.	**Date**	**Perpendicular baseline (m)**	**Interval (days)**	**No.**	**Date**	**Perpendicular baseline (m)**	**Interval (days)**
1	20090123	0	0	1	20090327	37.8	0
2	20090227	80.2	35	2	20090418	-30.9	22
3	20090508	-212.2	105	3	20090510	25.5	44
4	20090612	145.9	140	4	20090601	37.3	66
5	20090717	-35.5	175	5	20090623	-81.8	88
6	20090821	-110.6	210	6	20090908	37.8	165
7	20091030	-199.5	280	7	20091113	0	231
8	20091204	7.1	315	8	20091216	116.5	264
9	20100319	-26.8	420	9	20100702	-83.7	462
10	20100423	162.0	455	10	20100804	76.6	495
11	20100528	-228.0	490	11	20100906	6.9	528
12	20100702	42.7	525				
13	20100806	-366.2	560				
14	20100910	-45.3	595				

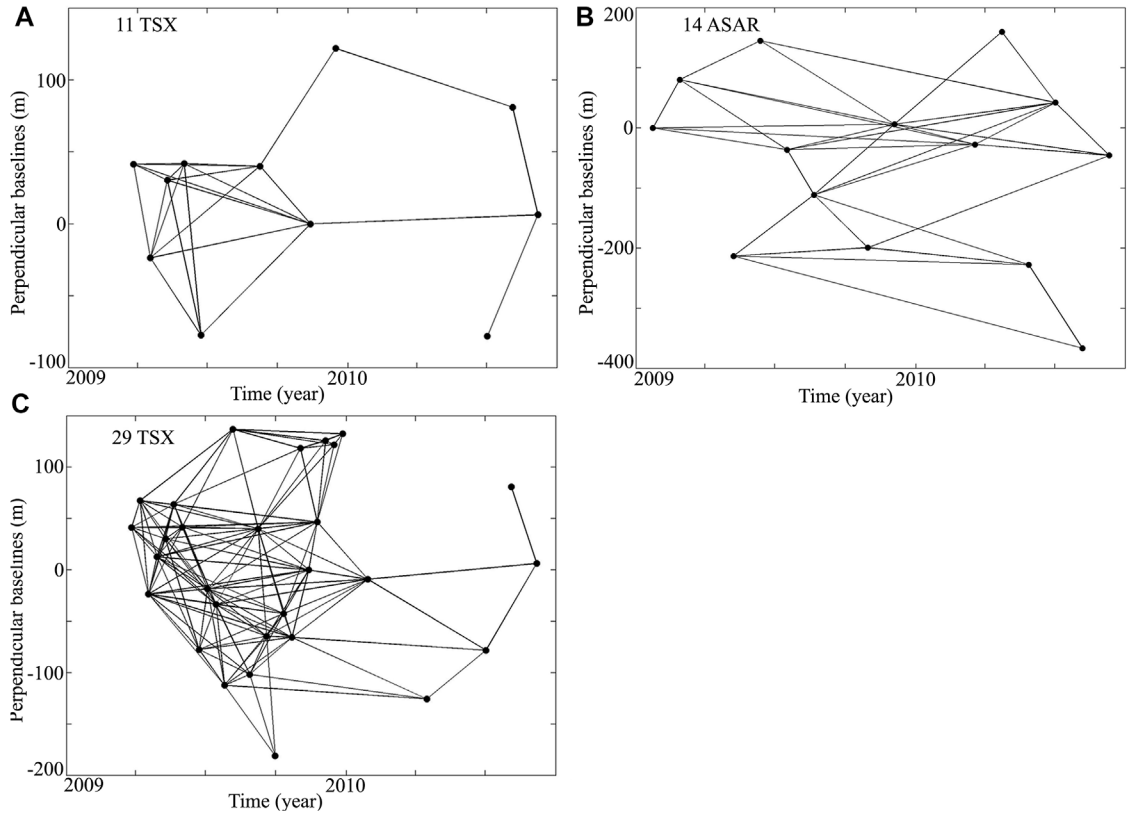

FIGURE 5 | Distribution of temporal and perpendicular baselines of interferograms generated from **(A)** 11 TSX acquisitions, **(B)** 14 ASAR acquisitions, and **(C)** 29 TSX acquisitions. The black dots denote the SAR acquisitions; black lines denote the interferograms.

A fully connected network of interferograms is the foundation for MT-InSAR analysis using the StaMPS-SB approach. However, it is difficult to automatically achieve the optimal network due to the irregular intervals of the 11 TSX acquisitions, especially with a wide gap (198 days) between 16 December 2009 and 2 July 2010. Therefore, the interferograms were initially generated with a relatively low threshold, that is, specifying 250 m as the temporal baseline, 90 days as the geometric baselines, and 0.5 as the coherence threshold. Then, on the premise of a connected network, the interferograms with low coherence are manually removed from the network of interferograms. In addition, some interferograms with high coherence were manually generated and appended to the original stacks to increase the temporal sampling. A total of 24 interferograms with high coherence are finally obtained (seen in **Figure 5A**) and used for MT-InSAR analysis.

Then, the ground deformation is estimated using the standard StaMPS-SB approach based on the 24 interferograms. Finally, 39892 SDFP pixels have been detected. The mean rate of deformation is converted to the vertical direction and compared with leveling measurements. The result is shown in **Figure 6A**. The negative rate indicates that the study area suffered ground subsidence during this period. In addition, the spatial pattern of subsidence is almost similar to that detected by Zhu et al. (2015) except for the one in zone Z1. A maximum subsidence rate of 90 mm/year is detected in zone Z1 in this study based on 24 interferograms generated from 11 TSX acquisitions. However, a maximum subsidence rate of 110 mm/year is suggested by Zhu et al. (2015) based on 48 TSX acquisitions.

Results From the Proposed Method Based on 11 TSX and 14 ASAR Acquisitions

In this section, the ground deformation is estimated using the proposed method by integrating 11 TSX and 14 ASAR acquisitions.

First, the ground subsidence is estimated using the standard StaMPS-SB approach based on 34 interferograms (as seen in **Figure 5B**) generated from 14 ASAR acquisitions. Also, the result is evaluated and validated by comparing it with the leveling measurements. The result is shown in **Figure 7B**. The comparison suggests an RMSE of 3.7 mm/yr and a correlation coefficient of 0.969, which demonstrates that the results derived from the ASAR dataset can be used as prior information. Then, the subsidence is subtracted from each interferogram generated from TSX acquisitions, and the residual deformation is extracted based on these double-differentiated TSX interferograms. Finally, 40147 SDFP pixels have been detected.

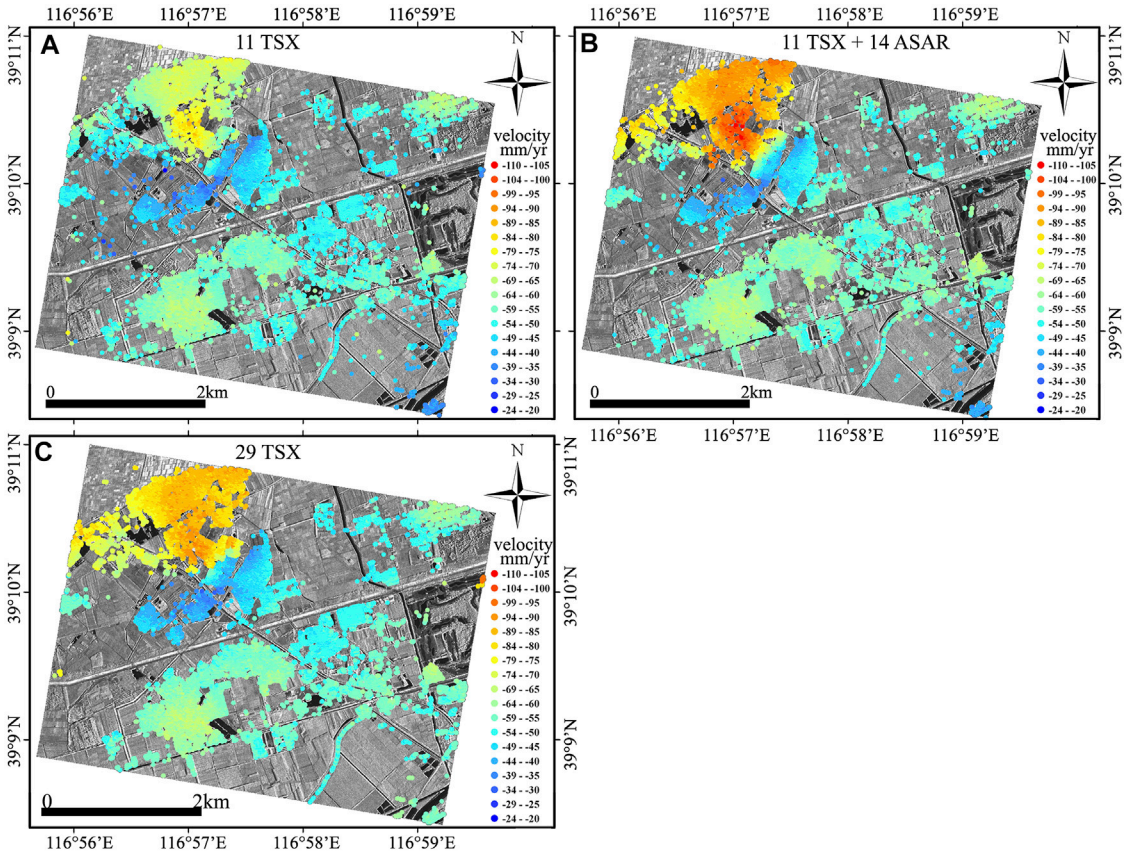

FIGURE 6 | Deformation rate derived from **(A)** 11 TSX acquisitions using the standard StaMPS approach, **(B)** 11 TSX acquisitions and 14 ASAR acquisitions using the proposed method, and **(C)** 29 TSX acquisitions using the standard StaMPS approach.

Figure 6B depicts the final results derived from the proposed method. As shown in **Figure 6**, the spatial distribution of the ground subsidence derived from the proposed method agrees with that of 11 TSX images except the one in zone Z1. A subsidence rate of 80–110 mm/yr is detected by the proposed method in zone Z1, and the results agree with those of Zhu et al. (2015) and Luo et al. (2014).

Results From the Standard StaMPS-SB Approach Based on 29 TSX Acquisitions

In order to further evaluate the performance of the presented method, we collect 29 TSX acquisitions used by Zhu et al. (2015). These acquisitions are acquired during the same period as the 11 TSX (i.e., from 27 March 2009 to 6 September 2010). 145 interferograms (as seen in **Figure 5C**) with a maximum temporal interval of 264 days and geometrical baselines of 117 m are generated based on the 29 acquisitions. Also, the ground subsidence is estimated using the standard StaMPS-SB approach and compared with that from the presented method. The spatial distribution of the subsidence rate is shown in **Figure 6C**.

Clearly, in **Figure 6**, the results obtained from the proposed method based on the integration of 11 TSX and 14 ASAR acquisitions (**Figure 6B**) agree with those of the standard StaMPS-SB approach based on 29 TSX acquisitions (**Figure 6C**).

DISCUSSION

This section is devoted to analyzing the performance of the proposed method by comparing the results with the leveling measurements.

Comparison Between the Leveling Measurements and the Results From 11 TSX Acquisitions

In order to quantitatively evaluate the performance of the standard StaMPS-SB approach with a few TSX acquisitions, the ground subsidence derived from 11 TSX acquisitions is compared with leveling measurements. Also, the results are shown in **Figure 7A**. It should be noted that the InSAR-derived subsidence rate is estimated by calculating the mean of the rate of all the SDFP pixels located within a 50 m radius of each leveling bench-marks (BM1–BM9). One standard deviation calculated from these SDFP pixels is also represented by the error bar in **Figure 7A**.

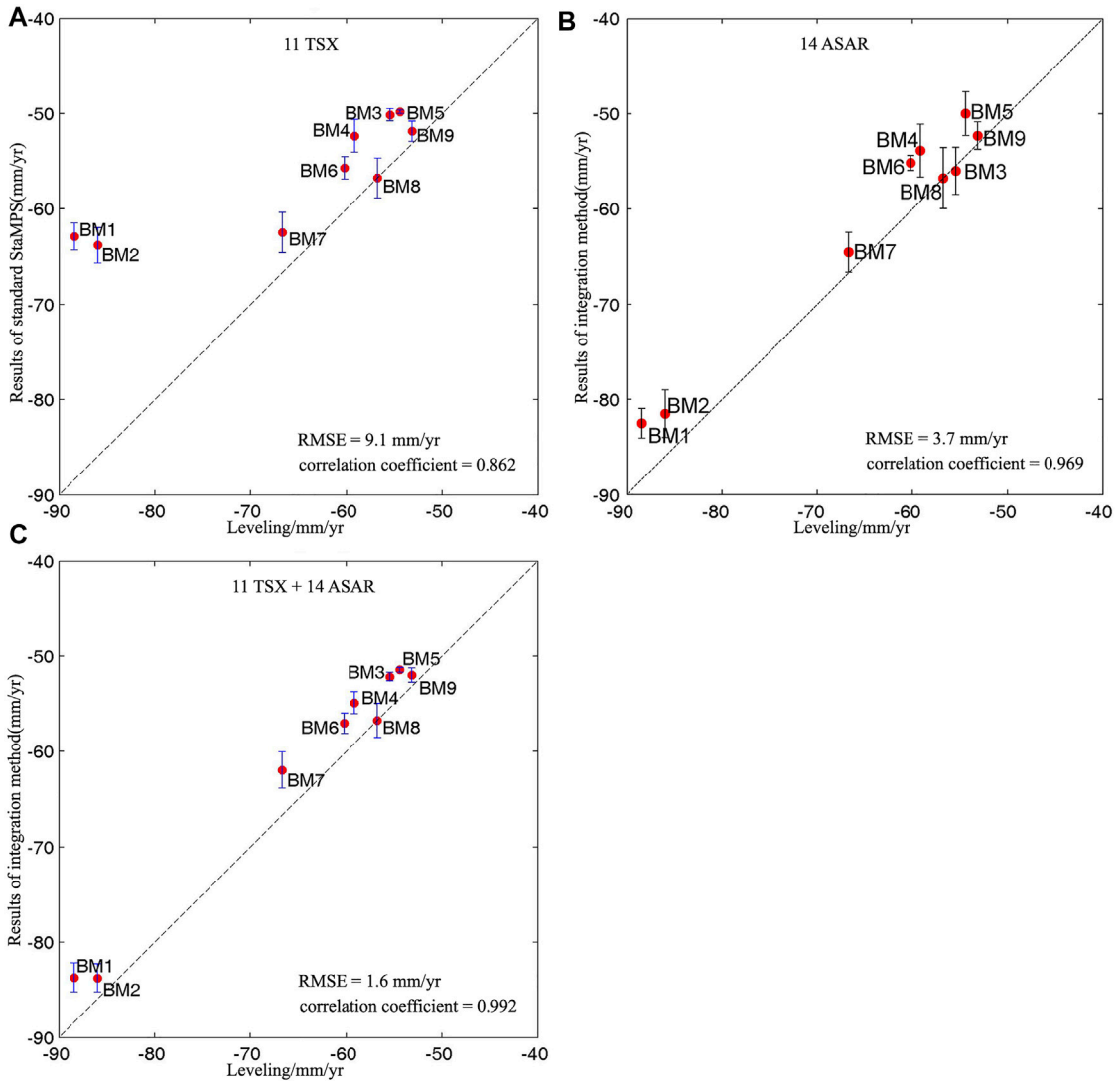

FIGURE 7 | Comparison between deformation rates derived from leveling measurement and **(A)** 11 TSX acquisitions using standard StaMPS-SB, **(B)** 14 ASAR acquisitions using standard StaMPS-SB and **(C)** integration of 11 TSX acquisitions and 14 ASAR acquisitions using the proposed method.

It can be seen from **Figure 7A** that the differences between these two distinct measurements are slight (about 5 mm/year) in BM3–BM9, where the rate of ground subsidence is less than 70 mm/year. The slight differences may result from some uncertainties, such as temporal uncertainty due to the different temporal resolution of distinct data, positional uncertainty due to inaccurate coordinate of leveling bench-marks and SDFP pixels, and the uncertainty caused by the conversion of ground subsidence from the LoS direction to the vertical direction.

However, there are significant differences between the two distinct measurements in BM1 (with a difference of 25.5 mm/year) and BM2 (with a difference of 22.1 mm/year), both of which are located in zone Z1. The subsidence is seriously underestimated using the standard StaMPS-SB approach based on the 11 TSX acquisitions. The statistical calculation between the InSAR-derived results and the leveling measurements suggests that the RMSE is up to 9.1 mm/yr, while the correlation coefficient is only 0.862.

Previous studies (Luo et al., 2014; Zhu et al., 2015) show that the ground subsidence is serious in zone Z1, where the maximum rate of subsidence is up to 110 mm/year. In order to detect the serious subsidence, more SAR acquisitions are needed for the standard StaMPS-SB approach to satisfy the assumption that the deformation is strongly correlated in space within a proper distance and can be accurately estimated using the band-pass filtering method. In addition, more SAR acquisitions are also needed to smooth the phase gradient as almost all phase unwrapping methods are based on the assumption that the interferometric phase field varies slowly. However, as only 11 TSX acquisitions are available, the ground subsidence is seriously underestimated using the standard StaMPS-SB approach.

Comparison Between the Leveling Measurements and the Results From 11 TSX and 14 ASAR Acquisitions

For further validation, the subsidence rate obtained from the proposed method is also compared with the leveling measurements, and the linear regression between these two measurements is calculated and shown in **Figure 7B**. Compared with that of the standard StaMPS-SB, the statistical calculation suggests that the RMSE and maximum difference reduce from 9.1 mm/yr to 1.6 mm/yr and 25.5 mm/yr to 4.7 mm/yr, respectively. Moreover, the correlation coefficient increases from 0.862 to 0.992 at the same time. The comparison demonstrates a significant improvement in the precision of deformation monitoring, which suggests that high-accuracy subsidence can still be achieved from a few TSX images by integrating with ASAR images.

In addition, it can also be seen from **Figure 6B** that although the accuracy of deformation has been improved, the subsidence rate on all nine benchmarks derived from the proposed method is less than the leveling measurements. These differences may be caused by the error of leveling measurement on BM8 which has been selected as the reference point to calibrate the InSAR results and the inaccurate location of BM8 as well.

In addition, more SDFPs, that is, 40147 SDFPs have been finally detected. According to the method that StaMPS-SB selects SDFP, some candidates will be first selected based on amplitude dispersion. Then, the candidates will be filtered in a small window, such as 50 m × 50 m, to determine the spatially correlated phase. If the difference of deformation between one pixel and others in the small patch is much greater, this pixel, even if it has a very stable phase response in all interferograms, will also be discarded.

Comparison Between the Leveling Measurements and the Results From 29 TSX Acquisitions

The comparison with leveling measurements suggests a correlation coefficient of 0.979 and an RMSE of 3.0 mm/year. Both the statistical analyses demonstrate that the results obtained from 29 TSX images can be used to evaluate the performance of the proposed method.

There are 33087 common SDFP pixels between the ones identified based on 11 TSX acquisitions and those based on 29 TSX acquisitions. Then, we compare the subsidence rate correspondence to these common SDFP pixels. The results are shown in **Figure 8A**. It can be seen from **Figure 8A** that there is a significant bias (about 20 mm/yr) between these two measurements. The difference of rate in about 22% of common SDFP pixels is more than 10 mm/yr, which results in a low correlation coefficient of 0.86 and a high RMSE of 7.4 mm/yr. The subsidence derived from 11 TSX acquisitions is underestimated when the deformation velocity reaches over 70 mm/yr in this study. This can be explained by the inference mentioned before, that is, the large deformation cannot be accurately estimated if there are no adequate acquisitions.

There are 33306 common SDFP pixels between the ones identified using the proposed method based on the integration of 11 TSX and 14 ASAR acquisitions and those using the standard StaMPS-SB approach based on 29 TSX acquisitions. The subsidence rates in correspondence to these common SDFP pixels are shown in **Figure 8B**. Compared with the results shown in **Figure 8A**, the difference between the results derived from the integration of 11 TSX and 14 ASAR acquisitions and that from the 29 TSX acquisitions is significantly reduced. The proportion of the difference with more than 10 mm/yr decreases from 22% to 4.5%. In a few SDFP pixels with a proportion of less than 0.4%, the difference in subsidence rate is more than 20 mm/yr, which may be caused by the errors in initial subsidence information obtained from ASAR data. However, the statistical calculation shows a significant improvement in the correlation coefficient which increases from 0.86 to 0.969, and in the RMSE, which decreases from 7.4 mm/yr to 3.9 mm/yr.

Comparison of Time Series Displacement

Figure 9 shows the evolution of the displacements of SDFPs located within a radius of 50 m of the eight benchmarks. It is difficult to accurately retrieve absolute time-series displacements because only two periods of leveling measurements are available. Therefore, the relative time series displacements at BM1 to BM9 are calculated by reference to these SDFPs near the BM8. It can be seen from **Figure 9** that the displacement will be underestimated if only 11 TSX data are available, especially when the actual displacement is relatively large. However, the presented method can effectively detect the time-series displacement by combining multi-sensor SAR data. In addition, the time series displacement derived from the present method is smoother than the other, which is due to the low-pass filtering in the time domain to extract the residual displacement.

Overall, the validation of the accuracies using the leveling measurements and the results obtained by different methods with different numbers of SAR acquisitions verify the ability of the proposed method to detect the deformation with high accuracy through a few high spatial resolutions of TSX integrated with the coarser resolution ASAR acquisitions.

CONCLUSION

In this study, a methodology integrating different SAR acquisitions derived from different SAR satellites with different wavelengths has been presented for MT-InSAR analysis. By integrating multiple SAR sensors, the presented method can overcome the limitation of imaging capability of a single SAR satellite.

We estimate the ground displacement using 11 TSX acquisitions and 14 ASAR acquisitions. In addition, we also estimate the ground displacement by integrating 11 TSX and 14 ASAR acquisitions based on the presented method. Both the InSAR-derived displacements are compared with the leveling data. The statistical calculation shows that the correlation is 0.862, 0.969, and 0.992 and the RMSE is 9.1 mm/yr, 3.7 mm/yr, and 1.6 mm/yr.

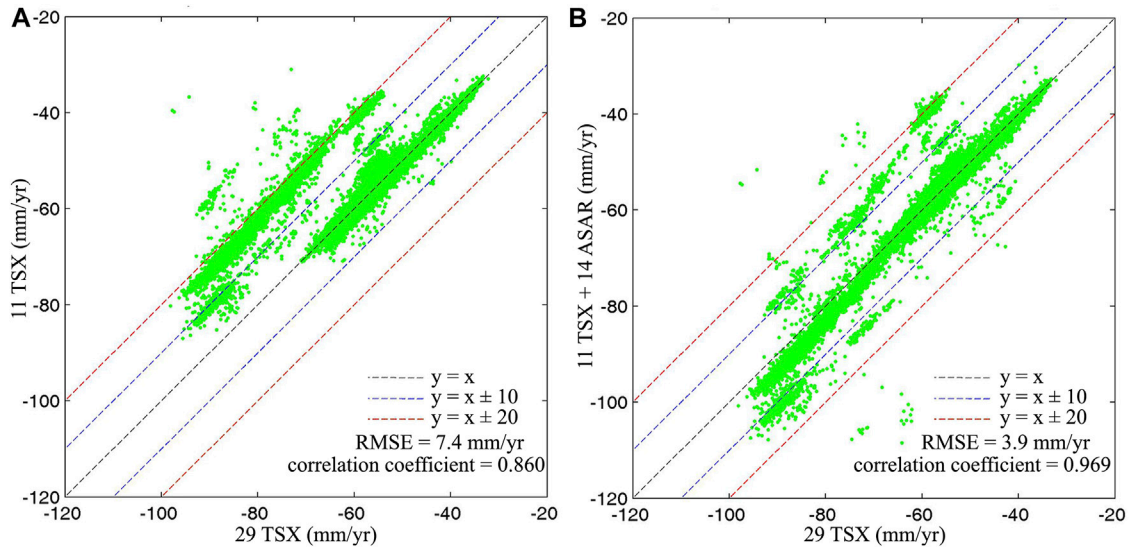

FIGURE 8 | Comparison between deformation rates derived from 29 TSX acquisitions and **(A)** 11 TSX acquisitions using standard StaMPS-SB and **(B)** integration of 11 TSX acquisitions and 14 ASAR acquisitions using the proposed method.

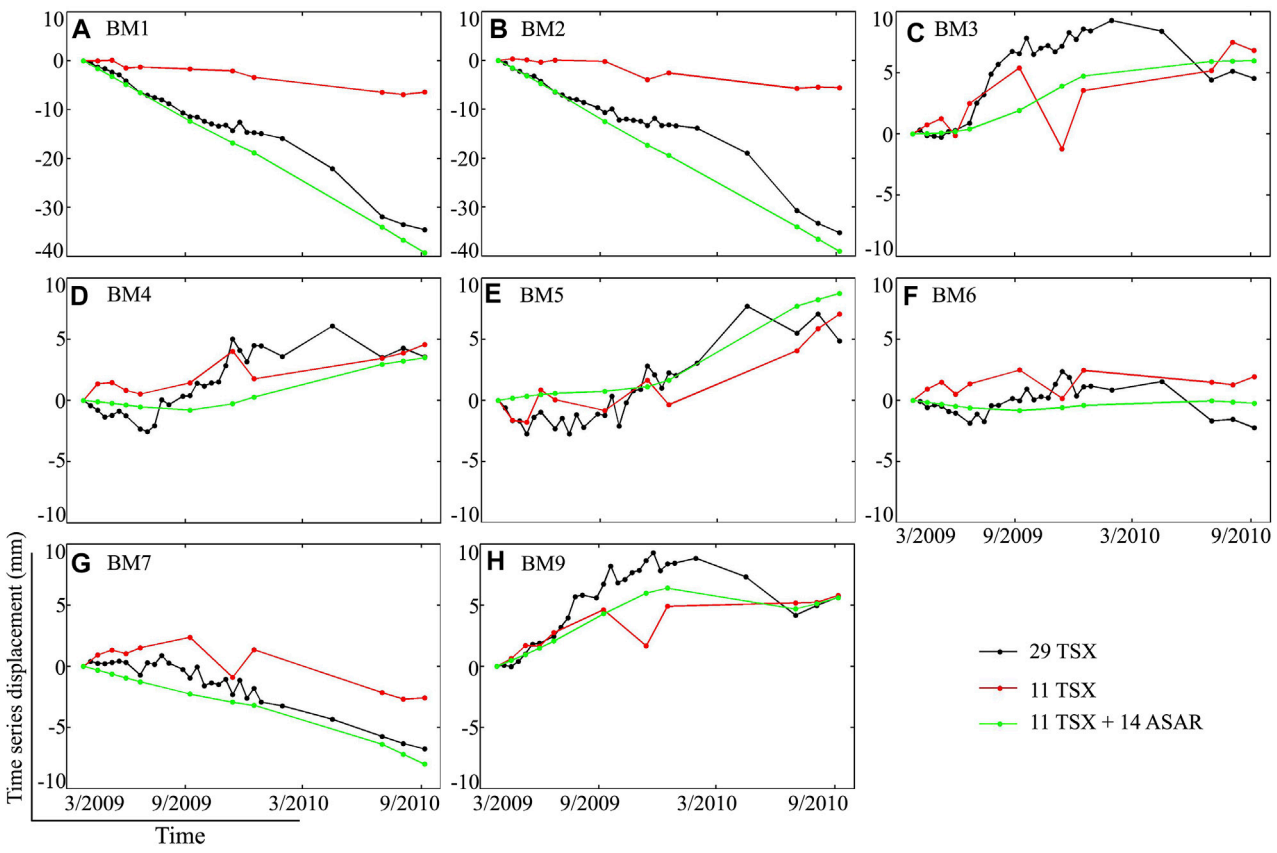

FIGURE 9 | Time series of displacement at **(A–G)** BM1 ~ BM7 and **(H)** BM9 derived from three sets of SAR datasets, that is, the 29 TSX acquisitions only, the 11 TSX acquisitions only, and the combination of 11 TSX and 14 ASAR acquisitions. It should be noted that the time series of displacement is relative to BM8.

In addition, we estimate the ground displacement using 29 TSX acquisitions over the same period and compare the results with that estimated from the integration of 11 TSX and 14 ASAR acquisitions. The correlation coefficient is 0.969 between the two distinct measurements. Furthermore, the RMSE is 3.9 mm/yr, which suggests that the accuracy of the InSAR-derived displacement using the integration of two small SAR datasets coincided with that of one large dataset.

The results from these experiments suggest that the presented method is capable of estimating ground displacement by integrating the datasets from multiple SAR sensors. Still, the presented method can extend the applications of archived SAR data on ground deformation monitoring and will potentially play an important role in the case of insufficient scenes of the image from a single SAR sensor.

DATA AVAILABILITY STATEMENT

The raw data supporting the conclusions of this article will be made available by the authors, without undue reservation.

AUTHOR CONTRIBUTIONS

CZ and JZ initiated the study; CZ and SL analyzed the data; CZ provided the software and wrote the manuscript. SL, WW, and LZ provided advice and reviewed the manuscript. All authors contributed to the article and approved the submitted version.

FUNDING

This research has been supported by the National Natural Science Foundation of China (41901373 and 41877283), the Natural Science Foundation of Hunan Province (grant no. 2019JJ50190), and the Science and Technology Innovation Program of Hunan Province (2021RC4037).

ACKNOWLEDGMENTS

We thank the StaMPS team for providing the software and the ESA for providing the SAR data. The authors would also like to thank the reviewers for their careful work and insightful suggestions.

REFERENCES

Bamler, R., and Hartl, P. (1998). Synthetic Aperture Radar Interferometry. *Inverse Probl.* 14 (4), R1–R54. doi:10.1088/0266-5611/14/4/001

Berardino, P., Fornaro, G., Lanari, R., and Sansosti, E. (2002). A New Algorithm for Surface Deformation Monitoring Based on Small Baseline Differential SAR Interferograms. *IEEE Trans. Geosci. Remote Sens.* 40 (11), 2375–2383. doi:10.1109/tgrs.2002.803792

Costantini, F., Mouratidis, A., Schiavon, G., and Sarti, F. (2016). Advanced InSAR Techniques for Deformation Studies and for Simulating the PS-Assisted Calibration Procedure of Sentinel-1 Data: Case Study from Thessaloniki (Greece), Based on the ENVISAT/ASAR Archive. *Int. J. Remote Sens.* 37 (4), 729–744. doi:10.1080/01431161.2015.1134846

Dehghani, M., Valadan Zoej, M. J., Hooper, A., Hanssen, R. F., Entezam, I., and Saatchi, S. (2013). Hybrid Conventional and Persistent Scatterer SAR Interferometry for Land Subsidence Monitoring in the Tehran Basin, Iran. *ISPRS J. Photogramm. Remote Sens.* 79 (4), 157–170. doi:10.1016/j.isprsjprs.2013.02.012

Dwivedi, R., Narayan, A. B., Tiwari, A., Singh, A. K., and Dikshit, O. (2017). Optimal Estimation of Interferometric Phase for Measuring Surface Deformation. *Int. J. Remote Sens.* 38 (5-6), 1339–1349. doi:10.1080/01431161.2017.1280627

Ferretti, A., Prati, C., and Rocca, F. (2000). Nonlinear Subsidence Rate Estimation Using Permanent Scatterers in Differential SAR Interferometry. *IEEE Trans. Geosci. Remote Sens.* 38 (5), 2202–2212. doi:10.1109/36.868878

Ferretti, A., Prati, C., and Rocca, F. (2001). Permanent Scatterers in SAR Interferometry. *IEEE Trans. Geosci. Remote Sens.* 39 (1), 8–20. doi:10.1109/36.898661

Gabriel, A. K., Goldstein, R. M., and Zebker, H. A. (1989). Mapping Small Elevation Changes over Large Areas: Differential Radar Interferometry. *J. Geophys. Res.* 94 (B7), 9183–9191. doi:10.1029/jb094ib07p09183

Hanssen, R. F., Weckwerth, T. M., Zebker, H. A., and Klees, R. (1999). High-Resolution Water Vapor Mapping from Interferometric Radar Measurements. *Science* 283 (5406), 1297–1299. doi:10.1126/science.283.5406.1297

He, Q. C., Liu, W. B., and Li, Z. M. (2006a). Land Subsidence Survey and Monitoring in the NorthChina Plain. *Geol. J. China Univ.* 12, 195–209. (In Chinese.). doi:10.3969/j.issn.1006-7493.2006.02.006

He, Q. C., Ye, X. B., Li, Z. M., and Liu, W. B. (2006b). The Status and Prevention Strategy of LandSubsidence in China. *Geol. J. China Univ.* 12, 161–168. (In Chinese.). doi:10.16108/j.issn.1006-7493.2006.02.002

Heuff, F. M. G., and Hanssen, R. F. (2020). "InSAR Phase Reduction Using the Remove-Compute-Restore Method," in IGARSS 2020 - 2020 IEEE International Geoscience and Remote Sensing Symposium, Waikoloa, USA, September 26–October 2, 2020.

Hooper, A. (2008). A Multi-Temporal InSAR Method Incorporating Both Persistent Scatterer and Small Baseline Approaches. *Geophys. Res. Lett.* 35 (16), 96–106. doi:10.1029/2008gl034654

Hooper, A. (2010). "A Statistical-Cost Approach to Unwrapping the Phase of InSAR Time Series," in Processing of Fringe 2009 Workshop, Frascati, Italy, November 30–December 4, 2009, 667, 1–5.

Hooper, A., Segall, P., and Zebker, H. (2007). Persistent Scatterer Interferometric Synthetic Aperture Radar for Crustal Deformation Analysis, with Application to Volcán Alcedo, Galápagos. *J. Geophys. Res. Solid Earth* 112, B04707. doi:10.1029/2006jb004763

Hooper, A., Zebker, H., Segall, O., and Kampes, B. (2004). A New Method for Measuring Deformation on Volcanoes and Other Natural Terrains Using InSAR Persistent Scatterers. *Geophys. Res. Lett.* 31, 611–615. doi:10.1029/2004gl021737

Hu, B., Zhou, J., Wang, J., Chen, Z., Wang, D., and Xu, S. (2009). Risk Assessment of Land Subsidence at Tianjin Coastal Area in China. *Environ. Earth Sci.* 59 (2), 269–276. doi:10.1007/s12665-009-0024-6

Kampes, B. M., and Hanssen, R. F. (2004). Ambiguity Resolution for Permanent Scatterer Interferometry. *IEEE Trans. Geosci. Remote Sens.* 42 (11), 2446–2453. doi:10.1109/tgrs.2004.835222

Lanari, R., Mora, O., Manunta, M., Mallorqui, J. J., Berardino, P., and Sansosti, E. (2004). A Small-Baseline Approach for Investigating Deformations on Full-Resolution Differential SAR Interferograms. *IEEE Trans. Geosci. Remote Sens.* 42 (7), 1377–1386. doi:10.1109/tgrs.2004.828196

Li, Z. W., Ding, X. L., and Liu, G. X. (2004). Modeling Atmospheric Effects on InSAR with Meteorological and Continuous GPS Observations: Algorithms and Some Test Results. *J. Atmos. Sol.-Terr. Phys.* 66 (11), 907–917. doi:10.1016/j.jastp.2004.02.006

Liu, G., Jia, H., Nie, Y., Li, T., Zhang, R., Yu, B., et al. (2014). Detecting Subsidence in Coastal Areas by Ultrashort-Baseline TCPInSAR on the Time Series of High-Resolution TerraSAR-X Images. *IEEE Trans. Geosci. Remote Sens.* 52 (4), 1911–1923. doi:10.1109/tgrs.2013.2256428

Luo, Q., Perissin, D., Lin, H., Zhang, Y., and Wang, W. (2014). Subsidence Monitoring of Tianjin Suburbs by TerraSAR-X Persistent Scatterers Interferometry. *IEEE J. Sel. Top. Appl. Earth Obs. Remote Sens.* 7 (5), 1642–1650. doi:10.1109/jstars.2013.2271501

Marghany, M. (2021). *Advanced Algorithms for Mineral and Hydrocarbon Exploration Using Synthetic Aperture Radar*. San Diego: Elsevier.

Marghany, M. (2013). DInSAR Technique for Three-Dimensional Coastal Spit Simulation from Radarsat-1 Fine Mode Data. *Acta Geophys.* 61 (2), 478–493. doi:10.2478/s11600-012-0061-5

Marghany, M. (2014). Hybrid Genetic Algorithm of Interferometric Synthetic Aperture Radar for Three-Dimensional Coastal Deformation. *SoMeT* 29, 116–131. doi:10.3233/978-1-61499-434-3-116

Marghany, M. (2022). *Remote Sensing and Image Processing in Mineralogy*. Boca Raton, USA: CRC Press.

Massonnet, D., and Feigl, K. L. (1998). Radar Interferometry and its Application to Changes in the Earth's Surface. *Rev. Geophys.* 36 (4), 441–500. doi:10.1029/97rg03139

Massonnet, D., Rossi, M., Carmona, C., Adragna, F., Peltzer, G., Feigl, K., et al. (1993). The Displacement Field of the Landers Earthquake Mapped by Radar Interferometry. *Nature* 364 (6433), 138–142. doi:10.1038/364138a0

Pawluszek-Filipiak, K., and Borkowski, A. (2020). Monitoring Mining-Induced Subsidence by Integrating Differential Radar Interferometry and Persistent Scatterer Techniques. *Eur. J. Remote Sens.* 54 (16), 1–13. doi:10.1080/22797254.2020.1759455

Sadeghi, Z., Valadan Zoej, M. J., and Dehghani, M. (2013). An Improved Persistent Scatterer Interferometry for Subsidence Monitoring in the Tehran Basin. *IEEE J. Sel. Top. Appl. Earth Obs. Remote Sens.* 6 (3), 1571–1577. doi:10.1109/jstars.2013.2259221

Sousa, J. J., Hooper, A. J., Hanssen, R. F., Bastos, L. C., and Ruiz, A. M. (2011). Persistent Scatterer InSAR: A Comparison of Methodologies Based on a Model of Temporal Deformation vs. Spatial Correlation Selection Criteria. *Remote Sens. Environ.* 115 (10), 2652–2663. doi:10.1016/j.rse.2011.05.021

Tiwari, A., Dwivedi, R., Dikshit, O., and Singh, A. K. (2016). A Study on Measuring Surface Deformation of the L'aquila Region Using the Stamps Technique. *Int. J. Remote Sens.* 37 (3-4), 819–830. doi:10.1080/01431161.2015.1136449

Wegmüller, U., Walter, D., Spreckels, V., and Werner, C. (2010). Nonuniform Ground Motion Monitoring with TerraSAR-X Persistent Scatterer Interferometry. *IEEE Trans. Geoscience Remote Sens.* 48 (2), 895–904. doi:10.1109/TGRS.2009.2030792

Yi, L., Zhang, F., Xu, H., Chen, S. J., Wang, W., and Yu, Q. (2011). Land Subsidence in Tianjin, China. *Environ. Earth Sci.* 62 (6), 1151–1161. doi:10.1007/s12665-010-0604-5

Zebker, H. A., Rosen, P. A., and Hensley, S. (1997). Atmospheric Effects in Interferometric Synthetic Aperture Radar Surface Deformation and Topographic Maps. *J. Geophys. Res.* 102 (B4), 7547–7563. doi:10.1029/96jb03804

Zebker, H. A., and Villasenor, J. (1992). Decorrelation in Interferometric Radar Echoes. *IEEE Trans. Geosci. Remote Sens.* 30 (5), 950–959. doi:10.1109/36.175330

Zhu, C., Zhang, Y., Zhang, J., Zhang, L., Long, S., and Wu, H. (2015). Recent Subsidence in Tianjin, China: Observations from Multi-Looking TerraSAR-X InSAR from 2009 to 2013. *Int. J. Remote Sens.* 36 (23), 5869–5886. doi:10.1080/01431161.2015.1109729

Conflict of Interest: The authors declare that the research was conducted in the absence of any commercial or financial relationships that could be construed as a potential conflict of interest.

Publisher's Note: All claims expressed in this article are solely those of the authors and do not necessarily represent those of their affiliated organizations, or those of the publisher, the editors, and the reviewers. Any product that may be evaluated in this article, or claim that may be made by its manufacturer, is not guaranteed or endorsed by the publisher.

frontiers | Frontiers in Earth Science

ORIGINAL RESEARCH
published: 14 July 2022
doi: 10.3389/feart.2022.948661

Source Model for the 2022 Qinghai Menyuan Ms 6.9 Earthquake Based on D-InSAR

Jiangtao Liao[1], Chuntao Liang[1,2], Chaoliang Wang[1], Feihuang Cao[1], Chengming Ye[1] and Yinghui Yang[2]*

[1]Key Laboratory of Earth Exploration and Information Techniques (Chengdu University of Technology), Ministry of Education, Chengdu, China, [2]State Key Laboratory of Geohazard Prevention and Geoenvironment Protection (Chengdu University of Technology), Chengdu, China

On 8 January 2022, an Ms 6.9 earthquake occurred in Menyuan County, Qinghai Province, China. This earthquake ruptured a patch of the Qilian-Haiyuan fault in the northeast margin of the Qinghai-Tibet Plateau. In order to understand the seismogenic structure of this earthquake and analyze the fault activity, we use differential synthetic aperture radar interferometry (D-InSAR) technology to obtain a complete co-seismic displacement field on the surface, and use pixel tracking algorithm to extract the trace of the ruptured fault. The slip distribution of the seismogenic fault was inverted using the steepest descent method, and the Coulomb stress change caused by the earthquake was also calculated. Surface deformation results show that the Menyuan earthquake produced obvious surface displacements in an area of 50 × 40 km^2. The displacements are mainly distributed in the western segment of the Lenglongling fault and the eastern segment of the Tolaishan fault. The maximum displacements in the ascending and descending orbits in the LOS direction are 59.7 and 94.7 cm, respectively. The co-seismic slip results show that the strike, dip and average slip angles of the seismogenic fault are 108°, 79° dipping to SW, and 4°, respectively. On the whole, the fault is mainly of left-lateral, with a small amount of thrust component and only one co-seismic rupture center in our inversion result. The rupture center is located at a depth of ~5 km below the surface, and the maximum slip is 3.1 m. The total seismic moment released by this earthquake is 1.28 × 10^{19} N·m, and the corresponding moment magnitude is 6.67. Finally, the static Coulomb stress change results show that parts of the Lenglongling fault, the Tolaishan fault, the Sunan-Qilian fault and the Minyue-Damaging fault are loaded, emphasizing the importance for earthquake risk assessment of these fault.

Keywords: Menyuan earthquake, D-InSAR, deformation filed, slip distribution, coulomb stress

OPEN ACCESS

Edited by:
Chen Yu,
Newcastle University, United Kingdom

Reviewed by:
Chuanjin Liu,
China Earthquake Administration, China
Yongsheng Li,
Ministry of Emergency Management, China
Alex Ng,
Guangdong University of Technology, China
Ziyadin Cakir,
Istanbul Technical University, Turkey

****Correspondence:***
Chuntao Liang
liangct@cdut.edu.cn

Specialty section:
This article was submitted to Environmental Informatics and Remote Sensing, a section of the journal Frontiers in Earth Science

Received: *20 May 2022*
Accepted: *23 June 2022*
Published: *14 July 2022*

Citation:
Liao J, Liang C, Wang C, Cao F, Ye C and Yang Y (2022) Source Model for the 2022 Qinghai Menyuan Ms 6.9 Earthquake Based on D-InSAR. Front. Earth Sci. 10:948661. doi: 10.3389/feart.2022.948661

INTRODUCTION

At 01:45 on 8 January 2022, a magnitude 6.9 earthquake occurred in Menyuan County, Haibei Prefecture, Qinghai Province (37.77 N, 101.26 E) with a focal depth of 10 km. The epicenter is 54 km away from Menyuan County, with an average altitude of about 3,674 m within 5 km (http://www.cenc.ac.cn/). The area is sparsely populated. Nine people were injured in the earthquake. Many buildings, including the Lanxin Railway, were severely damaged with a maximum intensity of IX

(China Earthquake Administration; Lu et al., 2022). As of April 1, two aftershocks of magnitude 5 or above were recorded, which occurred 26 min and 4 days after the earthquake, respectively, and the Ms 5.2 earthquake was the largest aftershock on January 12.

This earthquake occurred on the Qilian-Haiyuan fault zone on the northeastern margin of the Qinghai-Tibet Plateau (**Figure 1**). Since the Cenozoic, the northeastern margin of the Qinghai-Tibet Plateau has expanded into the mainland under the double effects of the continuous northeast compression of the Indian plate and the resistance of the adjacent strong Alashan block (Zhang et al., 2003; Shi et al., 2018). The GPS velocity field shows that the crustal displacement of the northeastern margin of the Qinghai-Tibet Plateau is NE-EW, and the continuous northward expansion is the major tectonic cause for the frequent occurrence of strong earthquakes in this area (Wang and Shen, 2020). Qilian-Haiyuan fault is a large active fault in the study area, which is dominated by strike-slip. It starts from the Muli-Jiangcang fault in the west, and stretches eastward as the Tuolaishan fault, the Lenglongling fault, the Jinan fault, the Qianghe fault, the Maomaoshan fault, the Laohushan fault, the Haiyuan fault, the Liupanshan fault. Since 1900, two M ≥ 8 earthquakes have occurred on this fault—Haiyuan M $8^{1/2}$ earthquake in 1920 and the Gulang M 8 earthquake in 1927 (Zhu et al., 2022). The Menyuan Ms 6.9 earthquake occurred in a region with a risk code of A3 in the middle part of Qilian Mountains (Xu et al., 2017). It is located at the intersection of the Lenglongling fault and the Tolaishan fault (Fan et al., 2022; Xu et al., 2022; Yang et al., 2022). The Lenglongling fault is connected to the Jinqianghe fault in the east and the Tolaishan fault in the west. It is a Holocene sinistral strike-slip and thrust fault with a strike of NWW and a total length of about 150 km (Xu et al., 2016). On 26 August1986 and 21 January2016, two historical earthquakes of M 6.4 occurred on a blind thrust fault developed on the northeast of Lenglongling fault, at 28 and 33 km from this epicenter, respectively (Liu et al., 2019; He et al., 2020).

After the Menyuan Ms 6.9 earthquake, some scientific research teams responded quickly, and made significant research achievements in the field geological surveys, precise location of aftershocks, focal mechanism solutions, fault slip distribution, regional Coulomb stress changes, regional deep structures and so on (Feng et al., 2022; Liang et al., 2022; Pan et al., 2022; Peng et al., 2022; Wang et al., 2022; Yang et al., 2022; Zhu et al., 2022). Field investigation reveals that the surface rupture mainly includes linear shear cracks, oblique tension cracks, tension shear cracks, extrusion bulge and other types. It is the rupture of the left-order part of the left-lateral strike-slip fault under the tensile stress regime, and it is considered that the fault is ruptured bilaterally initiating from the compressional bend (Li et al., 2022a; Pan et al., 2022). The aftershock location results show a distinct spatiotemporal migration exist from the west to the east (Fan et al., 2022; Xu et al., 2022; Yang et al., 2022). Focal mechanism results show that the earthquake is a strike-slip type. Further, the source characteristics of aftershocks vary from the mainshock zone to the east side. Focal mechanisms of aftershocks near the mainshock are similar to

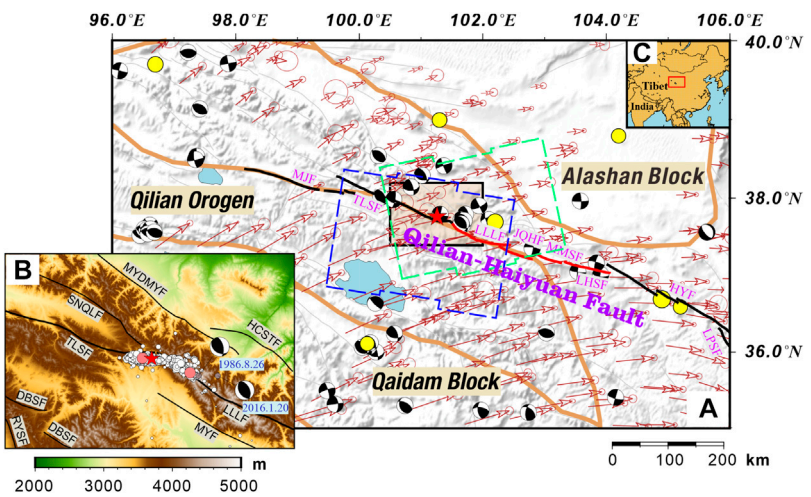

FIGURE 1 | Tectonic backgrounds of the Menyuan Ms 6.9 earthquake. **(A)** The green and blue dashed rectangles represent the data coverage of ascending and descending orbits of Sentinel-1 satellites, respectively; the black rectangle represents the scope of the study area. The black and red solid lines constitute together the Qilian-Haiyuan Fault, and the latter is seen as the Tianzhu Gap (Gaudemer et al., 1995). The yellow circles represent historical earthquakes with surface wave magnitude (Ms) larger than 7 since 1900 (data from Sichuan Earthquake Administration). Black beach balls represent focal mechanisms of M ≥ 5.0 events (Global CMT, since 1976). Brown arrows represent the GPS velocity field with respect to the Eurasian frame (Wang and Shen, 2020). The red star represents the Ms 6.9 earthquake. The background image is DEM from SRTM (Farr and Kobrick, 2000). **(B)** Topography of the study area [black box in Figure **(A)**] and aftershock distribution. The mainshock is marked by the red star. Pink circles represent two Ms ≥ 5.0 aftershocks (Yang et al., 2022); black beach balls represent the focal mechanisms of two Ms 6.4 Menyuan earthquakes in 1986 and 2016. The solid black line represents the surface fault trace (Xu et al., 2016). **(C)** Geographical location of the study area. The red box marks the extent of figure **(A)**. MJF: Muli-Jiangcang Fault, TLSF: Tuolaishan Fault, LLLF: Lenglongling Fault, JQHF: Jinqianghe Fault, MMSF: Maomaoshan Fault, LHSF: Laohushan Fault, HYF: Haiyuan Fault, LPSF: Liupanshan Fault, SNQLF: Sunan-Qilian Fault, MYDMYF: Minyue-Damaying Fault, HCSTF: Huangcheng-Shuangta Fault, MYF: Menyuan Fault, DBSF: Dabanshan Fault, RYSF: Riyueshan Fault.

TABLE 1 | Basic parameters of the SAR data.

Orbit direction	Track path	Time of acquisition		Perpendicular baseline(m)	Incidence (°)	Azimuth (°)	Time interval (day)
		References	Secondary				
Acending	128	20220105	20220117	38.19	35.93	349.54	12
Descending	33	20211229	20220110	56.59	38.10	190.22	12

that of the mainshock, and the reverse component increases to the east side obviously (Liang et al., 2022). The finite fault inversion results show that the fault is dominated by left-lateral strike-slip with a maximum slip of 3.5 m. The Coulomb stress change results show that the earthquake is located at the positive stress zone of the 2016 Menyuan earthquake (Li et al., 2022b; Peng et al., 2022). The historical strong earthquakes on the northeastern margin of the Qinghai-Tibet Plateau have a stress loading effect on the Muli-Jiangcang and Tuolaishan faults in the western segment of the Qilian-Haiyuan fault zone, as well as the Jinqianghe-Laohushan fault in the middle segment (Zhu et al., 2022). In addition, the thickness of crust changes dramatically in the eastern part of the Qilian block, and this earthquake is located at the transition zone where physical properties of the crustal medium rapidly change (Wang et al., 2022).

Results above show that the fault structure is complex. Some problems still remained unclear. For example, the influence of the earthquake on the adjacent faults is not resolved. Previous studies mainly focused on quick disaster emergency response after the earthquake. The ascending orbit images used in the InSAR-based deformation observation only covered part of the rupture area, so the interferogram was incomplete. Would the results be improved by using ascending orbit data that completely covered the rupture zone?

In this paper, the co-seismic displacement field is obtained by D-InSAR technology, using the data of synthetic aperture radar (SAR) in ascending and descending orbits covering the seismic rupture area. At the same time, based on Pixel Tracking technology, the range and azimuth offset maps of the ascending and descending orbits are obtained, and the surface fault traces are also extracted. Then, the linear inversion of the distributed slip model is carried out. Based on the finite fault model, the Coulomb stress change caused by the earthquake are calculated. Finally, and the stress condition of the adjacent faults after the earthquake is analyzed.

INSAR DATA AND PROCESSING

According to the principle of minimum time interval of SAR data coverage, the Level 1 Single-Look Complex data (SLC) in Sentinel-1 Interferometric Wide (IW) mode is used. The ascending orbit (T128A) and the descending orbit (T33D) each contain two images to form an interferometry pair. The detailed parameters of the image pairs are shown in **Table 1**. The time baselines of the satellite images of the ascending and descending orbits are both 12 days. The ascending orbit image pair were collected 3 days before and 9 days after the earthquake. The descending orbit image pair were collected 10 days before and 2 days after the earthquake. So, more afterslip is included in the ascending orbit pair. In addition, the corresponding spatial perpendicular baselines of the two pairs of images are both less than 60 m, indicating that the topographic phase has little influence on the interferometry phase, increasing the sensitivity of the deformation phase.

In this paper, the open-source software ISCE (InSAR Scientific Computing Environment, Rosen et al., 2012) is used for two-pass differential interference processing of the SAR data in ascending and descending orbits. Firstly, the software achieves accurate image registration through enhanced spectral diversity (ESD) algorithm (Fattahi et al., 2017), which makes the azimuth matching accuracy higher than 0.001 pixels, avoiding the phase jump caused by adjacent image bursts, and greatly improving the reliability of interference results. The precise orbit (POEORB) data of European Space Agency (ESA) is used to eliminate orbit errors (https://scihub.copernicus.eu/). The 30-m resolution SRTM elevation data product published by NASA was used to simulate the terrain phase, and the interferogram is obtained by the second difference. In order to improve the signal-to-noise ratio of the interferograms, the multi-look ratio of range direction and azimuth direction is set as 5: 1. A weighted power spectrum adaptive algorithm for phase filtering (Goldstein and Werner, 1998). Then, the phase unwrapping is carried out based on the minimum cost flow algorithm, to obtain the geocoded Line Of Sight (LOS) displacement. The atmospheric errors in InSAR measurement mainly come from the influence of the ionosphere and troposphere, and the ionosphere has less influence on the C band due to the relatively short wavelength (Gray et al., 2000). Therefore, the tropospheric atmospheric delay model provided by the General Atmospheric Correction Online Service (GACOS) of Newcastle University was used for atmospheric correction (Yu et al., 2018). The residual error of orbit will produce long wavelength noise, so a linear trend is removed from the line of sight (LOS) displacement result. Finally, the co-seismic LOS deformation field after atmospheric correction and detrending is obtained. (**Supplementary Figure S1**).

COSEISMIC DEFORMATION

In this paper, D-InSAR technology was used to obtain the interferograms of the ascending and descending orbit SAR data (**Figure 2**). Except for a small incoherent area in the deformation center caused by deformation jump on the fault trace, strong coherence is preserved among the most area, showing continuous interference fringes. Both ascending and descending interferograms show the typical "butterfly shape" of strike slip rupture (**Figures 2A,C**). The deformation zone is

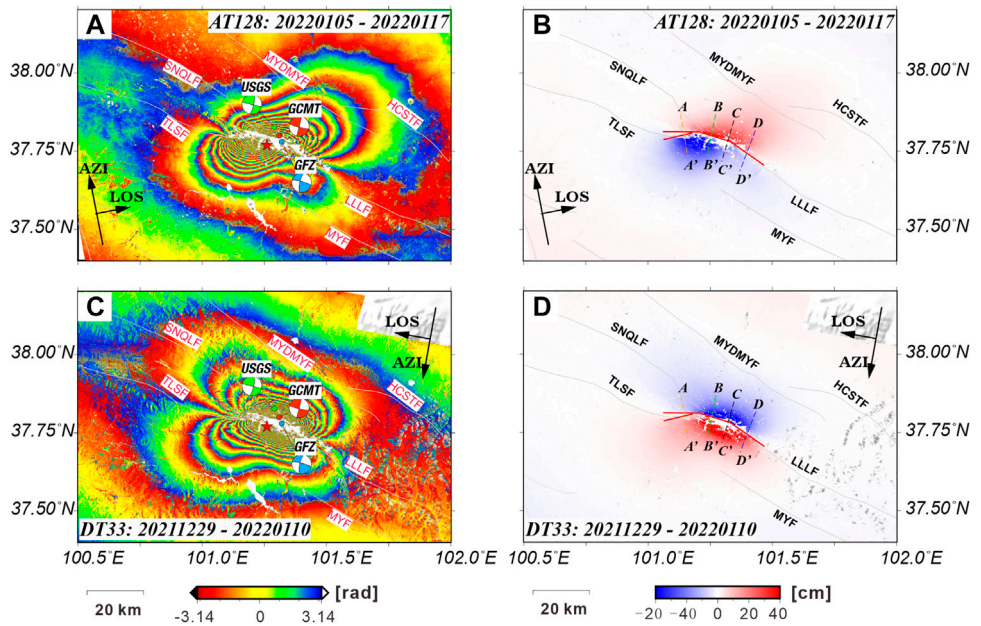

FIGURE 2 | Interferogram and co-seismic deformation field (LOS direction) of Menyuan Ms 6.9 earthquake. **(A,C)** are the interferograms of T128 ascending orbit and T33 descending orbit, respectively. Focal mechanism solutions from GCMT, GFZ, and USGS are displayed with the red, blue, and green focal spheres. The red star marks the epicenter of the mainshock. **(B,D)** are the LOS co-seismic deformation fields of T128 ascending orbit and T33 descending orbit, respectively. The dashed lines labeled by **(A–D)** are four cross-fault profiles shown in **Figure 3**, and the red solid lines represent the seismogenic faults. Black arrows indicate satellite flight direction (AZI) and right-looking observation direction (LOS).

about 50 × 40 km^2, mainly along the Lenglongling fault and the eastern section of Tuolaishan fault.

For an earthquake, the co-seismic deformation fields of ascending and descending orbits are different, which is mainly caused by the difference of incidence angle and flight azimuth (Hu et al., 2010). The relation between three component of deformation and the LOS displacement is:

$$u_{los} = \left[-sin\theta cos\alpha \quad sin\theta sin\alpha \quad cos\theta \right] * \begin{bmatrix} u_e \\ u_n \\ u_z \end{bmatrix} \tag{1}$$

Where u_{los}, u_e, u_n, u_z are the LOS, east, north and vertical displacement respectively; θ are the incidence angle of radar pulse; α represents the azimuth angle of satellite flight. According to the average incidence and azimuth angle of ascending and descending tracks (**Table 1**), the contribution values of the east-west, north-south and vertical displacements to the LOS displacement of ascending and descending orbits are (−0.5770, −0.1065, 0.8097) and (0.6072, −0.1095, 0.7869), respectively. It can be seen that the Sentinel-1 satellite is most sensitive to vertical deformation, but insensitive to north-south deformation. And the opposite characteristics and great differences between the ascending and descending interferograms are mainly due to east-west displacement. The results of T128 ascending orbit show that the displacement at the northern side of seismogenic fault are mainly positive with a maximum value of 42.72 cm (LOS direction), and are mainly negative at the southern side with a minimum value of -59.65 cm (LOS direction). On the contrary, the displacement results of T33 descending orbit show that negative values are mainly observed at the northern side (−71.52 cm) and positive values is mainly observed at the southern side (94.65 cm) of the fault. Considering the geometric characteristics of satellite flight and right-sided look and LOS changes, the earthquake is associated with sinistral strike-slip faulting. The absolute LOS displacement on the south side of the fault is greater than that on the north side, which may result from slip on dipping fault plane as suggested by focal mechanism solutions. Meanwhile, the focal mechanism results show that the earthquake contains a small amount of thrust component (**Table 2**). Thus, it could be inferred that the south side of the fault is the hanging wall, and the north side is the footwall, slightly inclined to SW.

Figure 3 shows four displacement profiles in the ascending and descending tracks. The displacement gradually decreases away from the fault. Compared with the AA' and DD' sections far from the epicenter, BB "and CC" sections near the epicenter have obviously larger relative displacements, indicating that the ground deformation caused by the earthquake decreases from the center to both sides. The surface displacement caused by the Menyuan Ms 6.9 earthquake gradually decreased from the center of the rupture zone to both ends, and the displacement on both sides of the cross-fault was opposite in direction but similar in size, indicating that the seismogenic fault has a high dip Angle.

TABLE 2 | Focal mechanism solutions of the Menyuan Ms 6.9 earthquake.

Source	Epicenter (°)	Depth (km)	Nodal plane 1 (°)	Nodal plane 2 (°)	Magnitude
			Strike dip rake	Strike dip rake	
USGS	37.828,101.290	13	13 75 178	104 88 15	Mw 6.61
GCMT	37.800,101.310	14.8	14 89 172	104 82 1	Mw 6.7
GFZ	37.780,101.320	15	193 74 172	285 82 16	Mw 6.6
Li et al	——	——	104 80 0 (AB)	109 80 5(BC)	Mw 6.7
Xu et al	37.77,101.258	4	197 74 171	290 81 16	Mw 6.62
Liang et al	37.77,101.26	4	196 69 174	288 85 21	Mw 6.4
This research	37.79,101.26	4.9	——	108 79 4	Mw 6.67

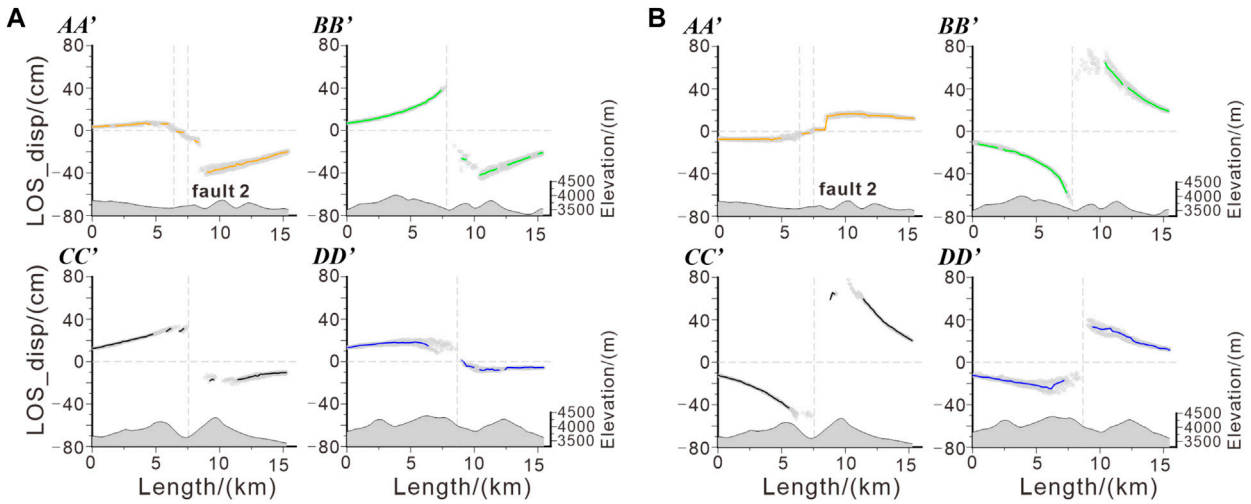

FIGURE 3 | Co-seismic displacement profiles of the Menyuan Ms 6.9 earthquake (LOS direction). **(A)** Cross-fault displacement profiles of the T128 ascending orbit, with profile location shown in **Figure 2**; **(B)** Cross-fault displacement profiles of the T33 descending orbit. Gray circles are the data within 1 km along the profile. The vertical gray dotted line indicates the location of the faults, of which the southern branch fault (fault2) is located about 1 km south from the main fault.

FAULT GEOMETRY CONSTRAINTS AND SLIP DISTRIBUTION INVERSION

After the Menyuan Ms 6.9 earthquake, different institutions and researchers quickly conducted focal mechanism inversion, and the results were somewhat different (**Table 2**). Xu et al. (2022) and Liang et al. (2022) have used more waveform data to obtain a more reliable solution of focal mechanism, which shows that the focal depth was shallow, both at 4 km. Compared with the teleseismic records, InSAR observations can provide more near-field constraints for the inversion of fault geometry and slip distribution. In order to determine the fine motion characteristics of seismogenic faults, the down-sampling process is carried out on the basis of co-seismic surface displacement, and then the slip distribution of the fault is inverted based on the classical elastic dislocation model.

InSAR co-seismic deformation field usually contains millions of points, and adjacent observation points have strong spatial continuity (Hanssen, 2001; Ji et al., 2017). In order to improve the calculation efficiency and reduce the influence of unreliable values in inversion, filter and downsampling preprocess are applied to the LOS displacement data. Firstly, the interferograms of ascending and descending orbit are masked according to the coherence. Sampling points with coherence greater than 0.5 are extracted to ensure the high quality co-seismic deformation data (Yu et al., 2020). Then, an adaptive quadtree method based on gradient variation is applied to downsample the co-seismic deformation data (Decriem et al., 2010; Bagnardi and Hooper, 2018). For each point, independent incidence and azimuth angles are used. This method retains the main characteristics of the original deformation field completely, and reduces the number of sampling points in the far field. Finally, 872 LOS displacement samples of the ascending orbit and

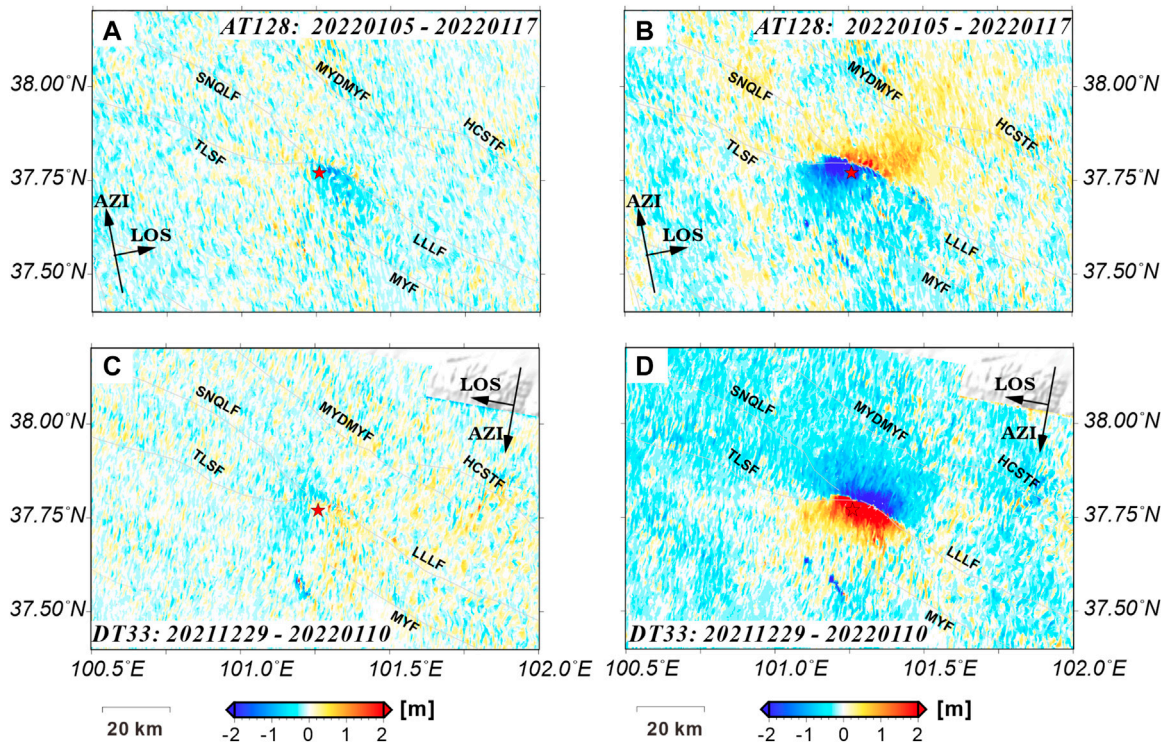

FIGURE 4 | The results of the Pixel-Tracking method for the ascending and descending orbit amplitudes. **(A,C)** are the range offset of the T128 ascending orbit and the T33 descending orbit, respectively, and the positive and negative values indicate the decreasing and increasing of the horizontal surface displacement along the distance direction from the satellite and to the target point (the range direction); **(B,D)** are the azimuth offset of the T128 ascending orbit and the T33 descending orbit, respectively, and the positive and negative values represent the forward and backward displacement of the horizontal displacement along the flight direction of the satellite, respectively. The red star indicates the epicenter. Black arrows indicate satellite flight direction (AZI) and right-looking observation direction (LOS).

908 LOS displacement samples of the descending orbit are obtained (**Supplementary Figure S2**).

Spatial Characteristics of the Fault

Fault traces on the surface are extracted from the range and azimuth offset map. Amplitude pixel tracking method is used to obtain the range and azimuth offset of the Menyuan Ms 6.9 earthquake (**Figure 4**). The basic principle of this method is to calculate the pixel offsets in the range direction and azimuth direction according to the cross-correlation of amplitudes on the basis of sub-pixel registration of two SAR images (Hu et al., 2010). This method greatly compensates the insensitivity of InSAR to the north-south ground displacement, and helps to explain the incoherent phenomenon caused by the local large rupture near the fault. The azimuth offset results of T128 ascending and T33 descending orbits are opposite on both sides of the fault, showing a sharp color discontinuity (**Figures 4B,D**). Utilizing the offset maps with the boundary between positive and negative offset values, the surface traces of seismogenic fault can be extracted by outlining the discontinuity (Zhang et al., 2011; Hua et al., 2021). The finally obtained surface trace is composed of two faults (**Figures 2B,D**), of which the average strike of the small south branch is 77°, and the main north fault is 108°, with a total length of 49.5 km.

In the addition, the four profiles of the co-seismic deformation fields of the ascending and descending orbits (**Figure 3**) show that the displacements on both sides of the cross fault are approximately complementary. The existing focal mechanism solutions show that the dip angle of the seismogenic fault is close to vertical (**Table 2**), so the range of dip angle is set to 70°–90°. In order to select the optimal dip angle, a grid search with step of 1° was conducted in the inversion (Li et al., 2018), and the optimal dip angle was obtained as 79° (**Figure 5A**).

Distributed Slip Model

According to the uniform isotropic elastic half-space dislocation model, the slip on the seismogenic fault plane can be linearly projected to the earth's surface by Green's function (Okada, 1985). The relationship between the slip distribution of the fault and the co-seismic displacement field is as follows:

$$u = G(m)\boldsymbol{s} + \varepsilon \tag{2}$$

where u represents the co-seismic displacement measured by InSAR; G(m) represents Green's function related to fault

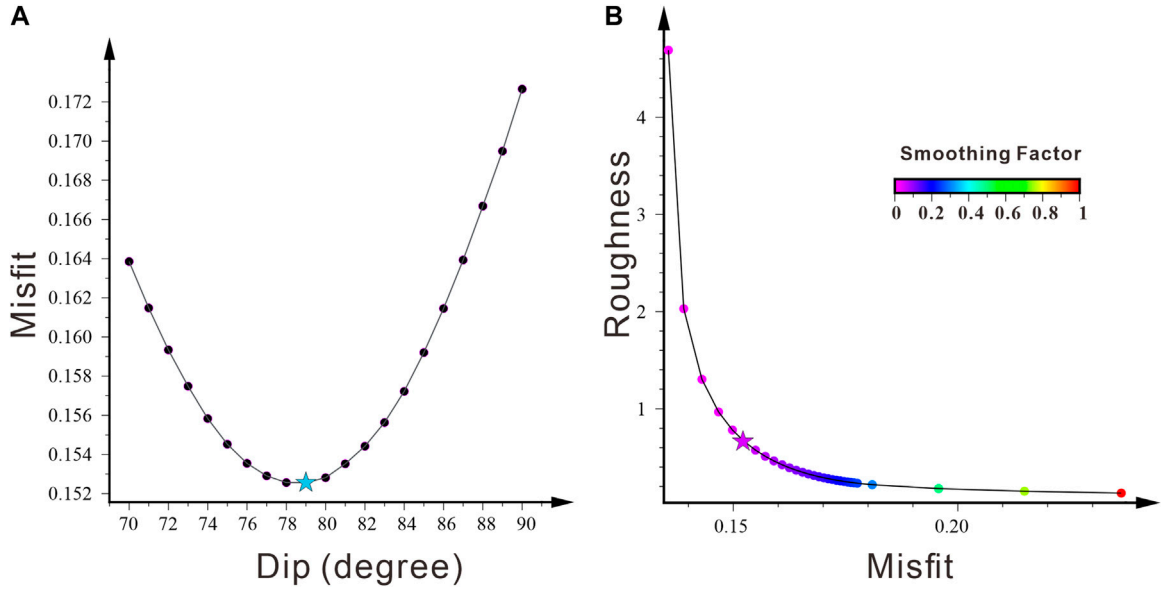

FIGURE 5 | Determination of the optimal fault dip angle and the smoothing factor. **(A)** The misfit-dip curve. The light blue star indicates the optimal dip angle of 79°. **(B)** The model roughness and the fitting residual curve. The star indicates the best smoothing factor of 0.05.

parameters m; $\boldsymbol{s}$ represents the slip vector on the fault plane; ε represents the data observation error.

Generally speaking, the inversion of fault parameters includes the location, length, width, depth, strike and dip angle of the fault, and the slip vector on the fault, which is a highly nonlinear problem. Usually "two-step" inversion is adopted. Firstly, geometric parameters of seismogenic faults are resolved using a nonlinear inversion method (Bagnardi and Hooper, 2018). Then, according to the linear relationship between u and $\boldsymbol{s}$, the least square solution is obtained (Feng and Li, 2010). Especially, the Menyuan Ms 6.9 earthquake produced obvious surface ruptures. So the geometric shape along strike of the fault can be determined according to the surface rupture (Fukahata and Wright, 2008). Further, the dip angle of faults can be estimated according to the aftershock distribution, focal mechanisms and tectonic settings. Therefore, the slip distribution of faults can be directly solved by a linear inversion method.

In this paper, the Steepest Descent Method (SDM) inversion method (Wang et al., 2013) was used to solve the rake and slip size of each discrete sub-fault in the distribution slip model. This method has been widely used in GPS and InSAR co-seismic displacement inversion (Chen et al., 2018; Shi et al., 2019; Yu et al., 2020; He et al., 2022). SDM is an iterative optimization algorithm with better convergence and less dependence on the initial value. In order to minimize the objective function in each calculation, a step size proportional to the negative gradient is used in each iteration.

Meanwhile, in order to ensure smoothness and continuity between each sub-faults, a smoothing factor is added in the inversion process, and the objective function is as follows:

$$F(m) = \|G(m)s - u\|^2 + \alpha^2\|H\tau\|^2 \quad (3)$$

where α^2 denotes the smoothing factor used to control the roughness of the slip distribution; H denotes the finite-difference approximation of the Laplace operator; τ denotes the shear stress drop.

In the process of inversion, Poisson's ratio is set to 0.25, the top depth of the fault is 0 km, and the dip angle is 79° (**Figure 5A**). Referring to the focal mechanisms of the mainshock (USGS, GCMT, and GFZ), the slip angle is empirically constrained to -15°–25° to accelerate the convergence. According to the relocation results of aftershocks, the aftershock concentrates at 5–10 km depth, and a few of aftershocks occurred between 11 and 20 km depth (Xu et al., 2022; Yang et al., 2022). Thus, the width of the fault was set to 20 km corresponding to the depth of 19.6 km. Then, the whole fault plane is divided into a 2 × 2 km rectangle, with 250 sub-faults in total. The maximum slip is set at 10 m. At the same time, the weight of ascending and descending orbit deformation was set to 0.8:1, taking into account the impact of afterslip in the ascending displacement. Independent incidence and azimuth angles are used for each sampling point (Zhang et al., 2011).

In order to further ensure the stability and reduce the uncertainty of the inversion, a grid search method was adopted to obtain the L-curve between model roughness and fitting residual for a series of smoothing factor (**Figure 5B**). Consequently, the optimal smoothing factor 0.05 was selected.

Figure 6 shows the fault slip distribution of the Menyuan Ms 6.9 earthquake. On the whole, the joint inversion results of ascending and descending orbits are similar to those of Yang et al. (2022), but different from those of Li et al. (2022a). This may be related to the difference in the geometry of faults. It can be seen from the slip distribution results that the slip is mainly

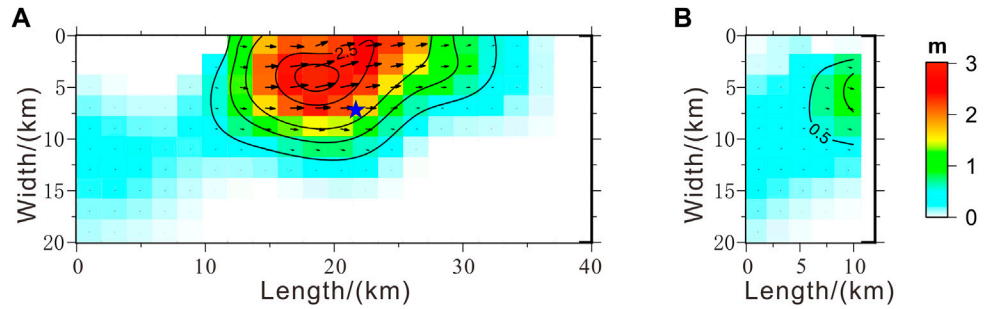

FIGURE 6 | Fault slip distribution of the Menyuan Ms 6.9 earthquake. **(A,B)** are the slip distributions of the main fault and the minor branch fault along the fault strike, respectively; black arrows represent the slip vector, and its direction represents the movement direction of the hanging wall relative to the foot wall; the blue star indicates the location of the mainshock determined by Yang et al. (2022).

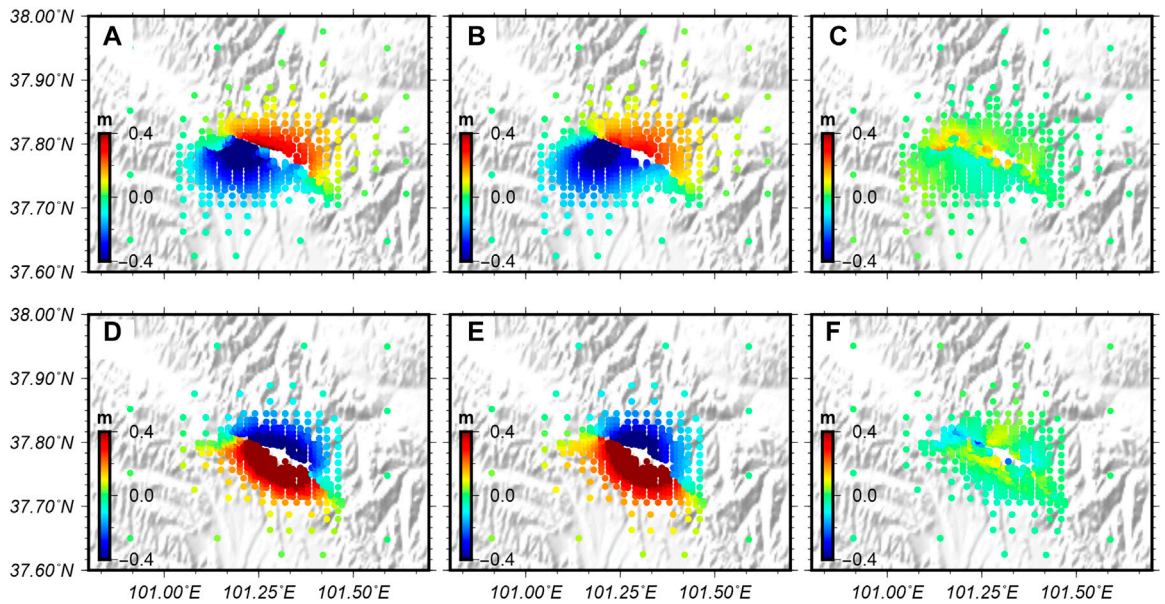

FIGURE 7 | Fitting results in distributed slip model inversion. **(A–C)** represent the observed deformation, simulated deformation and the fitting residual of the T128 ascending orbit, respectively; **(D–F)** are same for the T33 descending orbit. The background image is DEM.

concentrated in the strike range of 12–30 km, and 0–10 km along the dip. The maximum slip is 3.12 m at a depth of about 5 km, and the average slip of the main fault is 0.48 m (**Supplementary Figures S3–S5**).

Slip directions of fault patches show that the rupture is mainly sinistral strike-slip. In the slip center on the main fault, a small amount of thrust slip component exists.The inversion results show that the seismic moment is 1.28×10^{19} N·m, and the equivalent moment magnitude is 6.67, consistent with the GCMT result.

In the joint inversion results of ascending and descending orbits, the correlation coefficient between the observed and the simulated deformation is 98.87%. The root mean square error (RMSE) ascending descending orbits are 5.5 and 5.6 cm, respectively.

As can be seen from the spatial distribution of residuals (**Figures 7C,F**), the fitting residuals are small in the whole. The largest residuals appear in the area near the surface rupture zone. This may be caused by displacement errors from strong incoherence in the zone and the complexity of the very shallow rupture.

Figure 8 shows the histogram of fitting residuals. The distribution of ascending fitting residual is more concentrated (**Figure 8A**). Except for a few large residuals in the descending orbit, most of the residuals are close to zero, showing approximate Gaussian distribution. The ascending average fitting residual error is 1.52 cm with the variance of 2.8 mm, and the descending average fitting residual error is −0.93 cm with the variance of 3.1 mm.

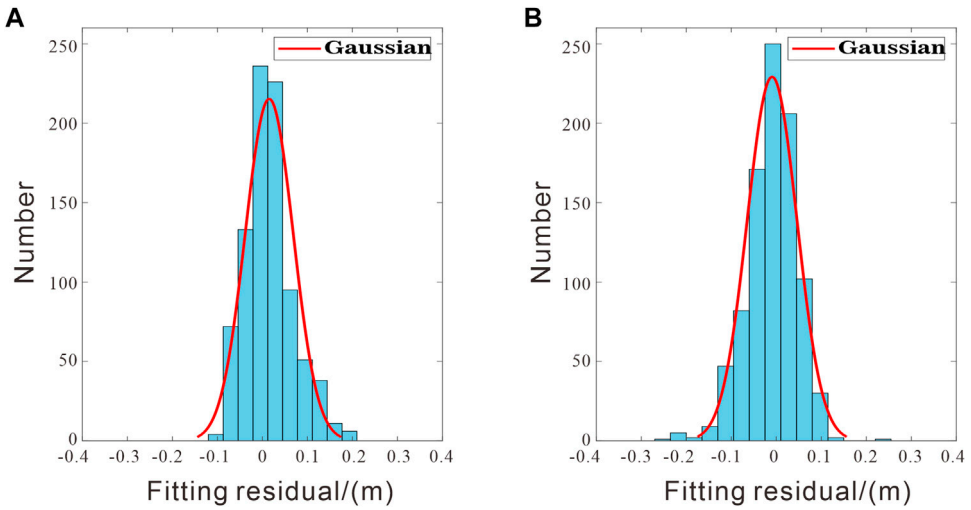

FIGURE 8 | Histograms of the fitting residuals. **(A,B)** represent the fitting residual histograms of the inversion results of the T128 ascending orbit and the T33 descending orbit. The red solid line indicates the Gaussian distribution curve fitted by the distribution.

DISCUSSION

Regional Seismogenic Environment and Source Characteristics

From the perspective of historical earthquakes, there were two Ms 6.4 earthquakes in 1986 and 2016 around the Lenglongling fault (**Figure 1**). Coulomb stress analysis results show that the 2016 Menyuan Ms 6.9 earthquake has a loading effect on the 2022 Menyuan Ms 6.9 earthquake (Li et al., 2022a; Peng et al., 2022). Judging from the trace of shallow fault, Menyuan Ms 6.9 earthquake occurred at the intersection of Tolaishan fault and Lenglongling fault (**Figure 1B**), which belongs to the compression-bending zone on the Qilian-Haiyuan fault zone, and is prone to stress concentration (Pan et al., 2022). Geological survey shows that although the Tuolaishan fault and Lenglongling fault are mainly left-lateral strike-slip faults, their slip rates are different: the eastern segment of the former is about 3–4 mm/a, while the latter is about 6.4 ± 0.7 mm/a (Guo et al., 2017). P-wave velocity structure shows that there is an obvious low-velocity zone below the earthquake source (Wang et al., 2022; Xu et al., 2022), and the eastern part of the Qilian Mountains is located at the region where crustal thickness changes dramatically. This makes the source region favorable to stress concentration (Wang et al., 2022).

Based on the co-seismic deformation field of the ascending and descending orbits obtained by InSAR, the fault slip distribution is inverted. Its focal mechanism shows that the Ms 6.9 earthquake was a sinistral strike-slip event with a small amount of thrust component. The average strike of the seismogenic faults was 108°, and the dip angle was 79°. The average rake is 4° and there is only one rupture center (**Figure 6**). Combining the spatial position of the maximum slip (**Figure 6A**) and the deformation coverage shown in the co-seismic deformation field (**Figure 2D**) and azimuth offset (**Figure 4D**) of T33 descending orbit, we can conclude that the seismogenic fault of this earthquake is the west part of the Lenglongling fault. It is belonged to a left-stepped echelon fault system, forming a tensional zone with the adjacent Tolaishan fault. Stress transfer between the faults is likely to occur, which may be the cause of surface rupture at the eastern end of Tolaishan fault (Pan et al., 2022).

To sum up, under the continuous northward expansion of the northeastern margin of the Tibetan Plateau, the shallow faults in the area around Menyuan are characterized by compressing and bending with inconsistent slip rates. In the deep crust, great differences of physical properties exist. In addition, the historical earthquake had a stress loading effect on the rupture. These conditions may jointly promote the strain accumulation in the western segment of Lenglongling fault and ultimately lead to the occurrence of this earthquake.

The Relationship Among Aftershock, Surface Rupture Traces and Co-seismic Slip Distribution

Figure 9 is the surface rupture trace delineated according to the obvious amplitude azimuth offset and the boundary between positive and negative displacement in the co-seismic deformation field (**Figures 2B,D**). Its overall shape is similar to the surface rupture distribution map shown by Peng et al. (2022). Coupled with the relocation of aftershocks, it is revealed that this earthquake produced obvious surface rupture. According to the aftershock distribution in **Figures 9A,B** the aftershocks in 2–9 days after the earthquake continued to expand in the SE direction along the surface rupture trace and are concentrated in the eastern section of the fault. Aftershocks are evenly distributed on both sides of the fault in the eastern segment. However, aftershocks are mainly distributed on the south side of the in the middle and western segment, indicating a possible deflection of the fault.

At the same time, there is an obvious varying dipping angles from east to west in the aftershock profiles (**Figure 10**). The fault plane is

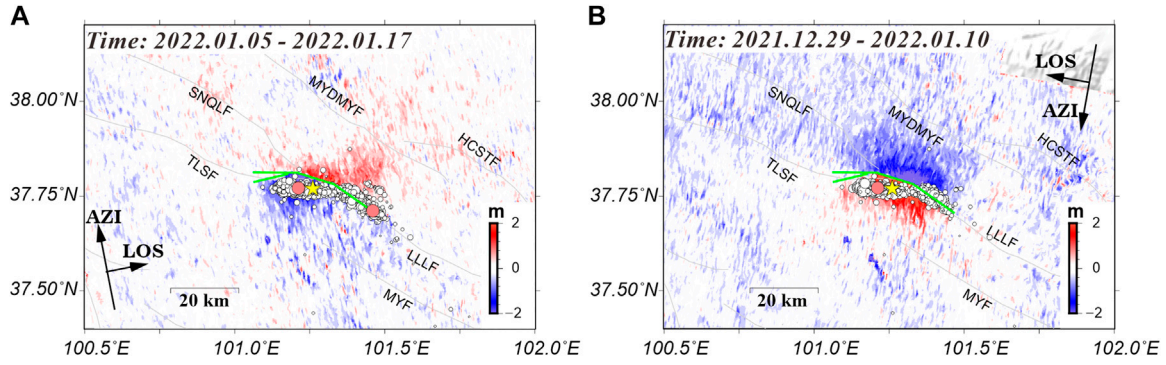

FIGURE 9 | Surface rupture traces and aftershock distribution. **(A)** The background image is the azimuth offset of the ascending orbit, and the small white circles represent the aftershocks in 9 days after the mainshock (Yang et al., 2022); **(B)** The background image is the azimuthal offset of the descending orbit, the white small circles represent the aftershocks of 2 days after the earthquake (Yang et al., 2022). Green lines denote the seismogenic faults; the yellow star represents the epicenter of the mainshock; pink circles represent two aftershocks with magnitude≥ 5.0, which occurred on January 8 and 12 from left to right, respectively.

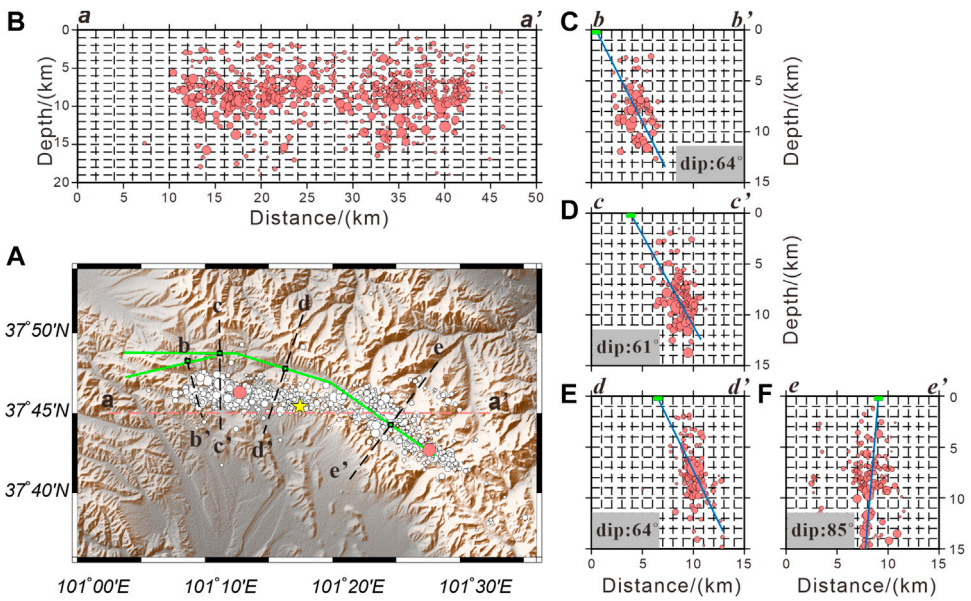

FIGURE 10 | Dip angles determined from aftershock profiles of different fault sections. **(A)** Green lines, the yellow star and pink circles denote the seismogenic faults, the epicenter of the mainshock and two aftershocks with magnitude ≥ 5.0, respectively. **(B–F)** represent the five aftershocks profiles (aa', bb', cc', dd', ee'). Fault positions are marked by the green rectangles.

determined by surface rupture and distribution of aftershocks. We tested a new fault geometry that each section has a different dip angle (**Supplementary Figure S6**). However, the results are similar to those obtained with uniform 79° dip (**Supplementary Figures S7, S8**) and the correlation coefficient between the observed and the simulated deformation is also over 98%. So 79° may be the average of these dips.

The aftershock (purple solid circles) is projected onto the seismogenic fault surface (**Figure 11**). The results show that the aftershock extended along the east and west sides from the source location within the depth range of 2–12 km. Meanwhile, the main shock depth (7.05 km) was close to the depth (5 km) where the maximum slip of the fault was 3.12 m. In addition, most of aftershocks occurred in the position where the co-seismic slip was small.

Therefore, the stress release associated with the aftershocks was either triggered by the mainshock or it was a compensation to the stress release associated with the mainshock.

Regional Seismic Hazard Assessment

In general, after an earthquake of moderate magnitude or above, the co-seismic dislocation of the fault will cause static co-seismic

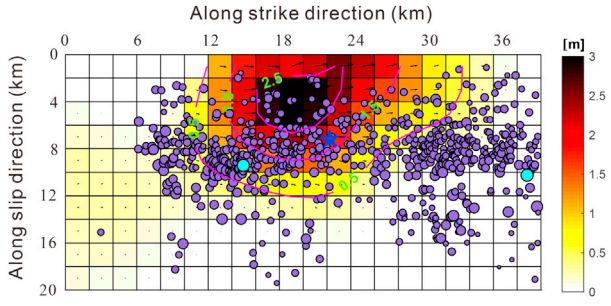

FIGURE 11 | Fault slip model of the main fault and aftershocks. Red lines represent the contour of the slip; the blue star represents the mainshock location determined by Yang et al. (2022); the cyan circles denote two aftershocks with magnitude ≥ 5.0.

permanent deformation, which will change the Coulomb stress in the near and far field. the Coulomb failure stress change (ΔCFS) can be used to analyze the triggering of aftershock, and the interaction between earthquakes and faults (King et al., 1994; Xu et al., 2018). According to Coulomb instability criterion, the Coulomb stress change can be expressed as:

$$\Delta CFS = \Delta\tau_s + \mu'\Delta\sigma_n \quad (4)$$

where $\Delta\tau_s$ represents the change in shear stress; μ' represents the effective coefficient of friction on the fault; $\Delta\sigma_n$ represents the change in normal stress (dilation for positive); ΔCFS represents the coulomb stress change on the receiver faults caused by the slip of the source fault, with a positive value indicating stress loading and a negative value indicating inhibition of rupture of the receiver fault. In this paper, Coulomb 3.3 software (Toda et al., 2011) was used to calculate the co-seismic Coulomb stress changes caused by Menyuan Ms 6.9 earthquake (**Figure 12**).

The receiver fault was set as seismogenic fault itself (strike = 108°, dip angle = 79°, dip angle =4°) with a friction coefficient of 0.4 (King et al., 1994). The co-seismic Coulomb stress changes at the depths of 0, 5, 10 and 15 km are calculated respectively (**Figure 12**). The results show that the coulomb stress loading region is mainly distributed in the eastern segment of Tuolaishan fault and the western segment of Lenglongling fault, and a few parts of the Minyue-Damaying fault, Minyue-Yongchang fault and Daban Mountain fault in the NS direction. The static Coulomb stress change at 10 km shows that the largest aftershock (Ms 5.2) occurred in the positive area of the Lenglongling fault 4 days after the mainshock. The aftershock mainly migrated towards to SE direction (Fan et al., 2022; Yang et al., 2022), which may be caused by stress loading yielded by the mainshock.

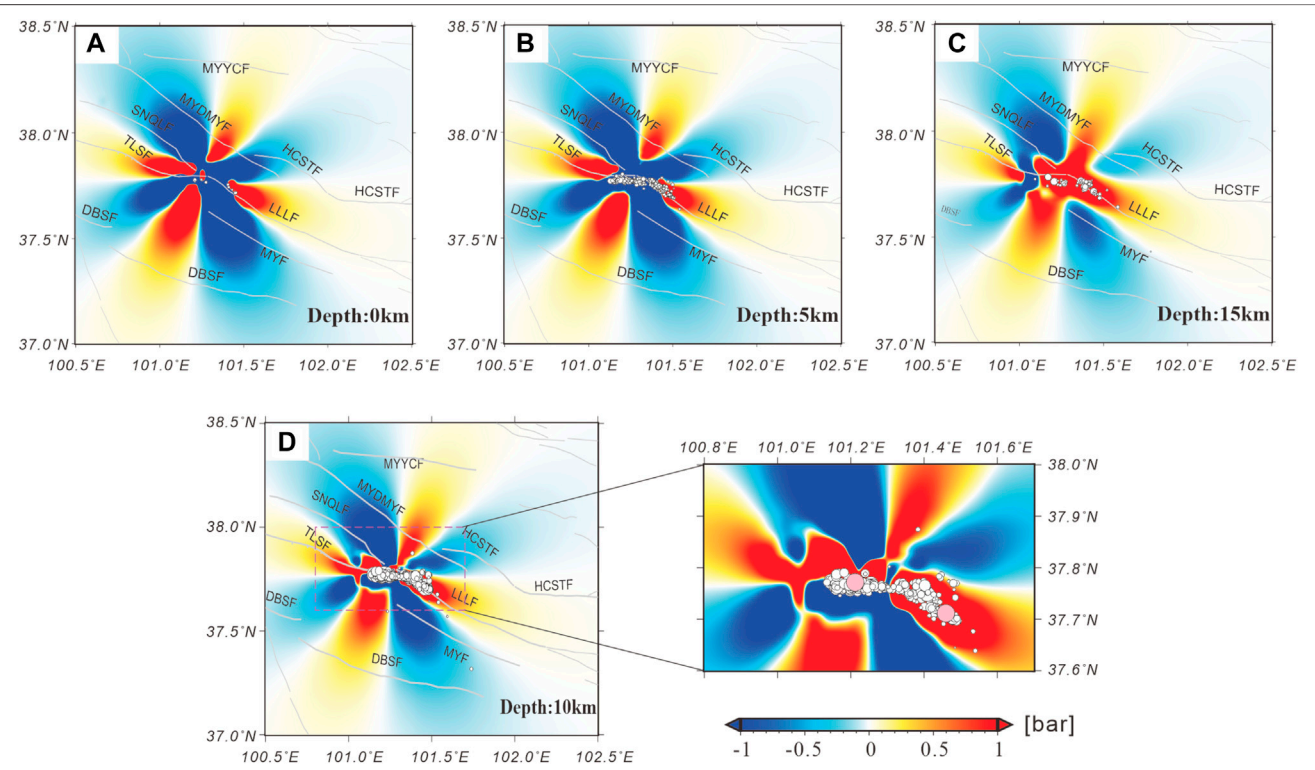

FIGURE 12 | Regional co-seismic static Coulomb stress changes at different depths. **(A–D)** represent the changes of static Coulomb stress at depths of 0, 5, 15, and 10 km, respectively. White circles represent aftershocks in 10 days after the earthquake, including two M ≥ 5 aftershocks (pink circles) (Yang et al., 2022), which are located at the specified depth within 2 km up and down; the gray solid lines indicate the fault traces in this area.

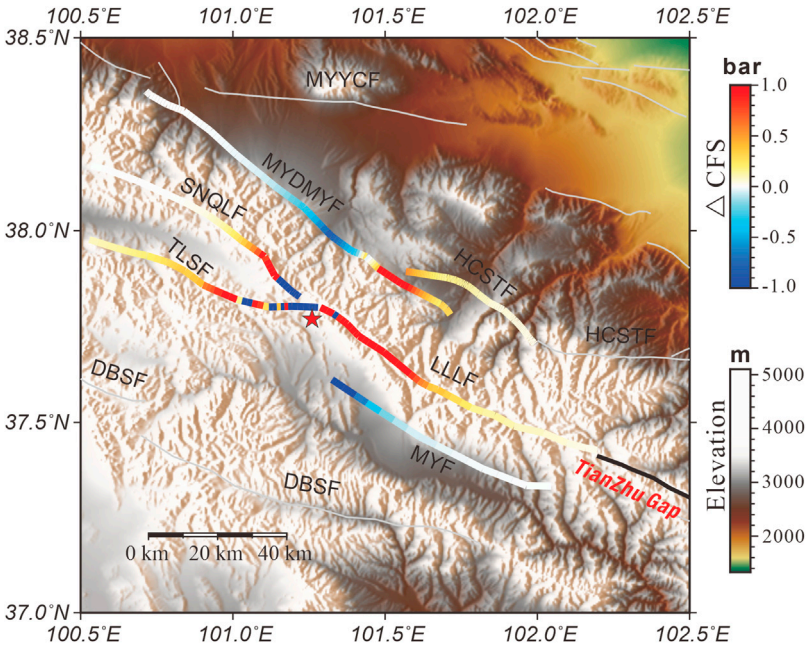

FIGURE 13 | Static Coulomb stress changes on the surrounding faults at depth of 10 km. The colored lines represent the changes of the static Coulomb stress on the surrounding faults caused by the dislocation of the seismogenic fault, and the positive represent the stress loading. Fault parameters are from Xu et al. (2016). The calculation parameters are: Menyuan Fault (reverse fault, dip 45°, rake 90°); Lenglongling Fault (left-lateral, dip 90°, rake 0°); Tolaishan Fault (left-lateral, dip 90°, rake 0°); Sunan-Qilian Fault (reverse fault, dip 45°, rake 90°); Minyue-Damaying fault (reverse fault, dip 45°, rake 90°); Huangcheng-Shuangta Fault (reverse fault, dip 45°, rake 90°). Grey lines indicate the fault traces in this area; black line indicates the "Tianzhu Gap", including the LLLF and the JQHF, MMSF, LHSF to its east. The background image is DEM.

There are many faults in this area, and the stress disturbance at the depth of 10 km on six faults is also calculated (**Figure 13**). The results show that some parts of the Lenglongling fault, the Tolaishan fault, the Sunan-Qilian fault, and the Minyue-Damaying fault are loaded, indicating high seismic risk in the future. At the same time, the whole Qilian-Haiyuan fault (**Figure 1A**), the Jinqianghe-Maomaoshan-Laohushan fault is located in the "Tianzhu Gap" between the present earthquake and the Haiyuan earthquake in 1920 (Gaudemer et al., 1995; Li et al., 2017), so the risk of these faults is also worth noting.

CONCLUSION

In this paper, the co-seismic deformation field (LOS direction) of Menyuan Ms 6.9 earthquake in 2022 is obtained by D-InSAR technology. The co-seismic slip distribution of the fault is inverted by the Steepest Descent Method, and the disturbance of Coulomb stress changes on the surrounding faults is calculated and analyzed. This provides a reference for further research on the seismogenic property and seismic risk of the Qilian-Haiyuan fault. The main conclusions are as follows:

1) The seismogenic fault of the Menyuan Ms 6.9 earthquake is the western segment of Lenglongling fault, and surface deformation filed caused by the co-earthquake is 50 km by 40 km approximately. According to the distribution of ground deformation in the LOS direction and azimuth offsets of the ascending and descending orbits. The Menyuan Ms 6.9 earthquake can be identified as a sinistral strike-slip event.
2) The co-seismic slip distribution shows that the main seismogenic fault strike 108°, dip 79° and rake 4°. The slip is concentrated at a depth of 0–10 km, with an average slip of 0.48 m and the maximum slip of 3.12 m, which is located at a depth of about 5 km. The seismic moment is 1.28×10^{19} N·m, and the corresponding moment magnitude is Mw 6.67.
3) The results of Static Coulomb stress changes show that some parts of Lenglongling fault, Tolaishan fault, Sunan-Qilian fault, and Minyue-Damaying fault are loaded by the Menyuan Ms 6.9 earthquake. Risk of strong earthquake on these faults in the future deserves attention.

DATA AVAILABILITY STATEMENT

Publicly available datasets were analyzed in this study. This data can be found here: https://search.asf.alaska.edu/#/.

AUTHOR CONTRIBUTIONS

JL processed the SAR data and wrote the manuscript; CL contributed to the conception of the research and result analysis; CW contributed to invert the slip distribution and calculate the Coulomb stress changes; FC contributed the related code and beautified the figures; CY and YY helped the result analysis with constructive discussions.

FUNDING

This research was funded by the National Natural Science Foundation of China (Grants 4217040570, 41674059).

ACKNOWLEDGMENTS

Sentinel-1A SAR data are provided by the European Space Agency. The historical earthquake catalogue is provided by Zhang Zhiwei, Sichuan Earthquake Administration. SDM inversion program is provided by professor Wang Rongjiang. Aftershocks data is provided by Yang Hongfeng, The Chinese University of Hong Kong. GMT software is used to create most figures in the paper.

SUPPLEMENTARY MATERIAL

The Supplementary Material for this article can be found online at: https://www.frontiersin.org/articles/10.3389/feart.2022.948661/full#supplementary-material

REFERENCES

Bagnardi, M., and Hooper, A. (2018). Inversion of Surface Deformation Data for Rapid Estimates of Source Parameters and Uncertainties: A Bayesian Approach. *Geochem. Geophys. Geosyst.* 19 (7), 2194–2211. doi:10.1029/2018GC007585

Chen, W., Qiao, X., Liu, G., Xiong, W., Jia, Z., Li, Y., et al. (2018). Study on the Coseismic Slip Model and Coulomb Stress of the 2017 Jiuzhaigou MS 7.0 Earthquake Constrained by GNSS and InSAR Measurements. *Chin. J. Geophys.* 61 (5), 2122–2132. doi:10.6038/cjg2018L0613

Decriem, J., Árnadóttir, T., Hooper, A., Geirsson, H., Sigmundsson, F., Keiding, M., et al. (2010). The 2008 May 29 Earthquake Doublet in SW Iceland. *Geophys. J. Int.* 181 (2), 1128–1146. doi:10.1111/j.1365-246X.2010.04565.x

Fan, L., Li, B., Liao, S., Jiang, C., and Fang, L. (2022). High-Precision Relocation of the Aftershock Sequence of the January 8, 2022, MS 6.9 Menyuan Earthquake. *Earthq. Science* 35 (2), 138–145. doi:10.1016/j.eqs.2022.01.021

Farr, T. G., and Kobrick, M. (2000). Shuttle Radar Topography Mission Produces a Wealth of Data. *Eos Trans. AGU* 81 (48), 583–585. doi:10.1029/EO081i048p00583

Fattahi, H., Agram, P., and Simons, M. (2017). A Network-Based Enhanced Spectral Diversity Approach for TOPS Time-Series Analysis. *IEEE Trans. Geosci. Remote Sens.* 55 (2), 777–786. doi:10.1109/TGRS.2016.2614925

Feng, W., He, X., Zhang, Y., Fang, L., Samsonov, S., and Zhang, P. (2022). Seismic Faults of the 2022 Mw6.6 Menyuan, Qinghai Earthquake and Their Implication for the Regional Seismogenic Structures. *Chin. Sci. Bull.* 617. doi:10.1360/tb-2022-015

Feng, W., and Li, Z. (2010). A Novel Hybrid PSO/simplex Algorithm for Determining Earthquake Source Parameters Using InSAR Data. *Prog. Geophys.* 25 (4), 1189–1196. doi:10.3969/j.issn.1004-2903.2010.04.007

Fukahata, Y., and Wright, T. J. (2008). A Non-linear Geodetic Data Inversion Using ABIC for Slip Distribution on a Fault with an Unknown Dip Angle. *Geophys. J. Int.* 173 (2), 353–364. doi:10.1111/j.1365-246X.2007.03713.x

Gaudemer, Y., Tapponnier, P., Meyer, B., Peltzer, G., Shunmin, G., Zhitai, C., et al. (1995). Partitioning of Crustal Slip between Linked, Active Faults in the Eastern Qilian Shan, and Evidence for a Major Seismic Gap, the 'Tianzhu Gap", on the Western Haiyuan Fault, Gansu (China). *Geophys. J. Int.* 120 (3), 599–645. doi:10.1111/j.1365-246X.1995.tb01842.x

Goldstein, R. M., and Werner, C. L. (1998). Radar Interferogram Filtering for Geophysical Applications. *Geophys. Res. Lett.* 25 (21), 4035–4038. doi:10.1029/1998GL900033

Gray, A. L., Mattar, K. E., and Sofko, G. (2000). Influence of Ionospheric Electron Density Fluctuations on Satellite Radar Interferometry. *Geophys. Res. Lett.* 27 (10), 1451–1454. doi:10.1029/2000GL000016

Guo, P., Han, Z., Jiang, W., and Mao, Z. (2017). Holocene Left-Lateral Slip Rate of the Lenglongling Fault, Northeastern Margin of the Tibetan Plateau. *Seismol. Geol.* 39 (2), 323–341. doi:10.3969/j.issn.0253-4967.2017.02.005

Hanssen, R. F. (2001). "Stochastic Model for Radar Interferometry. Radar Interferometry. Data Interpretation and Error Analysis," in *Remote Sensing and Digital Image Processing* (Dordrecht: Kluwer Academic Publishers) 2. doi:10.1007/0-306-47633-9

He, X., Zhang, Y., Shen, X., Zheng, W., Zhang, P., and Zhang, D. (2020). Examination of the Repeatability of Two Ms 6.4 Menyuan Earthquakes in Qilian-Haiyuan Fault Zone (NE Tibetan Plateau) Based on Source Parameters. *Phys. Earth Planet. Interiors* 299, 106408. doi:10.1016/j.pepi.2019.106408

He, Y., Wang, T., Fang, L., and Zhao, L. (2022). The 2020 Mw 6.0 Jiashi Earthquake: Coinvolvement of Thin-Skinned Thrusting and Basement Shortening in Shaping the Keping-Tage Fold-And-Thrust Belt in Southwestern Tian Shan. *Seismol. Res. Lett.* 93 (2A), 680–692. doi:10.1785/0220210063

Hu, J., Li, Z., Zhu, J., Ren, X., and Ding, X. (2010). Inferring Three-Dimensional Surface Displacement Field by Combining SAR Interferometric Phase and Amplitude Information of Ascending and Descending Orbits. *Sci. China Earth Sci.* 53 (4), 550–560. doi:10.1007/s11430-010-0023-1

Hua, J., Zhao, D., Shan, X., Qu, C., Zhang, Y., Gong, W., et al. (2021). Coseismic Deformation Field, Slip Distribution and Coulomb Stress Disturbance of the 2021 Mw7.3 Maduo Earthquake Using Sentinel-1 InSAR Observations. *Seismol. Geol.* 43 (3), 677–691. doi:10.3969/j.issn.0253-4967.2021.03.013

Ji, L., Liu, C., Xu, J., Liu, L., Long, F., and Zhang, Z. (2017). InSAR Observation and Inversion of the Seismogenic Fault for the 2017 Jiuzhaigou MS 7.0 Earthquake in China. *Chin. J. of Geophys.* 60 (10), 4069–4082. doi:10.6038/cjg20171032

King, G. C. P., Stein, R. S., and Lin., J. (1994). Static Stress Changes and the Triggering of Earthquakes. *Bull. - Seismol. Soc. Am.* 84 (3), 935–953. doi:10.1016/0148-9062(95)94484-2

Li, N., Zhao, Q., and Sun, H. (2018). InSAR Observation Results of the 2015 Tajikistan MS 7.4 Earthquake and its Tectonic Significance. *J. Geodesy Geodyn.* 38 (1), 43–47. doi:10.14075/j.jgg.2018.01.010

Li, Y., Gan, W., Wang, Y., Chen, W., Zhang, K., Liang, S., et al. (2017). Seismogenic Structure of the 2016 MS 6.4 Menyuan Earthquake and its Effect on the Tianzhu Seismic Gap. *J. Geodesy Geodyn.* 37 (8), 792829. doi:10.14075/j.jgg.2017.08.005

Li, Z., Gai, H., Li, X., Yuan, D., Xie, H., Jiang, W., et al. (2022a). Seismogenic Fault and Coseismic Surface Deformation of the Menyuan MS 6. 9 Earthquake in Qinghai, China. *Acta Geol. Sin.* 96 (01), 330–335. doi:10.19762/j.cnki.dizhixuebao.202212410.1111/1755-6724.14727

Li, Z., Han, B., Liu, Z., Zhang, M., Yu, C., Chen, B., et al. (2022b). Source Parameters and Slip Distributions of the 2016 and 2022 Menyuan,Qinghai Earthquakes Constrained by InSAR Observations. *Geomatics Inf. Sci. Wuhan Univ.* 47 (6), 887–897. doi:10.13203/j.whugis20220037

Liang, S., Zou, L., Liu, Y., and Zhang, X. (2022). Determination of the Focal Mechanism Solutions of the Earthquakes with MS ≥4.0 Occurred in the Mainland of China in January 2022. *Prog. Earthq. Sci.* 52 (02), 89–94. doi:10.19987/j.dzkxjz.2022-021

Liu, Y., Xu, C., and Wen, Y. (2019). InSAR Observation of Menyuan Mw5.9 Earthquake Deformation and Deep Geometry of Regional Fault

Zone. *Geomatics Inf. Sci. Wuhan Univ.* 44 (7), 1035–1042. doi:10.13203/j.whugis20190069

Lu, D., Chen, K., and Xi, N. (2022). Earthquake Ground Motion Intensity Map of the Menyuan, Qinghai M6.9 Earthquake on 8 January 2022. *Prog. Earthq. Sci.* 52 (02), 57–59. doi:10.19987/j.dzkxjz.2022-019

Okada, Y. (1985). Surface Deformation Due to Shear and Tensile Faults in a Half-Space. *Bull. Seismol. Soc. Am.* 75 (4), 1135–1154. doi:10.1785/BSSA0750041135

Pan, J., Li, H., Marie- Luce, C., Liu, D., Li, C., Liu, F., et al. (2022). Coseismic Surface Rupture and Seismogenic Structure of the 2022 Ms 6.9 Menyuan Earthquake, Qinghai Province, China. *Acta Geol. Sin.* 96 (01), 215–231. doi:10.19762/j.cnki.dizhixuebao.2022125

Peng, Z., Liu-Zeng, J., Deng, Y., and Toda, S. (2022). *Strong Earthquake Increases Seismic Hazard in Qinghai, China*. Temblor. doi:10.32858/temblor.230

Rosen, P. A., Gurrola, E., Sacco, G. F., and Zebker, H. (2012). "The InSAR Scientific Computing Environment," in 9th European Conference on Synthetic Aperture Radar (Nuremberg, Germany: EUSAR). Available at: https://ieeexplore.ieee.org/abstract/document/6217174, 730–733.

Shi, F., Shao, Z., Zhan, W., Ding, X., Zhu, L., and Li, Y. (2018). Numerical Modeling of the Shear Modulus and Stress State of Active Faults in the Northeastern Margin of the Tibetan Plateau. *Chin. J. of Geophys.* 61 (9), 3651–3663. doi:10.6038/cjg2018L0631

Shi, H., Zhang, Z., Chen, Y., He, P., and Yuan, S. (2019). Constraints on Coseismic Rupture Model of the 2017 MW6.3 Jinghe Earthquake from InSAR Data. *J. Geodesy Geodyn.* 39 (11), 1106–1111. doi:10.14075/j.jgg.2019.11.002

Toda, S., Stein, R. S., Sevilgen, V., and Lin, J. (2011). *Coulomb 3.3 Graphic-Rich Deformation and Stress-Change Software for Earthquake, Tectonic, and Volcano Research and Teaching-User Guide*. Reston, VA: U.S. Geological Survey. Open-File Report. doi:10.3133/ofr20111060

Wang, M., and Shen, Z. K. (2020). Present-Day Crustal Deformation of Continental China Derived from GPS and its Tectonic Implications. *J. Geophys. Res. Solid Earth* 125 (2). e2019JB018774. doi:10.1029/2019JB018774

Wang, Q., Xiao, Z., Wu, Y., Li, S., and Gao, G. (2022). The Deep Tectonic Background of the MS 6.9 Menyuan Earthquake on January 8, 2022 in Qinghai Province. *Acta Seismol. Sin.* 44 (2), 211–222. doi:10.11939/jass.20220010

Wang, R., Diao, F., and Hoechner, A. (2013). "SDM-A Geodetic Inversion Code Incorporating with Layered Crust Structure and Curved Fault Geometry," in EGU General Assembly Conference Abstracts (Vienna, Austria: General Assembly European Geosciences Union) 15 2411. Available at: https://gfzpublic.gfz-potsdam.de/pubman/item/item_1975902.

Xu, C., Wang, J., and Xiong, W. (2018). Retrospection and Perspective for Earthquake Stress Triggering. *Geomatics Inf. Sci. Wuhan Univ.* 43 (12), 2085–2092. doi:10.13203/j.whugis20180149

Xu, X., Han, Z., Yang, X., Zhang, S., Yu, G., Zhou, B., et al. (2016). *Seismic Tectonic Map of China and its Vicinity (In Chinese)*. Beijing, China: Earthquake Press. doi:10.12031/activefault.china.250.2016.db

Xu, X., Wu, X., Yu, G., Tan, X., and Li, K. (2017). Seismo-Geological Signatures for Identifying M≥7.0 Earthquake Risk Areas and Their Premilimary Application in Mainland China. *Seismol. Geol.* 39 (2), 219–275. doi:10.3969/j.issn.0253-4967.2017.02.001

Xu, Y., Guo, X., and Feng, L. (2022). Relocation and Focal Mechanism Solutions of the MS 6.9 Menyuan Earthquake Sequence on January 8, 2022 in Qinghai Province. *Acta Seismol. Sin.* 44 (2), 195–210. doi:10.11939/jass.20220008

Yang, H., Wang, D., Guo, R., Xie, M., Zang, Y., Wang, Y., et al. (2022). Rapid Report of the 8 January 2022 MS 6.9 Menyuan Earthquake, Qinghai, China. *Earthq. Res. Adv.* 2, 100113. doi:10.1016/j.eqrea.2022.100113

Yu, C., Li, Z., Penna, N. T., and Crippa, P. (2018). Generic Atmospheric Correction Model for Interferometric Synthetic Aperture Radar Observations. *J. Geophys. Res. Solid Earth* 123 (10), 9202–9222. doi:10.1029/2017JB015305

Yu, P., Qiao, X., Xiong, W., Chen, W., Nie, Z., Wang, D., et al. (2020). Source Model for the M W 6.0 Earthquake in Jiashi, China on 19 January 2020 from Sentinel-1A InSAR Data. *Earth Planets Space* 72 (1), 1–11. doi:10.1186/s40623-020-01300-4

Zhang, G., Qu, C., Shan, X., Zhang, G., Song, X., Wang, R., et al. (2011). The Coseismic InSAR Measurements of 2008 Yutian Earthquake and its Inversion for Source Parameters. *Chin. J. of Geophys.* 54 (11), 2753–2760. doi:10.3969/j.issn.0001-5733.2011.11.005

Zhang, P., Deng, Q., Zhang, G., Ma, J., Gan, W., Min, W., et al. (2003). Active Tectonic Blocks and Strong Earthquakes in the Continent of China. *Sci. China Ser. D Earth Sci.* 46, 13–24. doi:10.1360/03dz0002

Zhu, L., Dai, Y., Shi, F., and Shao, H. (2022). Coulomb Stress Evolution and Seismic Hazards along the Qilian-Haiyuan Fault Zone. *Acta Seismol. Sin.* 44 (2), 223–236. doi:10.11939/jass.20220012

Conflict of Interest: The authors declare that the research was conducted in the absence of any commercial or financial relationships that could be construed as a potential conflict of interest.

Publisher's Note: All claims expressed in this article are solely those of the authors and do not necessarily represent those of their affiliated organizations, or those of the publisher, the editors and the reviewers. Any product that may be evaluated in this article, or claim that may be made by its manufacturer, is not guaranteed or endorsed by the publisher.

frontiers | Frontiers in Environmental Science

ORIGINAL RESEARCH
published: 22 July 2022
doi: 10.3389/fenvs.2022.933200

Co- and Post-seismic Deformation Mechanisms of the 2020 Mw6.0 Jiashi Earthquake in Xinjiang (China), Revealed by Sentinel-1 InSAR Observations

T. Wang[1], S. N. Zhu[2], C. S. Yang[1], Y. J. Wei[2], C.Y. Zhao[1] and H.C. Hou[1]*

[1]College of Geology Engineering and Geomatics, Chang'an University, Xi'an, China, [2]China Institute of Geo-Environment Monitoring, Beijing, China

OPEN ACCESS

Edited by:
Yu Chen,
China University of Mining and Technology, China

Reviewed by:
Hong'An Wu,
Chinese Academy of Surveying and Mapping, China
Zhiwei Zhou,
Innovation Academy for Precision Measurement Science and Technology, (CAS), China
Jinwoo Kim,
Southern Methodist University, United States

***Correspondence:**
S. N. Zhu
jcyzhusainan@mail.cgs.gov.cn

Specialty section:
This article was submitted to Environmental Informatics and Remote Sensing, a section of the journal Frontiers in Environmental Science

Received: *30 April 2022*
Accepted: *14 June 2022*
Published: *22 July 2022*

Citation:
Wang T, Zhu SN, Yang CS, Wei YJ, Zhao CY and Hou HC (2022) Co- and Post-seismic Deformation Mechanisms of the 2020 Mw6.0 Jiashi Earthquake in Xinjiang (China), Revealed by Sentinel-1 InSAR Observations. Front. Environ. Sci. 10:933200. doi: 10.3389/fenvs.2022.933200

On 19 January 2020, an Mw6.0 earthquake occurred in Jiashi County, Xinjiang, China. This earthquake is a strong earthquake that occurred in the Kepingtage Belt. The monitoring and inversion of the co-seismic and post-earthquake will help further understand the geometry and movement properties of this tectonic belt. In this study, Sentinel-1A images were used to analyze the deformation of co-seismic and post-seismic events. The Okada elastic dislocation model was used to invert the geometric parameters of the fault and co-seismic slip distribution. The results showed that the maximum uplift and maximum subsidence deformations from the ascending images were 55 and 45 mm, respectively. The maximum uplift and subsidence deformations from the descending images were 62 and 28 mm, respectively. The inversion results show that the earthquake was induced by a fault with a length of 23.5 km, width of 4.7 km, and depth of 7.2 km. This earthquake was a typical dip-slip event. The distributed inversion results of post-earthquake deformation show that the maximum co-seismic slip and maximum post-seismic slip are located on the same fault plane, mainly distributed on the edge of the co-seismic fault, between the two faults.

Keywords: jiashi earthquake, co-seismic deformation, post-earthquake deformation, slip distribution, coulomb stress

1 INTRODUCTION

On 19 January 2020, an earthquake with Mw 6.0 occurred in the Jiashi area of Xinjiang, China. The focal depth was 16 km; aftershocks have continued since then. According to the China Earthquakes Networks Centre (CENC), four aftershocks with magnitudes greater than Mw 4.0 occurred around the main shock on the same day, including one Mw 5.2. This earthquake caused one death, two injuries, and damage to more than 4,000 houses. Some roads, bridges, reservoirs, and other facilities were damaged, causing a direct economic loss of 1.62 billion yuan (Ren et al., 2020). The Ministry of Emergency Management of China announced the top ten natural disasters in the country in 2020, and this Jiashi earthquake ranked seventh.

Many scholars conducted research after the earthquake (**Table 1**). Li. et al. (2021) determined the fault model based on the simulated annealing algorithm and used the Steepest Descent Method (SDM) to calculate the slip distribution of the fault. Wen et al. (2020) obtained the co-seismic

TABLE 1 | Focal mechanism solutions of the Jiashi earthquake.

	Mw	Longitude (°E)	Latitude (°N)	Np1 (Strike,Dip, and Rake)	Np2 (Strike,Dip, and Rake)
USGS	Mw6.0	77.108	39.835	221/20/72	60/71/96
GCMT	Mw6.0	77.19	39.80	196/38/31	80/71/124
CENC	Ms6.4	77.21	39.83	-	-
Chen et al. (2021)	-	-	-	270/15/85	-
Zhang et al. (2021)	Mw6.1	77.28	39.90	276/10.7/84.1	-
Zhu et al. (2017)	Mw5.87	-	-	76/81/109	190/21/26

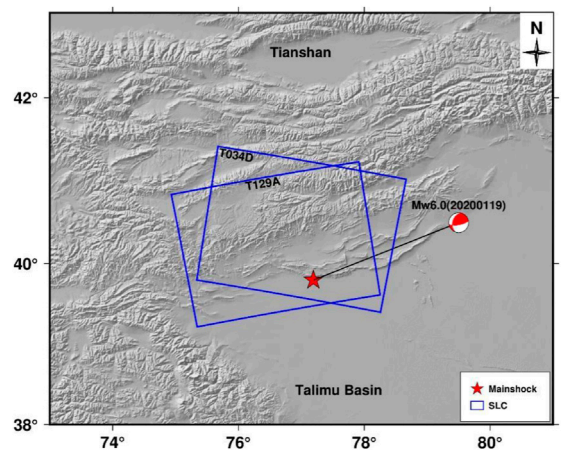

FIGURE 1 | Geological overview of the study area.

deformation field with Interferometric synthetic aperture radar (InSAR) and Global Positioning System (GPS), and the faults of the earthquake were analyzed. Zhang et al. (2021) inverted the parameters of the seismogenic fault and calculated the co-seismic slip distribution based on the triangular dislocation element. Guo et al. (2021) relocated the earthquake and studied the focal mechanism solution. The aforementioned studies used different datasets and methods to monitor earthquakes, and the results were different, these differences are mainly reflected in the magnitude of coseismic deformation, which may be related to the method. However, the evolution of post-earthquake deformation has not been studied. Therefore, we conducted a joint study on co-seismic and post-seismic deformation using InSAR technology and analyzed the impact of the earthquake on the surrounding faults. Concurrently, we analyzed the post-earthquake deformation trend. Our study provided new data for understanding the mechanism of earthquakes and activities of the Kepintag nappe belt.

2 REGIONAL GEOLOGICAL BACKGROUND

The 2020 Jiashi Mw6.0 earthquake is another strong earthquake with a magnitude greater than Mw 6.0, which has occurred in the Jiashi earthquake swarm since 2003. A strong Jiashi earthquake swarm occurred in the northern margin of the Tarim Basin on the northeastern side of the Pamir Plateau, adjacent to the Tianshan arc nappe structural belt to the north (**Figure 1**). The Pamir Plateau is one of the regions with the strongest continental plate dynamics, while the Tianshan Mountains are typical intercontinental collision orogenic belts in the world (Lai et al., 2002). The epicenter was located in the South Tianshan foreland fold-thrust belt, with the Tianshan fold belt in the north, the West Kunlun-Pamir Plateau in the southwest, and the rigid Tarim Basin in the east and south. The Pamir Plateau is the deepest part of the Indian Plate and is wedged into the Eurasian continent. The Tianshan Mountains also experienced strong compression, uplift, folding, and thrust southward, forming a typical Cenozoic orogenic belt in the continental interior (Qiao and Guo, 2007; Zhang, 2003). The relative movement between the South Tianshan Mountains and Tarim Basin resulted in a large stress difference on the tectonic boundary, making the area more seismically active. In the past 20 years, most of the intense activities occurring in the southwestern Tianshan Mountains have been concentrated on the Kepingtage thrust fault (Tu. et al., 2008; Xu et al., 2006). The earthquake occurred in the western segment of the Kepingtage fault zone at the southern foot of the Tianshan Mountains. The Kepingtage Fault is located on the northwestern margin of the Tarim Basin, where there are several rows of arc-shaped thrusting rock ridges extending from EW to NE, forming an arc-shaped structural belt protruding to the southeast (Fang et al., 2009). The Kepingtage Fault is approximately 220 km long and is divided into two segments, east and west, by the SN-trending Piqiang fault zone. The Kepingtage Fault has strong seismic activity, causing the alluvial fan to rupture and form several faults and steep ridges at the foot of the Kepingtag Mountain. This makes the epicenter area present a complex topography with a relative height difference of several kilometers (Guo et al., 2021). Therefore, the tectonic conditions in this area are complex, and the tectonic activities are strong. Research on the mechanism of this earthquake is of great significance for an in-depth understanding of regional fault activity and earthquake prediction.

3 DATA AND PROCESSING

Sentinel-1A images were used to obtain the co-seismic deformation fields. Two images closest to the earthquake were selected to reduce the impact of post-earthquake deformation and decoherence noise on the co-seismic deformation field as much as possible. The pre-earthquake image in the ascending orbit was

TABLE 2 | Detailed parameters of the co-seismic interference pair.

No.	Orbit	Pass Direction	Master Image	Slave Image	Incidence_angle	Perpendicular Baseline
1	T129A	Ascending	2020/01/16	2020/01/28	39.1273	9.410 m
2	T034D	Descending	2020/01/10	2020/01/22	33.6703	−58.273 m

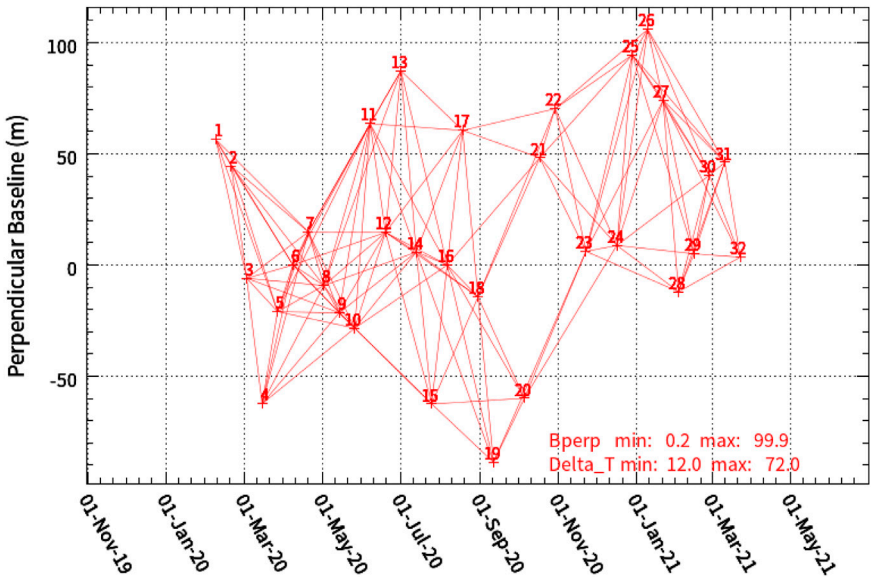

FIGURE 2 | Interferometric combination of post-earthquake deformation field.

obtained on 16 January 2020, and the post-earthquake image was obtained on 28 January 2020. The pre-earthquake image in descending orbit was acquired on 10 January 2020, and the post-earthquake image was acquired on 22 January 2020. The related parameters are listed in **Table 2**. The perpendicular baselines of the interference pair are 9.4 m and -58.3 m, respectively (**Table 2**).

Datasets were processed using the GAMMA software, which supports the whole process of SAR data processing (Werner et al., 2001). Differential interferometry (D-InSAR) was used to obtain the co-seismic deformation field (Massonnet et al., 1993; Shan, 2002), and the terrain phase was removed using the Shuttle Radar Topography Mission 30 m digital elevation model. We used precise orbital data to correct orbital deviation (https://s1qc.asf.alaska.edu/aux_poeorb/). The multi-look ratio in the range and azimuth was 8:2 to reduce noise in the interferogram. Because the phase in the original interferogram is wrapped, we adopted the minimum cost flow (MCF) method based on the Delaunay triangulation for phase unwrapping (Eineder et al., 1998; Werner and Wegmuller, 2002). Finally, we removed the terrain-related atmospheric delay error using the terrain correlation method.

Since the post-earthquake images from descending orbit have not been updated after 10 March 2020, they cannot meet the parameters required for long-term surface deformation monitoring. Therefore, we only collected Sentinel-1 SAR images from the ascending orbit to monitor post-earthquake deformation. A total of 32 images, covering the study area from 9 February 2020 to 23 March 2021, were processed using SBAS-InSAR. The SBAS-InSAR technology can generate a series of interferograms by setting temporal and spatial baseline thresholds. SBAS-InSAR technology not only ensures the quality of the interferograms but also increases the density of the coherent points. Differential processing and phase unwrapping are performed on high-quality interferograms, and finally, each subset is jointly solved by singular value decomposition (SVD) to obtain the time-series deformation (Berardino et al., 2002; Zhu, et al., 2017; Chen, et al., 2020). Interferograms were also multi-looked at a ratio of 8:2 in range and azimuth for post-earthquake deformation field monitoring. The spatial and vertical baselines were set at ±100 m and 80 days, respectively. The interference combinations are shown in **Figure 2**. Image registration was performed using amplitude-based image registration (Chen, et al., 2021). Gaussian filtering was applied to the interferograms to reduce noise and improve their coherence. Interferograms were unwrapped using the same method as that used for co-seismic deformation. A terrain-based correlation method was used to estimate and remove the atmospheric delay phase. Simultaneously, the trend error was estimated and eliminated based on a quadratic polynomial fitting

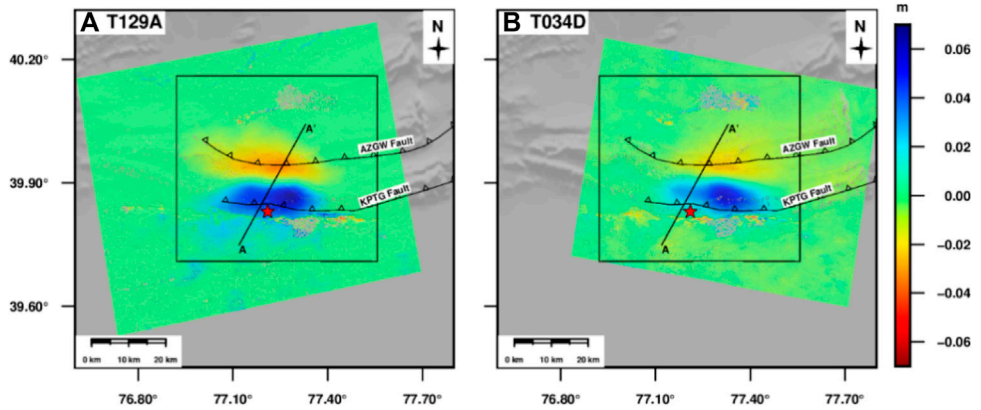

FIGURE 3 | Co-seismic displacement field of Jiashi earthquake. **(A)** is from ascending interferogram (T129A); **(B)** is from descending interferogram (T034D).

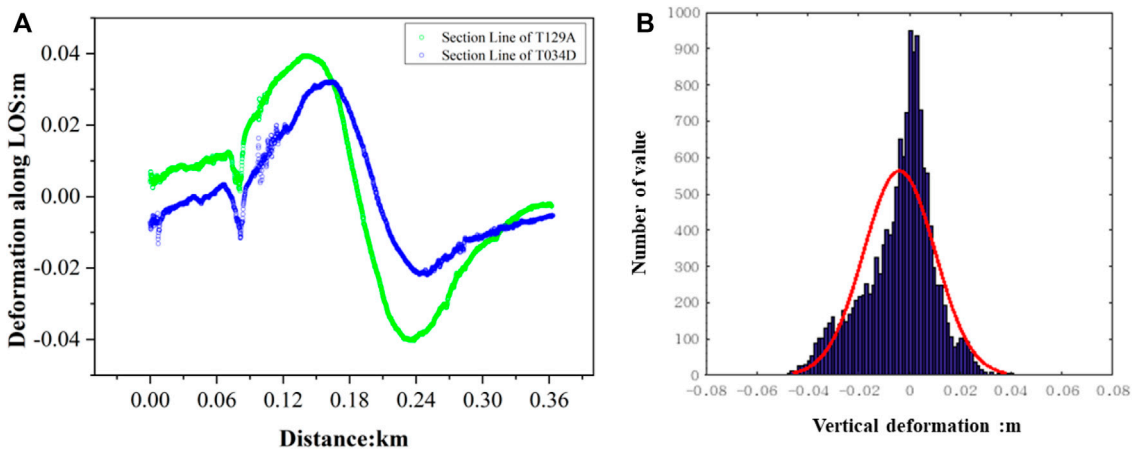

FIGURE 4 | Co-seismic displacement profile of AA′ from T129A and T034D, and residual distribution of the co-seismic deformation field.

model. Finally, interferograms with smaller atmospheric and unwrapping errors were selected and post-seismic deformation was obtained.

4 CO- AND POST-SEISMIC DEFORMATION ANALYSIS

4.1 Co-seismic Deformation Field

We obtained the co-seismic deformation field according to the above method (**Figure 3**). There are two thrust faults in this area (as shown in **Figure 3**): the Kepintag Fault and Ozgertawu Fault. Based on the monitoring results, the co-seismic deformation field was relatively integral and there was no sign of decoherence. This means that the fault did not rupture at the surface. The two deformation fields have the same situation, which is more consistent with others (Li, et al., 2021; Wen,et al., 2020; Wenting et al., 2020). The maximum uplift deformation in the line of sight (LOS) from the ascending images was 55 mm, and the maximum subsidence was 45 mm. The descending co-seismic deformation field showed that the maximum uplift and subsidence were 62 and 28 mm (**Figure 2**), respectively.

We extracted a profile for the co-seismic deformation, and the results are shown in **Figure 4A**. We observed that the deformation trends along the profile were similar. There was a slight difference in magnitude. We adopted an internal coincidence accuracy evaluation method to verify the accuracy of the results. First, we selected the public area of the deformation field and converted the deformation in the LOS to vertical deformation according to the incidence of each pixel. Then, the results from the descending images in the vertical direction subtracted those from the ascending images, and statistical analysis was performed on the difference. The results are shown in **Figure 4B**. The difference conforms to a normal distribution, and the standard deviation is 11 mm.

4.2 Post-earthquake Deformation Field

The period of an earthquake can be divided into three stages: interseismic, co-seismic, and post-seismic (Salvi et al., 2012). Interseismic refers to the relative motion of plates between

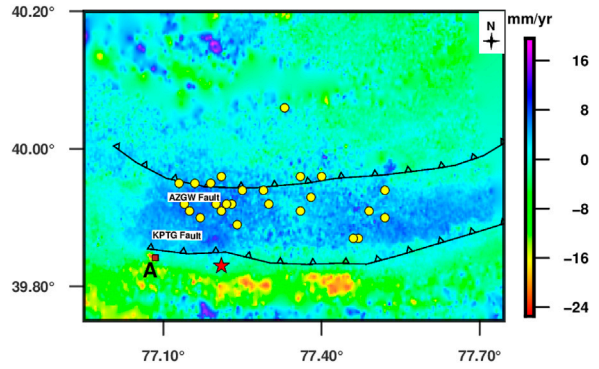

FIGURE 5 | Post-earthquake deformation rate. Yellow circles: aftershock, red star: epicenter, rectangle: selected point, KPTG and AZGW: two faults.

two earthquakes. This is the process of accumulating energy when the fault is in a locked state. If the energy accumulation of the faults reaches a maximum, the fault reaches the critical rupture condition. At this time, an earthquake occurs and the accumulated energy is gradually released. Post-earthquake deformation is the response and adjustment of the crust and upper mantle to change and can directly reflect the rheological properties of the lithosphere. The temporal and spatial distribution of post-earthquake data varies greatly, and the time scale can range from a few days to a few months to hundreds of years (Bürgmann et al., 2001; Gourmelen and Amelung, 2005). Its spatial scale can span a few kilometers near a seismogenic fault (Jónsson et al., 2003) or across a global scale (Casarotti et al., 2001). Three models are usually used to describe post-earthquake deformation: afterslip (Harrington and Brodsky, 2006), the coupling effect between the lower crust and the upper mantle with viscoelastic relaxation properties (Pollitz et al., 2000), and the pore rebound effect of the crustal porous medium (Peltzer et al., 1996). After an earthquake, all three deformation mechanisms may exist and function in different spaces and times. The afterslip occurs because after the earthquake, the fault continues to slide in the direction of co-seismic due to inertia; afterslip plays a role in a short time after the earthquake. Poroelastic rebound is the same as afterslip, mainly occurring in the upper crust, and the deformation trend is opposite to that of co-seismic (Pollitz et al., 2000; Jónsson et al., 2003). The viscoelastic relaxation effect was caused by the stress change between the lower mantle and the upper crust. The viscoelastic relaxation effect plays a role for a long time after an earthquake, and the effect in the far-field is more substantial (Pollitz et al., 2000). Therefore, we believe that the short-term viscoelastic relaxation effect was not the post-seismic deformation mechanism of this earthquake.

After an earthquake, the energy accumulated is often released slowly during the main shock and post-seismic events, squeezing the surrounding faults, and deforming the surrounding fractures, resulting in aftershocks. To analyze the influence of the post-earthquake on the surrounding faults, we used the SBAS-InSAR to obtain the deformation field after the earthquake, since the epicenter of the earthquake was relatively close to the Kepintag and Ozgwu faults (**Figure 5**). The time span of post-earthquake images is from 9 February 2020, to 23 March 2021. During the 447 days, the results showed that the overall uplift was dominant between the Kepingtage fault and the Ozgwu fault, with a maximum uplift of 8 mm (**Figure 5**). However, south of the Kepingtage fault is in a subsidence state, indicating that the blocks between the two faults are in a state of compression. Simultaneously, post-earthquake deformation mainly occurs on the fault, which belongs to the stress change caused by co-seismic rupture. The post-seismic deformation trend was the same as that of the co-seismic deformation, so the poroelastic rebound effect was excluded. Therefore, we initially believe that the post-earthquake deformation mechanism was an afterslip. In addition, aftershocks were distributed in the area with a larger deformation (**Figure 5**). We selected a point (square in **Figure 5**) in the region with significant deformation characteristics to extract the post-earthquake deformation time series (**Figure 6**). We used a post-earthquake afterslip model function to fit the post-earthquake deformation time series at this point (Barnhart et al., 2018)

$$y = a \times log_{10}(1 + t) \quad (1)$$

where y is the accumulated deformation in the LOS(m), t is the time interval from the mainshock after the earthquake, and a represents the coefficient of the logarithmic function.

The results show that when a = -0.01264 and t = 240 days after the main shock, the fitting results agree with the post-earthquake deformation time series results. The post-earthquake deformation trend is consistent with co-seismic deformation. Based on the extracted post-earthquake deformation time series, we believe that the post-earthquake deformation mechanism of the Jiashi earthquake was an afterslip.

5 INVERSION AND ANALYSIS OF FAULT

The inversion of co-seismic deformation is one of the important means to improve the understanding of seismogenic structures

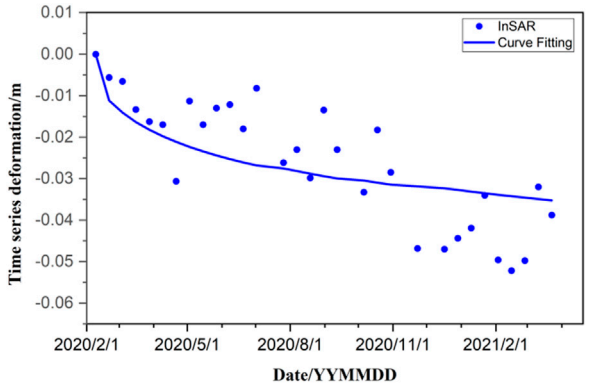

FIGURE 6 | Post-earthquake deformation time series and a fitting result at point A.

TABLE 3 | Fault parameters for uniform slip inversion.

	Optimal	Mean	Median	2.5%	97.5%
Fault Length (km)	23.461	23.373	23.368	22.413	24.361
Fault Width (km)	4.65	4.891	4.729	4.005	5.450
Fault Depth (km)	7.192	7.125	7.133	6.798	7.385
Fault Dip (°)	10.245	10.78	10.604	8.228	13.6489
Fault Strike (°)	266.379	266.328	266.323	265.49	267.193
Str-slip (m)	−0.182	−0.161	−0.162	−0.225	−0.095
Dip-slip (m)	0.586	0.539	0.548	0.43637	0.612

seismogenic fault as a rectangle embedded in a uniform elastic half-space model. In the inversion, the parameter was set to a length of 1–80 km, width of 3–80 km, depth of 5–80 km, strike angle of 90°–360°, and dip angle of 0–90°, with the strike-slip and dip-slip being -2 and 2 m, respectively. The Monte Carlo search method was used to search, and the best fitting value of each parameter of the fault was obtained, including the optimal and average values. The inversion results are presented in **Table 3**. **Figure 7** shows InSAR observations, models, and residuals. It can

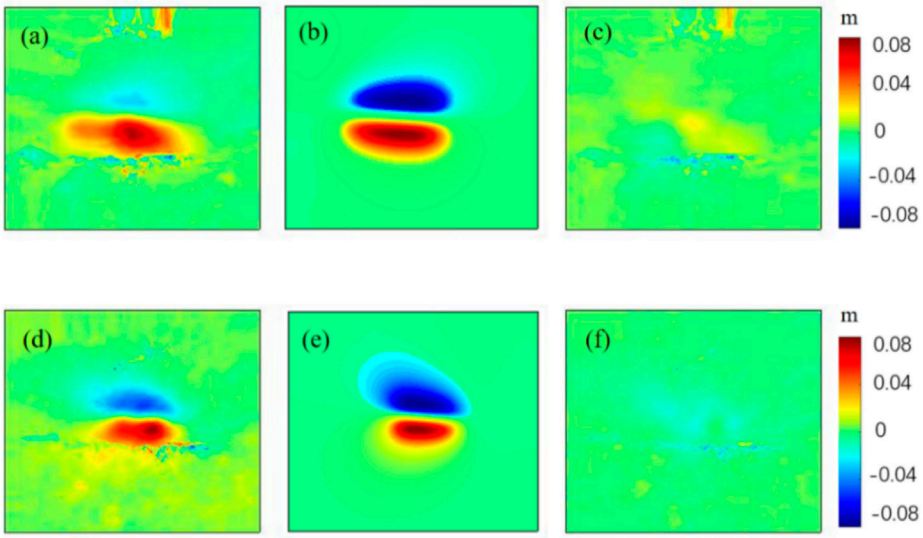

FIGURE 7 | Comparison of non-linear inversion results. **(A)**, **(B)**, **(C)** are observation ,model,residual from T064A respectively **(D)**, **(E)**, **(F)** are observation ,model, residual from T034D respectively.

and to evaluate regional earthquake disasters. In this paper, the Okada elastic dislocation model is used to study the co-seismic deformation. The inversion is divided into two parts. First, we assumed that the slip was uniform, and the Geodetic Bayesian Inversion Software (GBIS) was used to search for the source parameters. The fault is further divided into patches after the geometric parameters of the fault are obtained and the slip of each patch is calculated.

5.1 Co-seismic Uniform Slip Inversion

The inversion for this earthquake was implemented using the Okada elastic dislocation model in the open-source software GBIS (Bagnardi and Hooper, et al., 2018). It is necessary to downsample the InSAR data before inversion to improve efficiency. We adopted the quadtree sampling method, which can retain more points in the region with large deformation and retain fewer points in the region with smaller deformation. Co-seismic deformation inversion was then performed by setting the source parameters of the fault. The parameters included length, width, depth, strike angle, dip angle, strike-slip, and dip-slip. The Okada elastic dislocation model is equivalent to treating a

be seen that the model results reflect the InSAR observations well, and there are residuals at some epicenter points. The inversion results showed that the dip-slip was considerably larger than the strike-slip, and that the seismogenic fault was dominated by a dip-slip. The depth of the epicenter is 7.2 km, which is greater than the width 4.65 km of the fault, indicating that the seismogenic fault does not appear exposed to the surface.

5.2 Co-seismic Slip Distribution Inversion

The co-seismic deformation field can only grasp the destructiveness, damage range, and magnitude of the earthquake but cannot determine the geological structure of the earth's internal faults and the direction information of the seismogenic faults. Therefore, to analyze the geological structure of this earthquake, we used the SDM inversion program (Wang, et al., 2013a; Wang, et al., 2013b) to calculate the slip distribution of faults using the Okada elastic half-space dislocation model (Xu et al., 2010; Motagh et al., 2015). During the inversion, a co-seismic deformation field was used as the constraint, and an initial fault geometric model was established according to the GBIS inversion. Simultaneously, the fault was appropriately

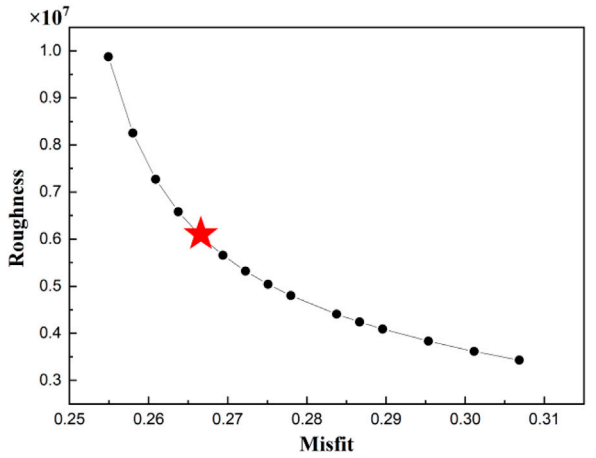

FIGURE 8 | Roughness and fitting residual curve.

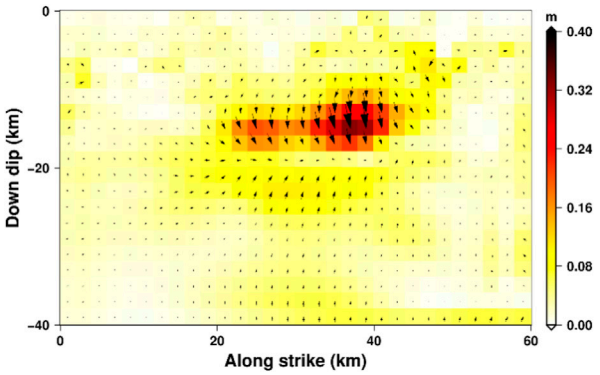

FIGURE 10 | Two-dimensional slip distribution. The arrow indicates the movement direction of the block.

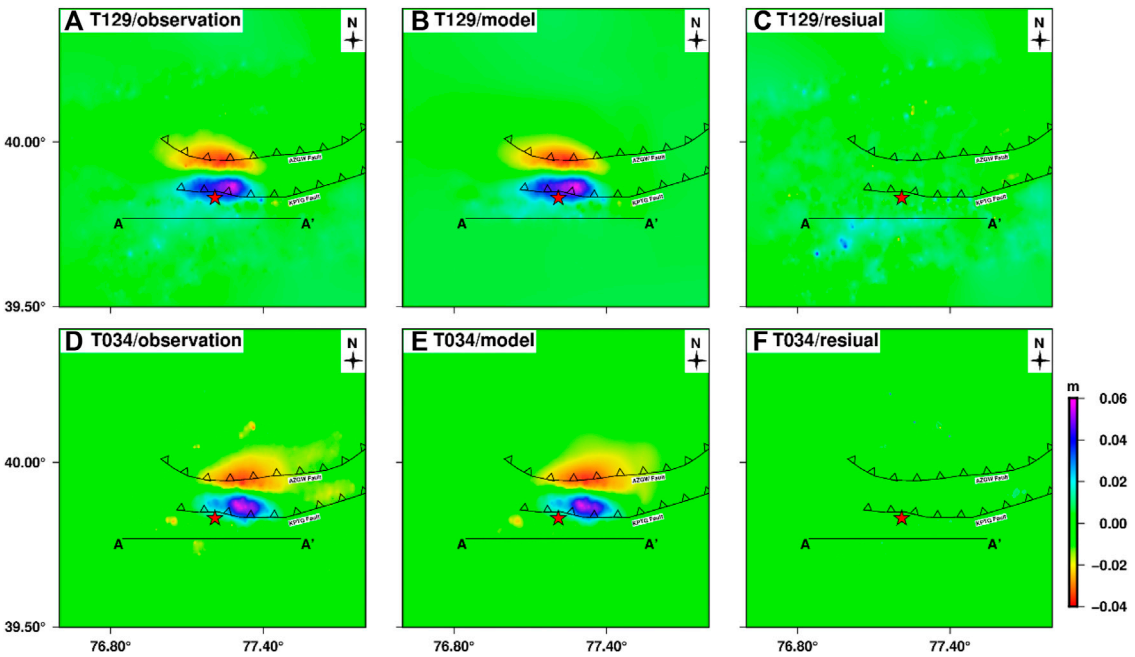

FIGURE 9 | Distributed slip inversion results. **(A)**, **(B)**, and **(C)** are observation, model, and residual, respectively, of T129A; **(D)**, **(E)**, and **(F)** are observation, model, residual, respectively, of T034D.

extended along the strike and dip, and the seismogenic fault was set to 60 km × 40 km. We divided the fault into 2 × 2 km patches along the strike and dip, with a total of 600 patches. The smoothing factor was determined by weighing the compromise curve between the roughness and the residual. Finally, a smoothing factor of 0.05 was selected as the optimal result (**Figure 8**). The distributed slip inversion is shown in **Figure 9**. The fitting result between the observation and the model was 96.2%, indicating our optimal model can fit the fault geometry reasonably well. Compared with others, the rectangular dislocation model can inverse this co-seismic deformation well. The residuals of the distributed slip inversion were considerably reduced compared with the uniform slip distribution inversion. **Figure 9** indicates that the ruptures are concentrated 22–46 km along the strike and 10–18 km along the dip. The average slip angle was −176.29°, the average slip was 0.04 m, and the magnitude was Mw6.1, indicating the co-seismic fault to be a reverse fault with a small strike-slip motion (**Figure 10**). According the focal mechanism solution from **Table 1**, this earthquake belongs to thrust type, indicating that our result is

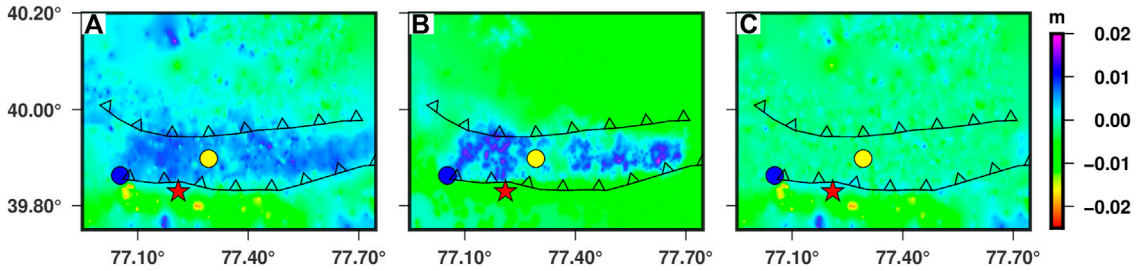

FIGURE 11 | Post-earthquake deformation inversion results. **(A)**, **(B)**, and **(C)** are observation, model, and residual, respectively. Yellow circles represent the largest co-seismic slip, and blue circles represent the largest post-earthquake slip.

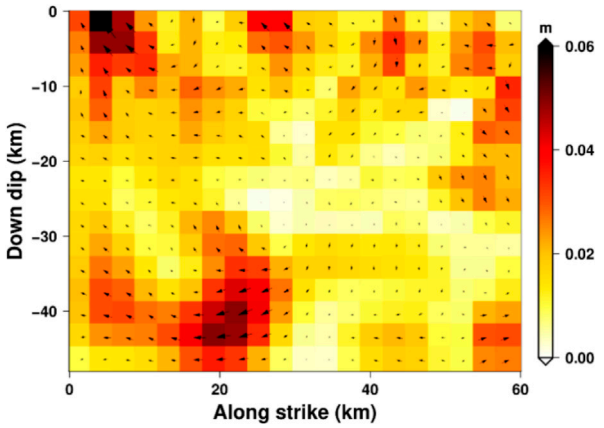

FIGURE 12 | Two-dimensional slip distribution results of faults after earthquake.

consistent with the USGS and GCMT. As shown in **Figure 10**, the epicenter of the Jiashi earthquake was located on the Kepingtag fault. We believe that this was a dip-slip earthquake that occurred on the Kepingtag nappe belt.

5.3 Post-earthquake Deformation Inversion

Figure 4 shows that the post-earthquake deformation and aftershocks are mainly concentrated between the Keping and Ozgwu faults and are located near the seismogenic fault. We used the SDM method to invert the accumulated deformation within 447 days after the earthquake to further analyze the post-earthquake deformation mechanism. According to the post-earthquake deformation, we set the fault length to 60 km and width to 48 km, to invert the post-earthquake slip distribution. The InSAR observations, model, and residuals are shown in **Figures 11A**,**B**,**C**, respectively. From the inversion, the simulation effect of the main deformation region after the earthquake was good and the residual was relatively small. Some minor deformations have not been simulated south of the Ozgwu Fault. Larger residuals were mainly distributed in the northwest corner (**Figure 11**), which may be related to the viscoelastic relaxation effect or tectonic movement changes. **Figure 12** shows the post-earthquake two-dimensional slip distribution. Several slip patches were found in the shallow fault layer. The first slip is located to the west of the Keping fault, approximately 14 km from the epicenter, 0–12 km along the strike, and 0–9 km along the dip, and the slip is 0.06 m. The second slip was located to the north of the epicenter, far from the epicenter, 15–24 km along the strike, and 36–45 km along the dip, and the slip reaches 0.05 m. These phenomena indicate that the post-earthquake geological tectonic activity in this area was only more active in these two places, and the magnitude was also small. Regional tectonic activity gradually stabilized after the earthquake, and further earthquakes were less likely.

Comparing the results of the co-seismic and post-earthquake slip distributions, the maximum slip of the co-seismic is 0.32 m and post-earthquake depth is 3.88 km. The maximum slip of post-earthquake is 0.06 m and the depth is 0.31 km. The maximum slip of co-seismic and the post-earthquake occurred on the same fault plane and were separated by 20 km. The post-earthquake deformation mechanism exhibits thrust and strike-slip, while co-seismic belongs to thrust. Similar mechanisms exist, but the co-seismic and post-seismic maximum slip patches are located at different locations on the same fault plane, suggesting that the post-seismic motion is likely driven by stress concentrations at the co-seismic patch edges (Amiri et al., 2020).

6 DISCUSSION

6.1 Earthquake Analysis

Presently, the greater the intensity and frequency of intermediate seismic activity in the western Himalayan tectonic structure, the more intense the strong earthquake activity in the Tianshan seismic belt. The active periods of several strong earthquakes in the history of the Tianshan area show migration from west to east (Zhang and Shao, 2014). This indicates that there is a dynamic relationship between the strong earthquake of the western Himalayan tectonic structure and the strong activity of the Tianshan seismic belt in Xinjiang, China, i.e., the West Himalayan tectonic knot has a triggering effect on the seismic activity of the Tianshan seismic belt. The earthquake occurred in the South Tianshan foreland fold-thrust belt, which is located northeast of the Pamir Plateau. The Pamir Plateau structure is mainly affected by the combined action of the northward subduction of the Indian plate and the southward subduction of the Tianshan Mountains (Sippl et al., 2013), indicating that the

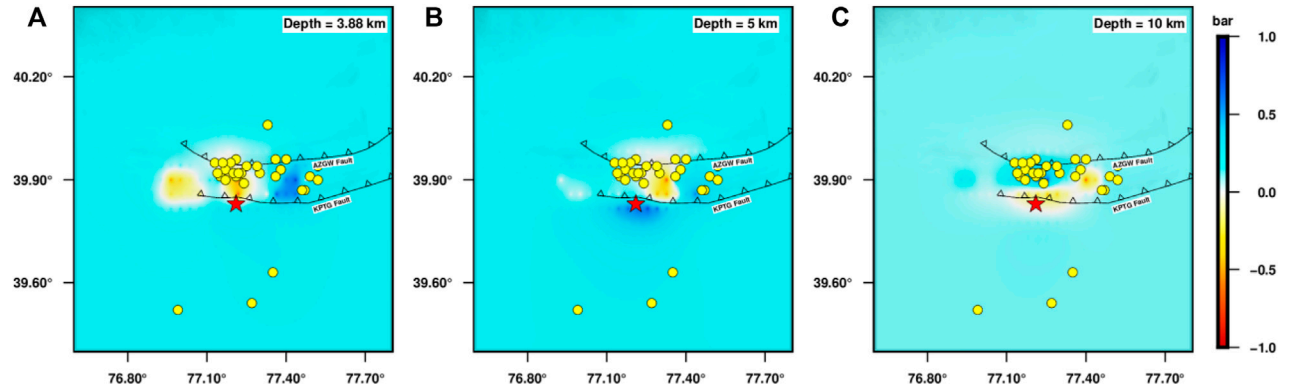

FIGURE 13 | Coulomb stress distribution at different depths. Red star: epicenter, yellow circle: the aftershock. Aftershock data was obtained from CENC.

Tianshan Block is thrust over the Tarim Basin. In such tectonic environments, moderate and strong earthquakes occur frequently in the Jiashi area. The Jiashi Mw6.0 earthquake occurred in an area with substantial thrusting movement and was an inevitable rupture event under a prominent tectonic background with a typical thrusting movement.

6.2 Coulomb Stress

The rupture of a co-seismic fault causes the redistribution of the surrounding stress. Based on Coulomb3.3 (Lin and Stein, 2004; Toda et al., 2005), we assumed that the shear modulus was 3.2×10^4 MPa; moreover, the friction coefficient was set to 0.4, and the Poisson's ratio was 0.25. Combined with the co-seismic slip distribution, we calculated Coulomb stress changes (**Figure 13A**). Simultaneously, taking the thrust fault as the receiver faults, the Coulomb stress was calculated at depths of 5 and 10 km (**Figures 13B,C**). If the Coulomb stress is positive, it is called the stress-loading area, and the corresponding risk increases. Conversely, if the Coulomb rupture stress is negative, fault rupture will be suppressed. The negative area is called the "stress shadow area," wherein the possibility of triggering an earthquake will be weakened (Yongge et al., 2002). However, this is an ideal scenario. The Coulomb stress distribution is more complicated and is generally affected by the fault geometry, crust, Green's function, and errors in observational data. Therefore, the calculation results of the Coulomb stress should be analyzed in detail. The result indicated that the co-seismic coulomb stress distribution was negative near the epicenter, suggesting that it was in a state of stress release. As the depth of projection increases, the stress range decreases gradually. The Coulomb stress at a depth of 5 km was in a state of stress loading near the epicenter, and the positive value of stress loading was around the Kepintag fault (**Figure 13B**). The depth was 10 km, and the stress loading was relieved. The Coulomb stress distribution is in good agreement with the shallow fault deformation mechanism, which may be related to various factors such as the actual fault geometry and formation properties.

7 CONCLUSION

We used Sentinel-1A images and D-InSAR to obtain the co-seismic deformation field of the 2021 Jiashi earthquake. The monitoring results show that the maximum uplift caused by the earthquake is 62 mm, located south of the epicenter, with a maximum subsidence of -45 mm, located north of the epicenter. The inversion of the Okada elastic uniform half-space model shows that the earthquake was induced by a length of 23.5 km, a width of 4.7 km, and a depth of 7.2 km. At the same time, the dip-slip component is larger than the strike-slip component, indicating that the seismic fault plane is dominated by dip-slip. The co-seismic slip distribution showed that the magnitude was Mw6.1, the main slip was concentrated at 22–46 km along the strike and 10–18 km along the dip, and the average slip angle was -176.29°. The regional fault is thrust with a small strike-slip component, which is consistent with the focal mechanism solution results given by the USGS, GCMT, and other institutions. Post-earthquake deformation monitoring based on SBAS InSAR technology showed that the post-earthquake deformation rate was 25 mm/yr within 447 days. The nature of the movement between them is uplifting deformation, and the post-earthquake deformation mechanism is afterslip.

DATA AVAILABILITY STATEMENT

The original contributions presented in the study are included in the article/Supplementary Material, further inquiries can be directed to the corresponding author.

AUTHOR CONTRIBUTIONS

SZ and CY conceived and designed the experiments; TW performed the experiments and drafted the manuscript. HH processed Sentinel-1A images. YW provided some suggestions of writing. CZ contributed to the InSAR and earthquake analysis.

FUNDING

This research was financed by the National Natural Science Foundation of China (NSFC) (No. 42174032), the Fundamental Research Funds for the Central Universities (CHD300102262206).

ACKNOWLEDGMENTS

We acknowledge the European Space Agency (ESA) for freely making available the Sentinel-1A data. Maps were prepared using the Generic Mapping Tools (GMT), Matlab and Origin software.

REFERENCES

Amiri, M., Mousavi, Z., Atzori, S., Khorrami, F., Aflaki, M., Tolomei, C., et al. (2020). Studying Postseismic Deformation of the 2010–2011 Rigan Earthquake Sequence in SW Iran Using Geodetic Data. *Tectonophysics* 795, 228630. doi:10.1016/j.tecto.2020.228630

Bagnardi, M., and Hooper, A. (2018). Inversion of Surface Deformation Data for Rapid Estimates of Source Parameters and Uncertainties: A Bayesian Approach. *Geochem. Geophys. Geosyst.* 19, 2194–2211. doi:10.1029/2018gc007585

Barnhart, W. D., Brengman, C. M. J., Li, S., and Peterson, K. E. (2018). Ramp-flat Basement Structures of the Zagros Mountains Inferred from Co-seismic Slip and Afterslip of the 2017 Mw7.3 Darbandikhan, Iran/Iraq Earthquake. *Earth Planet. Sci. Lett.* 496, 96–107. doi:10.1016/j.epsl.2018.05.036

Berardino, P., Fornaro, G., Lanari, R., and Sansosti, E. (2002). A New Algorithm for Surface Deformation Monitoring Based on Small Baseline Differential SAR Interferograms. *IEEE Trans. Geosci. Remote Sens.* 40, 2375–2383. doi:10.1109/tgrs.2002.803792

Bürgmann, R., Kogan, M. G., Levin, V. E., Scholz, C. H., King, R. W., and Steblov, G. M. (2001). Rapid Aseismic Moment Release Following the 5 December, 1997 Kronotsky, Kamchatka, Earthquake. *Geophys. Res. Lett.* 28, 1331–1334. doi:10.1029/2000GL012350

Casarotti, E., Piersanti, A., Lucente, F. P., and Boschi, E. (2001). Global Postseismic Stress Diffusion and Fault Interaction at Long Distances. *Earth Planet. Sci. Lett.* 191, 75–84. doi:10.1016/s0012-821x(01)00404-6

Chen, B., Li, Z., Yu, C., Fairbairn, D., Kang, J., Hu, J., et al. (2020). Three-dimensional Time-Varying Large Surface Displacements in Coal Exploiting Areas Revealed through Integration of SAR Pixel Offset Measurements and Mining Subsidence Model. *Remote Sens. Environ.* 240, 111663. doi:10.1016/j.rse.2020.111663

Chen, B., Mei, H., Li, Z., Wang, Z., Yu, Y., and Yu, H. (2021). Retrieving Three-Dimensional Large Surface Displacements in Coal Mining Areas by Combining SAR Pixel Offset Measurements with an Improved Mining Subsidence Model. *Remote Sens.* 13 (13), 2541. doi:10.3390/rs13132541

Eineder, M., Hubig, M., and Milcke, B. (1998). "Unwrapping Large Interferograms Using the Minimum Cost Flow Algorithm," in Proceedings of the IEEE International Geoscience & Remote Sensing Symposium, Seattle, WA, USA, 6-10 July 1998. doi:10.1109/igarss.1998.702806

Fang, M. L., Wang, S. H., Han, X. Q., and Zhao, S. Q. (2009). Trend Connection and Genetic Analysis of Cenozoic Nappe Rock Sheets in Keping. *Xinjiang. China Geol.* 36, 322–333. (in Chinese).

Gourmelen, N., and Amelung, F. (2005). Postseismic Mantle Relaxation in the Central Nevada Seismic Belt. *Science* 310, 1473–1476. doi:10.1126/science.1119798

Guo, Z., Gao, X., and Lu, Z. (2021). Relocation and Focal Mechanism of the Jiashi M6.4 Earthquake on January 19, 2020, in Xinjiang [J]. *Earthq. Geol.* 43, 345–356. (in Chinese).

Harrington, R. M., and Brodsky, E. E. (2006). The Absence of Remotely Triggered Seismicity in Japan. *Bull. Seismol. Soc. Am.* 96, 871–878. doi:10.1785/0120050076

Jónsson, S., Segall, P., Pedersen, R., and Björnsson, G. (2003). Post-Earthquake Ground Movements Correlated to Pore-Pressure Transients. *Nature* 424, 179–183. doi:10.1038/nature01776

Lai, Y. G., Liu, Q. Y., Chen, J. H., Guo, S., and Li, S. C. (2002). Shear Wave Splitting and Stress Field Characteristics in the Strong Earthquake Cluster in Jiashi, Xinjiang. *Chin. J. Geophys.* 01, 83.

Li, C. L., Zhang, G. H., Shan, X. J., Qu, C. Y., Gong, W. Y., Jia, R., et al. (2021). Advances in Geophysics InSAR Coseismic Deform. Field Fault SLIP Distrib, 6.4 Earthquake in Jiashi County, Xinjiang on January 19, 2020. *Inversion Ms* 36, 481–488. (in Chinese).

Lin, J., and Stein, R. S. (2004). Stress Triggering in Thrust and Subduction Earthquakes and Stress Interaction between the Southern San Andreas and Nearby Thrust and Strike-Slip Faults. *J. Geophys. Res.* 109, B02303. doi:10.1029/2003jb002607

Massonnet, D., Rossi, M., Carmona, C., Adragna, F., Peltzer, G., Feigl, K., et al. (1993). The Displacement Field of the Landers Earthquake Mapped by Radar Interferometry. *Nature* 364, 138–142. doi:10.1038/364138a0

Motagh, M., Bahroudi, A., Haghighi, M. H., Samsonov, S., Fielding, E., and Wetzel, H.-U. (2015). The 18 August 2014 Mw 6.2 Mormori, Iran, Earthquake: A Thin-Skinned Faulting in the Zagros Mountain Inferred from InSAR Measurements. *Seismol. Res. Lett.* 86, 775–782. doi:10.1785/0220140222

Peizhen, Z. (2003). Late Cenozoic Tectonic Deformation of Tianshan and its Foreland Basins. *Sci. Bull.* 48, 2499–2500. (in Chinese). doi:10.1007/BF02900310

Peltzer, G., Rosen, P., Rogez, F., and Hudnut, K. (1996). Postseismic Rebound in Fault Step-Overs Caused by Pore Fluid Flow. *Science* 273, 1202–1204. doi:10.1126/science.273.5279.1202

Pollitz, F. F., Peltzer, G., and Bürgmann, R. (2000). Mobility of Continental Mantle: Evidence from Postseismic Geodetic Observations Following the 1992 Landers Earthquake. *J. Geophys. Res.* 105, 8035–8054. doi:10.1029/1999jb900380

Qiao, X. J., and Guo, L. M. (2007). SAR Observational Study of Strong Earthquake Cluster in Jiashi, Xinjiang. *Geod. Geodyn.* 27, 7–13. (in Chinese).

Ren, J., Yalikun, A., Li, Z. Q., Wen, H. P., and Li, X. L. (2020). Accuracy Analysis of Rapid Damage Assessment for Ms6.4 Earthquake in Jiashi, Xinjiang, on January 19, 2020. *Earthq. Disaster Prev. Technol.* 15, 349–358. (in Chinese). doi:10.11899/zzfy20200212

Salvi, S., Stramondo, S., Funning, G. J., Ferretti, A., Sarti, F., and Mouratidis, A. (2012). The Sentinel-1 Mission for the Improvement of the Scientific Understanding and the Operational Monitoring of the Seismic Cycle. *Remote Sens. Environ.* 120, 164–174. doi:10.1016/j.rse.2011.09.029

Shan, X. J., Ma, J., Wang, C. L., Liu, J. H., Song, X. X., and Zhang, G. F. (2002). Extraction of the Focal Fault Parameters of the Mani Earthquake by Using the Surface Deformation Field Obtained by the Spaceborne D-INSAR Technology. *Sci. China D.* 32, 837–844. (in Chinese).

Sippl, C., Schurr, B., Yuan, X., Mechie, J., Schneider, F. M., Gadoev, M., et al. (2013). Geometry of the Pamir-Hindu Kush Intermediate-depth Earthquake Zone from Local Seismic Data. *JGR Solid Earth* 118, 1438–1457. doi:10.1002/jgrb.50128

Toda, S., Stein, R. S., and Richards Dinger, K. (2005). Forecasting the Evolution of Seismicity in Southern California: Animations Built on Earthquake Stress Transfer. *J. Geophys. Res.* 110. B05S16. doi:10.1029/2004JB003415

Tu, H. W., Wan, X. H., Gao, G., Luo, G. F., Hu, Y. J., and Ma, Z. (2008). Preliminary Study on Fault Properties and Stress Field Changes during the Jiashi Earthquake in Xinjiang from 1977 to 2006. *Prog. Geophys.* 23, 1038–1044. (in Chinese).

Wan, Y. G., Wu, Z. L., Zhou, G. W., Huang, J., and Qin, L. X. (2002). Research on Earthquake Stress Triggering. *Acta Seismol. Sin.* 2002 (5), 533–551.

Wang, R. J., Diao, F., and Hoechner, A. (2013a). SDM-A Geodetic Inversion Code Incorporating with Layered Crust Structure and Curved Fault Geometry. *EGU General Assem.*, 2013–2411.

Wang, R., Parolai, S., Ge, M., Jin, M., Walter, T. R., and Zschau, J. (2013b). The 2011 Mw 9.0 Tohoku Earthquake: Comparison of GPS and Strong-Motion Data. *Bull. Seismol. Soc. Am.* 103, 1336–1347. doi:10.1785/0120110264

Wen, S. Y., Li, C. L., Li, J., et al. (2020). Inland Earthquakes. Preliminary Discussion on. InSAR Coseismic Deform. *Field Charact. Seismogenic Struct. Ms6.4 Jiashi Earthq. Xinjiang January 19* 34, 1–9. (in Chinese). doi:10.16256/j.issn.1001-8956.2020.01.001

Werner, C., Wegmuller, U., and Strozzi, T. (2002). "Processing Strategies for Phase Unwrapping for INSAR Applications," in Proceedings EUSAR, Cologne, June 4–6, 2002.

Werner, C., Wegmüller, U., Strozzi, T., and Wisemann, A. (2001). "Gamma SAR and Interferometric Processing Software," in Proceedings of the ERS ENVISAT Symposium, Gothenburg, Sweden, 16-20 October 2001.

Wessel, P., Luis, J. F., Uieda, L., Scharroo, R., Wobbe, F., Smith, W. H. F., et al. (2019). The Generic Mapping Tools Version 6. *Geochem. Geophys. Geosyst.* 20, 5556–5564. version 6. 20. doi:10.1029/2019gc008515

Xu, C., Liu, Y., Wen, Y., and Wang, R. (2010). Coseismic Slip Distribution of the 2008 Mw 7.9 Wenchuan Earthquake from Joint Inversion of GPS and InSAR Data. *Bull. Seismol. Soc. Am.* 100, 2736–2749. doi:10.1785/0120090253

Xu, X. W., Zhang, X. K., Ran, Y. K., Cui, X. F., Ma, W. T., Sheng, J., et al. (2006). A Preliminary Study on the Seismogenic Structure of the Bachu-Jishi Earthquake (Ms6.8) in the Southern Tianshan Area. *Earthq. Geol.* 28, 161–178. (in Chinese).

Zhang, L. P., and Shao, Z. G. (2014). Analysis on Correlativity between Large Earthquakes in the Hindu Kush-Pamir and Tienshan Seismic Zone. *Earthq. Res. China.* 28, 177–187.

Zhang, W. T., Ji, L. Y., Zhu, L. Y., et al. (2021). A Typical Thrust Rupture Event Occurring in the Foreland Basin of the Southern Tianshan: The 2020 Xinjiang Jiashi MS 6. 4 Earthquake. *Seismol. Geol.* 43, 394–409. (in Chinese).

Zhu, J. J., Li, Z. W., and Hu, J. (2017). SAR Deformation Monitoring Method and Research Progress. *J. Geod. Geoinf. Sci.* 46, 1717–1733. (in Chinese). doi:10.11947/j.AGCS.2017.20170350

Conflict of Interest: The authors declare that the research was conducted in the absence of any commercial or financial relationships that could be construed as a potential conflict of interest.

Publisher's Note: All claims expressed in this article are solely those of the authors and do not necessarily represent those of their affiliated organizations, or those of the publisher, the editors and the reviewers. Any product that may be evaluated in this article, or claim that may be made by its manufacturer, is not guaranteed or endorsed by the publisher.

Advantages of publishing in Frontiers

OPEN ACCESS
Articles are free to read for greatest visibility and readership

FAST PUBLICATION
Around 90 days from submission to decision

HIGH QUALITY PEER-REVIEW
Rigorous, collaborative, and constructive peer-review

TRANSPARENT PEER-REVIEW
Editors and reviewers acknowledged by name on published articles

Frontiers
Avenue du Tribunal-Fédéral 34
1005 Lausanne | Switzerland

Visit us: www.frontiersin.org
Contact us: frontiersin.org/about/contact

REPRODUCIBILITY OF RESEARCH
Support open data and methods to enhance research reproducibility

DIGITAL PUBLISHING
Articles designed for optimal readership across devices

FOLLOW US
@frontiersin

IMPACT METRICS
Advanced article metrics track visibility across digital media

EXTENSIVE PROMOTION
Marketing and promotion of impactful research

LOOP RESEARCH NETWORK
Our network increases your article's readership